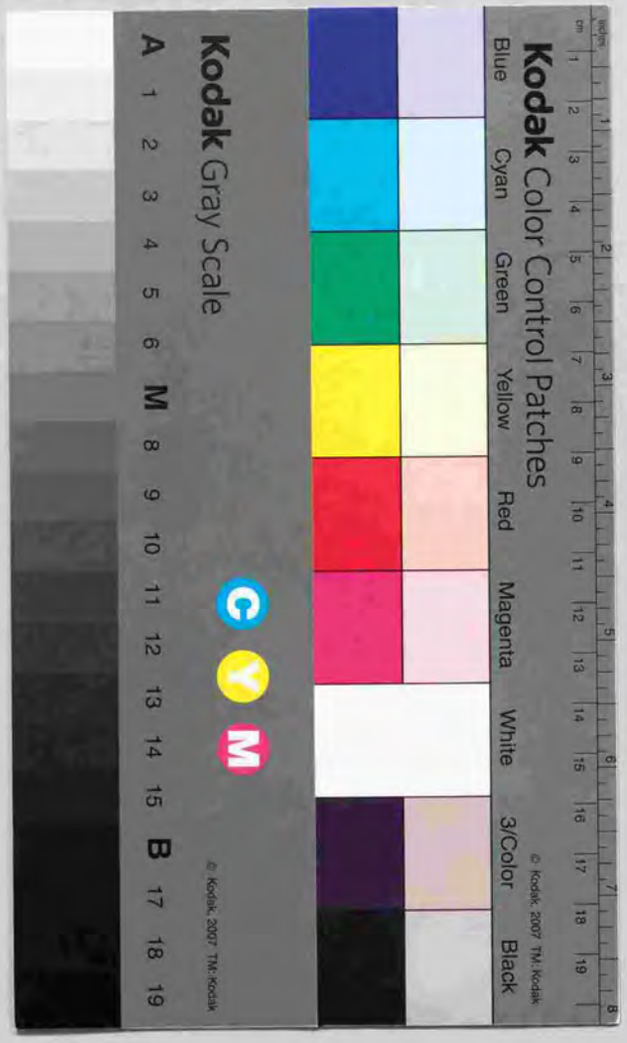

学位論文

Characteristics of Solar Flare Hard X-ray Sources as Revealed with the Hard X-ray Telescope aboard the Yohkoh Satellite

「ようこう」搭載硬 X 線望遠鏡による太陽フレアの硬 X 線源の研究

坂尾 太郎

1993 年 12 月 博士（理学）申請

(1)

Characteristics of Solar Flare Hard X–ray Sources as Revealed with the Hard X–ray Telescope aboard the Yohkoh Satellite

Taro Sakao

National Astronomical Observatory, Japan

December, 1993

Contents

Chapter 1

Extended Abstract of the Thesis

Solar flares are one of the most energetic phenomena that occur in the solar corona. The first recorded observation of a flare was made by two observers, Carrington, R.C. and Hodgson, R., independently on 1 September, 1859. They observed an intense flare – so intense that it was observable even in the visible continuum emission (white–light flare).

Although the first discovery of solar flares was made in the visible continuum light (white–light), most flares are not observed, or very hard to be observed, in white–light. On the other hand, they show strong contrast with the background emission when observed in some spectral lines such as in Hα (6563 Å). In fact, the term 'flare' itself has its origin in the Hα observations; the event looks as if fires spread in a grass field.

Since the Hα emissions (or absorptions) originate in the chromospheric layer of the solar atmosphere, a flare seen in Hα only represents chromospheric aspects of it; the whole event covers much wider phenomena and is more energetic than it looks in Hα. Total energy released by a flare sometimes reaches as high as, or even more than, 10^{32} ergs. It produces plenty of solar energetic particles, sometimes reaching relativistic energies, which then emit a wide range of electromagnetic radiation, from radio waves to γ–rays. Thus a flare is a very efficient accelerator of particles. In addition, plasmas are ejected from the sun by a flare, whose mass and velocity sometimes exceed $\sim 10^{10}$ tons and ~ 500 km/s, respectively, and shock waves propagate through the interplanetary space even beyond the Jupitar orbit.

The *Yohkoh* HXT experiment concentrates its focus on the energetic particle phenomena of solar flares; in hard X-rays we see acceleration, propagation, and confinement of energetic electrons. In this thesis, I try to fully describe the HXT experiment, from its historical background of hard X-ray flare observations, through the instrumentation, to newly acquired scientific results. The extended abstracts for the subsequent chapters follow :

Chapter 2 : Solar Flare Hard X-rays : An Introductory Review

The purpose of this chapter is to clarify the problems to be settled by the *Yohkoh* HXT experiment. First temporal and spectral characteristics of solar flare hard X-rays, based upon observations with (non-imaging) spectrometers, are briefly summarized. Then several hard X-ray emission models so far proposed are reviewed. These include:

(1) Nonthermal electron Bremsstrahlung with so-called "thick-target", "thin-target", or "trap-plus-precipitation" conditions;

(2) Thermal electron Bremsstrahlung; and from a slightly different view,

(3) Bremsstrahlung due to heated or accelerated electrons produced by ion (mainly proton) beams.

Subsequently the first hard X-ray imaging observations made in early 1980's with hard X-ray imagers aboard *SMM* and *Hinotori* are reviewed. Special attention is paid to their new findings as well as their limitations. Finally the problems to be settled by *Yohkoh* HXT are given.

Chapter 3 : Yohkoh Satellite : A Concise Summary

This chapter is to give the reader an overview of the *Yohkoh* satellite, and is organized as follows:

(1) Scientific payloads (the Hard X-ray Telescope (HXT), the Soft X-ray Telescope (SXT), the Bragg Crystal Spectrometer (BCS), and the Wide-Band Spectrometer (WBS)) : Scientific objectives, basic design, and performance are given for each instrument.

(2) Satellite basic systems: These include the power supply, attitude control, onboard data processing, command, and telemtry systems, etc. Special attention is paid to how automatically the observation mode is controled, as well as to how efficiently flare data are accumulated onto the data recorder within its limited capacity.

Chapter 4 : The HXT Experiment

The Hard X-ray Telescope (HXT) onboard *Yohkoh* is the world-first Fourier-synthesis hard X-ray imager, consisting of 64 elements. The instrument design and its main components (collimators (HXT-C), detector assembly (HXT-S), and electronics unit (HXT-E)) is described, following the design principle, the determination of baseline design, and the actual fabrication. It is stressed how the baseline design, which satisfies the scientific requirements but inevitably is a compromise with the feasibility, was actually realized.

In order to fully achieve the designed performance, HXT collimators and detectors, as well as electronics, need be carefully calibrated after integration. For this purpose many elaborated experiments were made before the launch. One of the most crucial is to precisely measure the modulation patterns of the individual collimators, which is described in detail.

Chapter 5 : Image Synthesis

Since HXT original data consist of raw photon count rates from the 64 elements, hard X-ray images of solar flares need be synthesized on the ground. An image synthesis program, supplemented by some additional tools, have been developped for this purpose. In actual image syntheses of a solar flare, the first step is to determine the image synthesis field of view in which the flare image is located. The mathematics and practice of this procedure is briefly discribed. The image synthesis principle which we adopt as the standard for the HXT image synthesis is the Maximum Entropy Method, which is discussed in detail.

Chapter 6 : The 15 November, 1991 Flare

In this chapter, HXT observations of an intense flare which clearly showed 'the double-source structure' is given. The flare occurred on 15 November, 1991 at 23:34 UT in the active region NOAA 6919 (S14W19) and was observed in unprecedented detail in hard and soft X-rays, as well as in radio and optical wavelengths. The flare showed a clear impulsive phase which is characterized by three distinct spikes in the time profile, and the subsequent post-impulsive phase. Hard X-ray imaging observations of this flare provide us with a typical example of what we would learn on the characteristics of solar flare hard X-ray sources. New findings from the analysis of this event is summarized below :

(1) During the impulsive phase, double sources are seen on both sides of the magnetic neutral line, in the energy bands above 33 keV. The double sources are most likely the footpoints of a single flaring magnetic loop. In fact they show close spatial correspondence with white-light brightenings observed with the optical telescope of SXT. On the other hand, in the 23-33 keV band of HXT, hard X-ray images show double sources at the peaks of spikes while at the valleys between them a single source located at the magnetic neutral line. This energy-dependent difference in hard X-ray ($\gtrsim$ 20 keV) sources can be understood if higher energy electrons have higher precipitation probability from the top of the flaring loop than lower energy ones. The distance between the double sources became larger with time.

(2) The following interesting characteristics of the hard X-ray double sources in the impulsive phase are revealed : (a) Hard X-ray fluxes from the double sources varies simultaneously within 0.1 s at 1σ level. This strongly suggests that hard X-rays ($\gtrsim$ 30 keV) are emitted near the footpoints of the flaring loop by accelerated electrons streaming down along the loop towards both ends. Thermal conduction fronts nor accelerated ions are unlikely to be able to explain the observed simultaneity, due to their slow velocity (typically $\sim$ 1000 km/s). (b) The double sources show asymmetry in hard X-ray flux; the brighter source is located in the weaker longitudinal magnetic field region than the darker source. This suggests that the brighter footpoint has larger electron precipitation due to weaker magnetic field convergence than the darker footpoint, hence is brighter in hard X-rays. (c) Also the brighter footpoint

shows a harder energy spectrum than the darker one. These three points will be further investigated in detail, using data from several other flares, in the next chapter.

(3) During the post-impulsive phase, the double sources are still seen in the energy bands above 33 keV, but with further increased separation in comparison with that of the impulsive phase double sources. Also the angle sustained by the line connecting the double sources and the magnetic neutral line becomes larger with time. This implies that particle acceleration still continues in the post-impulsive phase and that particle acceleration originally starts in a low lying, more sheared magnetic loop just above the neutral line and the acceleration takes place successively in overlying, less sheared loops with rising energy release sites.

(4) In the precursor phase, hard X-ray sources scatter across an area with a spatial extension greater than 1′, which is much larger than the area in which the impulsive phase hard X-ray sources are confined. This fact, together with Hα and Ca K-line observations, suggests that global re-structuring of coronal magnetic fields preceded the onset of the flare.

Chapter 7 : Observations of Hard X-ray Double Sources in Solar Flares

As is seen in the previous chapter, imaging observations of solar flare hard X-ray sources provide essential information on hard X-ray emission, propagation of accelerated electrons along the flaring magnetic loop, and acceleration processes themselves. In this chapter, a statistical study as well as detailed case studies of impulsive flares are made using imaging observations of hard X-ray sources with HXT. The main findings are summarized as follows :

(1) Out of 28 intense impulsive flares observed with HXT during the 15 months from 1 October, 1991 to 31 December, 1992, about 40 % showed double-source structure at the peak of hard X-ray emission in the 33–53 keV band. The others showed either multiple-source ($\gtrsim$ 30 %) or single-source ($\lesssim$ 30 %) structure. When double sources are seen, they are located on both sides of the magnetic neutral line. This suggests that the double sources are not formed by just a simple chance encounter of two single sources, but that they are magnetically conjugate with each other, *i.e.*, hard X-rays ($\gtrsim$ 30 keV) are emitted from the two footpoints of a single loop, which is one of the fundamental characteristics in solar flare hard X-ray emission.

(2) Detailed case studies on double sources seen in seven intense impulsive flares revealed : (a) In most cases (6 out of 7), hard X-rays are emitted from the double sources simultaneously within a fraction of a second, strongly suggesting that hard X-rays are emitted near the footpoints by accelerated electrons streaming down along the loop towards both ends. (b) For flares in which magnetic field data are available, 4 out of 5 showed that the brighter footpoint is located in the weaker magnetic field region. This suggests that the brighter footpoint has larger electron precipitation due to weaker magnetic field convergence than the darker footpoint, hence is brighter in hard X-rays. (c) The brighter footpoint tends to have a harder energy spectrum than the darker footpoint (5 out of 7). This can be understood by either of the followings : (i) Acceleration of electrons takes place parpendicular to the magnetic field line; higher-energy electrons with larger pitch angles are difficult to precipitate deep towards the darker footpoint due to the stronger magnetic field convergence than the brighter footpoint. (ii) As electrons precipitating to the darker footpoint cannot precipitate deep in the corona due to the stronger magnetic field convergence, they emit X-rays higher than those precipitating to the brighter footpoint. In this case, emissions from the darker footpoint will be a blend of thick- and thin- target emissions due to rather low plasma density as compared with the brighter footpoint where the X-rays are emitted by purely thick-target interaction. As thin-target emission produces a softer spectrum than that produced by thick-target emission for the same parent electron spectrum, the darker footpoint will have a softer energy spectrum.

Chapter 2

Solar Flare Hard X–rays : An Introductory Review

The (soft) X–rays from the sun was first detected on 6 August, 1948 with a V–2 rocket experiment performed by the U.S. Naval Research Laboratory (NRL; Burnight 1949). Subsequent experiments by the NRL group revealed that the sun is a significant emitter of X–rays and that the X–ray emission is related to solar activity (Byram *et al.* 1956, Kreplin 1961). As X–rays cannot reach to the ground due to absorption by the earth's atmosphere, observations of solar X–rays are made with satellites, rockets, or balloons, as will be described later.

When a flare occurs, significant amount of hard X–rays, not only soft X–rays, are emitted together with radiation in other wavelengths, such as radio and γ–ray. Figure 2.1 shows typical time profiles of a flare in different wavelengths. While soft X–rays show gradual time variation, hard X–rays show impulsive fluctuation in the early phase of a flare, followed by a gradual variation. The former is called the *impulsive phase* and the latter the *gradual phase* of a flare, respectively. It is generally accepted that a significant amount of flare energies is leberated during the impulsive phase, in the form of hard X–ray emission via Bremsstrahlung of impulsively accelerated particles. Therefore, hard X–rays are thought to be a powerful mean to investigate machanisms of solar flare particle acceleration and the nature of flares themselves.

In this chapter, I review spectral (section 2.1) and imaging (section 2.3) observations of solar flare hard X–ray sources, together with proposed hard X–ray emission mechanisms (section 2.2). In section 2.4 I review limitations of the previous imaging observations and problems remained for *Yohkoh* HXT.

2.1 Photon Energy Spectral Observations

2.1.1 The Spectrum

Using a balloon-borne experiment, Peterson and Winckler (1959) first detected hard X-rays from solar flares in the energy range 200–500 keV. Photon energy spectrum were guessed from this measurement consisting of only two data points. They attributed observed hard X-rays to Bremsstrahlung emission produced by high energy electrons of 0.5–1.0 MeV stopping in the solar photosphere. On the other hand, Chubb *et al.* (1966) claimed that the data which Peterson and Winckler obtained could equally be well fitted by Bremsstrahlung (free–free) emission from an isothermal plasma whose temperature exceeds 10^8 K. The thermal Bremsstrahlung spectrum can be expressed as (*e.g.*, Crannell *et al.* 1978) :

$$I(\varepsilon) = 1.3 \times 10^{-42} (n^2 V) \varepsilon^{-1.4} (k_B T)^{-0.1} e^{-\varepsilon/k_B T} \quad (\text{photons/cm}^2\text{/s/keV}) , \tag{2.1}$$

where n (/cm^3), V (cm^3), and T (K) are the density, volume, and temperature of the plasma, respectively, k_B (keV/K) is the Boltzman constant, and ε (keV) is the photon energy. $EM \equiv n^2 V$ is called the emission measure of the plasma.

Since then, various balloon-borne and spacecraft instruments have measured solar flare hard X-rays (*e.g.*, OGO–1 and OGO–3: Arnoldy *et al.* 1968; OGO–5: Kane 1969, Kane and Anderson 1970; OSO–5: Kane *et al.* 1979). These instruments measured spatially-averaged energy spectra of solar flare hard X-rays with ionization chambers (OGO–1 and OGO–3), or with NaI scintillation counters (OGO–5 and OSO–5). Energy spectra of the hard X-ray emission are, in general, roughly consistent with a power-law having a form of

$$I(\varepsilon) = A \varepsilon^{-\gamma} \quad (\text{photons/cm}^2\text{/s/keV}) , \tag{2.2}$$

(Kane 1969, Frost 1969) with the photon index γ ranging typically $3 \lesssim \gamma \lesssim 8$ (Dennis 1985).

This does not necessarily mean that the hard X-ray emission is always characterized by a single power-law spectrum (eq.(2.2)): a spectral break in the 60–100 keV range (Frost 1969, Kane and Anderson 1970, Frost and Dennis 1971) is observed for many flares. Such a double power-law or broken power-law can be expressed as :

$$\begin{aligned} I(\varepsilon) &= A \varepsilon^{-\gamma_1}, & \varepsilon \le \varepsilon_0; \\ &= A \varepsilon_0^{\gamma_2 - \gamma_1} \varepsilon^{-\gamma_2}, & \varepsilon > \varepsilon_0, \end{aligned} \tag{2.3}$$

where ε_0 is called the break energy. Elcan (1978) has studied energy spectra of 38 events observed with the hard X-ray (14–342 keV) spectrometer on OSO–7 and found that 28 events were better characterized by the double power-law fit (eq.(2.3)) or by the exponential fit (eq.(2.1)) than the single power-law fit (eq.(2.2)) at the peak of hard X-ray emission, and that the exponential and the double power-law fits were equally satisfactory. He suggested that a single-temperature thermal source with $T = 5.4 \times 10^7 - 3.6 \times 10^8$ K and $EM = 8.4 \times 10^{43} - 6.0 \times 10^{46}$ /cm^3 is responsible for the impulsive solar hard X-rays.

We need to be careful in interpreting the physics involved in the expressions such as eqs. 2.1 through 2.3. The formula is useful (or meaningful) only for parameterizing observed flare spectra. This is due mainly to uncertainties in deconvolving energy spectral response of detectors (*e.g.*, Dennis 1982). Furthermore, even if we want to derive a parent electron energy spectrum, due to a wide-band nature of the energy dependence of the electron Bremsstrahlung cross section with the scattering protons (discussed later; eq.(2.4)), it is quite difficult to extract fine details of the electron spectrum from an observed Bremsstrahlung continuum spectrum (Craig and Brown 1976).

Recently, however, solar flare hard X-rays in the energy range 15–200 keV have been obtained with very high spectral resolution (FWHM resolution less than 1 keV) (Lin *et al.* 1981, Lin and Schwartz 1987). Lin *et al.* used balloon-borne high-purity germanium (HPGe) detecters cooled with liquid nitrogen. As the spectral response of these detectors can be considered effectively as a δ-function, incident X-ray spectra can be determined from the observed count rate spectra directly, eliminating the need to assume an *a priori* spectral shape for the X-rays (Lin and Schwartz 1987). Study on the derivation of parent electron spectra from such high-resolution hard X-ray spectra, assuming Bremsstrahlung interaction, is now going on (*e.g.*, Johns and Lin 1992).

2.1.2 Spectral Evolution

In general, the hard X-ray spectrum is relatively soft at the start of the impulsive phase, becomes hardest at the peak of the emission, and then softens as the emission decreases. This soft-hard-soft behavior of the energy spectrum, typical of type B (see section 2.3.2) events, was first recognized by Kane and Anderson (1970) and later confirmed by many authors (Dennis *et al.* 1981, Dennis 1985). In some events, however, the spectrum continues to harden even after the peak (Hoyng *et al.* 1976, Kosugi *et al.* 1988). This soft-hard-harder spectral behavior is characteristic of the so-called type C (see section 2.3.2) flares (Tsuneta 1984*a*, Cliver *et al.* 1986).

2.1.3 Thermal and Non-Thermal Components

Using an NaI scintillation spectrometer aboard the OGO–5 satellite, Kane (1969) found that in the 26 June, 1968 flare, energetic ($\gtrsim 9.6$ keV) hard X-ray flares consist of two components : one showing impulsive time profiles whose peaks well correspond to the impulsive microwave radio bursts associated with the flares, while the other showing gradual time profiles which peak later than the impulsive peaks. He also found that energy spectrum of the impulsive components is consistent with a power-law and that the gradual component has an energy spectrum steeper than that for the impulsive components. He concluded that this result is consistent with the suggestion by Acton (1968) and Takakura (1969) that solar flare hard X-rays consist of both

thermal and non-thermal emission if the observed gradual component could be due to thermal emission.

The thermal component which Kane (1969) has found are commonly seen in flares with their temperature $T_e \sim (1-2)\times 10^7$ K; it may be composed of mainly heated plasma by the accelerated electrons which emit non-thermal X-rays (see section 2.3.3 for discussions on this issue). On the other hand, there are some observations which indicate the existence of very high temperature plasmas with their temperature reaching to, or exceeding 3×10^7 K (see *e.g.* Tanaka *et al.* 1982). Using balloon-borne HPGe detectors, Lin *et al.* (1981) and Lin and Schwartz (1987) observed a major flare on 27 June, 1980 and have found that below ~ 35 keV a very steep X-ray spectrum (equivalent to an ε^{-11} spectrum at 35 keV if fitted with a power-law, where ε is the photon energy) appeared at the peak of the impulsive burst and became increasingly dominant as the flare progressed. The steep spectrum was characteristic of a single temperature plasma with the temperature as high as 3.4×10^7 K, which was much higher than the previously measured values of $\lesssim 2\times 10^7$ K from soft X-ray observations. This was the first observation of the so-called super-hot component of flares; no scintillation detectors can well resolve such a steep spectrum. They suggested that the super-hot component may contain significant fraction of flare energy ($10^{28}-10^{31}$ ergs; depending on the assumed plasma density).

They also found that before the appearance of the super-hot component, the deconvolved incident hard X-ray spectrum was neither consistent with a single power-law nor a single-temperature thermal spectrum. The simplest spectral form consistent with the observation was a double power-law which breaks down at higher energies ($\gamma_1 < \gamma_2$ in eq.(2.3)). Suggesting that the double power-law shape can be reproduced at least qualitatively by thick target emission from electrons having energy spectra similar to those averaged over an auroral arc in the earth's auroral zone (Mozer *et al.* 1984), they argued that the double power-law shape indicates that electrons were accelerated by a DC electric field along magnetic field lines (Syrovatskii 1966, Knoepfel and Spong 1979).

2.2 Hard X-ray Emission Models and Their Difficulties

Solar flare hard X-ray emission is a continuum emission. It can be produced either by the interaction (Bremsstrahlung process; eq.(2.4)) of high energy electrons or ions with ambient cold medium, or by thermal Bremsstrahlung (free-free) of hot plasmas whose temperature exceeds 10^8 K. In this section I review various emission processes proposed for hard X-ray production. The processes can be divided into two processes : non-thermal and thermal processes. The non-thermal models consider beams of electrons as the primary energy badget; hard X-rays are emitted by Bremsstrahlung of the accelerated electrons with ambient cold plasma. The thermal models argue that super hot plasmas are first produced by the flare energy release and hard X-rays are emitted by thermal Bremsstrahlung (free-free) from the hot plasmas. There is other

claims such that the bulk of the released energy first resides in beams of ions and that hard X-rays are emitted by either thermal or non-thermal process of the accelerated ions. Such claims are also reviewed. As it is clear that solar atmosphere is composed of magnetized plasmas, magnetic fields (or magnetic loops) play a non-negligible role in all these processes.

2.2.1 Non-Thermal Models (Electron Beams)

Two major processes of hard X-ray production by Bremsstrahlung of non-thermal or suprathermal beams of electrons with ambient ions are *thick target* and *thin target* emissions (Brown 1971). The former assumes that electrons immediately lose their energy via (mainly) Coulomb collisions with dense ambient plasmas, such as when electrons stream downwards along magnetic loops and reaches the footpoints of the loops. On the other hand, the latter assumes that electrons continues to emit hard X-rays via Bremsstrahlung while they travel in low-density ambient plasmas along field lines. Such a case may occur when electrons are injected low in the corona and they emit X-rays as they travel upwards, or when electrons are trapped in a magnetic bottle in the corona and continue to emit X-rays.

Let us briefly summarize expressions for thick and thin target emissions. For Bremsstrahlung from electrons emitting hard X-rays in the 10–100 keV range, we may use direction-integrated, nonrelativistic, Bethe-Heitler cross section :

$$\begin{aligned}\sigma_{\rm B}(\varepsilon,E) &= \frac{8\alpha}{3}r_0^2\frac{m_ec^2}{\varepsilon E}\ln\frac{1+\sqrt{1-\varepsilon/E}}{1-\sqrt{1-\varepsilon/E}} \\ &= \frac{\kappa_{\rm BH}}{\varepsilon E}\ln\frac{1+\sqrt{1-\varepsilon/E}}{1-\sqrt{1-\varepsilon/E}} \\ &= 1.58\times 10^{-24}\frac{1}{\varepsilon}\ln\left[\left(\frac{E}{\varepsilon}\right)^{\frac{1}{2}}+\left(\frac{E}{\varepsilon}-1\right)^{\frac{1}{2}}\right] .\end{aligned} \tag{2.4}$$

Here $\alpha = e^2/\hbar c = 1/137$: the fine structure constant, $r_0 = e^2/m_ec^2$: the classical electron radius, ε: photon energy, and E: electron energy, respectively. $\kappa_{\rm BH} = (8\alpha/3)r_0^2m_ec^2 = 7.9\times 10^{-25}$ cm^2 keV is the constant in the Bethe-Heitler cross section, and ε and E are in units of keV. The energy loss rate by Coublomb collisions is expressed as follows :

$$\frac{dE}{dt} = -\sigma_{\rm E}(E)n_iv(E)E\ . \tag{2.5}$$

Here E is the electron energy, n_i is the target density, and $v(E)$ is the velocity of electrons. $\sigma_{\rm E}(E)$ is the cross section for the Coulomb energy loss and has the following form :

$$\sigma_{\rm E}(E) = \frac{2\pi e^4\ln\Lambda}{E^2} = \frac{K}{E^2}\ , \tag{2.6}$$

where $\ln\Lambda$ is the Coulomb logarithm (Spitzer 1962) and $K \equiv 2\pi e^4\ln\Lambda$, which has a value of $K \sim 55.7\pi e^4$ (e in units of esu) at $E = 50$ keV.

Thick target emission

Suppose that electrons with initial energy E_0 lose their energy via Coulomb collisions (eq.(2.5)). The number of photons per unit energy $\nu(\varepsilon, E_0)$ (photons/keV), at an energy of ε, produced by an electron is given as

$$\begin{aligned} \nu(\varepsilon, E_0) &= \int_{t_0(E=E_0)}^{t_1(E=\varepsilon)} n_i \sigma_B(\varepsilon, E(t)) v(t) dt \\ &= \int_{\varepsilon}^{E_0} \frac{\sigma_B(\varepsilon, E)}{E \sigma_E(E)} dE \ , \end{aligned} \tag{2.7}$$

by using eq.(2.5). Here n_i is the target ion (proton) density, $v(t)$ is the electron velocity. Note that the photon spectrum $\nu(\varepsilon, E_0)$ is independent of n_i, i.e. density of target ions. This is a significant characteristic of thick target emission. From the above equation, the X-ray photon spectrum $I(\varepsilon)$ (photons/cm^2/s/keV) at the earth's distance produced by electrons with their initial (or injection) energy distribution function $F(E_0)$ (electrons/s/keV) can be written as

$$\begin{aligned} I_{\rm thick}(\varepsilon) &= \frac{1}{4\pi R^2} \int_{\varepsilon}^{\infty} F(E_0) \nu(\varepsilon, E_0) dE_0 \\ &= \frac{1}{4\pi R^2} \int_{\varepsilon}^{\infty} F(E_0) \int_{\varepsilon}^{E_0} \frac{\sigma_B(\varepsilon, E)}{E \sigma_E(E)} dE dE_0 \\ &= \frac{1}{4\pi R^2 K} \int_{\varepsilon}^{\infty} F(E_0) \int_{\varepsilon}^{E_0} E \sigma_B(\varepsilon, E) dE dE_0 \ . \end{aligned} \tag{2.8}$$

If we assume a power-law distribution of injected electron flux :

$$F(E_0) = A E_0^{-\delta} \quad \text{(electrons/s/keV)} \ , \tag{2.9}$$

then the thick target hard X-ray spectrum observed at the earth will be

$$I_{\rm thick}(\varepsilon) = \frac{A}{4\pi R^2 K} \frac{1}{\varepsilon} \kappa_{\rm BH} \int_{\varepsilon}^{\infty} E_0^{-\delta} \int_{\varepsilon}^{E_0} \ln \left[\left(\frac{E}{\varepsilon} \right)^{\frac{1}{2}} + \left(\frac{E}{\varepsilon} - 1 \right)^{\frac{1}{2}} \right] dE dE_0 \ . \tag{2.10}$$

The above equation can be simplified by changing the order of integration considering the area of integration in (E, E_0) space (see, *e.g.*, Brown 1971)

$$I_{\rm thick}(\varepsilon) = \frac{A \kappa_{\rm BH}}{4\pi R^2 K} \cdot \frac{B(\delta - 2, \frac{1}{2})}{(\delta - 1)(\delta - 2)} \varepsilon^{-(\delta - 1)} \propto \varepsilon^{-(\delta - 1)} \ , \tag{2.11}$$

which is again a power-law, *i.e.*, if the electron injection spectrum is a power-law, then the resultant hard X-ray spectrum is also a power-law.

To summarize, under thick target interaction we obtain the electron injection spectrum $F(E_0) = A E_0^{-\delta}$ from a power-law hard X-ray spectrum $I_{\rm thick}(\varepsilon) = a \varepsilon^{-\gamma}$ under thick target assumption numerically as follows (Lin and Hudson 1976, Hudson *et al.* 1978) :

$$\begin{aligned} A &= 3.28 \times 10^{33} \gamma^2 (\gamma - 1)^2 B \left(\gamma - \frac{1}{2}, \frac{3}{2} \right) \cdot a \ , \\ \delta &= \gamma + 1 \ , \end{aligned} \tag{2.12}$$

where $B(p, q)$ is the beta function. Note that the hard X-ray spectrum has a smaller spectral slope than the electron spectrum ($\gamma < \delta$).

Thin target emission

In the case of thin target emission, the hard X-ray spectrum $I(\varepsilon)$ (photons/cm^2/s/keV) can be expressed as follows :

$$I_{\rm thin}(\varepsilon) = \frac{n_i}{4\pi R^2} \int_{\varepsilon}^{\infty} v(E) N(E) \sigma_B(\varepsilon, E) dE \ , \tag{2.13}$$

where $N(E)$ is, this time, the source spectrum of the injected electrons (in units of electrons/keV). Other symbols are the same as before.

For a power-law distribution of source electrons :

$$N(E) = A' E^{-\delta} \quad \text{(electrons/keV)} \ , \tag{2.14}$$

thin target emission will be

$$I_{\rm thin}(\varepsilon) = \frac{n_i A'}{4\pi R^2} \frac{\kappa_{\rm BH}}{\varepsilon} \sqrt{\frac{2}{m_e}} \int_{\varepsilon}^{\infty} E^{-(\delta + \frac{1}{2})} \ln \left[\left(\frac{E}{\varepsilon} \right)^{\frac{1}{2}} + \left(\frac{E}{\varepsilon} - 1 \right)^{\frac{1}{2}} \right] dE \ . \tag{2.15}$$

This equation can be simplified by evaluating the integral by parts :

$$I_{\rm thin}(\varepsilon) = \frac{n_i A' \kappa_{\rm BH}}{4\pi R^2} \sqrt{\frac{2}{m_e}} \frac{B(\delta - \frac{1}{2}, \frac{1}{2})}{\delta - \frac{1}{2}} \varepsilon^{-(\delta + \frac{1}{2})} \propto \varepsilon^{-(\delta + \frac{1}{2})} \ . \tag{2.16}$$

Thus, the resultant thin target emission is also a power-law.

The source electron spectrum $N(E)$ (electrons/keV; eq.(2.14)) from a power-law hard X-ray spectrum $I_{\rm thin}(\varepsilon) = a \varepsilon^{-\gamma}$ under thin target assumption is given numerically as follows (Hudson *et al.* 1978) :

$$\begin{aligned} A' &= 1.05 \times 10^{42} \frac{\gamma - 1}{B(\gamma - 1, \frac{1}{2})} \cdot \frac{a}{n_i} \ , \\ \delta &= \gamma - \frac{1}{2} \ . \end{aligned} \tag{2.17}$$

Unlike thin target emission, A' depends on the target ion density n_i. Note that in the case of thin target emission, hard X-ray spectrum has a larger spectral slope than electron spectrum ($\gamma > \delta$).

Trap plus precipitation (Partial precipitation)

A plausible situation for producing non-thermal hard X-rays is to inject and trap electrons near the top of the loop, and only a portion of the injected electrons escape from the trap and emit X-rays near the footpoints via thick target interaction. The rest of the electrons emits thin target X-rays (Takakura and Kai 1966, Brown 1974, Melrose and Brown 1976, Bai and Ramaty 1979). The trap is caused by magnetic mirroring of electrons. Such models are called trap plus precipitation models.

In some events, peak time of higher-energy hard X-ray emission is delayed as compared with lower-energy ones (Bai and Ramaty 1979, Vilmer *et al.* 1982, Bai and Dennis 1985). The trap

plus precipitation model can explain such delays by increasing electron lifetime with energy in the trap. Ratio between the numbers of trapped and precipitating electrons may change from event to event according to conditions of the trapping region.

Melrose and Brown (1976) have discussed temporal evolution of energy spectra of accelerated electrons and hard X-rays in the partial precipitation model. They have argued that the precipitation of electrons from the trap region is caused by Coulomb scattering of the electrons into the loss cone and the scattering is described in terms of diffusion in pitch angle of the trapped electrons. Rate of the pitch angle diffusion $\nu_{\rm D}$ is given as $\nu_{\rm D} = 2\nu_{\rm E}$ (Trubnikov 1965), where $\nu_{\rm E}$ is the energy loss rate of electrons due to Coulomb collisions : $\nu_{\rm E} \equiv \sigma_{\rm E} n_i v(E)$ (*c.f.* eq.(2.5)), with $\nu_{\rm E} \propto E^{-\frac{3}{2}}$. The precipitation rate $\nu_{\rm p}$ is approximated as follows with respect to the values of $\nu_{\rm D}$.

$$\begin{aligned} \nu_{\rm p} &\sim \nu_{\rm D} \qquad (\nu_{\rm D} \ll \tfrac{1}{2}\theta_0^2 \nu_{\rm b}) \\ &\sim \frac{1}{2}\theta_0^2 \nu_{\rm b} \qquad (\nu_{\rm D} \gg \tfrac{1}{2}\theta_0^2 \nu_{\rm b}) \end{aligned} \tag{2.18}$$

where θ_0 ($\theta_0 \ll 1$ has been assumed) is the loss cone angle which will be described in detail in section 6.4.2 and $\nu_{\rm b}$ is the bounce frequency of electrons in the trap. The former case in eq.(2.18) is called the weak diffusion limit where most of the accelerated electrons remain trapped while the latter called the strong diffusion limit where most of the electrons escape from the trap (Kennel 1969). They mainly considered the weak diffusion limit. In this case as the diffusion rate $\nu_{\rm D}$ is proportional to the energy loss rate $\nu_{\rm E}$ ($\nu_{\rm D} = 2\nu_{\rm E}$: Trubnikov 1965; or $\nu_{\rm D} \sim 2.9\nu_{\rm E}$: Hudson 1972), higher-energy electrons have smaller $\nu_{\rm D}$ than lower-energy electrons, *i.e.* electrons in the trap show hardening in their energy spectrum. They also have found that the emitted hard X-rays from the trap region and the loop footpoints, where the precipitating electrons emit X-rays by thick target interaction, show similar spectra in intensity and in spectral shape. In the case of the strong diffusion limit, as $\nu_{\rm p} \propto \nu_{\rm b} \propto E^{\frac{1}{2}}$ (note that the bounce frequency is proportional to the electron velocity), higher-energy electrons have higher precipitation rate towards the footpoints, which produces spectral softening of the electrons in the trap region.

2.2.2 Thermal Models

There is an alternative model for the Bremsstrahlung source responsible for the solar flare hard X-ray emission: a very high temperature plasma with $T_e \gtrsim 10^8$ K (*i.e.*, $k_B T_e \sim 10$ keV; see eq.(2.1)). In fact, thermal bremsstrahlung hard X-rays from such a plasma was one of the first proposed models to account for observed hard X-ray emission (Chubb 1966). This model has an advantage over the non-thermal thick target model such that the thermal electrons do not lose a large fraction of energy as they do in the thick target model. As the non-thermal Bremsstrahlung yield of 10–100 keV electrons is $10^{-4} - 2 \times 10^{-5}$ (Simnett 1986), non-thermal electron energies calculated from the observed hard X-ray flux assuming the thick target interaction (and a certain lower cut-off energy, say 20 keV) often exceed energies contained in soft X-ray plasmas

produced by the same flare even by an order of magnitude (see Wu *et al.* (1986) for details). In the thermal model, all the energies that thermal electrons have can, in principle, go into X-ray emission. Thus this model is much more energetically efficient than the thick target model.

Crannel *et al.* (1978) and Mätzler *et al.* (1978) have suggested that the hot plasma is confined by a strong time varying magnetic field and hard X-ray emissions are modulated by the adiabatic compression and decompression of the volume. They also predicted a correlation between X-ray emission measure and plasma temperature, which has in fact been observed for some events.

However, simple thermal models may be implausible to be adopted. For example, Kahler (1971*a*, *b*) has pointed out that electrons with $T_e \sim 10^8$ K can easily escape from the thermal plasma due to the very long collisional mean free path and hence such a high temperature plasma cannot be maintained. Also there is a problem such that the conductive cooling time of the hot plasma may be much shorter than the observed burst duration. Brown *et al.* (1979) have suggested that these points can theoretically be overcome. They argued that when electrons escape from the plasma, strong reverse currents are set up which are unstable to the growth of ion-accoustic waves. These waves (= ion-accoustic turbulent fronts) are formed on both ends of the high temperature plasma and they significantly increase electron collision frequency, hence the hot plasma is confined by these waves (see also Smith and Lilliequist 1979, Vlahos and Papadopoulos 1979).

Using joint microwave and hard X-ray data, Batchelor *et al.* (1985) studied relation between rise time of hard X-ray impulsive bursts and loop lengths estimated from radio observations, assuming that the hard X-ray and microwave emitting electrons are the same. They concluded that the hard X-ray source is confined by ion-accoustic conduction fronts which move down towards the loop footpoints at the ion-sound speed $c_S = 9100\sqrt{T_e}$ cm/s ($c_S \sim 1000$ km/s for $T_e \sim 10^8$ K).

2.2.3 Other Possibilities (Ion Beams)

Simnett (1986) has reviewed several difficulties of the electron beam hypothesis in producing hard X-rays (such as in section 2.2.2) and have proposed that the bulk of the energy in the impulsive phase is initially transferred to $10^2 - 10^3$ keV protons, instead of (beams of) electrons. He suggested that the high energy protons stream down along magnetic loops and produce high temperature plasmas at the footpoints of the loops, and that hard X-rays are emitted by thermal Bremsstrahlung from the hot plasmas whose temperature as high as $T_e \sim 10^8 - 10^9$ K. Recently Simnett (1991) and Simnett and Haines (1991) has argued that, instead of thermal bremsstrahlung, hard X-rays are emitted by electrons accelerated in a runaway process caused by a primary proton beam near the footpoints. He discussed that a primary proton beam, which is neutralized by accompanying electrons of the same velocity, propagate collisionlessly downwards towards the chromosphere. When the neutral beam reaches the chromosphere, electrons are scattered while ions continue to precipitate deeper due to difference in their mass. This produces

an electric field along the beam propagation direction, and the electric field thus produced cause runaway acceleration of electrons near the footpoints and non-thermal hard X-rays comes from interactions of the accelerated electrons in the chromosphere.

Heristchi (1986) has proposed that the hard X-rays are produced by inverse Bremsstrahlung emission of high energy protons ($\gtrsim 1$ MeV) with ambient electrons. However, such process has previously been rejected since number of protons required is so large and such protons above 10 MeV would produce nuclear γ-rays $10^3 - 10^4$ times larger than observed (Emslie and Brown 1985).

2.3 New Views from SMM and Hinotori

In 1969, first imaging observation of solar flare hard X-ray sources, though in one-dimension, was performed using a balloon-borne modulation collimator (Takakura *et al.* 1971; see Bradt *et al.* 1968 for a description on modulation collimators). Using the modulation collimator instrument, with its FWHM beam size $1.32'$, Takakura *et al.* for the first time succeeded in obtaining one-dimensional location and size of hard X-ray source in the 30–60 keV range. They found that the center of the hard X-ray source is on the line passing through the center of the Hα flare region and that the size of the source is considerably smaller than that of Hα ($\sim 1'$ in hard X-rays while $\sim 3'$ in Hα). As Vaiana *et al.* (1968) have shown that the structure of a soft X-ray source resembles that of an Hα flare, result obtained by Takakura *et al.* implies that the size of hard X-ray source is significantly smaller than that of soft X-ray source.

However, this was the only hard X-ray imaging observations of solar flares before the launch of *SMM* and *Hinotori*. Detaild study of solar flare hard X-ray sources had to be awaited until the launch of these satellites. In this section, first I briefly describe the instruments of the hard X-ray telescopes aboard *SMM* and *Hinotori*. Then I present new findings on solar flare hard X-ray sources by these satellites.

2.3.1 Instruments

SXT aboard Hinotori

The hard X-ray telescope (SXT; *Solar X-ray Telescope*, Makishima 1982. Oda 1983, Takakura *et al.* 1983) aboard *Hinotori* satellite (launched in 1981; Kondo 1982, Tanaka, Y. 1983) utilized a rotating modulation collimator with a NaI scintillation counter. The counter itself has no spatial resolution. The *Hinotori* SXT made use of the spin of the satellite for obtaining two dimensional images of solar flares. SXT could detect hard X-rays from any portion on the solar disk (*i.e.*, the field of view covered the whole sun). An image scan was made every ~ 8 s (half of the spin period). The telescope consists of two independent sets of grid-plus-detector assembly. The NaI detectors have two energy channels, one is 15–40 keV and the other 6–13 keV. The lower energy channel was only used occasionally during the decay phase of flares. Typical spatial resolution was $\gtrsim 10''$ and time resolution was ~ 8 s (see table 4.1).

HXIS aboard Solar Maximum Mission (SMM)

The Hard X-ray Imaging Spectrometer (HXIS; Van Beek *et al.* 1980) aboard the *SMM* satellite (launched in 1980) consists of 900 mini proportional counters and collimators. The collimators consist of two plates located parallel with each other and each plate has many (~ 900) pinholes on it. The collimators determines field of view of each proportional counters, thus providing angular resolution of the telescope. Unlike *Hinotori* SXT, the field of view of HXIS was only $2'40''$ (fine field of view) or $6'24''$ (coarse field of view). This rather small field of view prevented HXIS from observing many flares effectively. HXIS had 6 energy bands between 3.5–30 keV and designed time resolution was 0.5–7 *s* (table 4.1). Since effective area of each counter was small ($\lesssim 1$ cm^2), the effective time resolution was larger than 10 s.

Unfortunately, HXIS was operational only in 1980. Therefore, only a limited number of flares were observed and, unfortunately, no flare was observed simultaneously with the SXT aboard *Hinotori*.

2.3.2 Flare Characteristics

One of the important findings that *Hinotori* as well as *SMM* observations made is that, from hard X-ray point of view, solar flares can be classified into three with respect to their temporal, spectral, and spatial characteristics : *type A*, *type B*, and *type C* flares (table 2.1). This classification was first proposed by the *Hinotori* team (Tanaka 1983) and was further discussed by many authors (Tsuneta 1983, Tanaka *et al.* 1983, Sakurai 1985, Dennis 1985, Tanaka 1987, and Dennis 1988), while recently Bai and Sturrock (1989) have proposed a classification other than the canonical A,B,C, based on hard X-ray and γ-ray observations. In this section, I describe characteristics of solar flare hard X-ray sources according to the type A, B, and C classification.

Type B flares (Impulsive flares) :

Most flares belong to this type as will be described later. Type B flares show typical impulsive spikes (with time scales of a few seconds) in hard X-rays. Energy spectra of these flares show soft-hard-soft behavior (section 2.1.2) during each spike. Also, they show the double power-law (breaking down; *i.e.*, $\gamma_1 < \gamma_2$ in eq.(2.3)) or exponential shape on the rise and at the peak while they become a single power-law or double power-law which breaks up during the decay (*e.g.* Winglee *et al.* 1992). In general, type B flares consist of two phases; the impulsive phase and the gradual phase. The former consists of a chain of spikes of random amplitude for a duration from tens of seconds to $10 - 20$ minutes. The latter, though not necessarily be seen, shows a smooth, spikeless time profile.

Hard X-ray emission in type B flares originates mainly from low altitude in the corona, possibly from footpoints of magnetic loops at around the peak of the emission. Later hard X-ray sources evolve to more compact, high altitude sources. Hoyng *et al.* (1981) reported that in the case the 10 April, 1980 flare observed with HXIS, it is likely that two high energy emission patches correspond to footpoints or legs of some of loops while another emission patch which has softer spectrum than the others corresponds to the thermal source located at the top of these loops. They argued that their result favors the thick target model of the hard X-ray emission.

Some of the impulsive flares observed with HXIS showed the double-source structure. Duijveman *et al.* (1982) have studied 10 April, 21 May, and 5 November, 1980 flares, all of which showed double sources in the 16–30 keV band. They have shown that in each case, the double sources, most likely correspond to footpoints of a flaring loop, brightened simultaneously within $5 \sim 10$ s and argued that this result is strong evidence for the exsistence of electron beams and that hard X-rays are produced by the thick target interaction (see also Hoyng *et al.* 1981). However, using the Maximum Entropy image deconvolution technique, MacKinnon *et al.* (1985) studied the same events and found that the footpoints are much less visible above the noise level in the higher energy band, *i.e.*, the footpoints have softer spectrum than the midpoints of the two footpoints. Also, they argued that when taking the Poisson noise statistics into account, footpoint synchronism was either not probable at all, or substantially less close than reported by Duijveman *et al.*. They have shown that due to the poor counting statistics, the poor time resolution of the observations, and rather wide pixel size ($8'' \times 8''$), it is impossible to differentiate between an electron beam and a thermal model interpretations; a loop filled by a high temperature plasma ($T_e \gtrsim 10^8$ K) is also satisfactory for accounting for the observations.

Sakurai (1983, 1985) have compared locations of hard X-ray sources observed with *Hinotori* SXT with respect to potential magnetic fields deduced from photospheric magnetic fields. He found that the sources, showing the double-source structure, not necessarily corresponds to footpoints of loops or loop top. He concluded that magnetic fields which produce type B flares may be strongly sheared hence coronal fields derived by potential field calculation are inadequate for comparing with the type B hard X-ray sources.

Type C flares (Gradual hard flares) :

This type of flares were only observed with *Hinotori* SXT (Tsuneta *et al.* 1984*a*), not with *SMM* HXIS. It seems that type C flares occurred more frequently in 1981 than in 1980, possibly due to a change in the occurrence frequencies of different types flares according to the phase of solar cycle. Takakura *et al.* (1984*a*) have shown that among 30 flares observed with *Hinotori* SXT, 7 belong to type C. Type C flares show gradually varying hard X-ray emission on time scales of a few minutes and the flares sometimes last more than 30 minutes. Hard X-ray sources of type C flares are located high in the corona with their height $h = 2 \times 10^4 - 9 \times 10^4$ km. Source size is large as compared with those of type A or B events; typically $> 20''$ in FWHM and sometimes

reaching as large as $70'' \times 30''$ (Takakura *et al.* 1984*b*). Potential field calculations based on photospheric magnetic fields show that the sources are located at the top of a magnetic loop or at an arcade of loops where the field strength is ~ 50 G (Sakurai 1983, 1985).

Relatively strong microwaves are observed from these flares (microwave-rich events; Kai *et al.* 1985, Bai and Dennis 1985, Bai 1986). The microwave emission is emitted by the gyro-synchrotron from accelerated electrons in magnetic fields are observed from these flares (microwave-rich events; Kai *et al.* 1985, Bai and Dennis 1985, Bai 1986). Microwave spectrum show a relatively low peak frequency in comparison with type B case, suggesting that microwaves are emitted high up in the corona where magnetic fields are weaker. In fact, in a typical type C flare occurring on 13 May, 1981, hard X-ray source was located at $h \sim 4 \times 10^4$ km above the limb (Tsuneta *et al.* 1984*a*). Also the height of the microwave source derived from one-dimensional interferometric observations made at 35 GHz (Kawabata *et al.* 1983) was in agreement with this value.

One of the properties which characterizes this type of flares is that they show continuous and gradual hard X-ray spectral hardening during the course of flares (Kosugi *et al.* 1988). In fact, energy spectrum above $\gtrsim 50$ keV hardens with time with γ decreasing monotonically from $\gamma \gtrsim 5$ at the early phase of flare to $\lesssim 2$ in the late phase after the peak. Also spectrum is better fitted by a power-law; single temperature fitting is inconsistent with the observations.

The above observations suggest existence of high-energy electrons trapped in the coronal loops. Using a perfect trap model, Bai and Dennis (1985) analyzed the 13 May, 1981 flare and argued that the observed spectral hardening can well be explained by the energy-dependent decay of electrons in the ambient plasma whose density is 5×10^8 /cm^3. However, this value is two orders of magnitude smaller than the density derived from soft X-ray observations (3×10^{10} /cm^3; Tsuneta *et al.* 1984*a*). Therefore continuous energy injection at the source location is suggested during the course of type C flares.

Type A flares (Super-hot thermal flares) :

Time profiles of this type of flares (Tanaka *et al.* 1982, Tsuneta *et al.* 1984*b*) show gradual rise and fall (with time scales ~ 1 min) in the energy range below ~ 40 keV. Although impulsive emissions are seen in the higher energy range, they are weak as compared with those in type B flares. Energy spectra of type A flares can be fit by thermal emission from $T_e = 3 - 4 \times 10^7$ K plasma (X-rays below 40 keV) and a power-law component whose photon index $\gamma \gtrsim 7$ is observed above 40 keV. Radio emission from type A flares is very weak. Hard X-ray sources of type A flares are compact; whose diameter typically $\lesssim 10''$, or $\lesssim 5000$ km. Also the sources are located relatively low in the corona (< 6000 km; Tsuneta *et al.* 1984*b*).

For a limb event which occurred on 7 October, 1981, Tanaka (1987) compared evolution of positions of hard X-ray source and the Hα loop prominence system and obtained the density of the hard X-ray source to be $\gtrsim 10^{11}$ /cm^3 with either conduction or radiative cooling (Feldman

et al. 1982) taking into account. Also density of hard X-ray sources derived from the source size and Fe XXVI emission measure (Tanaka *et al.* 1982, Tsuneta *et al.* 1984*b*) exceeds 10^{11} /cm^3. Such a high density of hard X-ray sources is a characteristic of this type of flares. To confine high density ($\gtrsim 10^{11}$ /cm^3) and high temperature ($T_e > 3 \times 10^7$ K) plasmas in a loop, magnetic field strength of more than 330 G around the hard X-ray source is required (Tsuneta *et al.* 1984*b*).

Most flares belong to type B, or at least they have type B characteristics. Kosugi *et al.* (1988) have studied about 400 flares observed with HXRBS (Orwig *et al.* 1980) aboard *SMM* and with the Nobeyama 17 GHz polarimeter. They have found that only 3 events are super-hot thermal (type A), 13 events are gradual (type C), 62 are associated with microwave gradual rise and fall (GRF) events, while the others are impulsive events.

A variety of flare characteristics described above might be explained by differing environments, such as plasma density and convergence of magnetic fields, at the flare site. On the other hand, (1) the primary energy release mechanisms themselves, and (2) what determines the ratio between non-thermal particle acceleration and direct heating which may be working in type A flares, are not yet known. Detailed comparion of *e.g.* temperature and density of the flaring site in type A flares with other types of flares has led Tsuneta (1985, 1987) to argue that the Dreicer field

$$E_{\rm D} = \frac{12\pi e^3 n_e \ln\Lambda}{k_B T_e} = 3\ln\Lambda \frac{e}{\lambda_{\rm D}^2} \qquad (\lambda_{\rm D} : \text{Debye length}) \tag{2.19}$$

(Dreicer 1959) would play an important role in controlling the above (2). Also he showed that an electric field $E \gtrsim 0.3 E_{\rm D}$ with reasonable flare coronal parameters result in a runaway acceleration (*i.e.* DC acceleration) of electrons producing sufficient amount of hard X-ray fluxes to match the observations (see also Holman 1985).

Various mechanisms for the primary energy release have been proposed (Vlahos *et al.* 1984) : many of them (*e.g.* DC electric field acceleration, turbulent acceleration) seem to work equally well in solar flares and their relative importance for taking part in the acceleration processes is not yet been definitively revealed (see a review by Benz 1987).

2.3.3 Chromospheric Evaporation

Precise measurements of the Ca XIX and Fe XXV resonance line profiles with Bragg crystal spectrometers aboard *SMM* and *Hinotori* have revealed that line broadening as well as a blue-shifted component exist in the early phase of flares (Doschek *et al.* 1980, Antonucci *et al.* 1982, Tanaka *et al.* 1982). Non-thermal random velocity of plasmas, which is inferred from the line broadening, is of the order of 100 km/s. The velocity obtained from the maximum blue-shifted component reaches as high as 400 km/s (Tanaka and Zirin 1985). Flares with the blue-shifted components are only observed at a heliocentric angle < 68 deg in the *Hinotori* results (Tanaka

et al. 1982), and no systematic blue-shifts were observed in none of the analyzed 11 flares at a heliocentric angle > 60 deg (Antonucci *et al.* 1984). In limb flares, only broadened spectral lines persist (Tanaka 1986). Therefore the observed blue-shifts represent a systematic upflow of plasmas.

Antonucci *et al.* (1982) proposed the concept of chromospheric evaporation in which beams of electrons precipitate into dense footpoints of magnetic loops, emit hard X-rays via thick target interaction with ambient plasmas, and the heated plasma would evaporate into the low density corona along the loops. Canfield *et al.* (1987, 1990) and Zarro *et al.* (1988) have confirmed that there is momentum balance between the upflowing plasma derived from the blue-shifted component and the downflowing cool gas derived from the red-shifted component of the Hα line (Ichimoto and Kurokawa 1984). These observations may give strong support to the chromospheric evaporation scenario. However, there are many other scenarios that may explain the observed blue-shifted components (see, *e.g.* Canfield *et al.* 1990, Winglee *et al.* 1992).

The chromospheric evaporation scenario has a close relationship with the so-called Neupert effect (Neupert 1968, Hudson 1991). The Neupert effect predicts that time derivative of soft X-ray light curve would give hard X-ray (instantaneous) count rates based on the assumption that hard X-rays are emitted by thick target emission of precipitating electrons interacting with cool ambient plasma near the footpoints. While electrons emit hard X-rays via electron-ion Bremsstrahlung, they lose significant amount of energy via electron-electron scattering. As the energy deposited by electrons may heat the plasma, soft X-rays from the heated plasma are expected to be the time integral of the hard X-ray count rates. Also, the hot plasma would evaporate upwards in the corona (*i.e.*, chromospheric evaporation), thus is observed as the blue-shifted components.

2.4 Problems Remained for Yohkoh HXT

There was a great controversy between *Hinotori* SXT and *SMM* HXIS results in the early phase of observations. Most of the flares with SXT observed showed single sources; for example Takakura *et al.* (1984) have studied hard X-ray images of 30 intense *Hinotori* flares and found that in most cases hard X-ray images show the single-source structure. On the other hand, in a few cases hard X-ray images observed with HXIS showed double-sources. This discrepancy may be explained as follows : (1) Occurrence frequency of each type of flares changed with the phase of solar cycle: In 1980, *SMM* observed mostly type B flares while after 1981 type A and C flares occurred more frequently than in 1980 and they were well observed with *Hinotori*. Hard X-ray sources of type A and C flares may show different source structure (possibly single sources) from those of type B flares. (2) Angular resolution of *Hinotori* SXT was not sufficient enough to resolve fine structures of hard X-ray sources. Tsuneta (1987) suggested that this is in fact the case and he pointed out that we would see more footpoint emissions (manifested

themselves as double sources) with telescopes with higher angular resolution than SXT. (3) Thermal emission from plasmas with temperature $T_e = (1-2) \times 10^7$ K may have contaminated the energy bands of SXT as well as HXIS. In this case, we may observe emissions from high temperature plasmas which are supposed to be located at the loop top and dominated over the emissions from the footpoints, hence showing single-source structure. Sakurai (1991) has pointed that if the detector had been more sensitive to higher energy X-rays than SXT's, we would have observed the X-ray emission more concentrated near the loop footpoints in the case of type B flares.

As for the origin of hard X-ray emission, especially in type B flares, whether the emissions are of non-thermal or thermal origin is not yet known. An observational key to solve this question is to investigate footpoint synchronism as was attempted by Duijveman *et al.* (1982). Since sensitivity of HXIS was not very high, such an attempt has not yet been successful.

To investigate whether the chromospheric evaporation is actually taking place in (at least type B) flares would give an essential clue to reveal the role of accelerated electrons in solar flares. However, due mainly to lack of imaging observations in purely non-thermal energy range (say, $\gtrsim$ 30 keV), such an investigation has not yet fully been done.

In summary, despite fruitful success and findings on the new aspects of solar flare hard X-ray emission with *SMM* and *Hinotori*, these results need to be considered as somewhat preliminary ones. Problems listed up above, which are essential to reveal mechanisms of hard X-ray production, propagation of accelerated particles, and particle acceleration themselves, remain unsolved. The hard X-ray telescope (HXT) aboard *Yohkoh* satellite aims to give answers to these problems. In the subsequent chapters, we will see how solar flare hard X-ray sources look like and what kind of new and essential findings are made with HXT.

Table 2.1: Classification of solar flares proposed by the *Hinotori* team.

Flare type	Time profile	Spectrum	Suggested origin
Type B (impulsive flare)	Impulsive variability	Power-law (or exponential) above $\sim$ 15 keV	Impulsive acceleration of particles
Type C (gradual hard flare)	Spikeless broad peak	Power-law with gradual hardening	Continuous acceleration of electrons (partial trapping)
Type A (super-hot thermal flare)	Gradual rise and fall	Thermal emission with $T_e \sim (3-4) \times 10^7$ K	Direct heating of coronal plasma

Figure Captions

Figure 2.1: A schematic representation of time profiles of a typical solar flare in different wavelengths (after Kane 1974).

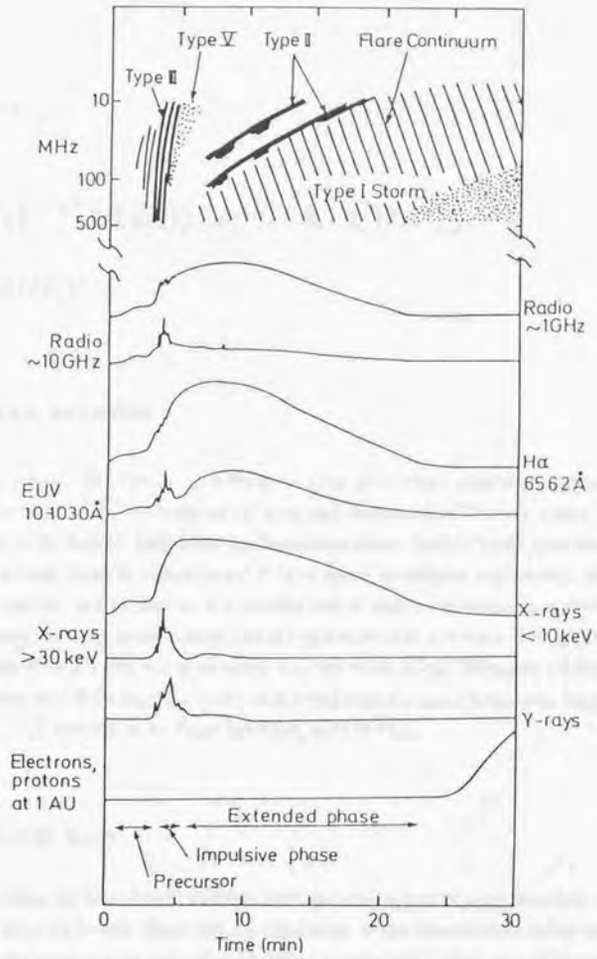

Figure 2.1

Chapter 3

Yohkoh Satellite : A Cocise Summary

3.1 Yohkoh Satellite

Yohkoh (Ogawara *et al.* 1991; figure 3.1) is the second Japanese solar–observing satellite following *Hinotori*. It was launched by the Institute of Space and Astronautical Science, Japan (ISAS) at 11:30 local time on 30 August, 1991 from the Kagoshima Space Center (KSC) with the M–3SII–6 launcher. Principal scientific objectives of *Yohkoh* are to investigate high energy phenomena related to solar flares, such as particle acceleration and X–ray/γ–ray emission in flares, as well as pre–flare energy build-up in the corona and the global coronal structure. For achieving these objectives, *Yohkoh* carries two X–ray imagers, *i.e.*, the Hard X–ray Telescope (HXT) and the Soft X–ray Telescope (SXT), together with two spectral analysis instruments (the Bragg Crystal Spectrometer (BCS) and the Wide Band Spectrometer (WBS)).

3.1.1 Spacecraft Body

Yohkoh is a rectangular box–shaped satellite with the dimensions of approximately 100 cm $\times$ 100 cm $\times$ 200 cm, and weighs about 380 kg. The body of the spacecraft is made up of seven panels : one center panel and six side (or surrounding) panels. HXT, SXT, and BCS are mounted on either side of the center panel. The center panel acts as a common optical bench for these instruments (figure 3.2). WBS is mounted on the top panel which faces the sun. Two external solar–cell paddles, each of which consists of three separate panels, are attached on two side panels of the spacecraft. The solar paddles supply $\sim$ 570 W of electric power during spacecraft daytime at the beginning of mission.

3.1.2 Orbit

The initial orbit of *Yohkoh* is semi-circular with its eccentricity $e \sim 0.02$ and the semi-major axis $\sim$ 7,500 km. Its apogee and perigee are about 792 km and 517 km, respectively. The inclination of the orbit is $i \sim 31.3°$, and the period is $P \sim 97$ min. *Yohkoh* revolves around the earth typically 15 times in a day. Figure 3.3 shows the trajectory of the orbit projected on the earth.

The spacecraft enters shadow of the earth (*i.e.*, the sun is hidden by the earth when viewing from the spacecraft) for about 40 min every revolution around the earth. This period is called 'spacecraft night'. When *Yohkoh* is in spacecraft night, no solar observations made but cosmic γ-ray burst observations (*c.f.* section 3.2.4) are continuously conducted.

Most part of the spacecraft orbit is below the radiation belt which surrounds the earth above the equator. However, when the spacecraft passes above Brazil (and nearby South Atlantic Ocean area), it enters the radiation belt because the altitude of the belt is anomalously lower there (SAA: South Atlantic Anomaly of the radiation belt). During the SAA passage most of the high voltage power supplies are turned off so as to protect the instruments from damages and accidents caused by intense particle radiation.

3.1.3 Operation

Out of the 15 revolutions of *Yohkoh* around the earth, we can send/receive signals to or from the satellite at KSC (which is called uplink and downlink, respectively) typically 5 times in a day. The contact times range from $\sim$ 12 to $\sim$ 16 minutes according to the elevation of the sattelite. During these KSC contacts, commands are uplinked to *Yohkoh* and observed data are downlinked to the ground (see section 3.3.3 and 3.3.4 for details). Besides KSC contacts, we have about 10 contacts in a day at NASA's Deep Space Network (DSN) stations; Madrid, Canberra, and Goldstone. During the DSN contacts, only downlinks of data are conducted; no command is uplinked to *Yohkoh*.

3.1.4 Attitude Control

Since two major scientific instruments aboard *Yohkoh*, namely HXT and SXT, take images of the sun with high spatial resolutions of 5″ and 2″, respectively, it is essential to precisely control the attitude of the spacecraft. *Yohkoh* is a three-axis stabilized spacecraft with its Z-axis pointing towards the sun center. Y-axis is directed parallel to the solar north-pole direction. Stability of the Z-axis pointing is $\sim 1''$/s and several arcsec/min. For the attitude control of the spacecraft, following attitude sensors send signals to the Attitude Control Electronics (ACE) : Inertial Reference Unit (IRU), Two-dimensional Fine Sun Sensor (TFSS), Non-spin type Solar Aspect Sensor (NSAS), Star Tracker (STT), and Geomagnetic Aspect Sensor (GAS). TFSS and NSAS monitor the position of the sun and provides attitude information attitude around X and

Y axes of the satellite. Sun-presence signals from NSAS is also used for triggering interruption OGs (section 3.3.3) for day-night transition of the spacecraft. STT monitors the position of Canopus, providing attitude information around Z axis. IRU (high-precision gyros) and GAS (monitors earth's magnetic fields) provides information around the three axes.

Signals sent to ACE are processed by the Attitude Control Processor (ACP). Then, attitude control signals are sent from ACE to three types of actuators : Momentum Wheels (MW), Magnetic Torquers (MTQ), and Control Momentum Gyros (CMG).

Figure 3.4 shows a block diagram of various instruments which compose the satellite. Functions of several of these instruments are described in this chapter.

3.2 On-Board Scientific Instruments

3.2.1 Hard X-ray Telescope (HXT)

HXT (Kosugi *et al.* 1991; figure 3.5) is a Fourier-synthesis type telescope which takes images of solar flares with advanced capabilities over the previous hard X-ray telescopes aboard *SMM* and *Hinotori*. Its angular and temporal resolutions are $\sim 5''$ and 0.5 s, respectively, with the energy range of 15–100 keV (nominal values). The field of view of HXT covers the whole sun with the basic 'synthesis aperture' (*c.f.* section 4.1) being 2′06″. HXT consists of 64 bi-grid modulation subcollimators (SC's). Each of them samples a two-dimensional spatial Fourier component of the hard X-ray brightness distribution. A photomultiplier tube with a NaI(Tl) crystal is used as an X-ray detector for each subcollimator. Details of HXT are described in the next chapter.

3.2.2 Soft X-ray Telescope (SXT)

Since the *Skylab* observations in early 1970's, it has been known that soft X-ray imaging observations of solar corona provide direct information on structures of the X-ray emitting corona through which we can infer coronal magnetic field topology, as well as temperatures and emission measures of the coronal plasma at individual points in it. In order to understand energy release mechanisms in solar flares, it is of crucial importance to know what magnetic field topology leads to the occurrence of solar flares and how magnetic energy is exclusively converted into other forms in flares. Even apart from flare physics, it is quite important to study coronal magnetic field structure and physical conditions (temperature, density, etc.) of coronal plasmas in time scales ranging from minutes (*e.g.*, for studies on transient phenomena such as jets) to years (*e.g.*, for studies on solar cycle dependence of coronal magnetic fields).

SXT (Tsuneta *et al.* 1991; figure 3.6) is a grazing incidence reflecting telescope in the soft X-ray band (3–60 Å, or 0.2–4.1 keV) developed under a Japan-U.S. collaboration. SXT has advanced characteristics over the soft X-ray telescope aboard *Skylab* in that it takes images with (a) high cadence, especially suited for imaging dynamic phenomena such as flares, (b) with

high dynamic range and angular resolution, and (c) with continuous imaging of the corona over several years.

Optical surface of the SXT mirror consists of two hyperboloids of revolution, which give an overall focal length of $\sim$ 1.4 m (Nariai 1987, 1988). This optics provides better angular resolution for a wider field on a flat focal plane than the familiar paraboloid–hyperboloid combination. SXT is one of the first instruments to be flown in orbits that utilizes a charge coupled device (CCD) (1024 $\times$ 1024 pixels) as a focal plane X–ray device. Pixel size of the CCD is 18 μm $\times$ 18 μm, or 2.46″ $\times$ 2.46″. The field of view of SXT is $\sim 42' \times 42'$, thus covering the whole sun. Two filter wheels and a shutter mechanism are mounted in front of the CCD detector to provide soft X–ray images with desired energy band and exposure. Soft X–ray data from SXT consist of two kinds of image data : Full Frame Images (FFIs) and Partial Frame Images (PFIs), so as to meet scientific requirements as much as possible within limited telemetry capacity as is shown below. FFIs are the full sun images whose cadence is lower (typically once in 5 $\sim$ 10 minutes) than that of PFIs. PFIs consist of a portion (*e.g.* 64 $\times$ 64 pixels) of full sun images and are taken frequently (*e.g.* once in 15 s). While FFIs are suited for studying global structure of coronal magnetic fields, PFIs are suited for continuously observing dynamic phenomena, such as flares and evolution of active regions.

It is of crucial importance to precisely overlay soft X–ray images of the solar corona with *e.g.* Hα, magnetograph, and radio images taken at ground–based observatories. Such an overlay provides stereoscopic information on various physical processes which take place along magnetic loops. For this purpose, in addition to the X–ray optics described above, SXT has an aspect telescope (in visible light) whose optical axis is co–aligned (within $\sim 1''$) with that of the X–ray telescope. With this aspect telescope, images of the photosphere such as those of sunspots, plages, white–light flares, and the visible solar limb are taken nearly simultaneously with soft X–ray images.

Observations with SXT are carried out in a sophisticated manner. A sequence of observations (*e.g.* selection of filter pairs and exposure duration) is intelligently controlled by an on–board microprocessor (data processor observation control table (SXT Table). The SXT table is revised by a ground observer according to the activity of the sun as well as special operation plan of SXT observations.

3.2.3 Bragg Crystal Spectrometer (BCS)

High temperature plasmas ($T_e \gtrsim 10^7$ K) are produced as a result of energy release in solar flares. X–rays are emitted from these plasmas as line emission from ions with various ionization states as well as continuum emission by thermal Bremsstrahlung (free–free). The line emission is an excellent measure to diagnose physical parameters, such as temperature and emission measure, of the hot plasmas.

Using Bragg reflection on bent crystals, BCS (Culhane *et al.* 1991), a U.K.–Japan joint experiment, takes energy spectrum of X–rays in four wavelength bands with high energy resolution ($\lambda/\Delta\lambda \sim$ a few thousand). BCS consists of four bent–crystal spectrometers with four position sensitive (wedge–wedge type) proportional counters (figure 3.7). The four wavelength bands cover S XV (5.0385 Å), Ca XIX (3.1769 Å), Fe XXV (1.8509 Å), and Fe XXVI (1.7780 Å), respectively. Through the line spectroscopy in these wavelength bands, BCS obtains information on the temperature, emission measure, and motion of hot plasmas produced in solar flares. Figure 6.6 (b) shows an example of Bragg crystal spectra obtained with BCS in the Ca XIX energy band. BCS has almost ten times larger sensitivity in comparison with the previous Bragg crystal spectrometers aboard *SMM* (Acton *et al.* 1980), *P78–1* (Doscheck 1983), and *Hinotori* (Kondo 1983). This high sensitivity enables BCS to observe flares with higher temporal resolution ($\lesssim 1$ s) than the previous instruments.

BCS has its own microprocessor which records BCS data with high time resolution (~ 1 s) into its own queue memory during the course of a flare. At the times when the spacecraft enters night after observing the flare, the microprocessor starts to transfer the stored data to DP and the data are then edited as telemetry outputs (specifically recorded onto BDR; section 3.3.2). In addition to the data stored in the queue memory, BCS continuously transmits observed data to DP with lower temporal resolution than the stored data both in the flare and quiet modes (see section 3.3.1).

3.2.4 Wide Band Spectrometer (WBS)

WBS (Yoshimori *et al.* 1991) observes soft X–ray, hard X–ray, and γ–ray spectra of flares in a wide energy range at one time. Emissions in hard X–rays and γ–rays include continuum Bremsstrahlung emission from accelerated electrons as well as line emission of nuclear γ–rays. Soft X–rays are produced by thermal Bremsstrahlung (free–free) emission of plasmas and also by line emission (such as of Fe ions). Energy spectra in this wide energy range are expected to provide us with usuful information on high energy particles and high temperature plasmas produced in flares.

WBS consists of four types of spectral analysis instruments : the Soft X–ray Spectrometer (SXS), the Hard X–ray Spectrometer (HXS), the Gamma–Ray Spectrometer (GRS), and the Radiation Belt Monitor (RBM). The SXS, HXS, and GRS observe high energy X–rays and γ–rays from solar flares. Especially the GRS detectors have higer sensitivity to X–rays and γ–rays than previous detectors by use of BGO ($Bi_4Ge_3O_{12}$) crystals as scintillators. A brief description on SXS, HXS, and GRS is given in table 3.1 (see also figure 3.8). A wide spectral range of 2 keV to 100 MeV is covered with these three instruments. In the hard X–ray range, HXS has 32 energy channels between 20–600 keV for the pulse–height (PH) data with temporal resolution of 1 s, which enables detailed study of solar flare energy spectra. For the pulse–count data (PC), which provides high temporal resolution of 0.125 s, HXS has 2 energy channels (20–50, and 50–600 keV). Numbers of energy channels as well as temporal resolution of WBS output data

are summarized in table 3.2.

In addition to providing energy spectral information of flares, the spectrometers act as flare-alart instruments which trigger the flare mode (section 3.3.1) of *Yohkoh*. Currently, output signals from SXS is used for triggering the flare mode.

RBM is not a solar observation instrument. Facing parpendicular to the sun, it monitors radiation belt environment of the spacecraft. RBM consists of two different types of detectors. One is a NaI (Tl) scintillation detector and the other is a Si detector (semi-conductor device). These two detectors are directed parpendicular to the sun so that they are insensitive to solar flare X-rays and γ-rays. When the pulse count rate from the NaI detector or the Si detector exceeds a certain threshold level, an alarm signal for the radiation belt passage is sent to DP. When DP receives this alarm, it makes several (scientific) instruments reduce their high voltage supplies in order to protect the instruments (see also section 3.1.2).

WBS has a capability of not only observing solar flares, but also it can observe cosmic γ-ray bursts. HXS and the NaI detector of RBM are also utilized as a cosmic γ-ray burst detecting system when the sun is quiet or the spacecraft is during night. If the HXS pulse count rate in 50-600 keV or the RBM pulse count rate in 60-300 keV exceeds a certain threshold level, both pulse count data and pulse height data are recorded as cosmic γ-ray burst data. The data are temporalily stored in a transient memory of WBS and is telemetered down to the ground at the beginning of reproduction of the Bubble Data Recorder (BDR; see section 3.3.2).

3.3 Commands, Data Processing, and Telemetry Output

3.3.1 Data Processor and Mode Control

On-board scientific instruments, especially SXT, need be controlled in a sophisticated way so as to exploit their capabilities within the limited telemetry data rate and capacity of BDR (section 3.3.2). This control is achieved by the Data Processor (DP). The DP aboard *Yohkoh* automatically controlls the observing mode. The DP also controlls operation of the on-board instruments, collects data from them, and edits the data in several formats. Data thus collected and edited by DP are then recorded onto BDR or telemetered directly to the ground.

Yohkoh has four observing modes (flare, quiet, night, and BCS-out modes) and three telemetry data rates (bit-rates; high : 32 kbps, medium : 4 kbps, and low : 1 kbps). Observing modes and telemetry data rates are closely coupled with each other. For instance, data in flare mode can only be recorded in high or medium bit-rates, and the data rate is so controlled as to record the flare impulsive phase data in high time resolution. Night time data, in which no solar observation data are included, are recorded only in low bit-rate. Combination of the observing modes and the bit-rates is called the DP mode. For instance, flare-mode with high bit-rate is called flare-high mode and so on. The DP changes the DP mode automatically according to

various events such as occurrence of flares (flare-high mode is triggered) or sunset (night-low mode is triggered) by the interruption OGs (see section 3.3.3).

3.3.2 Bubble Data Recorder (BDR)

Data taken between two downlink stations are recorded onto an on-board bubble memory called Bubble Data Recorder (BDR). BDR can record 10 Mbytes of data ($\sim$ 42 min in the high bit-rate). Recorded data are downlinked at KSC or DSN (Deep Space Network) stations. The BDR is quite often filled up with recorded data since time intervals between two downlink stations are usually longer than the time interval in which BDR can record data in high bit-rate.

When the BDR is filled up with data, newly recorded data usually overwrite older data. Since solar flares are transient phenomena, DP adopts a unique rule to protect flare data from overwriting. The flare data is protected in such a way as follows. *Data importance level* is set to newly acquired data while *write protection level* to the data already recorded on the BDR. The BDR is devided into 20 blocks and the latter level are set for each of the BDR blocks. The recorded data is protected from overwriting unless the data importance level is higher than the data protection level. For example, flare data usually has data importance and write protection levels of 2 while quiet sun data has data importance level of 1 and write protection level 0. This protects flare data (protection level 2) from being overwritten by quiet sun data (importance level 1), while quiet sun data are overwritten by newly acquiered quiet sun data as well as flare data.

It is of crucial importance, especially for SXT, to study pre-flare coronal conditions which eventually lead to explosive energy release. With this respect, BDR has a unique capability to protect pre-flare data as well as flare data themselves. When a flare occurs, the write protection level of a BDR block just prior to the flare-recorded BDR block is re-set to the same level as the flare-recorded block itself. In addition to the protection of pre-flare data, non-flaring full-sun images taken with SXT are protected as follows : If quiet mode data are continuously recorded for more than 4 BDR blocks, then the write protection levels of the first 4 blocks are re-set to the highest level of 3. This enables us to obtain daily full-sun images and to study long term changes in structures of coronal magnetic fields.

3.3.3 Commanding

All operations of the spacecraft and of the on-board instruments are performed by uplink commands. These uplink commands are sent from KSC during contacts of about 15 minutes duration each for 5 orbits per day. Commands uplinked to *Yohkoh* from the ground are first demodulated and decoded by the command decoder (CMD) and then interpreted by the telemetry command unit (TCU). TCU distributes each interpreted command to the instrument specified by the instrument code included in the command.

Besides discrete commands that are executed individually, there are packages of commands called OGs (Organized Commands). An OG can contain up to 32 discrete commands. When an OG is issued, each command contained in the OG is sequentially executed every 0.25 s. OGs are edited by commands and stored in the TCU memory, which can store 128 OGs. Several OGs are automatically triggered according to interruption messages from specific on–board instruments. For example, sunrise/sunset OGs (for initiating and ceasing observations) are trigged by sun–presence signals from a sun sensor (NSAS), and a flare OG (setting up for observing flares) by soft X–ray count rates from SXS. Several OGs are triggered for emergencies like low voltage of the batteries, failure in spacecraft attitude control, and so on. Such OGs which are automatically triggered are called the 'interruption OG's.

When *Yohkoh* is out of contact from KSC, spacecraft operations such as downlink at DSN stations need be controlled by a program timer. The TCU has a function of issuing a series of OGs at specified times with the minimum interval of 32 seconds. This series of OGs is called an operation program (OP). An OP can contain up to 128 OGs. The operation according to OP is initiated by an OP START command. Usually one OP is uploaded every day so that it covers one day of operation.

SXT tables (*c.f.* section 3.2.2) are uploaded to the spacecraft in a similar way as OPs.

3.3.4 Telemetry

Communications between *Yohkoh* and ground stations are conducted through two telemetry channels; one at S–band (2.2 GHz) and the other at X–band (8.4 GHz). At the KSC, the S–band telemetry is used for receiving commands and transmitting real–time data at 32 kbps. The X–band telemetry is used for transmitting reproduced data from BDR at 262 kbps. On the other hand, at DSN stations only BDR reproduced data are transmitted to the ground using S–band (262 kbps) and no real–time data is available during the BDR dump.

Once data are transferred to DP, DP edits the data into the so–called telemetry frame format and records them onto BDR and also directly downlinks them to the ground. The telemetry frame format consists of 64 frames per each major frame (2 s for bit–hi, 16 s for bit–med, and 64 s for bit–low). Each frame consists of 128 words (= 128 bytes). Data from the on–board instruments have their telemetry allocation according to the current frame format, which is specified by the DP mode. For example, in the quiet–mode, SXT data (quiet sun soft X–ray images) have large telemetry allocation while in the flare–mode some of the SXT data allocation is replaced by flare data from HXT. Basic data such as status of each scientific instruments have their own telemetry allocation regardless of the DP modes.

3.4 Data Archive

3.4.1 Data Flow and SIRIUS Database

Telemetry data downlinked at KSC is directly transferred to ISAS at Sagamihara, while data from DSN stations are once transferred to the Jet Propulsion Laboratory (JPL) at Pasadena, U.S., then transferred to ISAS through a NASA Communication (NASCOM) line. Both KSC and DSN downlinked data are archived in a database called SIRIUS in their raw telemetry format (*c.f.* section 3.3.4). SIRIUS contains not only *Yohkoh* data but all the data from ISAS satellites and rocket experiments. Data archived in SIRIUS are accessed by mainframe computers at ISAS.

3.4.2 Reformatted Database

In addition to the SIRIUS database, there is another database for *Yohkoh* called 'reformatted database' (Morrison *et al.* 1991). This database is created from SIRIUS. Here all the *Yohkoh* data are re–formatted so that data from each scientific instruments (HXT/SXT/BCS/WBS) and attitude data are contained separately in the reformatted database. The reformatted database is accessed on workstations and it makes analyses of *Yohkoh* data and comparison with data from ground–based observatories much easier. The reformatted data are copied onto magnetic medium (EXABYTE tapes) and are distributed to many institutions including foreign countries.

Table 3.1: WBS Instruments

Instruments	Detector	Energy range
SXS	two gas proportional counters (Xe gas)	2–30 keV
HXS	a photomultiplier with a NaI (Tl) crystal	20–600 keV
GRS	two photomultipliers with BGO* crystals	0.2–100 MeV

(*) $Bi_4Ge_3O_{12}$.

Table 3.2: Number of energy channels and temporal resolution of the WBS outputs. In the following SXS–1/2 corresponds to two different gas proportional counters and GRS–1/2 to two detector photomultipliers (after Yoshimori *et al.* 1991).

Spectrometer	Output	PH-data (time resolution)	PC-data (time resolution)
SXS	SXS-1	128-ch (2–30 keV) (2 s)	2-ch (0.25 s)
	SXS-2	128-ch (2–30 keV) (2 s)	2-ch (0.25 s)
HXS	HXS	32-ch (20–600 keV) (1 s)	2-ch (0.125 s)
GRS	GRS-1	128-ch (0.2–10 MeV) (4 s)	4-ch (0.25 s)
		16-ch (8–100 MeV) (4 s)	2-ch (0.5 s)
	GRS-2	128-ch (0.2–10 MeV) (4 s)	4-ch (0.25 s)
		16-ch (8–100 MeV) (4 s)	2-ch (0.5 s)

Figure Captions

Figure 3.1: A schematic view of *Yohkoh* satellite. The scientific instruments, Hard X-ray Telescope (HXT), Soft X-ray Telescope (SXT), Bragg Crystal Spectrometer (BCS), and Wide Band Spectrometer (WBS) detectors (SXS, HXS, GRS, and RBM) as well as other instruments are indicated in the figure. The spacecraft coordinates are given at the bottom right.

Figure 3.2: Inside view of *Yohkoh* satellite seen from $+Z$ direction (*top*; top view) and $-X$ direction (*bottom*; side view). HXT and SXT optics are mounted on the center panel, which acts as a common optical bench for the two.

Figure 3.3: Orbit projection of *Yohkoh* satellite on the earth. Locations of three DSN stations (Goldstone, Madrid, and Canberra) as well as Kagoshima Space Center (KSC) are shown.

Figure 3.4: A block diagram of various instruments aboard *Yohkoh* satellite. Functions of some of these instruments are descibed in the text.

Figure 3.5: Schematic drawing of the HXT instrument. HXT consists of three major parts : the X-ray optics (collimator; HXT–C), the detector assembly (HXT–S), and the electronics box (HXT–E). HXT–C is mounted on the center panel of the spacecraft body while HXT–S on the base plate and HXT–E on one of the side panels. The aspect sensor system (HXA) is installed along the central axis of HXT–C and HXT–S (after Kosugi *et al.* 1991).

Figure 3.6: Schematic illustration of the optical concept of SXT (*top*), and sub–assemblies which constitutes SXT (*bottom*) (after Tsuneta *et al.* 1991).

Figure 3.7: BCS detectors. The units BCS–A and BCS–B are mounted on the opposite sides of the spacecraft center panel. Both BCS–A and B consists of two spectrometers. Fe XXVI and Fe XXV line profiles are obtained with BCS–A, while Ca XIX and S XV profiles with BCS–B (after Culhane *et al.* 1991).

Figure 3.8: Cross-sectional view of SXS (*left*), HXS (*middle*), and GRS (*right*) detectors. HXS and GRS consist of photomultiplier tubes with scintillation crystals while SXS consists of a gas proportional counter (after Yoshimori *et al.* 1991).

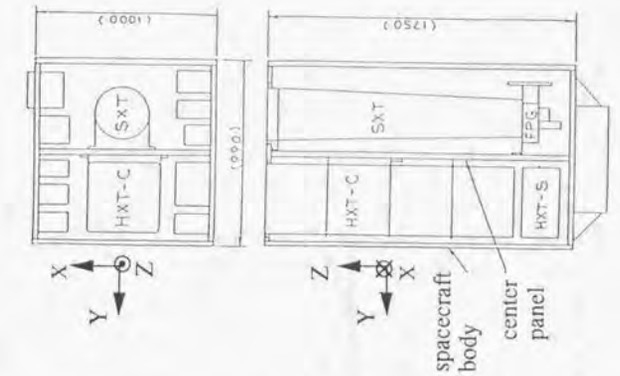

Figure 3.2

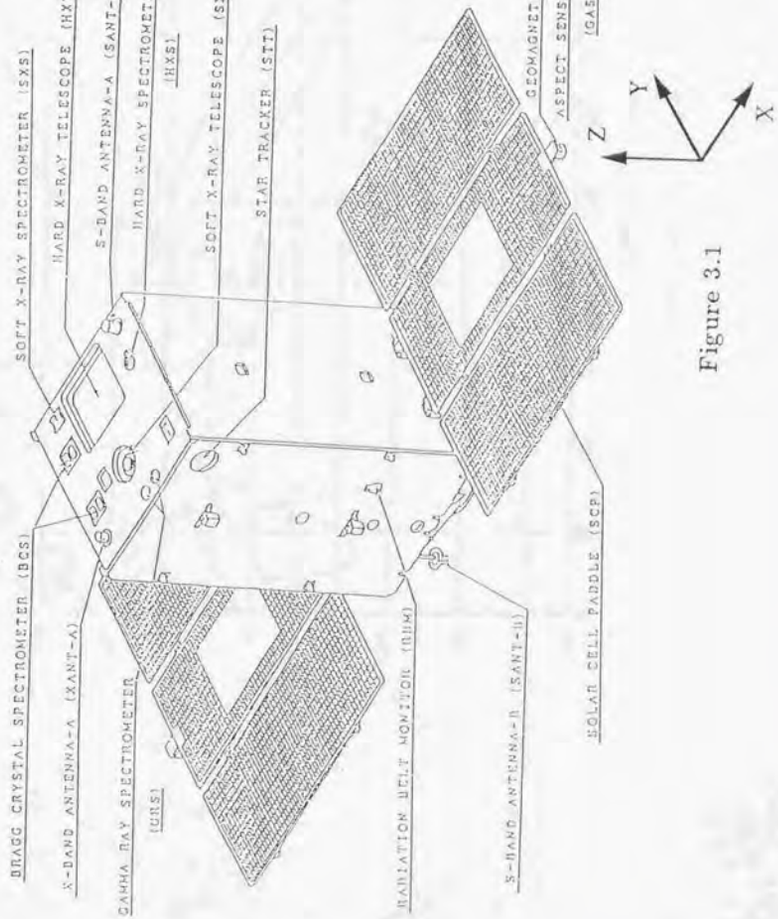

Figure 3.1

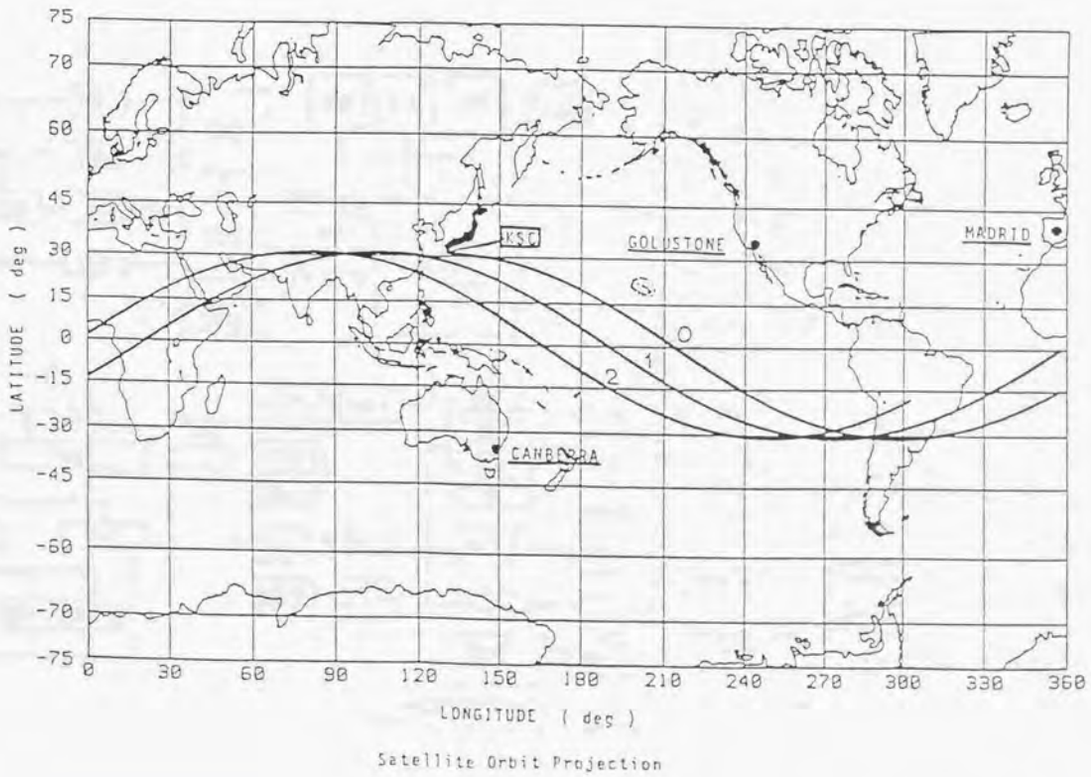

Satellite Orbit Projection

Figure 3.3

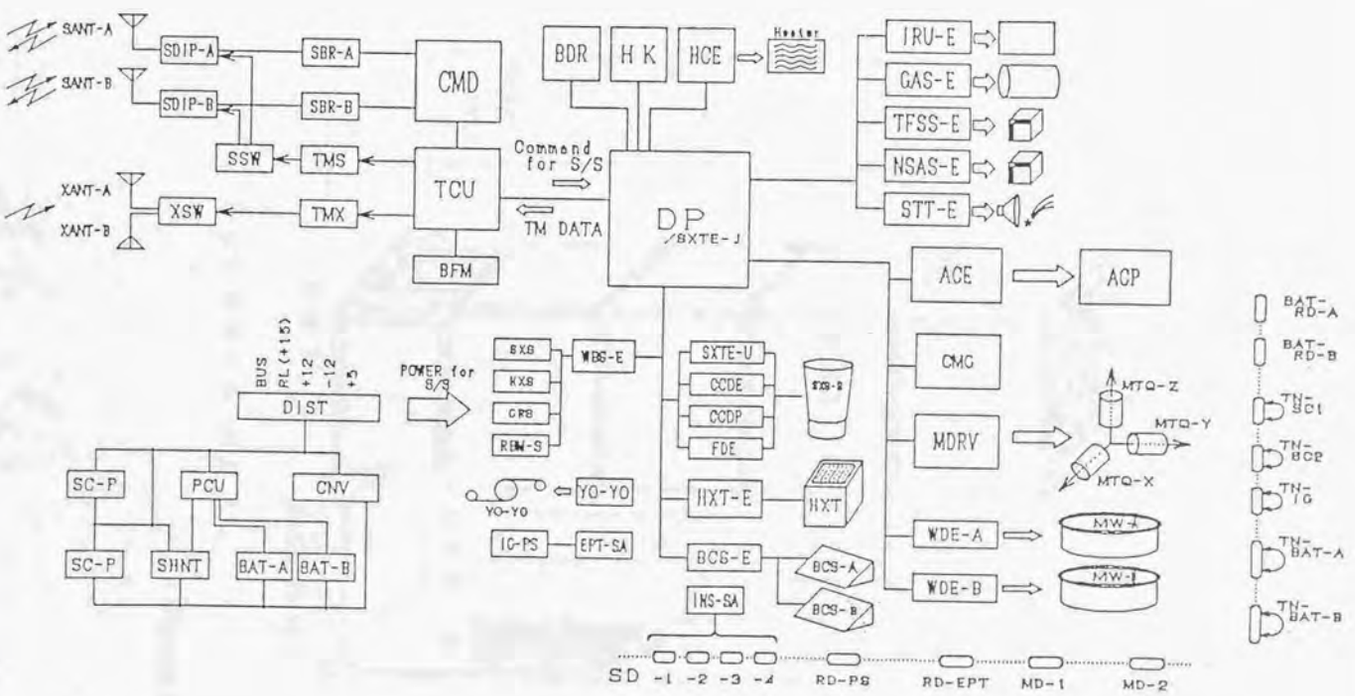
SANT-A
SANT-B
XANT-A
XANT-B
SDIP-A
SDIP-B
SSW
XSW
SBR-A
SBR-B
TMS
TMX
CMD
TCU
BFM
Command for S/S
TM DATA
BDR
H K
HCE
Heater
DP /SXTE-J
IRU-E
GAS-E
TFSS-E
NSAS-E
STT-E
ACE
ACP
CMG
MDRV
MTQ-Z
MTQ-Y
MTQ-X
WDE-A
WDE-B
MW-A
MW-B
BUS
PCL (+15)
+12
-12
+5
DIST
SC-P
SC-P
PCU
CNV
SHNT
BAT-A
BAT-B
POWER for S/S
BXS
KXS
CPS
REW-S
MBS-E
YO-YO
YO-YO
IG-PS
EPT-SA
SXTE-U
CCDE
CCDP
FDE
SXS-2
HXT-E
HXT
BCS-E
BCS-A
BCS-B
INS-SA
SD -1 -2 -3 -4
RD-PS
RD-EPT
MD-1
MD-2
BAT-RD-A
BAT-RD-B
TN-BC1
TN-BCP
TN-IG
TN-BAT-A
TN-BAT-B

Figure 3.4

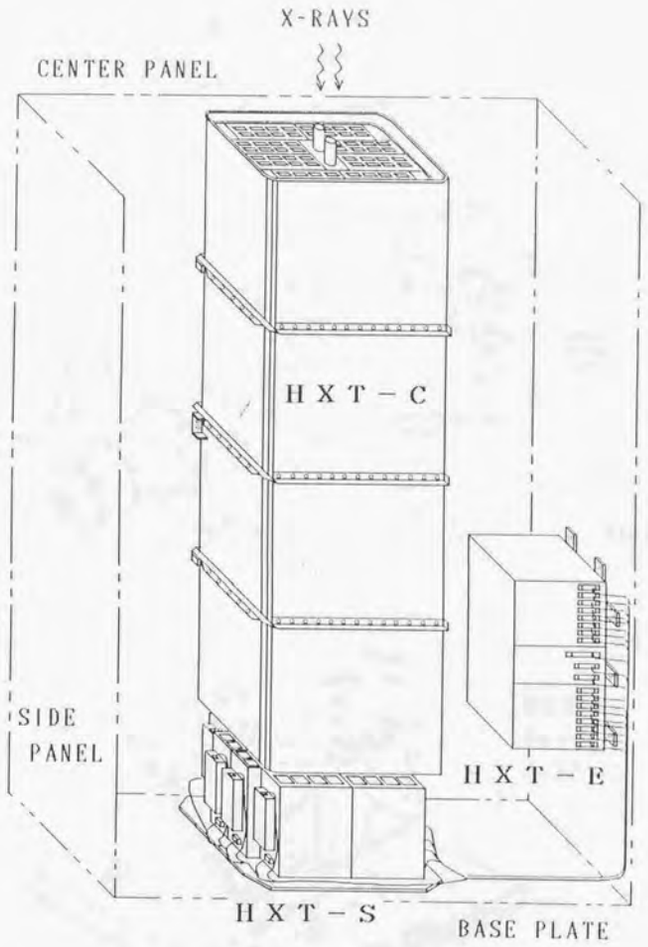

S O L A R – A H X T

Figure 3.5

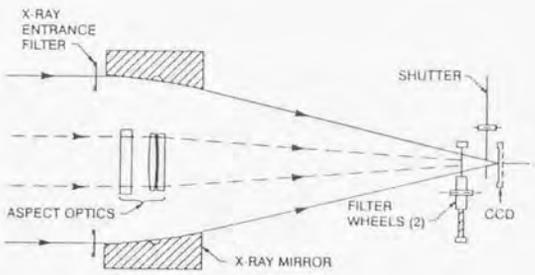

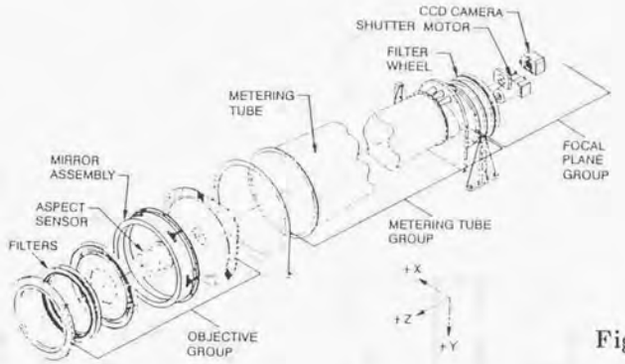

Figure 3.6

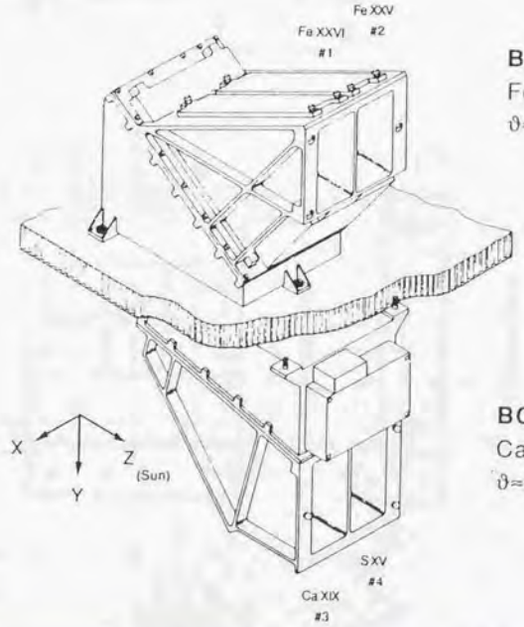

Figure 3.7

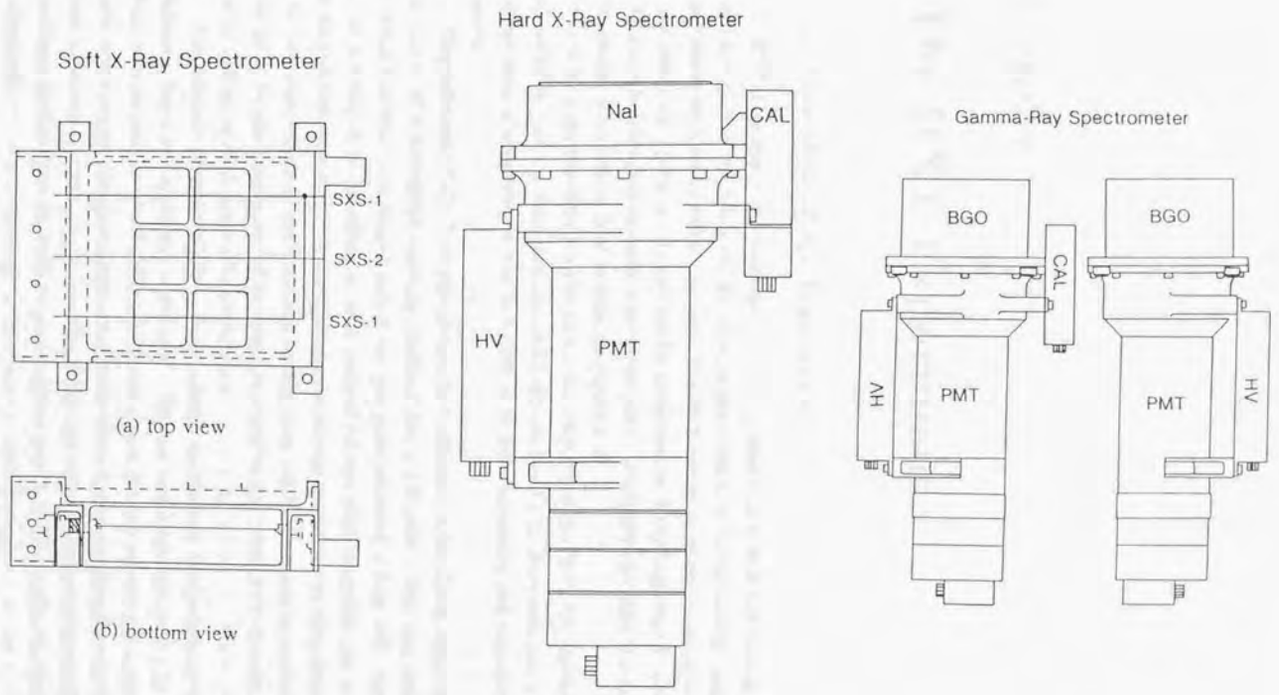
Soft X-Ray Spectrometer
SXS-1
SXS-2
SXS-1
(a) top view
(b) bottom view
Hard X-Ray Spectrometer
NaI
CAL
HV
PMT
Gamma-Ray Spectrometer
BGO
BGO
CAL
HV
PMT
PMT
HV

Figure 3.8

Chapter 4

The HXT Experiment

4.1 Overview of the Instrument

The HXT is the first X-ray telescope that directly adopts the Fourier synthesis principle (Makishima *et al.* 1978) for taking images, which is quite similar to the one used in image restoration procedures for radio interferometer data. The HXT utilizes 64 bi-grid modulation collimators, each measuring a particular spatial Fourier component of X-ray brightness distribution. A set of count rate data are telemetered down to the ground and synthesized there into an image using the Fourier transform, at least in principle (figure 4.1).

The HXT consists of three major parts : the collimator optics (HXT-C), the detector assembly (HXT-S), and the electronics unit (HXT-E) (see figure 3.5). Since each part is functionally independent of each other, it was so divided as to make fabrication and management of HXT easier.

The collimator (HXT-C; C abbreviation for Collimator) is the X-ray optics part of HXT. It consists of a rectangular metering tube (417 mm × 376 mm × 1400 mm) made of CFRP (carbon fiber reinforced plastic) with X-ray grid plates attached at both ends. Each grid plate is an assembly of 64 subcollimator grids made of 0.5-mm thick tungusten and is mounted on a molybdenum base plate. Figure 4.2 shows the arrangement of the 64 subcollimator grids on the base plate. Merit of this particular configuration will be explained in section 4.3.2, while details of the grid fabrication will be described in section 4.4.1. The HXT-C weighs about 13.5 kg, including the HXA optics (discussed later).

The detector assembly (HXT-S; S abbreviation for Sensors) is a package of 64 individual detectors, has a size of 465 mm × 392 mm × 223 mm, and weighs about 17.1 kg (figure 4.3). Each detector consists of a NaI(Tl) scintillation crystal (25 mm square) and a photomultiplier tube with a pre-amplifier assembled as a module. Every 8 detectors are grouped into a unit and have a common high voltage power supply. Eight high voltage supplies are attached to HXT-S. Analogue signal outputs from the 64 pre-amplifiers as well as HXA signals are sent to HXT-E individually.

The electronics unit (HXT-E; E abbreviation for Electronics) is 374 mm × 246 mm × 220 mm in size and weighs about 10.8 kg. HXT-E processes hard X-ray signals and transmits digital count data to DP. It first converts pulsed analogue signals from each of the X-ray detectors into 6-bit digital pulse-height data, and accumulates the counts in four energy bands. After 0.5-s accumulation of counts by 12-bit scalers, HXT-E transmits the photon count data to DP once every 0.5 s. Signals from the 64 photomultipliers are processed individually and simultaneously. The HXA signals are also processed and digitized in HXT-E. In addition to the above signal processing, HXT-E controls power and mode of the whole HXT instrument according to commands issued by ground observers.

In addition to these three HXT components, there is another component called HXA (Hard X-ray Aspect system). This is a high-accuracy solar aspect system of the HXT experiment, mounted at the central area of both HXT-C and HXT-S. The HXA consists of a pair of small ($\phi = 10$ mm) optical lenses with neutral density filters mounted on the top grid plate of HXT-C, a pair of fiducial marks fixed to the bottom grid plate of HXT-C, and a pair of one-dimensional CCDs (2048 pixels each) attached to HXT-S. On the CCD, the lenses focus the optical images of the sun as well as shadows of the fiducial marks, giving accurate position of the solar limb relative to the HXT-C axis. From this information, we can obtain relative position of the HXT optics axis to the sun center. Details of this procedure will be given in section 4.11.3.

4.2 Background

4.2.1 Modulation Collimators

Before describing the Fourier synthesis technique, here we first explain basics of the bi-grid modulation collimators which we utilize in HXT. A bi-grid modulation collimator (*e.g.* Bradt *et al.* 1968, Oda *et al.* 1983) is composed of a pair of identical one-dimensional grids, placed in parallel to each other with a spacing of D. Each grid is made of a number of straight wires opaque to X-rays, arranged periodically with a pitch of p. The wire diameter and the slit width are both set to $p/2$ so that each grid has 50% average transmissivity.

Suppose that a parallel X-ray beam incident on the top grid plate (the one which is facing towards the incident beam) passes through the collimator and is detected by an X-ray detector behind the bottom grid. Due to the mutual shadowing effect of the two grids, transmissivity of the collimator to such a beam is periodically modulated in one dimenison, with a period of

$$\lambda = \frac{p}{D}, \tag{4.1}$$

as the beam propagation direction changes. The modulation pattern thus produced is a periodical triangular function, as is shown in figure 4.4 (a).

To be quantitative, let (x, y) be the sky plane orthogonal to the collimator axis, and let us specify the propagation direction of an X-ray beam by its projected coordinate on the (x, y) plane. (Note that x and y are given by angles rather than physical positions.) Then the modulation pattern or transmission function is given in Fourier expansion as

$$M_C(kr) = \frac{2}{\pi^2}\left\{\frac{\pi^2}{8} + \cos(kr) + \frac{1}{9}\cos(3kr) + \frac{1}{25}\cos(5kr) + \cdots\right\} . \tag{4.2}$$

In the above equation, k is the wavenumber defined as

$$k = \frac{2\pi}{\lambda} , \tag{4.3}$$

and r is the distance on the (x, y) plane perpendicular to the grid pattern, given as

$$r = x\cos\theta + y\sin\theta , \tag{4.4}$$

where θ is the position angle (measured counter-clockwise from the x-axis) of the line normal to grid wires projected on the (x, y) plane (see figure 4.5 for definitions). Note that the term 'position angle' used here is defined in a different way from the one used in the actual image synthesis procedure (described in chapter 5) as well as in the actual identification of HXT grids which will appear later in this chapter. Definition of position angle θ used in the actual image synthesis is given in figure 5.2.

$M_C(kr)$ is a periodical triangular function oscillating between 0 and 0.5. If we disregard the DC component involved in this triangular modulation pattern, the pattern is approximated by a trigonometric (cosine or sine) function, since upon the Fourier series expansion the n-th harmonic coefficients rapidly decreases as $1/n^2$ for odd n's with all the even number harmonics being null.

4.2.2 Fourier Synthesis Technique

If we denote a hard X-ray brightness distribution on the sky plane as $B(x, y)$, the X-ray count rate obtained through a bi-grid modulation collimator with effective area A is given as

$$b_C(k, \theta) = b_C(k\cos\theta, k\sin\theta) = A\int B(x, y)M_C(kr)\,dx\,dy . \tag{4.5}$$

Here the integral is taken over the field of view of the collimator. If we further approximate $M_C(kr)$ with its fundamental cosine function, $b_C(k, \theta)$ is a cosine-type spatial Fourier component of $B(x, y)$ corresponding to the wavenumber k and the angle θ (plus DC component).

In addition to this collimator, let us consider another collimator which has the same pitch and position angle but whose 'phase' is shifted by $\pi/2$ from that of the first one, *i.e.*,

$$M_S(kr) = M_C(kr - \frac{\pi}{2}) . \tag{4.6}$$

Here the suffix S denotes *sine collimator* whereas C *cosine collimator*. A cosine collimator is easily changed into a sine one by shifting relative positions between the two grids perpendicular to the wires by $p/4$ (see figure 4.4 (b)).

The count rate data obtained through the sine collimator is given as

$$b_S(k,\theta) = b_S(k\cos\theta, k\sin\theta) = A\int B(x,y)M_S(kr)\,dx\,dy\,, \tag{4.7}$$

which is again approximated by a sine-type spatial Fourier component of $B(x,y)$ (plus DC component). Thus, by observing a distribution $B(x,y)$ through a pair of cosine and sine collimators having the same wavenumber k and position angle θ, we uniquely determine a spatial Fourier component of $B(x,y)$ corresponding to k and θ. Thus, by adopting the (U,V) coordinates for the Fourier plane which is condugate to (x,y), it can be said that a pair of cosine and sine collimators measures the complex Fourier component $b(U,V) = b_C + ib_S$, where $U = k\cos\theta$ and $V = k\sin\theta$. Consequently, if k and θ are allowed to vary as two independent variables, or if we have many cosine-sine collimator pairs with different values of k and θ so as to sample, on the (U,V) plane, a sufficient number of spatial Fourier components, then we can restore $B(x,y)$ through inverse Fourier transform. This is the Fourier synthesis principle to be actually employed in HXT. Note that this is almost the only technique under current-day technology which can afford a desired angular resolution in a wide field of view for hard X-ray imaging observations of solar flares, if we exclude the Rotating Modulation Collimator (RMC) technique which has been used in the *Hinotori* experiment (Makishima 1982) on-board the spin-stabilized satellite.

Although the best way of sampling the (U,V) plane is a matter of extensive discussion, one practical way is to select several position angles (*e.g.* 0, 30, 60, ..., 150 degrees), and along each position angle, sample wavenumbers in harmonic series as $k_0, 2k_0, 3k_0, 4k_0, \ldots, nk_0$. Here k_0 is fundamental wavenumber, and the quantity

$$\lambda_0 = \frac{2\pi}{k_0} \tag{4.8}$$

determines a dimension of 'syntehsis aperture'. Spatial structures with angular scales in the range between λ_0 and λ_0/n are effectively measured, while those larger than λ_0 or smaler than λ_0/n are not, so that the combination of k_0 and n gives the practically available field of view (synthesis aperture) and the angular resolution. In this sense n is often called *dynamic range* for the image synthesis.

4.2.3 HXT Design Goals

The objective of HXT experiment is to take images of hard X-rays produced by solar flares, with much improved performance than its two predecessors : the hard X-ray imager experiment (Makishima 1982) on-board *Hinotori* and the HXIS experiment on-board *SMM* (Van Beek *et al.* 1980). In designing the HXT instrument, the following goals were set.

1. The angular resolution should be as high as $\sim 5''$, a factor of ~ 2 or more improvement compared to the *Hinotori* and *SMM* predecessors. Also the restored image should be free, as much as possible, from spurious structures due to image synthesis artifacts.

2. The imagery should be done simultaneously in several energy bands covering 15–100 keV. Imaging observations of flares above $\sim$ 30 keV, which is essential to study purely non-thermal hard X-ray emission, has not been done before.

3. The time resolution of successive images is required to be as high as 0.5 s, in order to resolve time variations of hard X-ray emission during impulsive flares.

4. The optics should have a wide field of view which covers the whole sun, and the image synthesis aperture should be no smaller than $\sim 2'$, tyical upper limit of the size of a flaring region. In other words, HXT should be able to make images in a $2' \times 2'$ frame regardless of flare location on the solar disk.

5. A large effective area (say, $\gtrsim 50$ cm^2; *c.f.* 8 cm^2 for each of the two detectors aboard *Hinotori* and 0.07 cm^2 for each detector aboard *SMM*) need be achieved in order to detect much more flares than before.

6. Hard X-ray images need be overlaid, with an accuracy of about $1''$, upon soft X-ray images (from SXT) as well as ground-based optical and radio images.

These design goals of the HXT instrument are summarized in table 4.1 in comparison with those of the two predecessors.

4.3 The Baseline Design

4.3.1 Grid Configuration

If modulation patterns of the collimators are really cosine and sine functions, and also if measurements were made at sufficient (k,θ)-points (*i.e.*, good UV coverage), it is easy to reconstruct $B(x,y)$ via an inverse Fourier transform. However, since the modulation patterns are triangular, rather than trigonometric, and since only a limited number of (k,θ)-points are measured due to a limited number of subcollimators which is practically fabricable, simple inverse Fourier transform cannot be applicable to our case. Instead, we adopted image synthesis procedures like CLEAN (Högbom 1974) and the Maximum Entropy Method (MEM; Frieden 1972, Gull and Daniell 1978, Willingale 1981). Through various computer simulations and taking into account practical limitations, we investigated optimum configuration of UV coverage as well as other related items including the necessary improvement of image synthesis procedures (see Kosugi *et al.* 1991). Results and consequent discussions we made are briefly summarized as follows :

1. The fundamental period of repetition of the modulation patterns (synthesis apature) was decided to be $\sim$2 arc min (exactly $2'06''$), since observations from *Hinotori* and *SMM* suggested that the angular extent of most flares is within $\sim$2 arc min.

2. We chose the highest wavenumber to be 8 (*i.e.*, $k = 1, 2, \ldots, 7, 8$). This is a compromise between the fabricability of the finest grids ($k = 8$) and a desired angular resolution. As the separation of the two grid plates is ~1.4 m, which is determinded by the size of the spacecraft, the finest grid pitch need be as fine as $p \sim 100\mu$m. This finest pitch gives an angular repetition period of 15.8″.

3. (k, θ)-points in the UV plane were selected on polar-coordinate grid points, not on rectangular-coordinate grid points (see figure 4.6). This is for avoiding ambiguity with the fundamental period in determining the flare position (see section 5.1.2).

4. Through the simulations, we confirmed that a UV coverage with more than ~ 50 cosine-sine (or complex) Fourier pairs is desirable for obtaining good images. Also we found that if we use a set of Fourier elements alone, synthesized images tend to deteriorate for relatively extended flares. We can decrease the degree of deterioration by replacing Fourier elements at low wavenumbers (k) with so-called 'fanbeam elements', whose wire width w_W, in our case, is three times larger than the slit width w_S, *i.e.* $w_W = 3w_S$ (figure 4.7). In general, fanbeam elements are suited for suppressing spuriouses in synthesized images whereas Fourier elements are better for achieving higher angular resolution.

   Using MEM, we confirmed that an angular resolution as high as 5″ can be attained with 15″-pitch Fourier elements as the finest grids.

5. In order to make reliable images in the four energy bands, outputs from the collimators are required to be well calibrated in such a way that output gains can be adjusted within ~ 1 % accuracy. Also it is required to accurately measure phases and amplitudes of the modulation patterns; position errors of the phases need to be estimated within $1'' \sim 1.5''$ accuracy and errors in amplitudes, which is equivalent to errors in effective area of the HXT detectors, need be estimated within 5 % accuracy.

Table 4.2 shows the selected configuration of fanbeam/Fourier elements. Examples of synthesized images obtained from the simulations using the actual design of UV coverage (figure 4.6) are shown in figure 4.8.

4.3.2 Grid Size and Arrangements

It is highly requested that HXT has a wide field of view (covering the whole sun) so as to avoid re-pointing of the spacecraft or instrument pointing system and to observe as many flares as possible. In order to achieve this, each grid on the top (sun-side) plate has been decided to have a size of 37 mm square, much larger than 23 mm square for the bottom (detector-side). Since the separation of the top and bottom plates is ~1.4 m, this combination of grid sizes ensures a field of view of $\sim 35' \times 35'$. The grids give a simple total geometric area of ~ 69 cm^2, assuming that the aperture ratios for Fourier and fanbeam grids are 0.5 and 0.25, respectively.

The 64 grid elements are arranged in such a way that slits of the individual grid direction run circularly and finer grids are situated nearer the center of the plate, as far as possible, so as to minimize undesirable effect due to possible mutual rotation between the top and bottom grid plates (see section 4.4.2).

4.3.3 Detectors

Detectors for HXT are for detecting hard X-rays efficiently in the energy range of 15–100 keV. A set of 64 NaI (Tl) crystals with photomultiplier tubes are used as the detectors of HXT. Each of the phototubes are located just behind the bottom grids. Size of the NaI (Tl) crystals is 25 mm × 25 mm so that all X-ray photons that pass through the bottom grids (23 × 23 mm^2 each) hit the corresponding crystal. Thickness of the crystals is 0.5 mm so that hard X-rays up to 100 keV would be photoelectrically absorbed efficiently. In addition to increasing detection efficiency of higher energy hard X-rays, decreasing contamination of lower energy hard X-rays is of crucial importance. As solar flares have steep energy spectra with thermal emission significantly dominant below ~ 10 keV (see section 2.1.3), contamination of the thermal component into the HXT energy band would lead to a serious increase of dead time and pulse pile-up in the photon counting. To avoid this, the crystal is surrounded by an aluminum case which is 0.8 mm (±0.01 mm) thick at the front of the crystal. This case acts as a filter which cuts off lower energy hard X-ray photons. Details of spectral responses of HXT are given in section 4.5.1.

4.4 X-ray Optics (HXT-C)

4.4.1 Grid Fabrication

Since the HXT grids are required to stop hard X-rays up to 100 keV, the grids need be made of a high atomic-number (Z) material so that X-rays are photoelectrically absorbed efficiently (note that photoelectric-absorption cross section $\sigma_{ph} \propto Z^5$.) Also as the collimators are required to be coaligned with high precision ($\sim 1''$) with each other, the material need be that with low thermal expansion coefficient α. Since the finest grids have a pitch of 105 μm, it is also necessary that the grid material has a high Young ratio E so that the grid wires would not be damaged by *e.g.*, strong vibration at the time of launch. Figure 4.9 shows comparison of various material with respect to mass density ρ, mass absorption coefficient κ at a photon energy of 100 keV, thermal expansion coefficient α, thermal expansion coefficient K, and Young ratio E. From these considerations we chose tungsten for the material of the HXT grids. Thickness of the tungsten grids is 0.5 mm and more than 98 % of hard X-rays at 100 keV are stopped, while at the energy of the K-edge of tungsten (at 69.6 keV), the absorption efficiency is decreased to be ~ 83 %.

In fabricating the grids, the electric discharge method, whose accuracy of fabrication is quite high (nearly 1 μm), can be used for the grids whose slit width is $\gtrsim$ 0.2 mm. This method was actually applied for the fanbeam grids. Figure 4.10 (a) shows a pair of fanbeam grid plates. Four grids with an identical position angle are fabricated on a single plate. While this method provides us with high precision fabrication for the fanbeam grids, it cannot be used for the Fourier grids, whose slit widths (less than 0.15 mm) and pitches (less than 0.3 mm) are too fine. Instead, the photo-etching method was adopted for the Fourier grids. As this method can only be applied to grids whose thickness is smaller than, or at most as small as its slit width, 10 identical thin tungusten films (thickness 50 μm each) were stacked to form a 0.5 mm thick grid. Eight Fourier grids were fabricated on one film as shown in figure 4.11. Fanbeam grids as well as base grid plates (section 4.4.2) were fabricated by Toray Precision Co., Ltd., while Fourier grid films were fabricated by Dai-Nippon Insatsu Co., Ltd.

4.4.2 Grid Assembly

Four fanbeam and six Fourier grid plates are mounted on a single base grid plate made of molybdenum 1.5 mm thick for each of the top and bottom grid assemblies. Figure 4.2 shows the assembled 64 grids on the base plate. Grid wire directions run in a circular way and finer grids are situated near the center of the plate (see section 4.3.2). The tungsten films for Fourier elements as well as fanbeam plates are stacked onto the base plate using knock-pins (2 mmϕ) with positional accuracy of $\sim 5\mu$m. The grid assembly (both top and bottom), including the base plates, weighs about 5 kg.

4.4.3 Collimator Body

The two grid plates of the HXT collimators are required to be fixed firmly with each other so as to avoid relative lateral shift, mutual rotation, relative difference in expansion or shrinkage between the plates, and distortion. They might be caused by temperature variation in orbit as well as mechanical shocks at the time of launch. For example, a relative shift of one grid plate of 0.1 mm would cause a shift of its modulation pattern by $\sim 15''$, which is by far the allowed value for the angular resolution of $\sim 5''$. Thus, the material for the collimator body to which the grid plates are mounted should have (a) high rigidity, (b) low thermal expansion coefficient ($\alpha \ll 1 \times 10^{-5}$ /deg; otherwise a displacement of the order of 0.1 mm might be caused by a temperature variation of $\sim$ 10 deg, which might occur in orbit), (c) low density, and (d) high transparency for hard X-rays since the two grid plates are attached to face plates of the collimator box. The HXT collimator body is made of CFRP (Carbon-Fiber Reinforced Plastic), which is characterized by its low density $\rho \sim 1.7$ g/cm^3 and small thermal expansion coefficient $\alpha < 1 \times 10^{-6}$ /deg (figure 4.9). The CFRP box (see figure 3.5) is $\sim$ 1.3 mm thick at the side plates and $\sim$ 2.1 mm thick at the face plates. Three stiffners encircle the side plates of the body.

These stiffners are also used as mounting points to the spacecraft body. The collimator body itselt weighs about 8.0 kg and was manufactured by Nihon-Hikoki Co., Ltd.

4.5 Detector System (HXT-S)

4.5.1 Detector Module

Figure 4.12 shows a schematic drawing of a detector module. The module consists of a NaI (Tl) scintillation crystal and a photomultiplier tube with a high-voltage breeder and a pre-amplifier installed. Each crystal is 25 mm $\times$ 25 mm square and 5 mm thick, so that the crystal well covers the corresponding aperture of each bottom grid and more than 94 % of incident X-ray photons at 100 keV are photoelectrically absorbed. The crystal is surrounded by an aluminum case whose thickness at the photon incident side is 0.8 mm ($\pm$0.01 mm). The case in front of the crystal acts as an X-ray filter so that it avoids contamination from thermal soft X-ray emission of flares into the HXT energy bands and possible pulse pile-up due to this contamination in the photon counting. Figure 4.13 shows the spectral response of HXT. In the figure, photon detection efficiency of the NaI (Tl) crystal, thickness the alumimun case, the CFRP face plates, and the tungusten grids (0.5 mm thick) are taken into account.

In order not to be damaged by vibrations at the time of launch, the photomultiplier tube (HPK 2497 from the Hamamatsu Photonics Co., Ltd.) is of an anti-vibration type. The tube is magnetically shielded by μ-metal so as to suppress gain variation which otherwise might be caused by the earth magnetic field variation in orbit. Typical energy resolution (FWHM value) of the detectors is given experimentally by

$$\frac{\Delta E}{E} = 1.3 \times \frac{1}{\sqrt{E}} \quad (E \text{ in keV}) \tag{4.9}$$

(figure 4.14), which is similar to typical values for NaI scintillators thus far known.

It is essential for synthesizing images to adjust gain of the 64 detectors equally within $\sim$ 1 % (*c.f.* section 4.3). For calibrating the detector gain, a small radioisotope source, ^{241}Am, is attached on at the center of each of the aluminum filter in front of the NaI crystal. The ^{241}Am sources emit 59.5 keV X-rays as is shown in figure 4.27 (b) and (c). Each calibration source emits X-rays at an average count rate of several cts/s. An accumulation time of 600 s (typical time duration in a KSC contact passage) enables us to determine the 59.5 keV peak position at an accuracy of 0.5 keV, thus leads to gain adjustment within $\sim$ 1 % accuracy. Since the geometrical size of the source is small (4 mm^2; $\sim$ 0.6 % of the aperture) and the average X-ray count rate is small in comparison with that from flares, the calibration sources do not interfere observations of flares so much. Note that the contribution from the calibration sources can be subtracted accurately enough from the observed count rates by using pre-flare or post-flare count rate data as background and hence we can obtain hard X-ray counts even from weak flares.

In order to avoid pulse pile-up, time constant of charge amplifiers (pre-amplifiers) is set to ~ 10 μs so that each detector can measure X-rays up to nearly 10^5 cts/s (see figure 4.15). Since this value is larger than the expected X-ray count rate (10^4 cts/s; spectrum and filter characteristics taken into account) from largest flares, HXT can observe flares without any significant distortion of count rates by pulse pile-up.

Gain of each pre-amplifier was adjusted equally to each other within 1 % accuracy before launch. This mades subsequent in-orbit gain adjustment (see section 4.11.2) much easier.

4.5.2 High Voltage Power Supply

One DC-DC converter, or high-voltage (HV) power supply unit, supplies high voltage to eight detector modules (figure 4.16), so in total 8 HV units are attached to HXT-S. The HV supplies about 935 V in the nominal case. The input voltage is 12 V. The HV output is set by commands to be in one of equally spaced 8 levels between 795 and 1037 V.

Since the spacecraft enters the radiation belt (SAA) once in an orbit (section 3.1.2), the HV outputs need be reduced at the time of SAA entry in order to avoid possible damages to the photomultiplier tubes. The outputs are reduced to nearly zero without turning off the control circuit of the unit, thus enables to supply stable HV outputs just after exit of SAA. This HV reduction function is also used at the time of spacecraft night for saving spacecraft power.

4.5.3 Detector Assembly

Eight detector modules are assembled into a case made of magnesium. The magnesium case not only has low mass density ($\rho = 1.74$ g/cm^3) but also is easy to fabricate. Eight magnesium cases are mounted on an aluminum base plate so that they comprise a package of 64 detectors, with the 8 HV power supply units attached outside on the both sides of this package (see figure 4.3).

4.6 Data Processing Electronics (HXT-E)

Analogue signals from the 64 pre-amplifiers of the detectors are sent to the electronix box of HXT (HXT-E) and are processed individually by 64 independent circuit modules (figure 4.17). The analogue signals are first gain-adjusted by operational amplifiers. Gain of each amplifier is controlled in a wide range ($\pm 32\%$) in equally spaced 64 steps, which makes it possible to adjust gain of the 64 detector outputs within ~ 1 % accuracy. Then the signals are converted into digital ones by 6-bit flash A/D converters (FADC; RCA CA3306D). The A/D conversion is performed whenever the input signal level exceeds a certain analogue discrimination level (analogue lower discrimination; ALD). The ALD can be set to correspond either to $\sim$15-keV or to $\sim$ 19-keV photon energy. HXT-E was fabricated by Meisei Electronics Co., Ltd.

The HXT-E has two modes of operation; Pulse Count mode (PC mode) and Pulse Height mode (PH mode). Digital signals from the FADCs are processed in a different manner according to the mode.

PC mode processing :

The PC mode is the HXT normal mode for flare observations. Each FADC output (binary digit from 0 to 63) is encoded for binning and sent into one of the four 12-bit scalers. The four scalers represent the four energy bands of HXT : the L band includes 1 (or 4)-7, M1 band 8-15, M2 16-31, and H 32-63, respectively (see table 4.3). The digital value corresponding to the lower limit of the L band (digital lower discrimination; DLD) is selectable between values of 1 or 4. Pulses with its digital value lower than DLD are not counted in any of the four channels. Photon counts are accumulated for 0.5 s by the scalers, and 256 (= 64 detectors $\times$ 4 bands) photon count data are sent every 0.5 s to the spacecraft data processor (DP) simultaneously. As each scaler has 12 bits, the maximum count rate of HXT without scaler overflow is 4095 cts / 0.5 s.

PH mode processing :

The PH mode (or the HXT CAL mode) is prepared for calibration purpose of the detector gain. The PH mode is usually set during spacecraft night and energy spectra of ^{241}Am calibration sources are taken in 64 energy channels between 15-100 keV. This mode starts and ends when so commanded from the ground. In this mode, each of the FADC outputs is sent together with detector module number directly to a counter memory, where the photon count is binned in 64 channels directly corresponding to the digital pulse heights. The memory consists of two buffers, each being 4096 (= 64 $\times$ 64)-channel 8-bit counters. A set of PH data is sent to DP every 8 seconds. Figures 4.27 (b) and (c) show examples of the PH data output from detector modules.

4.7 Aspect System (HXA)

The aspect system, HXA, provides indispensable information to locate hard X-ray sources relative to the solar disk within an accuracy of $\sim$ 1 to 2 arc sec. The HXA enables us to accurately measure the coalignment between HXT and spacecraft axes, including compensation for possible in-orbit thermal distortion in the coalignment between the two.

The HXA optics consists of two identical systems (HXA-X and HXA-Y; figure 4.18 and 4.19). Each of them takes (one-dimensional) images of the sun in wide-band visible light and is composed of the following components. (a) An achromatic, doublet imaging lens (10 mmϕ) with filters on the top grid plate. The lens (BSC7-N) is highly tolerant against in-orbit radiation damage which leads to a loss of transparency. (b) A set of fiducial marks placed at the bottom grid plate. (c) A one-dimensional CCD (2048 pixels) placed at the top of HXT-S. The CCD

gives white light distribution of the sun together with fiducial shadows (figure 4.20). We can obtain relative direction of the X-ray axis of HXT and the optical axis of HXA via the location of fiducial shadows (see section 4.10.4). Two CCDs are set in a direction orthogonal to each other.

Video signals from the CCDs are processed by HXT-E and the following two types of data are sent to DP (see figure 4.21). (a) Addresses of the CCD pixels at which the video signal output crosses a certain threshold level. This type of data is sent to DP every second (in the high bit-rate case). The threshold level is selectable from four levels by a command from the ground. (b) One-dimensional brightness distributions of the sun (figure 4.20), digitized in 6-bits and sent to DP once every 64 s (in the high bit-rate case).

4.8 Spacecraft Interface

Figure 3.5 shows arrangement of the three major HXT components (HXT-C, HXT-S, and HXT-E) in the spacecraft. The collimator body (HXT-C) is mounted onto the center panel while the detectors (HXT-S) on the base plate. The HXT-C and HXT-S are mounted within $\sim$ 1 mm accuracy to each other so that each grid aperture in the bottom grid plate is geometrically well coincided to the corresonding detector.

4.9 Commands and Telemetry Formats

4.9.1 HXT Commands

Figure 4.22 shows tables of commands for HXT. The HXT commands are sent to HXT-E through TCU and are executed by HXT-E. Like other instruments aboard *Yohkoh*, two types of commands, *i.e.*, (a) discrete commands (DCs) and (b) block commands (BCs), are prepared for HXT.

Discrete Commands (DCs)

Most of the DCs are used for turning power on/off of HXT components such as analogue electronics and high-voltage power supply. Commands for turning high-voltages on (THV-1 $\sim$ THV-7 ON commands) can be executed only following HV ENA (high-voltage enable) command every time to avoid an accidental turn-on of high-voltages. Such protected commands are called 'double commands'.

Block Commands (BCs)

BCs are used for changing the detector gain, high-voltage level, and discrimination level. A 'BC-ENA' DC needs be executed prior to setting any BC. All items (detector gain etc.) controlled by

BCs have their default values as shown by underlines in figure 4.22. These values are re-set to default ones when power off (and on) DC is executed for the corresponding HXT-E components.

4.9.2 Data Handling in DP

Data transfered from HXT-E to DP are then edited into the telemetry frame format according to the DP mode (see section 3.3.1). In this section I briefly describe HXT data processing in DP.

Telemetry allocation for HXT count data

In the flare-mode, HXT count rate data of all the four energy bands have their telemetry allocation. The time resolution is 0.5 s (in high bit-rate case). On the other hand in the quiet mode (and also in any other mode than the flare-mode), only the L band count rate data accumulated every 2 s (in high bit-rate case) have the allocation and the data in the M1, M2, and H bands are not edited at all. This is not unreasonable since few hard X-ray counts are expected to be detectable for HXT from quiet sun especially in the higher energy bands. The L band data in non flare-modes are used for studying small flares which do not trigger the flare-mode. Other HXT data such as from HXA, power status of the instrument, and gain of the detector amplifiers, have their telemetry allocation regardless of the DP mode.

Pre-storage of X-ray count data

Since the flare-mode is triggered by increased count levels of SXS, HXS, or BCS, data at the onset of flares tend to be lost (especially those from M1, M2, and H bands). To avoid this demerit, X-ray count data of HXT is pre-stored for 4 seconds in DP regardless of the DP modes. Then DP telemeters out the pre-stored data with additional time delay depending on the bit-rate. For example, in the telemetry data with time tag of T_0, HXT count rate data accumulated from $T_0 - 4.5$ s to $T_0 - 4.0$ s have their allocation in the case of high-bitrate while from $T_0 - 8.5$ s to $T_0 - 4.5$ s for medium-bitrate.

Data compression

12-bit HXT count data are compressed in DP into 8 bits (bit reduction) according to the following relation (after 4-s integration in medium bit-rate case) :

$$\begin{aligned} m &= n && (n = 0 \sim 15), \\ m &= \mathrm{T}[4\sqrt{n}] && (n = 16 \sim 4080), \\ m &= 255 && (n = 4081 \sim 4095). \end{aligned} \tag{4.10}$$

Here T[n] represents the truncated integer value of n. On the ground the original count n is decompressed from m, when digital error $\Delta n'$ due to the bit reduction is always smaller than the Poisson noise statistical error by a factor of two, because

$$\Delta n' < \frac{(m+1)^2 - m^2}{16} \sim \frac{m}{8} \sim \frac{\sqrt{n}}{2} . \tag{4.11}$$

From this relation, it is guaranteed that n' estimated from 8–bit m has nearly the same standard deviation as the original n. Decompression of n from m are performed quite easily by using a table for $m - n$ conversion.

4.10 Pre–Launch Calibration

In this section, I discribe pre–launch calibration of modulation patterns of the HXT grids, calibration of the detectors, and coalignment measurements between the HXT–HXA axes. For calibrating the modulation patterns, we used optical (visible light) and X–ray measurements independently. Optical measurements were mainly used for measuring phases of the modulation patterns precisely. On the other hand, X–ray measurements were used for obtaining modulation amplitudes of the patterns as well as average grid transmission.

4.10.1 Optical Measurements of Modulation Patterns

The main objective of the optical measurements is to measure phase of each modulation pattern precisely. In case of the actual collimator, the phases need be known within $\sim 1''$ accuracy (or $\sim 7\mu$m on one grid plate with the separation of the plates $D \sim 1400$ mm). For the optical measurements, we utilized a pair of grid assembly (= grid plates) with its separation $D \sim 10$ mm (hereafter I call this pair of grid plates 'shortened' collimator). This shortening of the separation D enables us to measure much more easily the phases than it would be in the case of $D \sim 1400$ mm. In fact, for the $D = 10$ mm grid separation, a length of 7 μm corresponds to an angle of $2.4'$, which is large enough to measure. Detailed description of the measurements and results will be presented by Inda–Koide (1993), the essence of which is as follows.

We measured Moiré patterns which are formed by illuminating diffuse white light to the collimator (figure 4.23) by a one–dimensional CCD located behind the shortened collimater and set orthogonal to the grid wire direction. Relative phase of each modulation pattern was obtained as the location of peak transmission of the Moiré pattern. Although the Moiré patterns themselves were affected by diffraction of light through two grid layers, this effect was symmetric around each peak transmission angle and hence did not affect measurements of the phases.

4.10.2 X–ray Measurements of Modulation Patterns

X–ray measurements of modulation patterns were carried out using a 25–meter X–ray beam facility at the Institute of Space and Astronautical Science (ISAS). Figure 4.24 is a schematic drawing of the measurement system, *i.e.* beam generator, beam line, HXT grids, and reference components. Electrons accelerated in a high–voltage (50 kV) electric field hit a Cu target and X–rays are emitted by Bremsstrahlung emission. Electric current supplied to the beam generator

was 40 mA. An example of energy spectrum of X–rays produced by the beam generator is shown in figure 4.25. The X–ray beam is well–collimated at the exit of the beam line; it spreads out from the line with an angle of $\sim 0.01°$, which is small enough in comparison with the angular size of the measured modulation patterns (see below).

The measurements were carried out using a shortened collimator whose separation D of the two grid plates is $D = 100$ mm. If we use the actual collimator, *i.e.* if $D \sim 1400$ mm, it would make the measurements quite difficult. For example, since the finest angular pitch of the actual modulation patterns is $15.8''$, the actual collimator would require measurements with pointing accuracy of $\sim 1''$, which is quite difficult to achieve. A pair of the grid plates, assembled on the CFRP face plates, were fixed to each other ($D = 100$ mm) using the shortened collimator.

The collimator was fixed on a stage mounted on a rotator. It is rotated in θ and φ directions as well as in X and Z directions as are shown in figure 4.24. The movement of the rotator was controlled by electric pulse signals from a personal computer via a parallel TTL interface. The average minimum steps of the movement were ~ 10 μm for X and Z directions and $\sim 10''$ for θ and φ directions, respectively. Incident angle of X–rays to each grid pair was changed by rotating the grid plates in either θ or φ direction. While moving the table in the X or Z direction, X–rays passing through each of the 64 grid pairs were measured with a NaI(Tl) crystal and photo–multiplier tube detector which was set behind the grid plates.

Before starting X–ray measurements, we located the grid plates normal to the X–ray beam as accurately as possible. As the modulation patterns had the fundamental angular pitch of $\lambda_0 \sim 0.5$ degree for the $D = 100$ mm collimator (note that the fundamental grid pitch d_0 is 840 μm), we set the grid plates normal to the beam within 0.5 degree accuracy. This was achieved by using (1) a small witness mirror (~ 3 cmϕ) attached to one side of the grid plates and (2) an auto–collimator whose cross–shaped, hair–cursor fiducial light is reflected by the witness mirror.

Although the rotator itself was controlled fairly well by sending electric pulses to the stepping motors, there might be possible fluctuations due to backlashes in control steps. Hence it was important for this measurement to know the absolute movement of the shortened collimator. To achieve this, a small semi–conductor laser and a two–dimensional position sensitive diode (PSD) were also mounted on the rotator. Size of PSD was ~ 12 mm $\times 12$ mm. Laser beams were reflected by a high–flatness mirror which was located ~ 50 cm behind the rotator and PSD received the reflected beams. The PSD outputs four linear analogue signals in voltage : two in the horizontal direction (PSD–X) and the other two in the vertical (PSD–Y) direction. Center–of–gravity position of the laser light on PSD was obtained by simply taking linearly–weighted averages of the two output voltages both in the horizontal and vertical directions. The linearity of the output voltages with respect to the position of the light was quite good; with the difference between the actual and the estimated (assuming the linear relation) positions smaller than 0.1 mm, which corresponds to an angle smaller than $\sim 14''$ in our setup. The four outputs

were first A/D–converted and then transfered to the personal computer via IEEE–488 interface (figure 4.24). In order to avoid stray lights which might shift the center–of–gravity position of lights illuminating PSD, an interference filter was mounted in front of PSD which selectively passes the laser light. Also a neutral density filter was mounted to adjust intensity of the laser light injecting on PSD, which enables PSD to output a proper range of voltages.

X–ray counts from the detector photomultiplier was accumulated for 5 s by a scaler. Transfer of the accumulated counts to the same computer as well as control of the scaler from the computer were carried out via IEEE–488 interface.

With this setup, we measured (1) X–ray modulation patterns and (2) average transmission of the 64 collimators as shown below.

Modulation patterns

The modulation pattern of each collimator was measured by moving the rotator in either θ or φ direction depending on the position angle of the collimator to be measured. For example, if the position angle is 0° or 30°, the table was rotated in the θ direction and if the position angle was 60° or 90°, then in the φ direction.

Once the 5–s accumulation of X–ray counts was finished, the collimator was rotated in either θ or φ direction by $\sim 10''$ (by sending a pulse to either $\theta-$ or $\varphi-$ stepping motors) to measure X–ray transmission at a different X–ray incident angle. A total of 140 data points were measured during one scan of a modulation collimator, which gave a transmission pattern in a range of $\sim 0.4°$ (note that the fundamental pitch for the shrinked collimator with $D = 100$ mm is 0.48°). It took about 15 minutes to complete a scan for one collimator. In order to know the absolute phases of the modulation patterns, modulation patterns of reference grids (= alignment patterns; shown as 0A840, 90A840, and 90A750 in figure 4.10 (b)), whose highest peaks in $\theta-$ and $\varphi-$ scans give angular direction of HXT axis, were also measured.

Figure 4.26 (a) and (b) show examples of measured X–ray modulation patterns for fanbeam and Fourier grids : (a) A set of four fanbeam patterns with position angle $\theta = 90°$, and (b) *Top left* : modulation pattern of a reference grid shown as 90A840 (and also 90A750) in figure 4.10 (b) (position angle $\theta = 90°$). The position (in PSD–X out put in this case) of the peak of this pattern gives HXT axis in the horizontal (*i.e.* X–) direction. Other three figures are modulation patterns of Fourier grids with position angle $\theta = 90°$. Absolute phases of these patterns are directly obtained by comparing with the reference pattern. Vertical error bars represent 1σ level of measured X–ray counts while horizontal bars indicate positional errors. Figure 4.26 (c) shows an example of combined modulation patterns of two reference grids ($p = 840$ μm and 750 μm) with position angle $\theta = 90°$. We see that the highest peak in the right hand side of the figure, formed by an overlap of 840 μm and 750 μm peaks, gives HXT axis location in the horizontal (X–) direction. Scan range of figure 4.26 (a) is shown by a bar in the lower right of figure 4.26 (c).

Average transmission

In order to reconstruct reliable images, we need to know precisely DC levels and amplitudes (see section 4.11.1 for definitions of these terms) together with phases of the modulation patterns. Although the measurements described above are quite complete, there is another way to measure DC levels (in other words, average transmission) of the patterns in a more stable and precise manner. The measurements of average transmission were carried out by simply locating each of the grid assembly (top and bottom, separately) normal to the X–ray beam. Average transmission of a collimator is then given as a product of transmission of a corresponding pair of top and bottom grids. In order to measure raw X–ray beam intensity as well as to calibrate possible fluctuation in the beam intensity, direct X–ray counts from the beam were measured frequently during the measurements.

Together with the optical measurements, the above two X–ray measurements, with fluctuation of the X–ray beam taken into account, were compiled to give phase, DC level, and amplitude of the modulation patterns. Results of the measurements, combined with post–launch calibration, are presented in table 4.4 (a) and (b) (see also section 4.11.1).

4.10.3 Detector Calibration

Temperature compensation for ADC channels

As channel widths of each flash A/D converters (FADCs) might not be equal to each other and also vary with temperatures, the channel widths were measured at several temperatures which are likely in orbit. For this purpose, we used a pulse signal generator whose pulse height increases at a constant rate and measured the channel widths at $-10°$C, 0°C, and $+10°$C (figure 4.27 (a)). An example of in–orbit ^{241}Am line profiles before and after this correction are shown in figure 4.27 (b) and (c), respectively. The data were obtained by an HXT CAL measurement (see section 4.6) with data accumulation time of 600 s. As the in–orbit temperature of HXT–E is $\sim +9°$C, we use the channel widths measured at $+10°$C.

4.10.4 Measurements of HXT–HXA Axes

In order to overlay obtained hard X–ray images with other image data, it is of crucial importance to know relative position between HXT and HXA axes with an accuray better than $\sim 2''$. Since detailed procedure and results will be given by Sawa *et al.* (1993) and Masuda (1993), I only briefly describe the essence of the pre–launch experiment.

Figure 4.28 shows schematic view of the measurements. Diffuse white light was illuminated from the detector–side grid plate. Color diffraction patterns, formed by the reference grids (*e.g.* 0A840, 90A840, and 90A750 in figure 4.10 (b)), were focused on the focal plane of a camera through a long–focal–length lense. As the camera system is focused to the infinity, diffraction

patterns observed directly give angular information of the diffracted light (Makishima 1977). These diffraction patterns give position of the HXT axis including a periodic ambiguity of the fundamental pitch. This ambiguity however, can be removed once we overlay HXT images with other images after launch. Together with the diffracted light, light passing through HXA fiducial grids (*c.f.* figure 4.10 (b)) was also focused by the camera through HXA lenses. Figure 4.29 shows an example of the diffraction patterns and HXA fiducial grids taken with the camera. As we can tell positions of HXA fiducial shadows on HXA CCDs, location of the HXT optical axis relative to the sun center is derived from the HXA CCD outputs.

4.11 In–Orbit Calibration of the HXT

4.11.1 Calibration of HXT–C Parameters

Although we measured parameters for the grids such as phases and amplitudes of modulation patterns in detail before launch, it is possible that these parameters would slightly change due to mechanical vibration and shock at the time of lauch. Therefore it is desirable to estimate in–flight parameters of the HXT grids, and if necessary, to revise the pre–launch values of them. By use of hard X–ray data from flares, we estimated the following parameters : (1) Mutual rotation angle $\theta_{\rm R}$ between the top and bottom grid plates, and (2) DC level, amplitude, and phase of each modulation pattern. Detailed procedure for estimating the above parameters will be described by Inda–Koide (1993). Here in the following, I will describe the essential points. $\theta_{\rm R}$ was estimated, when synthesizing images, by systematically changing $\theta_{\rm R}$, hence by changing phases of modulation patterns, and monitoring χ^2 values as well as image quality such as smoothness of images. This procedure has been adopted for several flares and $\theta_{\rm R}$ is now estimated to be $\theta_{\rm R} \sim -1.0 \times 10^{-4}$ radian (or $\sim 20''$), where the minus sign means that the sun–side grid plate is rotated counter–clockwise relative to the detector–side plate when viewing the sun. Similarly, the phase and amplitude of each modulation pattern were estimated by using several flare data, but in this case simultaneously, to search for a set of parameters that gave the best imaging results. As a result, we found that a set of parameters thus found was almost similar to the pre–launch one; well within the required accuracy of the parameters listed in section 4.3.1. Even the pre–launch set of parameters gives satisfactory images.

Summary of the modulation pattern parameters are listed in table 4.4 ((a) for fanbeam and (b) for Fourier grids, respectively). The table incorporates results from the post–lauch calibration of the mutual rotation angle while the modulation pattern parameters obtained from the pre–launch calibrations are listed in the table. This set of parameters gives satisfactory results in the image synthesis, even if we do not use modulation pattern parameters derived by the post–launch calibration. In the table, K is the serial number of modulation collimators, S# is the corresponding sensor numbers, k is the spatial wavenumber, PA (θ) is the position angle, DC (d) is the *DC level*, Amp. (f) is the *amplitude*, 'Phase' (φ) is the *phase*, and $\varphi_{\rm rot}$ is the

correction added to the phases φ corresponding to a unit mutual rotation angle of $\theta_{\rm R} = 1 \times 10^{-4}$ radian. The quantities d, f, and φ are conventionally defined as in figure 4.30 for both fanbeam and Fourier grids. Note that for fanbeam grids, d is always equal to f and that $T_p = d + f$ gives peak transmission. It is worthwhile to point out that if grids are fabricated as designed, *i.e.* $w_W = 3w_S$ for fanbeam grids and $w_W = w_S$ for Fourier grids (w_W and w_S are wire– and slit–widths of a grid, respectively), then the designed quantities $\bar{d}$ and $\bar{f}$ would be $\bar{d} = \bar{f} = 0.125$ for fanbeam grids and $\bar{d} = \bar{f} = 0.25$ for Fourier grids, respectively.

For each collimator, the actual phase $\varphi_0(\theta_{\rm R})$ of the modulation pattern is given as :

$$\varphi_0(\theta_{\rm R}) = \varphi + \varphi_{\rm rot}\theta_{\rm R} \ , \tag{4.12}$$

where $\theta_{\rm R}$ is given in units of 1×10^{-4} radian.

4.11.2 Calibration of Pulse–Height Response

The detector gain suffers from a secular variation, though only slightly, during a long mission life. As mentioned in section 4.3.1, gain of the detectors need be adjusted equally to each other within ~ 1 % accuracy. Hence, we have been making HXT CAL measurements typically once a month (see section 4.6) when the *Yohkoh* KSC contacts are in night time. X–rays from the ^{241}Am calibration source are accumulated for about 10 minutes, yielding typically $\sim 7000 - 8000$ counts for each detector. From the set of 64 line profiles thus obtained, we make a template profile by averaging the 64 profiles. By taking cross–correlation between the template and each line profile of the ^{241}Am source at 59.5 keV, the line center position (in units of 64 energy channels of HXT CAL outputs) is well determined with an accuracy of 0.1 ch. Gain of the detectors is then adjusted in ~ 1 % accuracy so that the ^{241}Am line center will be located at the energy channel of $C_{\rm PH} = 37.0$ ch. Note that this adjustment gives the following channel–energy relationship :

$$E = 1.252 \times (C_{\rm PH} + 10.1) \ , \quad \text{where } 0 \le C_{\rm PH} < 64 \ . \tag{4.13}$$

The four energy bands of HXT are then given as L : 13.9 – 22.7, M1 : 22.7 – 32.7, M2 : 32.7 – 52.7, and H : 52.7 – 92.8 keV, respectively (see section 4.6 and table 4.3). Detailed procedure of the detector gain calibration will be described by Masuda (1993).

4.11.3 Overlay of HXT Images with Other Images

As is described in section 4.10.4, angular offset of the HXT axis from the HXA axis was measured in a satisfactory accuracy of $\sim 2''$. Here I only briefly describe procedures to overlay HXT images with other images. Detailed description of the procedure as well as resultant images will be given elsewhere (Masuda 1993).

Overlay with SXT images :

The sun center position derived from HXA outputs can be related to the SXT CCD pixel address. This procedure was prepared by J.-P. Wülser (private communication) by taking regression between positions of HXA sun center and the sun center derived from full-sun SXT images with orbital and secular variations taken into account. Then, HXT images are located on the SXT images. As the SXT CCD is tilted from the HXT X (or Y) directions, the tilt angle of $\sim 0.7°$ need be incorporated in the overlay.

Overlay with images from ground observatories :

Overlay of HXT images with images taken at ground-based observatories such as radio and optical (*e.g.* Hα) can be done as follows. As we know angular offset of the HXT axis from the sun center, we can locate HXT images on the solar disk once we know the solar north-pole direction (or the direction of the celestrial north). This information is derived from attitude history of the spacecraft within a typical accuracy of 0.1°.

In addition to the above method which utilizes HXA information, we can overlay HXT images with other images in a practical manner using soft X-ray images taken with SXT. As soft X-ray images (especially taken with the Be filter of SXT, with which the highest temperature component of a flare is imaged among the SXT filters) generally resembles to hard X-ray images in the L band, we can overlay the two images so that the overall profiles and bright portions of the sources would match with each other. The accuracy of overlay with this method is typically $\sim 2''$. When making overlay with images from ground observatories, we can utilize optical images taken with the optical telescope of SXT. By matching SXT sunspot images with sunspots imaged at ground observatories, and/or matching the solar limb, HXT images are overlaid with radio and optical images with an accuracy of $\sim 3''$.

4.12 Summary

Since the beginning of the observations in October 1991, the HXT has observed, with an event recognition threshold of 3 cts/s/SC, a total of 774 flares by the end of September 1993, including 13 *GOES* X-class flares, 252 M-class flares, and 500 C-class flares. Some initial results of imaging observations with HXT, together with statistics of observed flares are described in Kosugi *et al.* (1992), Matsushita *et al.* (1992), and Sakao *et al.* (1992). These results show that HXT is in fact a powerful instrument for understanding high energy aspects of solar flares as was described in chapter 3. In the next chapter, I give breif description on the image synthesis procedure which is actually utilized in the HXT image synthesis. In chapters 6 and 7, I describe imaging observations of hard X-ray sources of several impulsive flares with the HXT instrument. The observational results, especially the characteristics of hard X-ray 'double sources', are

analyzed and discussed from my own viewpoint of particle acceleration and hard X-ray emission mechanisms, with respect to geometry of magnetic fields in which flares take place.

Table 4.1: Design goals of the HXT instrument (comparison with its predecessors; after Kosugi *et al.* 1991)

	HXT (SOLAR-A)	HINOTORI imager	HXIS (SMM)
Collimator type	Multi-el. bigrid MC	Rotating bigrid MC	Multi-el. IC
No. of elements	64 SC's	2 (orthogonal)	(F)304; (C)128
Size of elements	23 mm □	120 mm ∅	7.5 mm ∅
Image acquisition	2D Fourier synthesis	1D scans → 2D image	1 el./1 pixel
Angular resolution	~5"	~10"	8" (32")
Field of view	whole Sun	whole Sun	2'40" (6'24")
Synthesis aperture	2'06"	2'12"	2'40" (6'24")
Time resolution	0.5 s	~10 s	1.5–9 s
Energy bands (keV)	4 channels Ch. L: 15(19)–24 Ch. M1: 24–35 Ch. M2: 35–57 Ch. H: 57–100	1 channel 5(17)–40	6 channels 3.5–5.5–8.0 8.0–11.5–16 16–22–30
Detector	NaI(Tl) scint. (25 mm □ × 64)	NaI(Tl) scint. (120 mm ∅ × 2)	Gas prop. counter (7.5 mm ∅ × 900)
Effective area	~70 cm^2	~8 cm^2 × 2	0.07 cm^2 $pixel^{-1}$

Note: MC = modulation collimator; IC = imaging collimator; SC = subcollimator; 2D = two-dimensional; 1D = one-dimensional; (F) = fine field of view; (C) = coarse field of view.

Table 4.2: Parameters of fanbeam/Fourier elements.

	Fanbeam elements		Fourier elements					
No. of elemments	16 (4 × 4 PA)		48 (4 × 2 (cosine, sine) ×6 PA)					
Position angle (degree)	0, 45, 90, 135		0, 30, 60, 90, 120, 150					
Phases	4 $(0, \pi/2, \pi, 3\pi/4)$		2 (cosine, sine)					
Wavenumber coverage	$k = 1, 2$		$k = 3, 4, 5, 6, 7, 8$					
Wavenumber (k)	1	2	3	4	5	6	7	8
Pitch (μm)	840		280	210	168	140	120	105
(arc sec)	126		42.0	31.5	25.2	21.0	18.0	15.8
Slit width (μm)	210		140	105	84	70	60	60
Wire width (μm)	630		140	105	84	70	60	45
Material	0.5 mmt tungusten		0.05 mmt tungusten films × 10					
Fabrication	Electric discharge method		Photo-etching					

Table 4.3: Four PC channels in the observation mode (PC mode).

Energy band	Digital data value	Energy range (keV)	
		nominal	actual
L	1(4) – 7	15.0(19.0) – 24.4	13.9(17.7) – 22.7
M1	8 – 15	24.4 – 35.2	22.7 – 32.7
M2	16 – 31	35.2 – 56.8	32.7 – 52.7
H	32 – 63	56.8 – 100.0	52.7 – 92.8

Values in the parenthesis correspond the digital lower discrimination (DLD) level of 4.

Table 4.4: (a) Modulation pattern parameters of the HXT fanbeam grids.

K	S#	k	PA (θ)	ID	DC (d)	Amp. (f)	Phase (φ)	φ_{rot}
01	14	1	0	1	0.106	0.106	-0.012	-0.018
02	15	1	0	2	0.108	0.108	0.242	-0.013
03	11	1	0	3	0.108	0.108	0.489	-0.013
04	10	1	0	4	0.106	0.106	0.747	-0.018
05	70	1	45	1	0.116	0.116	0.008	0.000
06	71	1	45	2	0.113	0.113	-0.240	0.004
07	75	1	45	3	0.115	0.115	-0.496	0.000
08	74	1	45	4	0.115	0.115	-0.752	-0.004
09	00	1	90	1	0.106	0.106	-0.041	-0.019
10	01	1	90	2	0.111	0.111	-0.282	-0.019
11	05	1	90	3	0.111	0.111	-0.539	-0.013
12	04	1	90	4	0.111	0.111	-0.799	-0.013
13	64	1	135	1	0.106	0.106	-0.014	0.000
14	65	1	135	2	0.110	0.110	0.270	0.004
15	61	1	135	3	0.115	0.115	0.497	0.000
16	60	1	135	4	0.109	0.109	0.715	-0.004

Table 4.4: (b) Modulation pattern parameters of the HXT Fourier grids.

K	S#	k	PA (θ)	ID	DC (d)	Amp. (f)	Phase (φ)	$\varphi_{\rm rot}$
17	62	3	30	C	0.171	0.168	-0.051	0.041
18	66	3	30	S	0.164	0.164	-0.303	0.049
19	51	3	60	C	0.190	0.180	0.217	-0.003
20	50	3	60	S	0.192	0.170	-0.061	-0.025
21	45	3	120	C	0.194	0.177	-0.002	-0.003
22	44	3	120	S	0.197	0.181	0.247	-0.011
23	30	3	150	C	0.204	0.194	0.056	0.052
24	34	3	150	S	0.209	0.195	-0.196	0.044
25	12	4	0	C	0.206	0.183	-0.068	-0.031
26	16	4	0	S	0.197	0.184	0.167	-0.031
27	55	4	60	C	0.205	0.170	0.008	-0.005
28	54	4	60	S	0.199	0.178	-0.259	-0.034
29	21	4	90	C	0.211	0.191	-0.250	-0.032
30	20	4	90	S	0.204	0.189	-0.057	-0.032
31	31	4	150	C	0.227	0.172	0.041	0.051
32	35	4	150	S	0.237	0.187	-0.227	0.040
33	06	5	0	C	0.187	0.173	-0.073	0.039
34	02	5	0	S	0.194	0.172	0.164	0.039
35	76	5	30	C	0.204	0.178	-0.102	-0.001
36	72	5	30	S	0.211	0.191	-0.303	0.013
37	25	5	90	C	0.227	0.178	-0.309	-0.013
38	24	5	90	S	0.220	0.176	-0.127	-0.013
39	41	5	120	C	0.236	0.176	0.025	-0.029
40	40	5	120	S	0.207	0.177	0.257	-0.042
41	63	6	30	C	0.223	0.165	-0.125	0.054
42	67	6	30	S	0.204	0.154	-0.366	0.070
43	53	6	60	C	0.240	0.154	0.285	0.025
44	52	6	60	S	0.244	0.152	-0.059	-0.019
45	47	6	120	C	0.198	0.161	-0.003	0.025
46	46	6	120	S	0.219	0.164	0.246	0.009
47	32	6	150	C	0.281	0.168	0.012	0.049
48	36	6	150	S	0.284	0.184	-0.300	0.033
49	13	7	0	C	0.215	0.173	0.060	-0.018
50	17	7	0	S	0.219	0.179	0.388	-0.018
51	57	7	60	C	0.183	0.147	0.144	0.029
52	56	7	60	S	0.199	0.156	-0.145	-0.022
53	23	7	90	C	0.202	0.152	-0.233	-0.056
54	22	7	90	S	0.220	0.156	-0.149	-0.056
55	33	7	150	C	0.232	0.163	-0.100	0.025
56	37	7	150	S	0.232	0.178	-0.380	0.007
57	07	8	0	C	0.174	0.173	0.179	0.021
58	03	8	0	S	0.230	0.171	0.440	0.021
59	77	8	30	C	0.242	0.147	-0.128	0.035
60	73	8	30	S	0.218	0.140	-0.330	0.057
61	27	8	90	C	0.232	0.167	-0.375	-0.021
62	26	8	90	S	0.255	0.167	-0.208	-0.021
63	43	8	120	C	0.193	0.144	0.076	-0.004
64	42	8	120	S	0.229	0.151	0.285	-0.025

Figure Captions

Figure 4.1: Schematic illustration of the concept of image synthesis with HXT. Each bi-grid modulation collimators samples two-dimensional spatial Fourier component of hard X-ray sources.

Figure 4.2: Arrangement of the 64 subcollimator grids on the base plate (top view). The slit directions of each grids are shown by the hatching. The sine and cosine Fourier element pairs are represented by solid and dotted hatching lines, respectively. Number of the lines denote the wave number of each Fourier element. The spacecraft coordinate is shown in the figure (after Kosugi *et al.* 1991).

Figure 4.3: The detector assembly (HXT-S; top view). Squares with octal numbers in it represent 64 scintillation counters. Every 8 counters are grouped into a sub-module and have a common high voltage power supply (shown as 'HV' in the figure). Two inclined rectangular boxes near the center of the HXT-S denotes two one-dimensional CCDs for the HXA. The spacecraft coordinate is shown in the figure (after Kosugi *et al.* 1991).

Figure 4.4: Schematic drawing of (a) cosine and (b) sine grids of modulation collimators with their modulation patterns ($M_C(x)$ and $M_S(x)$, respectively).

Figure 4.5: Relationship among the distance r, the position angle θ, and a two-dimensional brightness distribution. Note that in the actual image synthesis procedure and in identifying HXT grids, I use different definitions of xy-coordinate and position angle θ from the one shown here (see figure 5.2).

Figure 4.6: Arrangement of subcollimators in the UV plane. Each dot denotes the position angle θ and the wavenumber k of a pair of cosine-sine Fourier elements. Each arrow near the origin of the UV plane corresponds to a set of four fanbeam grids with the same position angle. Note that the definition of position angle in this figure is the same as the one in figure 4.5.

Figure 4.7: Modulation patterns for a set of fanbeam elements. Four fanbeam elements, with the same position angle and whose phases of modulation patterns are successively shifted by $\pi/2$, compose a set (denoted as G1, G2, G3, and G4). Note that in the figure, modulation patterns of G1 and G2 are shifted by $\pi/2$ in phase with each other.

Figure 4.8: Exapmles of image–synthesis simulations by MEM for the actual HXT design. *Top* : original maps. *Bottom* : restored maps. Contour levels are 10% steps (solid lines) and 5% (dashed lines) of the peak in each map. Size of the maps is $\sim 2' \times 2'$ (after Kosugi *et al.* 1991).

Figure 4.9: Comparison of various material with respect to (a) mass density ρ and mass absorption coefficient κ at a photon energy of 100 keV, (b) thermal expansion coefficient α and thermal expansion coefficient K, and (c) mass density ρ and Young ratio E.

Figure 4.10: (a) A pair of fanbeam grid plates (position angle $\theta = 45°$) for top and bottom grid assemblies (110 % in scale). The slits have a width of 210 μm and a pitch of 840 μm. Three small slits at the lower left corner of each grid plate are optical alignment patterns with a slit width of 100 μm and a pitch of 840 μm (for 0A840 and 90A840) or 750 μm (for 0A750). These alignment patterns are utilized when mounting the grid assemblies to the top and bottom face plates of the collimator body (see *e.g.* Bradt *et al.* for the alignment of grid assemblies by use of optical diffraction patterns produced by (reference) grids). (b) Fiducial grids for HXA (126 % in scale). This grid plate is fixed to the bottom grid assembly. Slits at the top and bottom of the plate are the reference grids which are used to obtain HXT axis (*c.f.* section 4.10.2). Pitch (840 μm or 750 μm) and position angles (0° or 90°) of the refenrence grids are shown in the figure.

Figure 4.11: (a) A Fourier grid plate (100 % in scale; position angle $\theta = 120°$) for the top grid assembly. Pitch (in μm) and cosine/sine type of the grids are shown in the figure. Three parallel lines in each of the grid are supporting wires which run orthogonal to the grid wires. (b) A Fourier grid plate (100 % in scale) for the bottom grid assembly which corresponds to the plate (a). (c) Magnification of a part of Fourier grid (a) (200 % in scale).

Figure 4.12: Schematic drawing of a detector module. The detectors of HXT consist of a set of 64 identical photomultiplier tubes with NaI (Tl) scintillation crystals (after Kosugi *et al.* 1991).

Figure 4.13: Spectral responses of HXT–S and HXT–C. The efficiency of the NaI (Tl) crystal for detecting X–ray photons is shown by the thick line. The transmission efficiencies of the Al filter (0.8 mm thick) alone and plus the two CFRP face plates (each 2.1 mm thick) are shown by dashed and thin lines, respectively. The absorption efficiency or the stopping power of the tungsten grids (0.5 mm thick) is shown in dotted line (after Kosugi *et al.* 1991).

Figure 4.14: Relation of energy resolution ΔE (FWHM value) of a typical HXT detector against incident photon energy E. Energy resolution of the detector is expressed as $\Delta E/E = 1.3 \times E^{-1/2}$ (E in keV), which is similar to typical values for NaI scintillators thus far known.

Figure 4.15: Configuration of electric circuits of an HXT detector module (a photomultiplier, a high–voltage breeder, and a pre–amplifier).

Figure 4.16: Schematic view of an HXT high–voltage (HV) power supply unit. Eight HV power supply units are prepared for the 64 detectors.

Figure 4.17: Block diagram of the X–ray signal processing circuit module. Each of the 64 identical modules processes each analogue output from the corresponding detector (after Kosugi *et al.* 1991).

Figure 4.18: Schematic drawing of HXA optics. Both HXA–X and HXA–Y have the same system with fiducial grid and one–dimensional CCD orthogonal to each other. The lense for HXA–X (–Y) is mounted on the top grid plate while the fiducial grid (figure 4.10 (b)) is on the bottom grid plate. The CCDs are mounted on HXT–S.

Figure 4.19: Schematic view of the two one–dimensional HXA CCDs. The two CCDs (for HXA–X and HXA–Y) are set orthogonal to each other and are mounted at the central area of HXT–S as is shown in figure 4.2.

Figure 4.20: An example of HXA CCD output, *i.e.* one–dimensional intensity distribution of the sun, for both HXA–X and Y. Four narrow dips in each of the figure are the shadows of the fiducial marks.

Figure 4.21: Block diagram for HXA signal processing.

Figure 4.22: Discrete commands (DC) and block commands (BC) for HXT. B0 in the block command table represents the most significant bit (MSB), while B7 the least significant bit (LSB), of a variable consisting of 8 bits (= 1 byte).

Figure 4.23: Examples of CCD output showing Moiré pattern formed by diffuse white light through the shortened collimator : (a) a fanbeam grid, and (b) Fourier grids of a cosine–sine pair (after Inda 1991).

Figure 4.24: Schematic drawing of the X–ray measurement system.

Figure 4.25: *Top* : energy spectrum of X-rays generated by ISAS beam generator with acceleration voltage of 50 kV and electric current of 30 mA. *Bottom* : energy spectrum of X-rays from ^{241}Am for giving absolute energy scale to pulse height channels of a pulse height analyzer used in the measurement. The highest peak in the figure corresponds to 59.5 keV.

Figure 4.26: Example of measured X-ray modulation patterns. (a) A set of four fanbeam patterns with position angle $\theta = 90°$. (b) *Top left* : combined modulation pattern of two reference grids (position angle $\theta = 90°$) shown as 90A840 and 90A750 in figure 4.10 (b). The other three patterns are also from the same position angle. *Bottom left* : modulation pattern of a cosine-type Fourier grid whose pitch $p = 210$ μm. *Top right* : a cosine-type grid with $p = 105$ μm (*i.e.* the finest grid). *Bottom right* : a sine-type grid with $p = 105$ μm. (c) An example of combined modulation patterns of two reference grids 90A840 and 90A750 in figure 4.10 (b) ($p = 840$ μm and 750 μm, $\theta = 90°$). See text for details.

Figure 4.27: (a) Relative channel widths of FADCs (for sensors S00 and S01) at +10°C. (b) Sample ^{241}Am line profiles obtained by an HXT CAL measurement after launch, before corrections for FADC channel widths. (c) Same as (b), but after the channel width correction.

Figure 4.28: Schematic view of HXT-HXA axes measurement system. The axes were measured separately for HXA-X and HXA-Y. The auto-collimator was used as a reference between the two measurements.

Figure 4.29: Diffraction patterns of reference grids taken with the long-focal-length camera. *Top*: Diffraction pattern of a reference grid shown as 90A750 in figure 4.10 (b) (pitch $p = 750$ μm and position angle $\theta = 90°$). A thin cross in the figure is the reference hair-cursor light from the auto-collimator. *Bottom* : Diffraction patterns of reference grids whose position angles $\theta = 0°$ and 90° with the same pitch of $p = 840$ μm (0A840 and 90A840 in figure 4.10 (b), respectively). Overlaid is a shadow of HXA fiducial grids.

Figure 4.30: Definition of the DC level (d), amplitude (f), and phase (φ) for fanbeam (a) and Fourier (b) grids. For fanbeam grids, d is always equal to f.

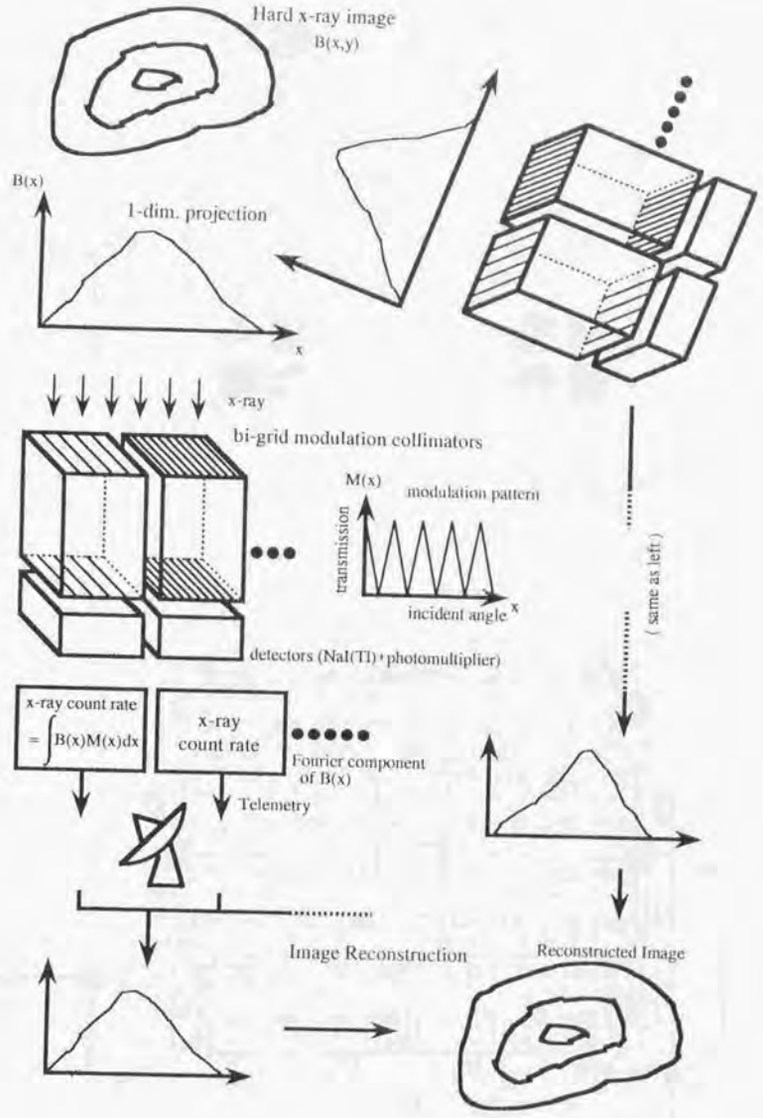

Figure 4.1

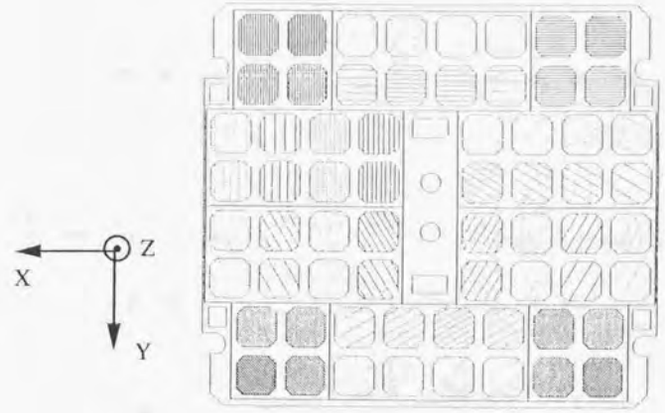

Figure 4.2

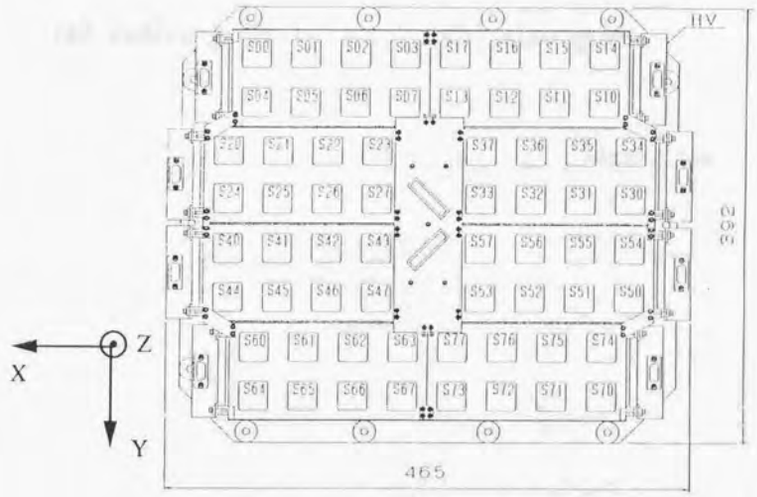

Figure 4.3

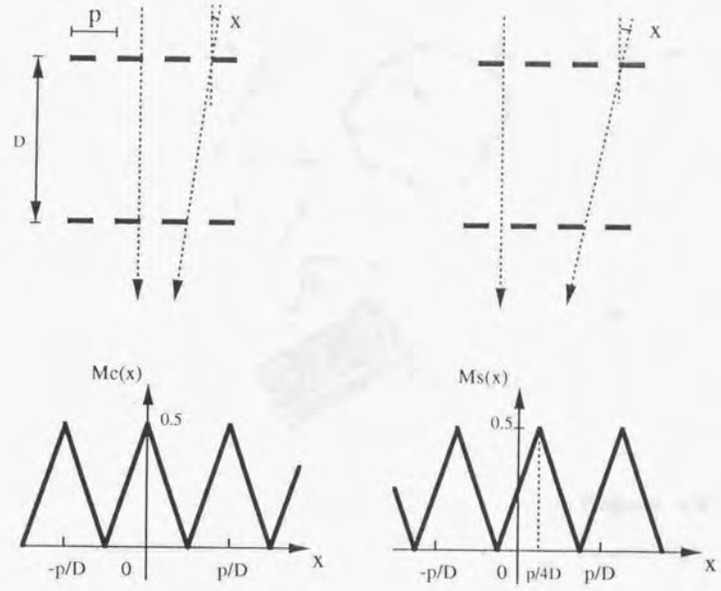

(a) cosine grids (b) sine grids

Figure 4.4

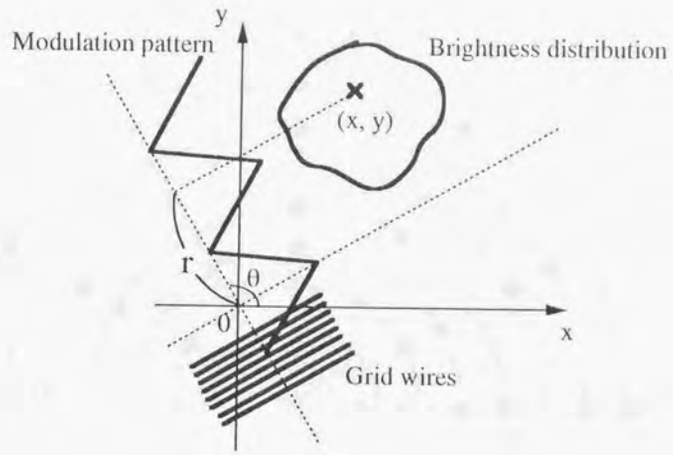
y
Modulation pattern
Brightness distribution
(x, y)
r
θ
0
x
Grid wires

Figure 4.5

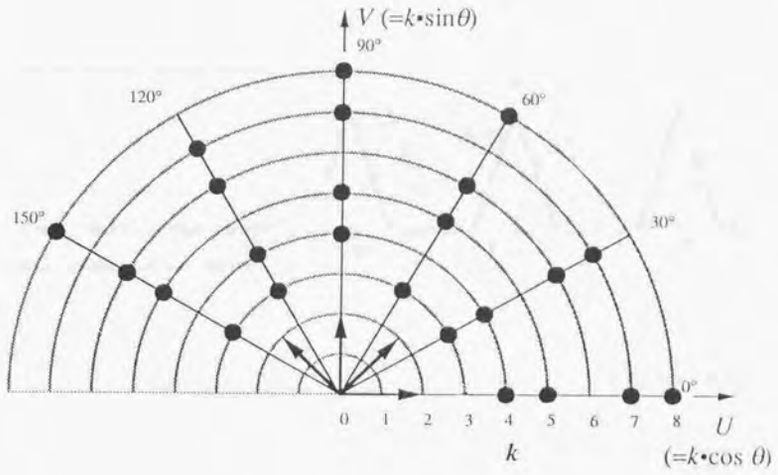

Figure 4.6

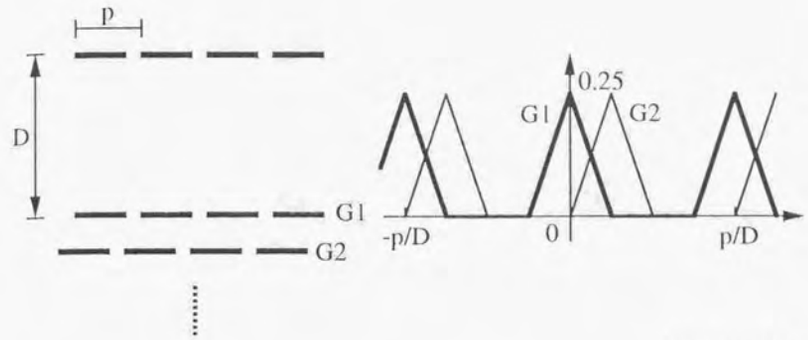

Figure 4.7

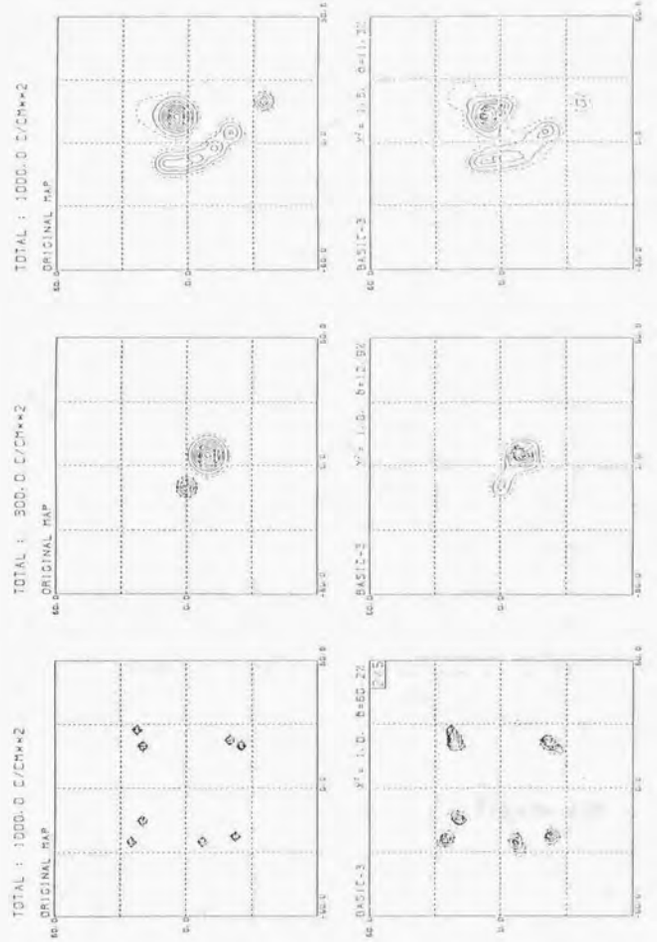
TOTAL : 1000.0 C/CM**2
ORIGINAL MAP
TOTAL : 300.0 C/CM**2
ORIGINAL MAP
TOTAL : 1000.0 C/CM**2
ORIGINAL MAP
BASIC-3
BASIC-2
BASIC-3

Figure 4.8

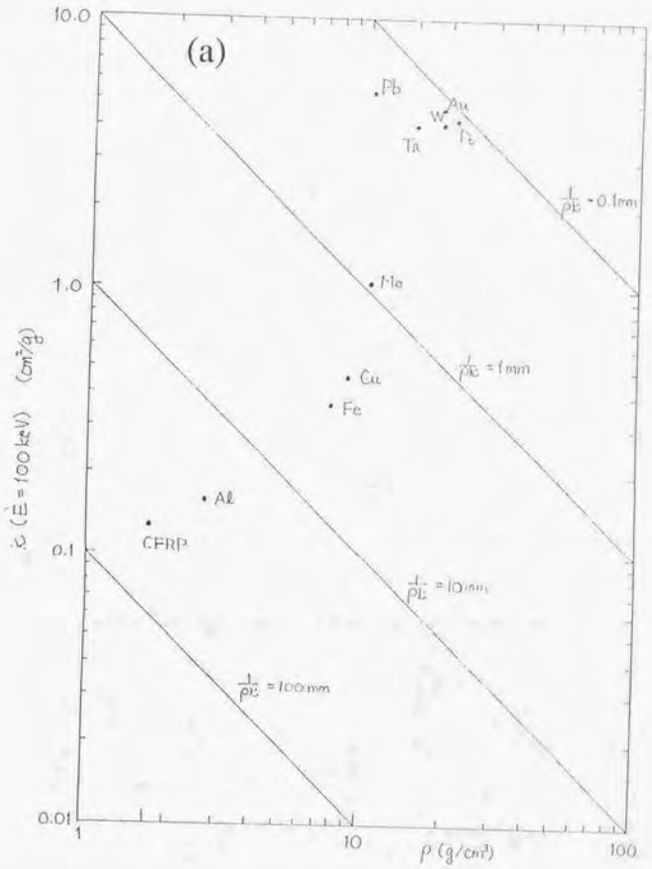
(a)
10.0
1.0
0.1
0.01
1
10
100
ρ (g/cm³)
κ (E = 100 keV) (cm²/g)
Pb
Au
W
Ta
Ti
Mo
Cu
Fe
Al
CFRP
1/ρΣ = 0.1mm
1/ρΣ = 1mm
1/ρΣ = 10mm
1/ρΣ = 100mm

Figure 4.9

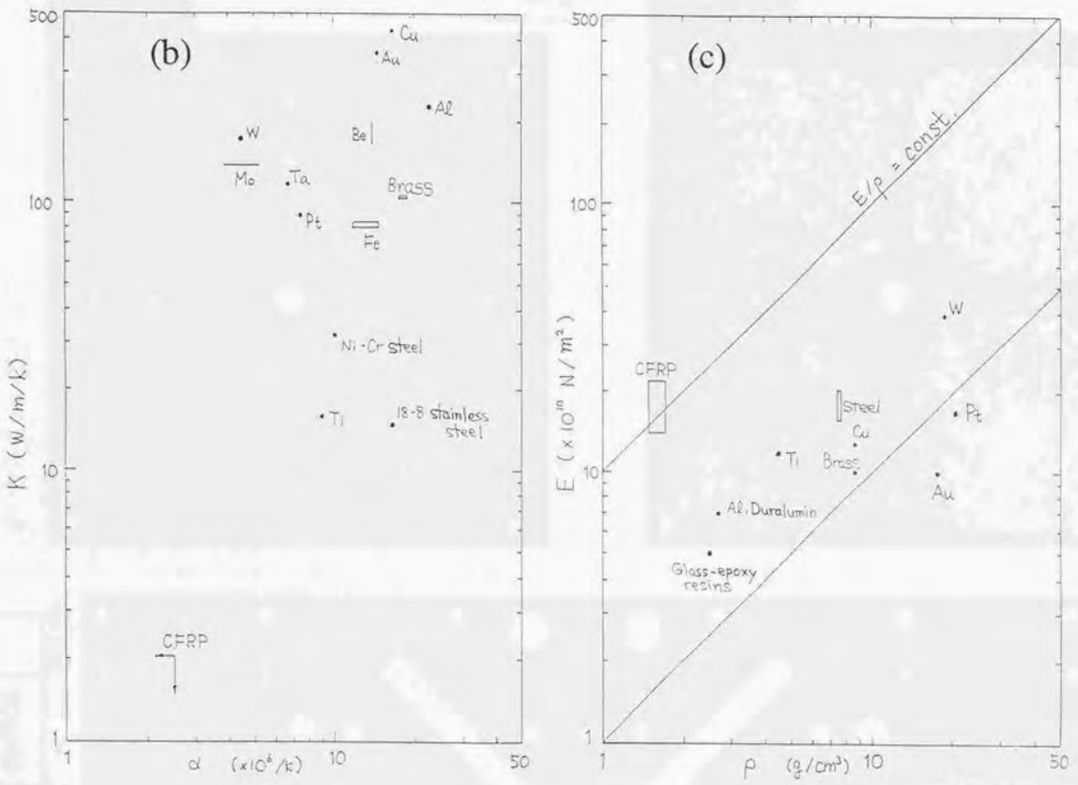

Figure 4.9 (*continued*)

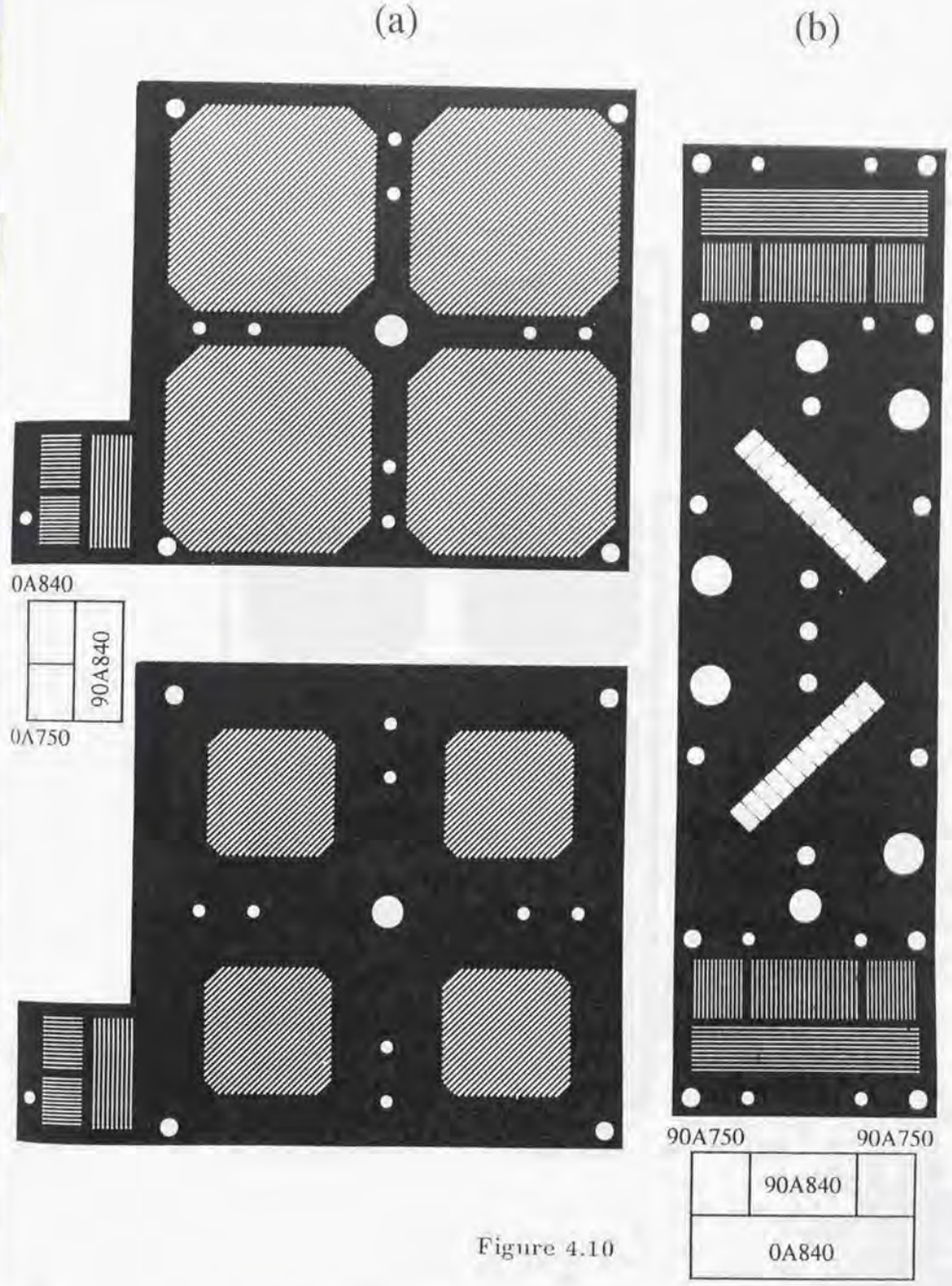

Figure 4.10

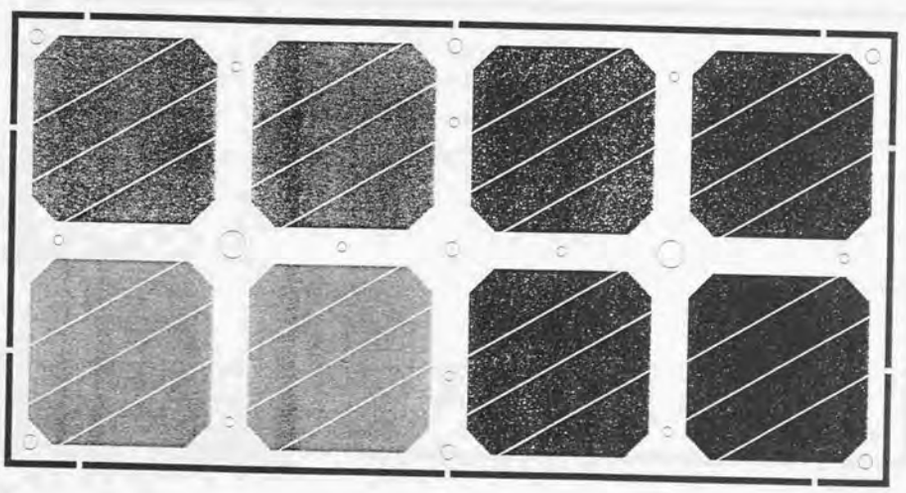

Figure 4.11 (a)

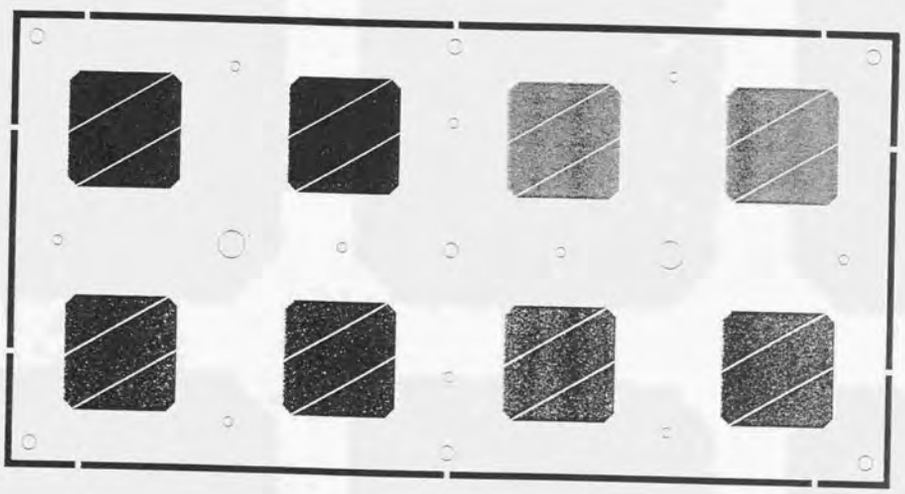

Figure 4.11 (b)

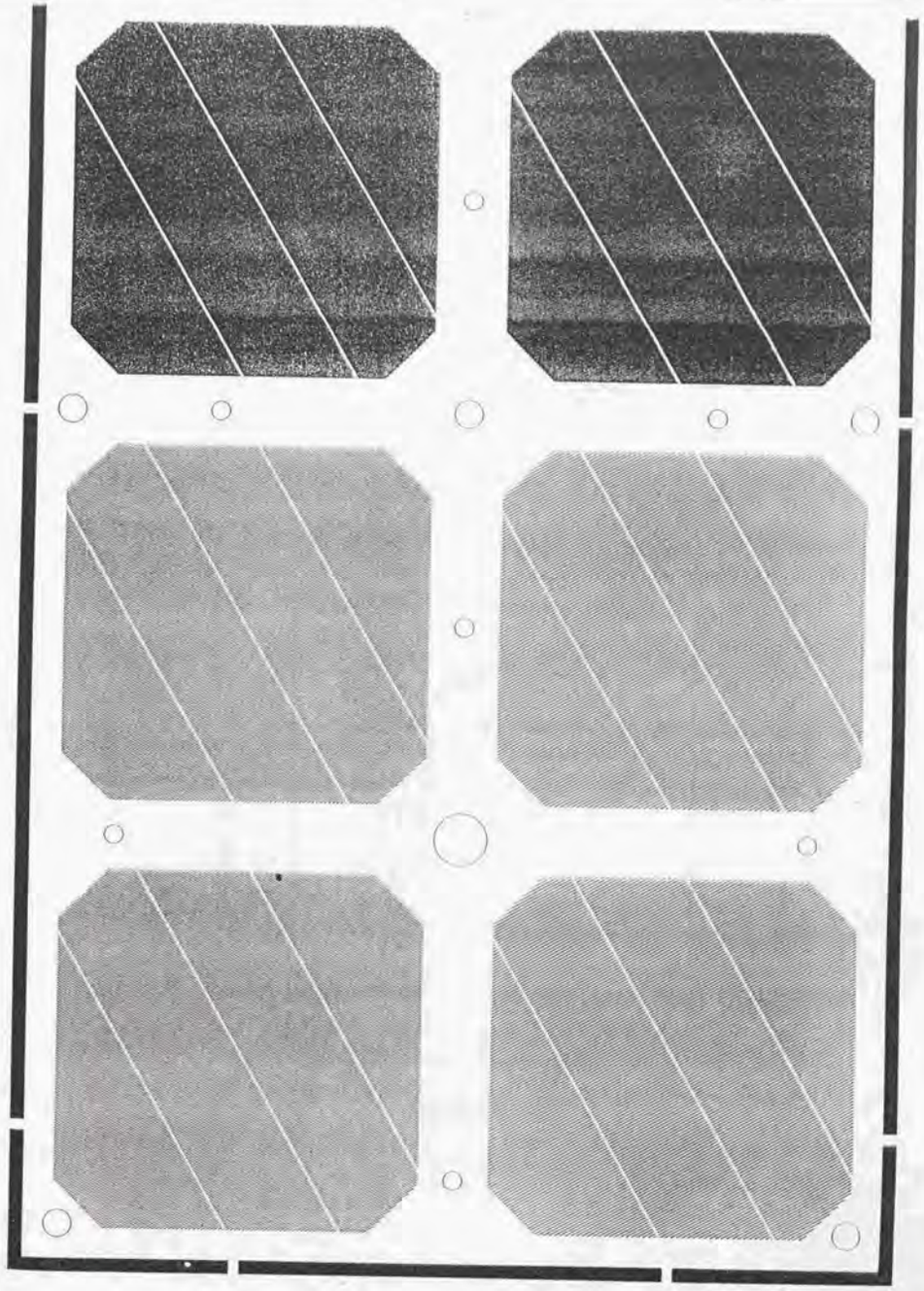

Figure 4.11 (c)

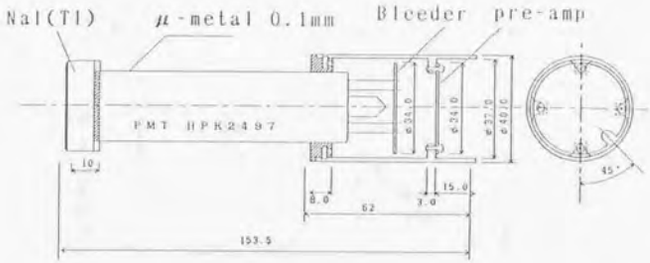

Figure 4.12

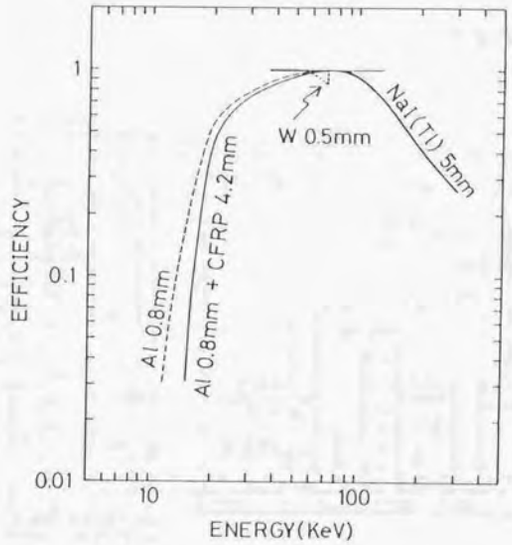

Figure 4.13

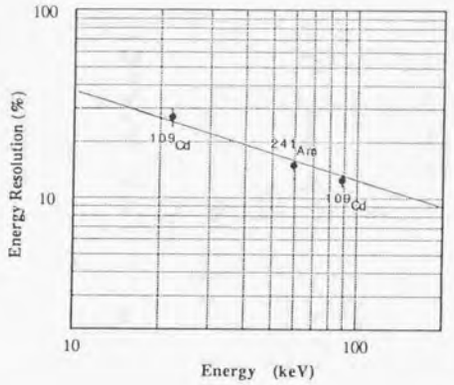

Figure 4.14

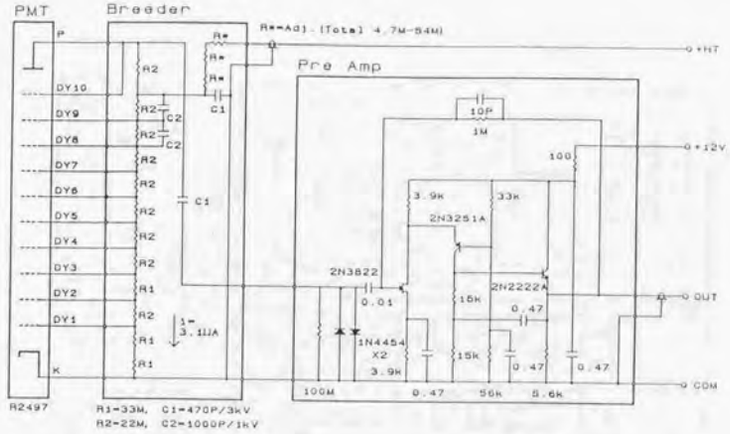

Figure 4.15

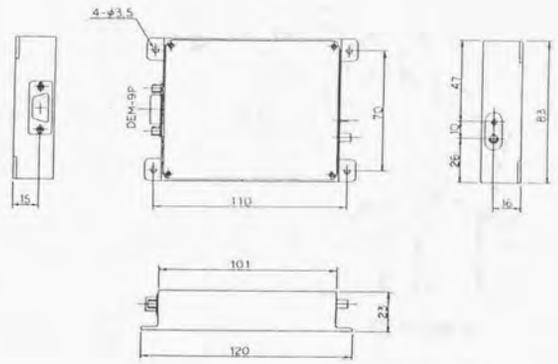

Figure 4.16

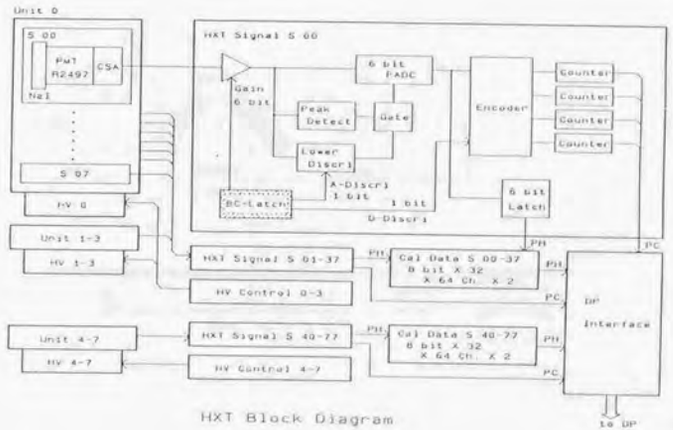

Figure 4.17

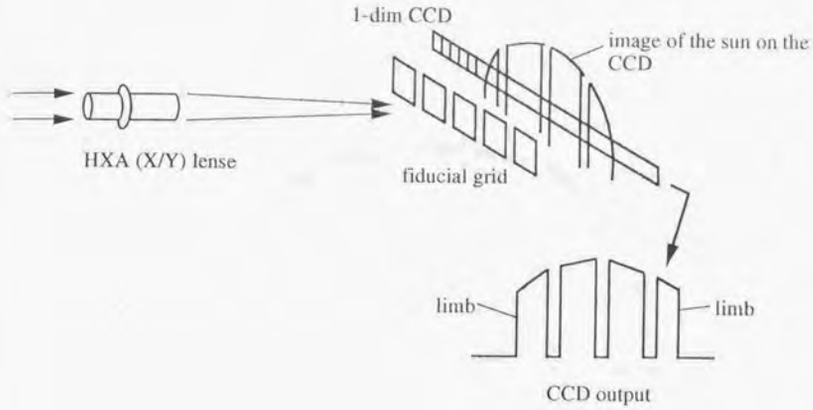

Schematic drawing of HXA-X (-Y) optics

Figure 4.18

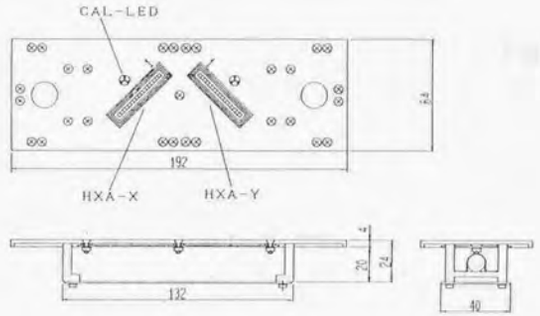

Figure 4.19

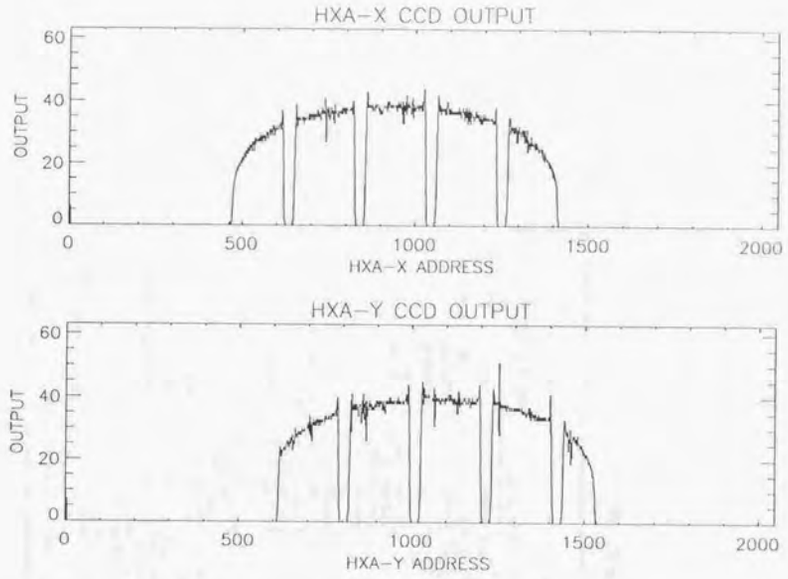
HXA–X CCD OUTPUT
OUTPUT
60
40
20
0
0
500
1000
1500
2000
HXA–X ADDRESS
HXA–Y CCD OUTPUT
OUTPUT
60
40
20
0
0
500
1000
1500
2000
HXA–Y ADDRESS

Figure 4.20

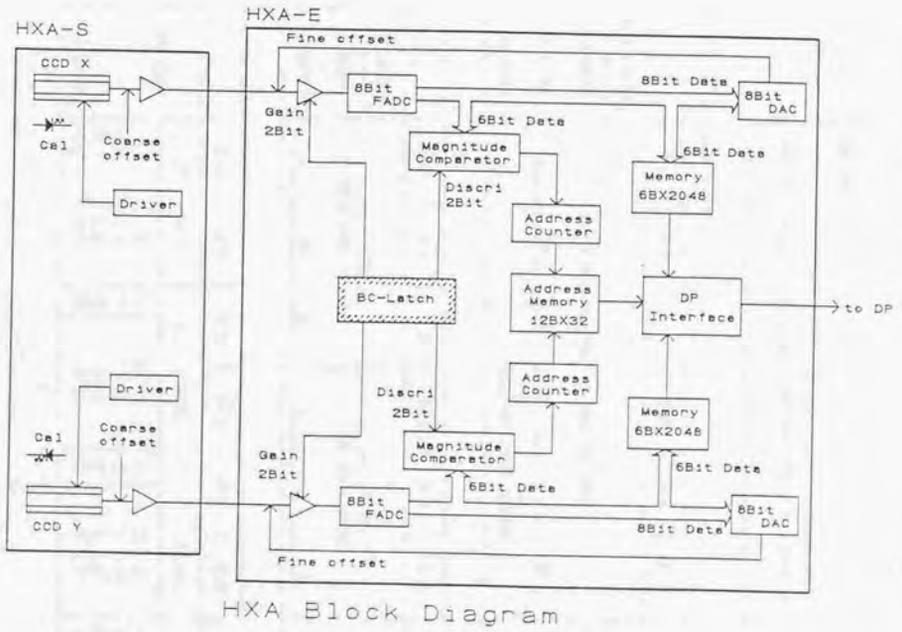

HXA Block Diagram

Figure 4.21

1. Discrete Commands (DCs)

Y X	0	1	2	3	4	5	6	7
0			HXT OFF	A OFF	HV RED OFF	HXT CAL OFF	HXA OFF	HXA CAL OFF
1	BYPS ON	HXT1 ON	HXT2 ON	A ON	HV RED ON	HXT CAL ON	HXA ON	HXA CAL ON
2	THV OFF	HV ENA	HV DIS				BC ENA	BC EXEC
3	THV0 ON	THV1 ON	THV2 ON	THV3 ON	THV4 ON	THV5 ON	THV6 ON	THV7 ON

2. Block Commands (BCs)

	B0	B1	B2	B3	B4	B5	B6	B7
GAIN CONTROL CH. 0~63							D. LD	A. LD
10000000 ~ 10111111	FINE GAIN CONTROL 1% STEP 64 LEVEL						1; 19keV	1; 19keV
	1	0	0	0	0	0	0; 15keV	0; 15keV
11000000	CH.0~63 GAIN CONTROL							

	B0	B1	B2	B3	B4	B5	B6	B7
HV CONTROL HV-0·1~6·7	HV-0 LEVEL 20 % STEP (GAIN)			HV-1 LEVEL 20% STEP (GAIN)				
11100000 ~ 11100011	1	0	0	1	0	0		

	B0	B1	B2	B3	B4	B5	B6	B7
HXA GAIN	X GAIN		X DISCRI		Y GAIN		Y DISCRI	
	11 × 1.6		11 16/64		11 × 1.6		11 16/64	
	10 × 1.3		10 12/64		10 × 1.3		10 12/64	
	01 × 1.0		01 8/64		01 × 1.0		01 8/64	
11100100	00 × 0.7		00 4/64		00 × 0.7		10 4/64	

Figure 4.22

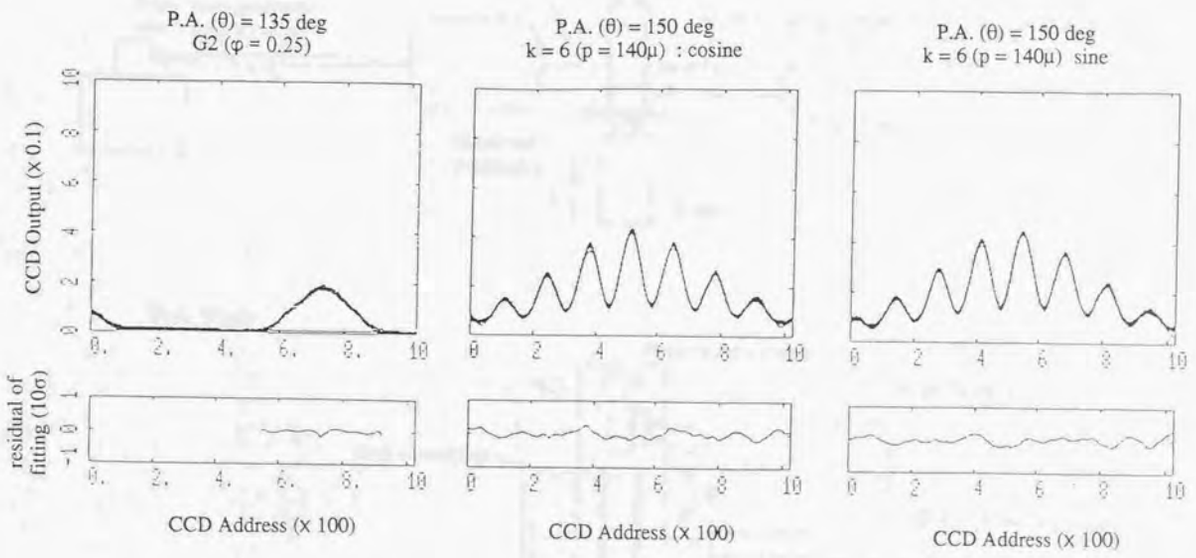

(a) Fanbeam grid

(b) Fourier grids

Figure 4.23

Side View

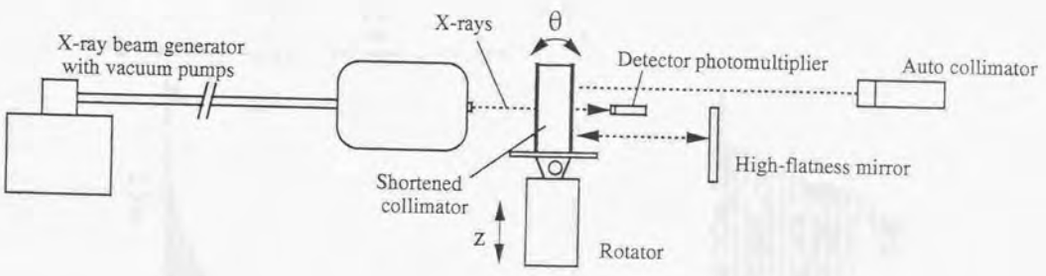

Top View

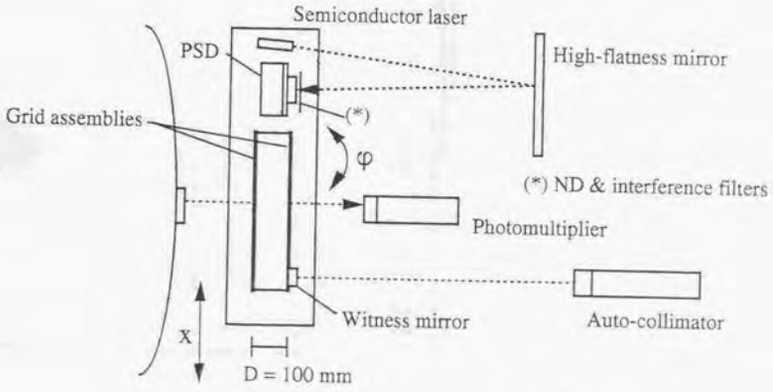

Figure 4.24

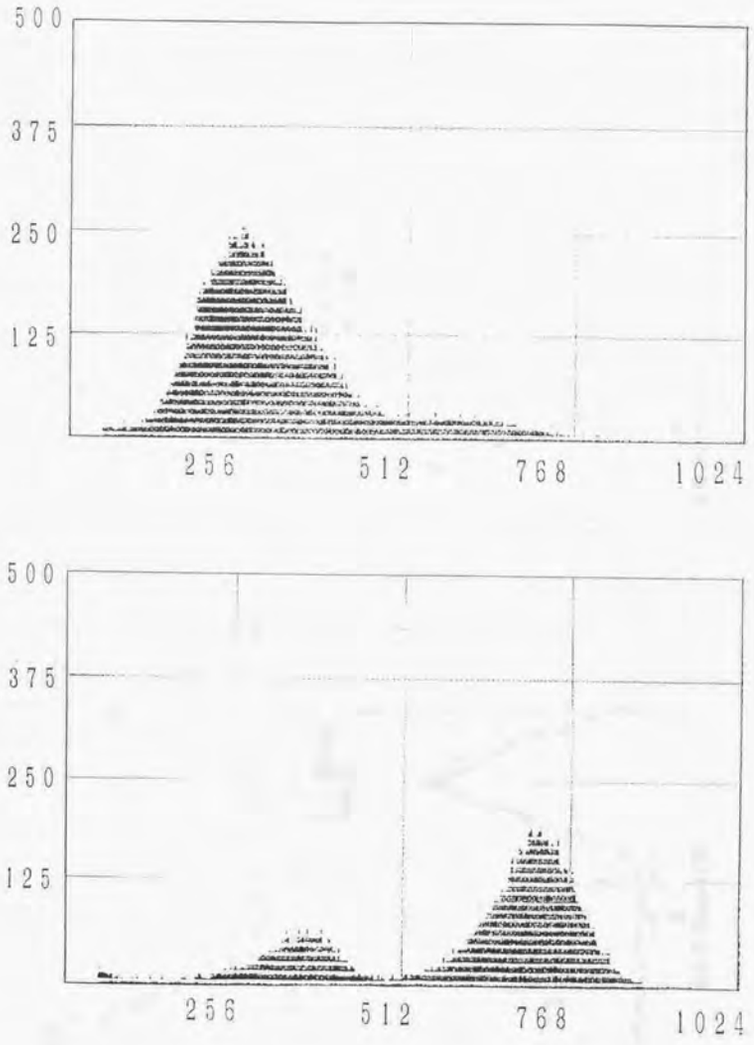
500
375
250
125
256
512
768
1024
500
375
250
125
256
512
768
1024

Figure 4.25

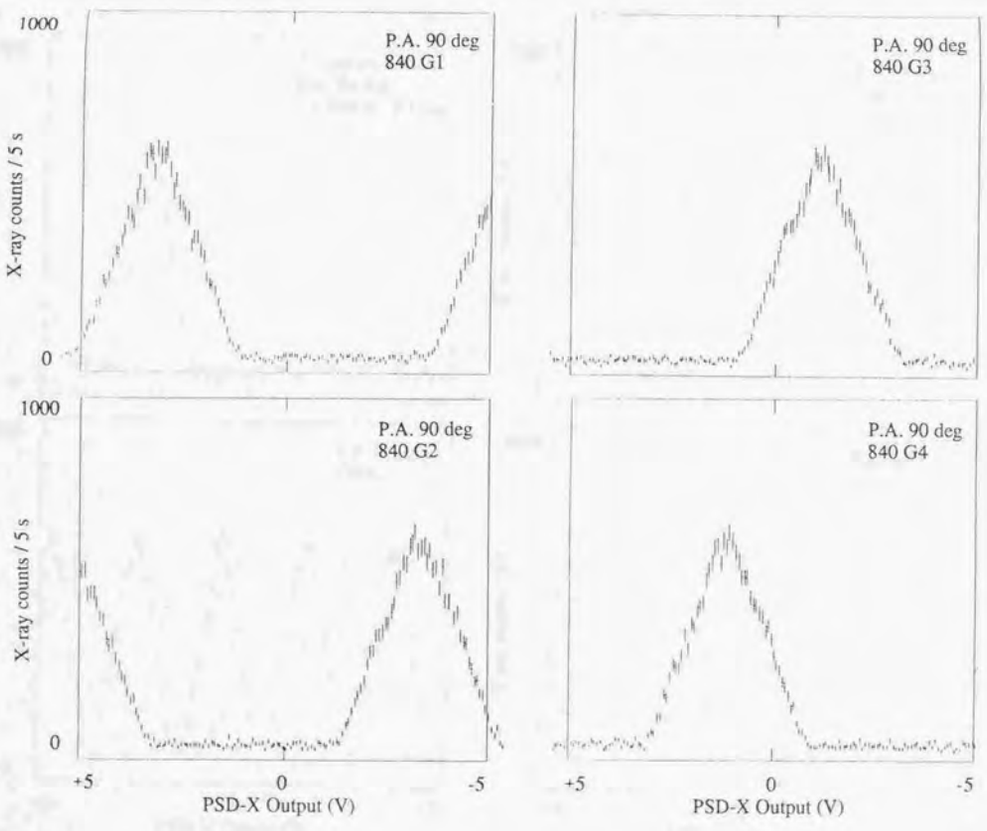
1000
P.A. 90 deg
840 G1
X-ray counts / 5 s
0
P.A. 90 deg
840 G3
1000
P.A. 90 deg
840 G2
X-ray counts / 5 s
0
P.A. 90 deg
840 G4
+5
0
-5
PSD-X Output (V)
+5
0
-5
PSD-X Output (V)

Figure 4.26 (a)

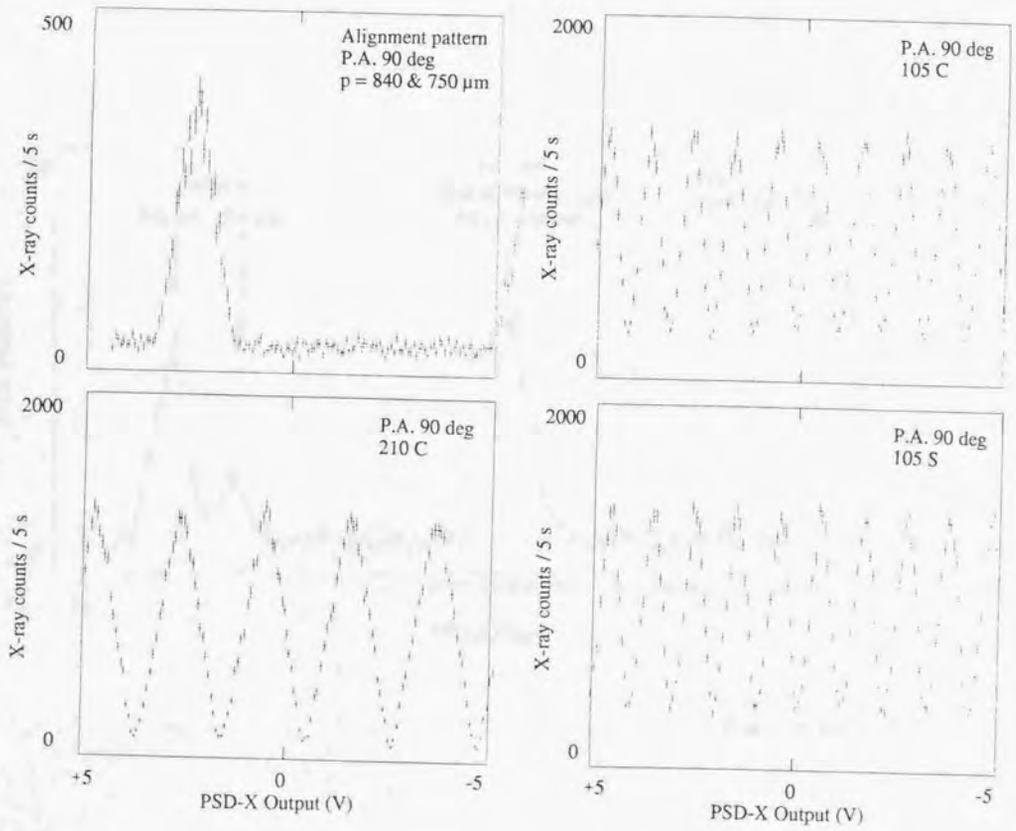
Alignment pattern
P.A. 90 deg
p = 840 & 750 µm
P.A. 90 deg
105 C
P.A. 90 deg
210 C
P.A. 90 deg
105 S
X-ray counts / 5 s
PSD-X Output (V)
500
2000
0
+5
-5

Figure 4.26 (b)

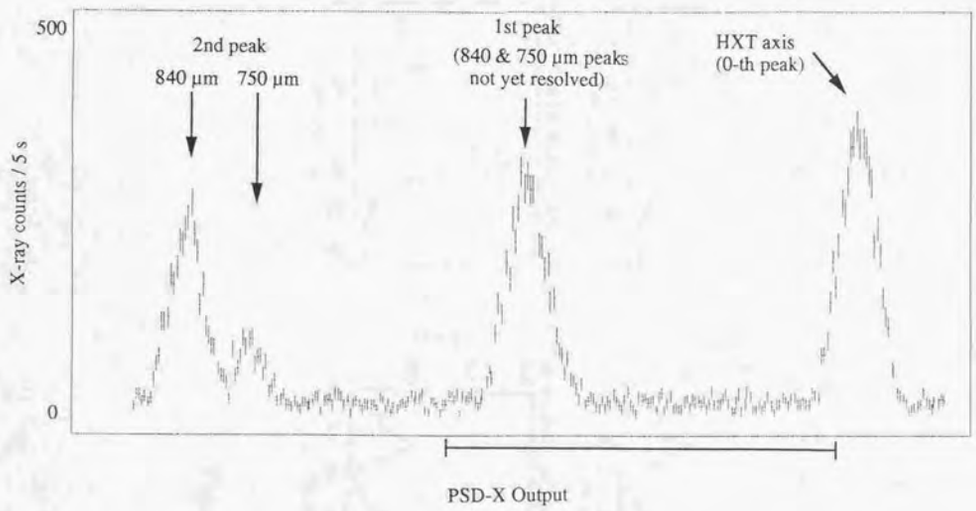
500
0
X-ray counts / 5 s
2nd peak
840 μm 750 μm
1st peak
(840 & 750 μm peaks
not yet resolved)
HXT axis
(0-th peak)
PSD-X Output

Figure 4.26 (c)

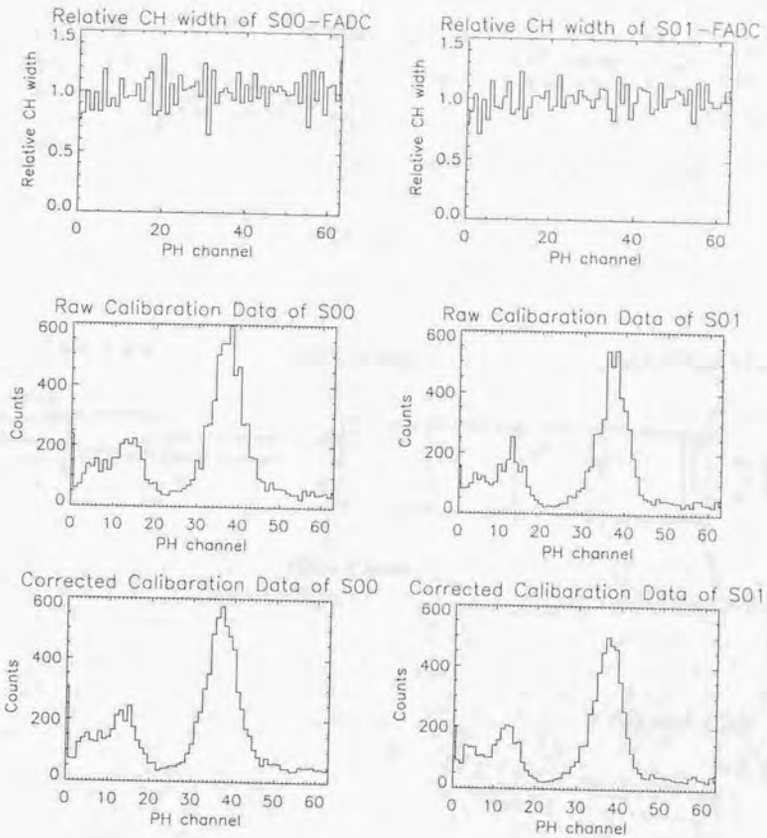
Relative CH width of S00-FADC
Relative CH width
PH channel
Relative CH width of S01-FADC
Relative CH width
PH channel
Raw Calibaration Data of S00
Counts
PH channel
Raw Calibaration Data of S01
Counts
PH channel
Corrected Calibaration Data of S00
Counts
PH channel
Corrected Calibaration Data of S01
Counts
PH channel

Figure 4.27

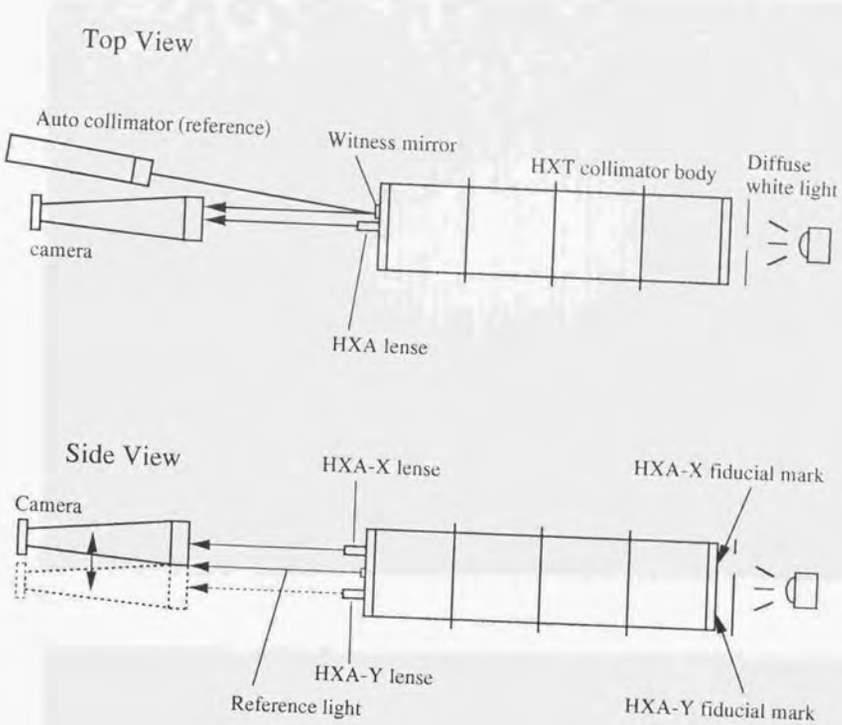
Top View
Auto collimator (reference)
Witness mirror
HXT collimator body
Diffuse white light
camera
HXA lense
Side View
HXA-X lense
HXA-X fiducial mark
Camera
HXA-Y lense
Reference light
HXA-Y fiducial mark

Figure 4.28

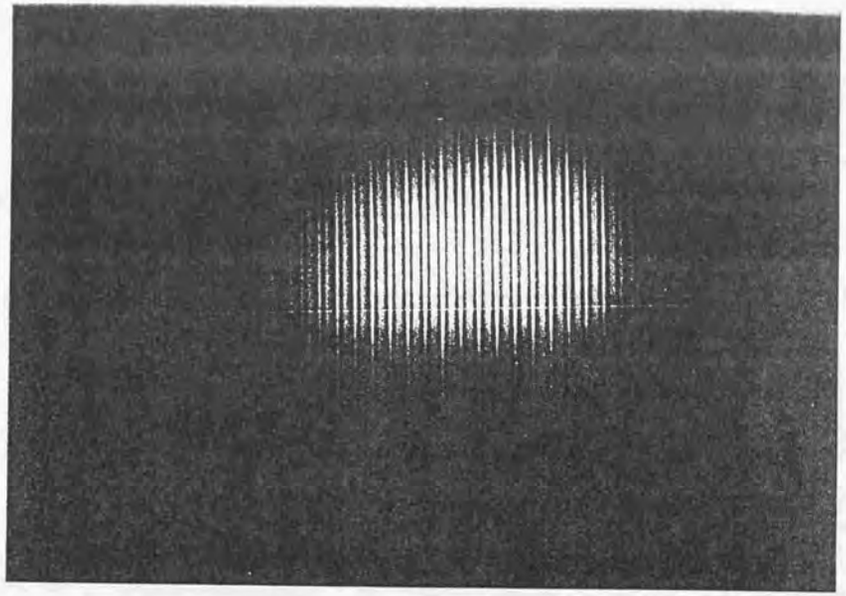

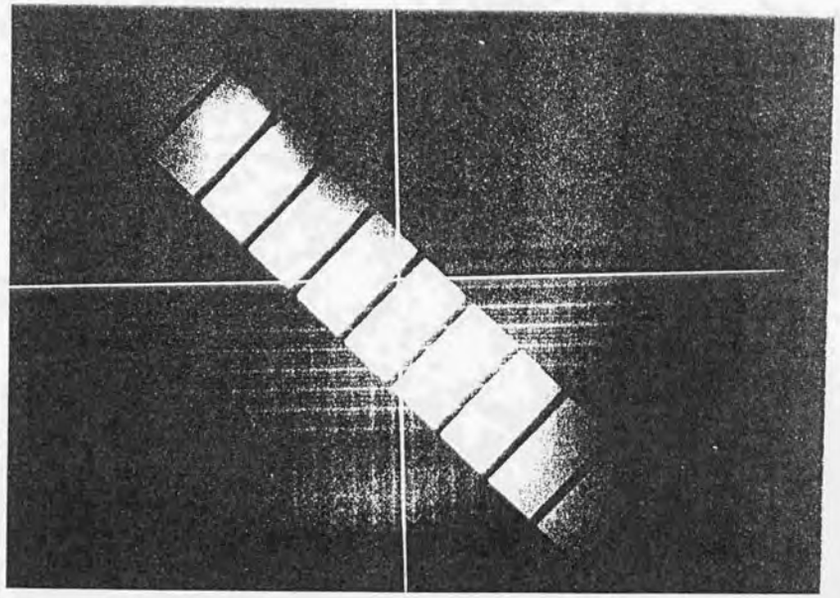

Figure 4.29

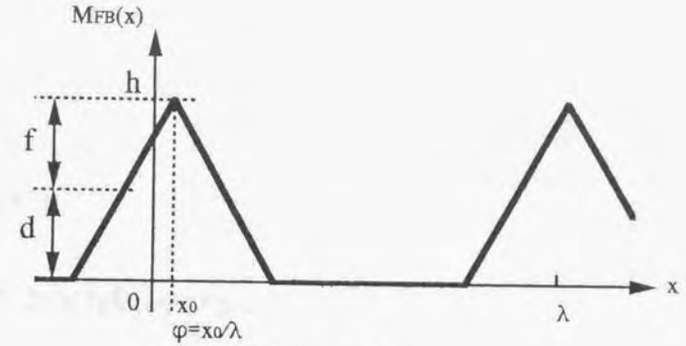

(a) Fanbeam grid

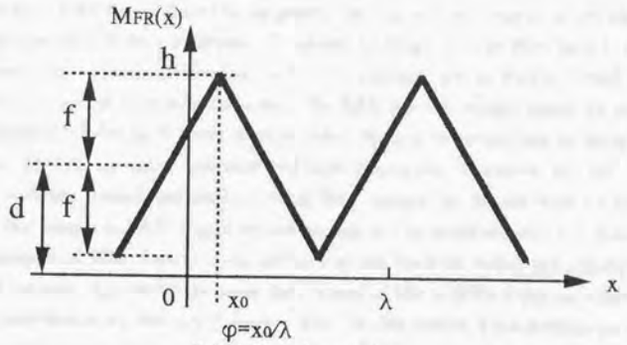

(b) Fourier grid

Figure 4.30

Chapter 5

Image Synthesis

5.1 Image Synthesis Software

5.1.1 Overview

Count rate data of HXT downlinked to the ground are regarded as a time series of sets of 64 two-dimensional spatial Fourier components. To obtain an image of solar flare hard X-ray sources it is necessary to perform, in principle, a two-dimensional inverse Fourier transform (image reconstruction) to a set of downlinked data. The HXT has four energy bands for studying the spectral variation of the hard X-ray sources. Also we need to reconstruct as many images as possible so that we can study temporal evolution of sources. Moreover, in order to extract maximum scientific output, precise location of HXT images on the sun must be known so as to overlay the images to SXT images as well as optical and radio images. For these purposes I have developed an HXT data analysis software system both on mainframe computers as well as on workstations. The former accesses data stored in the SIRIUS database while the latter is for the reformatted database (*c.f.* section 3.4). In this section I concentrate on mainframe programs developed for a general use in synthesizing HXT images. Here the Maximum Entropy Method is adopted as a standard image synthesis procedure. Programs on workstations are essentially the same as those on mainframe computers. Figure 5.1 shows a schematic diagram of the software system. No detailed description will be given regarding the data arrangement part of the system, because it is so simple that this figure explains almost everything.

5.1.2 Determination of Flare Location on the Sun

As is mentioned in section 4.3.1, the modulation collimators of HXT have a fundamental repetition pitch of 126″, which is a fundamental size of the synthesis aperture. Before starting image synthesis, we first need to define the synthesis aperture, which can be achieved by roughly estimating the flare location (position of the highest hard X-ray intensity in the source) in the HXT coordinate. Then we set an image synthesis field of view (usually equals to the synthesis

aperture) centered on the estimated location. The image synthesis is performed assuming that no hard X-ray photon comes from outside this image synthesis field of view.

The procedure for determining flare location (x_0, y_0) consists of the following steps. The coordinate is given in section 4.10.2 and x_0 and y_0 in units of HXT pitch ($= 126''$).

1. Extract HXT pulse count rates in every 0.5 s (in the high bitrate case; 4 s for the medium bitrate) in a certain energy band from the SIRIUS database, decompress the data (section 4.9.2), and accumulate them for a specified time interval. After this step, a set of 64 photon counts from the 64 detectors is prepared.

2. From the photon count data set, make a dirty map which covers the whole sun. Details for making the dirty map is given below.

3. List up positions of peaks in the dirty map. The flare location (x_0, y_0) may not necessarily correspond to the highest peak; this is especially so when hard X-ray sources scatter in a relatively diffuse area. About 50 % of flares thus far analyzed have their location where the program suggested as the 1st candidate. More than 80 % of the flares are listed within, say, the first $5 \sim 10$ candidates. Even if the situation is worse, we can practically obtain the location by use of the corresponding Hα flare location reported in *the Solar Geophysical Data* as well as the location suggested by SXT.

   The location (x_0, y_0) need not be so accurate; about $10'' \sim 20''$ accuracy is usually enough for synthesizing images. Even if (x_0, y_0) is not accurate enough, this only results in synthesized sources located in the image synthesis field of view at a position shifted from its center which makes no problem in synthesizing images.

In the following, I briefly describe how to construct dirty maps used for the determination of flare locations. Suppose we have a limited number of two-dimensional Fourier components (*i.e.* limited number of UV coverage) of a brightness distribution. If we simply reconstruct a two-dimensional map by the inverse-Fourier transform (from the data with DC level subtracted), we obtain a *dirty map* with spurious structure such as side-lobes and repetitive patterns, due to the limited UV coverage and the fundamental period of the Fourier transform, respectively. The map contains negative data points as we subtract DC level from each of the observed Fourier component.

Even in this dirty map, we may see enhancement of brightness at the location where the real source is situated. The enhancement is, in fact the largest one in the dirty map as far as the source is more or less point-like (in the sence that the source is not much extended in comparison with the fundamental period) and as far as we have enough counting statistics for making the map. As solar flare hard X-ray sources are, in most cases, expected to be point-like in the above sense, we utilize this dirty map from which we make the first guess of the flare location on the sun. The modulation patterns of HXT are not trigonometric. Nevertheless, as

our main interest here is to obtain *rough* positions of flares, we construct dirty maps using the first Fourier-amplitude term in the Fourier expansion of each modulation pattern as is given below.

Before describing the dirty map procedure itself, it is useful to show Fourier expansion of fanbeam and Fourier modulation patterns for later explanation. Fourier expansion of fanbeam and Fourier patterns ($M_{\rm FB}(x)$ and $M_{\rm FR}(x)$, respectively; note that x is given by angles rather than physical positions) shown in figure 4.30 is given as follows :

(a) Fanbeam patterns :

$$M_{\rm FB}(x) = \frac{h}{4} + \frac{4h}{\pi^2}\sum_{n=1}^{\infty}\frac{1}{n^2}\left(1-\cos\frac{\pi n}{2}\right)\cos\frac{2\pi n(x-x_0)}{\lambda}$$
$$\simeq \frac{h}{4} + \frac{4h}{\pi^2}\left\{\cos\frac{2\pi(x-x_0)}{\lambda} + \frac{1}{2}\cos\frac{4\pi(x-x_0)}{\lambda}\right\} . \qquad (5.1)$$

(b) Fourier patterns :

$$M_{\rm FR}(x) = \frac{h}{2} + \frac{4h}{\pi^2}\sum_{n\ :\ {\rm odd}}^{\infty}\frac{1}{n^2}\cos\frac{2\pi n(x-x_0)}{\lambda} \simeq \frac{h}{2} + \frac{4h}{\pi^2}\cos\frac{2\pi(x-x_0)}{\lambda} . \qquad (5.2)$$

Dirty map

Let $b^0_K (K = 1 \sim 64)$ be background-subtracted photon counts obtained by the 64 modulation collimators. Here the suffix K correspond to the serial number for the collimators used in table 4.4. The fanbeam grids correspond to $K = 1 \sim 16$ while $K = 16 \sim 64$ are the Fourier grids. I define incident *DC count* $\Sigma_{\rm DC}$ as follows :

$$\Sigma_{\rm DC} = \sum_{K=1}^{16}\frac{\tilde{d}_{\rm FB}}{d_K}b^0_K , \qquad (5.3)$$

where d_K represents 'DC level' of the K-th fanbeam pattern and is given in table 4.4 and $\tilde{d}_{\rm FB}$ is the designed value of DC level for fanbeam modulation patterns : $\tilde{d}_{\rm FB} = 0.125$ (see also section 4.11.1). The quantity $\Sigma_{\rm DC}$ is the expected incident count for each collimator from a flat (or gray) brightness distribution. Using $\Sigma_{\rm DC}$, we evaluate DC level-subtracted incident counts for each collimator $\hat{b}_K$ from b_K as follows :

$$\begin{aligned} \hat{b}_K &= \frac{1}{\tilde{\alpha}_{\rm FB}}\frac{\tilde{d}_{\rm FB}}{d_K}b_K - \Sigma_{\rm DC} && \text{(for fanbeam grids; } K = 1 \sim 16) , \\ \hat{b}_K &= \frac{1}{\tilde{\alpha}_{\rm FR}}\left\{\frac{\tilde{f}_{\rm FR}}{f_K}(b_K - d_K\Sigma_{\rm DC})\right\} && \text{(for Fourier grids; } K = 17 \sim 64) , \end{aligned} \qquad (5.4)$$

where $\tilde{d}_{\rm FR}$ and $\tilde{f}_{\rm FR}$ are the designed values of DC level and amplitude for Fourier grids, respectively ($\tilde{d}_{\rm FR} = \tilde{f}_{\rm FR} = 0.25$), $\tilde{\alpha}_{\rm FB}$ and $\tilde{\alpha}_{\rm FR}$ are designed values of aperture ratio for fanbeam and Fourier grids, *i.e.* $\tilde{\alpha}_{\rm FB} = 1/16$ and $\tilde{\alpha}_{\rm FR} = 1/4$.

With these $\hat{b}_K$, *Fourier components* F^+_K and F^-_K of the fundamental pitch (*i.e.* $k = 1$) for each of the position angles, 0°, 45°, 90°, and 135° are obtained from the fanbeam counts by the following equations :

$$F_K^+ = \frac{1}{4}\left\{(\tilde{b}_K + \tilde{b}_{K+1}) + (\tilde{b}_K + \tilde{b}_{K+3})\right\}$$
$$F_K^- = \frac{1}{4}\left\{(\tilde{b}_K + \tilde{b}_{K+1}) - (\tilde{b}_K + \tilde{b}_{K+3})\right\} \qquad (K = 1, 5, 9, 13)\ . \tag{5.5}$$

These equations are derived if we note that the (designed) phase of the $(K+1)$–th ($K = 1, 5, 9, 13$) fanbeam collimator is shifted by $\pi/4$ from the K–th collimator, and that of the $(K+3)$–th, $3\pi/4$, and that incident and observed counts are related with each other in such a way as eqs.(4.2), with the modulation pattern approximated by Fourier expansion given in eq.(5.1). Taking these into account we conclude from eq.(5.5) that F_K^+ and F_K^- are, respectively, good approximation to Fourier amplitudes for $\cos kx$ and for $\sin kx$ with $k = 1$. We do not use Fourier components with $k = 2$ in the procedure described here.

As for Fourier grids, $\tilde{b}_K$ directly gives K–th Fourier component (*c.f.* eq.(5.2)) :

$$F_K = \tilde{b}_K \qquad (K = 17, \ldots, 64)\ . \tag{5.6}$$

Using the Fourier components obtained from both fanbeam and Fourier grids, each pixel value P_{ij} of the dirty map is obtained as follows :

$$\phi_{ij,K} = x_i \cos k_K \Theta_K + y_i \sin k_K \Theta_K - \varphi_{0,K}\ , \tag{5.7}$$

$$P_{ij} = \sum_{K \in G} F_K \cos 2\pi\phi_{ij,K}\ , \tag{5.8}$$

here G is a set of collimators consisting of four fanbeam elements whose (designed) phase is 0 and all the Fourier elements. In the above equation, $\Theta_K = \theta_K + \pi/2$, where θ_K is the position angle of K–th grid, and (x_i, y_i) is expressed in the HXT coordinate in units of HXT pitch. $\varphi_{0,K}$ is the actual phase of K–th modulation pattern as given in section 4.11.1.

5.1.3 Image Synthesis

The next step is to actually synthesize images. Before describing the image synthesis procedure in detail, let me briefly summarize essence of the procedure. The image synthesis procedure comprises of the following steps :

1. Obtain a set of 64 photon counts from the 64 detectors in the same way as is described in section 5.1.2.

2. Subtract background data from the above photon count data set. The background data itself is prepared in the same procedure as above.

3. After setting the image synthesis field of view centered on (x_0, y_0), an image is reconstructed from the count set by Maximum Entropy Method (MEM). The reconstructed image data, as well as additional information such as start and end time of the photon count data set and the resultant values of the image synthesis procedure (*e.g.* χ^2 value) are stored in an image file.

A series of photon count data sets can also be produced by the above procedure for processing multiple images (in one energy band) at one time. In this case the image file produced by the image synthesis procedure also contains a series of images corresponding to each count set together with additional information. In the following I describe details on the synthesis procedure.

The response matrix

Let $b_K^0 (K = 1 \sim 64)$ be background–subtracted photon counts obtained by the 64 modulation collimators as in section 5.1.2. Suppose B_{ij} is the two–dimensional brightness distribution of hard X–ray sources. Here we consider the brightness distribution in $N \times N$ pixels, *i.e.* $1 \le i, j \le N$. Let $N_0 \times N_0$ pixels have the same size as the synthesis aperture of the HXT, *i.e.* $126'' \times 126''$. Note that $N \times N$ pixels gives the image synthesis field of view, which is not necessarily the same as the synthesis aperture. In the actual image synthesis, I usually set $N = 64$ while $N_0 = 51$. This choice, $N_0 = 51$, gives a pixel size of $126''/51 = 2.47''$, which is almost the same as the pixel size of the SXT CCD ($2.46''$; *c.f.* section 3.2.2). This is very convenient in comparing HXT and SXT images to each other.

The observed X–ray count rate b_K^0 for the K–th modulation collimator, due to the brightness distribution B_{ij}, is given by using two–dimensional *response matrix* $P_{ij,K}$ as follows :

$$b_K^0 = \sum_{i,j=1}^{N} P_{ij,K} B_{ij}^0 + n_K^0\ , \tag{5.9}$$

where n_K^0 represents uncertainties in b_K^0 due to Poisson statistics and systematic errors inevitably included in observations. Let (i_0, j_0) be the pixel numbers at the center of the image synthesis field of view, *i.e.*, $(i_0, j_0) = ((N+1)/2, (N+1)/2)$. Note that (i_0, j_0) need not necessarily be integers; in the case of $N = 64$, $(i_0, j_0) = (32.5, 32.5)$. Setting A to be the geometrical area (including both slit and wire areas) of each collimator ($A \cong 6$ cm^2), the K–th response matrix $P_{ij,K}$ is given by the following expression :

$$P_{ij,K} = A \cdot M_K(k_K r_{ij,K}) \equiv A \cdot M_K(\phi_{ij,K})\ , \tag{5.10}$$

where $\phi_{ij,K} \equiv k_K r_{ij,K}$ is the phase (not necessarily $0 \le \phi_{ij,K} < 1$) in the transmission function M_K (= modulation pattern; *c.f.* section 4.2.2), k is the wavenumber of the modulation pattern, and $r_{ij,K}$ is a signed distance from the center of the field of view (x_0, y_0) (or (i_0, j_0)) to the point $D_{ij,K}$ in figure 5.2. Note that $D_{ij,K}$ is the projection of the (i,j)–th pixel to the line l_K which is normal to the wires (or slits) of the K–th collimator grid. The angle Θ_K in figure 5.2 is given by $\Theta_K = \theta_K + \pi/2$ where θ_K is the position angle of the grid (see table 4.4). The distance, $r_{ij,K}$, is given as :

$$r_{ij,K} = \left(x_0 + \frac{i - i_0}{N_0}\right)\cos\Theta_K + \left(y_0 + \frac{j - j_0}{N_0}\right)\sin\Theta_K\ . \tag{5.11}$$

In the image synthesis procedure, I use approximate forms of $M_K(\phi)$ as follows :

(a) Fanbeam grids :

$$\begin{aligned} M_K(\phi) &= 4p_K \cdot (\phi_{\rm frac} - \varphi_{0,K}) + p_K \qquad (-0.25 \le \phi_{\rm frac} - \varphi_{0,K} < 0) , \\ &= -4p_K \cdot (\phi_{\rm frac} - \varphi_{0,K}) + p_K \qquad (0 \le \phi_{\rm frac} - \varphi_{0,K} < 0.25) , \\ &= 0 \qquad\qquad\qquad\qquad\qquad\quad (\text{for other } \phi_{\rm frac}) . \end{aligned} \tag{5.12}$$

Here $p_K = d_K + f_K$ and $\phi_{\rm frac} \equiv \phi - [\phi]$, where $[\phi]$ is the largest integer that is no greater than ϕ.

(b) Fourier grids :

$$M_K(\phi) = f_K \cos 2\pi(\phi - \varphi_{0,K}) + d_K . \tag{5.13}$$

If $M_K(\phi) < 0$ at some ϕ, then $M_K(\phi)$ is replaced by zero; *i.e.*, $M_K(\phi) \ge 0$ for all ϕ. Note that the fanbeam modulation patterns are approximated by triangular patterns while the Fourier modulation patterns by sinusoidal patterns. In eqs.(5.12) and (5.13), $\varphi_{0,K}$ is the phase of modulation collimator with mutual rotation between the top and bottom grid plates taken into account (section 4.11.1). Expression for $\varphi_{0,K}$ is given in eq.(4.12).

The maximum entropy image reconstruction

The Maximum Entropy Method which we are using in the image synthesis is based on the one developed by Gull and Daniel (1978) and Willingale (1981). The MEM is a procedure in which a quantity called *entropy* (S) is defined (see eq.(5.15)) and an image which maximizes the entropy is regarded to be the best solution among those which do not contradict with the observation. Here the observational error is taken into account as described below. The method has advantages in that (1) it tends to choose the smoothest solution among the solutions consistent with the observations, (2) inherently reconstruct positive images, and (3) easily handles the observational errors if they obey the Poisson statistics. The MEM is especially powerful for guessing the original distribution from a limited number of observations. In our case we reconstruct hard X-ray images in $N \times N = 64 \times 64$ pixels from a set of only 64 data; a simple inverse-Fourier method would give too dirty images with many spurious sources due to enhanced side-lobes of the point spread function.

Now let us return to eq.(5.9). The maximum entropy solution which corresponds to eq.(5.9) can be written as

$$b_K = \sum_{i,j=1}^{N} P_{ij,K} B_{ij} , \tag{5.14}$$

where B_{ij} gives MEM image of hard X-ray sources. We adopt the entropy expression given originally by Frieden (1972) :

$$S = -\sum_{i,j=1}^{N} \left(\frac{B_{ij}}{\overline{B^0}}\right) \cdot \ln\left(\frac{B_{ij}}{\overline{B^0}}\right) , \tag{5.15}$$

and $\overline{B^0}$ is the average incident hard X-ray photon counts per pixel :

$$\overline{B^0} = \frac{1}{N^2} B^0_{\rm tot} . \tag{5.16}$$

Larger entropy S implies less structures in the image (or, I can say, smoother images), *i.e.*, maximizing entropy under no observational constraints simply gives flat brightness distribution : $B_{ij} = \text{const.}$ In eq.(5.15), $B_{ij}/\overline{B^0}$ is the normalized pixel counts and hence the above entropy expression is independent of the absolute value of B_{ij} itself. The total number of incident photons, $B^0_{\rm tot}$ in eq.(5.16), is approximately evaluated from fanbeam counts $b^0_K (K = 1 \sim 16)$:

$$B^0_{\rm tot} = \frac{1}{\alpha}\left(\sum_{\theta=0^\circ} b^0_K + \sum_{\theta=45^\circ} b^0_K + \sum_{\theta=90^\circ} b^0_K + \sum_{\theta=135^\circ} b^0_K\right) = \frac{1}{\alpha}\sum_{K=1}^{16} b^0_K , \tag{5.17}$$

where α is a factor which represents the average aperture summed up for each of the four fanbeam grid sets with the same position angle θ :

$$\alpha = \frac{1}{4}\left(\sum_{\theta=0^\circ} p_K + \sum_{\theta=45^\circ} p_K + \sum_{\theta=90^\circ} p_K + \sum_{\theta=135^\circ} p_K\right) = \frac{1}{4}\sum_{K=1}^{16} p_K \sim 0.88 . \tag{5.18}$$

The principle of the image synthesis is to obtain a two-dimensional brightness distribution B_{ij} which maximizes the entropy S among those which gives b_K consistent with the observations b^0_K, *i.e.*,

$$\chi^2_{\nu=64} \equiv \frac{1}{64}\sum_{K=1}^{64} \frac{(b_K - b^0_K)^2}{{\sigma^0_K}^2} \sim 1.0 , \tag{5.19}$$

where σ^0_K is a standard deviation of the photon count error which includes both Poisson and systematic errors. Then, this principle becomes equivalent with maximizing the following quantity $\tilde{S}$,

$$\tilde{S} = S - \frac{\lambda}{2}\chi^2 . \tag{5.20}$$

Here λ (or $\lambda/2$) is a parameter which compromises relative weight between observations (expressed as χ^2) and entropy S. To increase λ means to put more weight on the observations than the entropy term or smoothness of images, hence χ^2 value decreases while synthesized images (B_{ij}) contain increased structure. The final image is obtained when the χ^2 value satisfies eq.(5.19). By taking partial derivatives of eq.(5.20) with respect to B_{ij} to be zero, we obtain

$$B_{ij} = \overline{B^0} \exp\left[-S_{\rm unit} + \lambda\overline{B^0}\sum_{K=1}^{64}\left\{\frac{1}{{\sigma^0_K}^2}\left(b_K - \sum_{m,n=1}^{N} P_{mn,K} B_{mn}\right) P_{ij,K}\right\}\right] . \tag{5.21}$$

Here $S_{\rm unit}$ is the unit entropy per pixel, *i.e.* $S_{\rm unit} = S/N^2$. Starting from a uniform initial brightness distribution $B^{(0)}_{ij}$, or so-called gray map, we obtain the maximum entropy image B_{ij} at a given λ by successively taking weighted average of iteration in eq.(5.21) as follows :

$$B_{ij}^{(l+1)}$$

$$= (1-\gamma)B_{ij}^{(l)} + \gamma\overline{B^0}\exp\left[-S_{\rm unit}^{(l)} + \lambda\overline{B^0}\sum_{K=1}^{64}\left\{\frac{1}{{\sigma_K^0}^2}\left(b_K - \sum_{m,n=1}^{N} P_{mn,K}B_{mn}^{(l)}\right)P_{ij,K}\right\}\right] .$$

$$(l = 0, 1, 2, 3, \ldots) \qquad (5.22)$$

Here $B_{ij}^{(l)}$ is the image after l–th iteration, and γ is a weighting factor called *iteration gain*. Note that a larger γ makes the iteration more stable but the convergence slower. Usually $\gamma \sim 0.02-0.1$ gives satisfactory convergence of images within reasonable number of iteration. A condition for the convergence of $B_{ij}^{(l)}$ is given as

$$\frac{\left\|B_{ij}^{(l+1)} - B_{ij}^{(l)}\right\|}{\left\|B_{ij}^{(l)}\right\|} \equiv \delta \ll 1 , \qquad (5.23)$$

where δ lies typically in the range $\delta \sim 0.01 - 0.03$ in the image synthesis program, and $\left\|B_{ij}^{(l)}\right\|$ is defined as

$$\left\|B_{ij}^{(l)}\right\| = \sqrt{\sum_{i,j=1}^{N}\left(B_{ij}^{(l)}\right)} . \qquad (5.24)$$

In many cases, the iteration eq.(5.22) gives satisfactory convergence. However, the exponential term in eq.(5.22) may sometimes cause convergence of the iteration difficult, since small changes in the index of the exponential would result in large changes in $B_{ij}^{(l+1)}$. To make the convergence more stable, if the total flux in the resultant $B_{ij}^{(l)}$ differs significantly from the observations, *i.e.*

$$\left|\sum_{i,j=1}^{N} B_{ij} - B_{\rm tot}^0\right| > \sqrt{B_{\rm tot}^0} , \qquad (5.25)$$

then $B_{ij}^{(l)}$ is practically re–normalized to have the observed total flux $B_{\rm tot}^0$:

$$B_{ij}^{(l)} \Longrightarrow \left(\frac{B_{\rm tot}^0}{\sum B_{ij}^{(l)}}\right) B_{ij}^{(l)} . \qquad (5.26)$$

As λ in eq.(5.22) cannot be determined from the observations, we assume certain values of λ in the iteration. In the actual iteration we start with $\lambda \sim 0.2$ and when the iteration converges, increment λ by a certain amount (typically ~ 0.1) and restarts the iteration (eq.(5.22)) with the new λ. Converged B_{ij} obtained by the last sequence of iterations (with the old λ) is used as the initial brightness distribution $B_{ij}^{(0)}$ in the new iteration sequence.

Figure Captions

Figure 5.1: Schematic diagram of HXT software system.

Figure 5.2: Signed distance between the projection of (x, y) onto line l_K, which is denoted as $D_{ij,K}$, and the center of the image synthesis field of view (x_0, x_0). See text for details. Note that the definition of position angle θ is different from the one in figure 4.5.

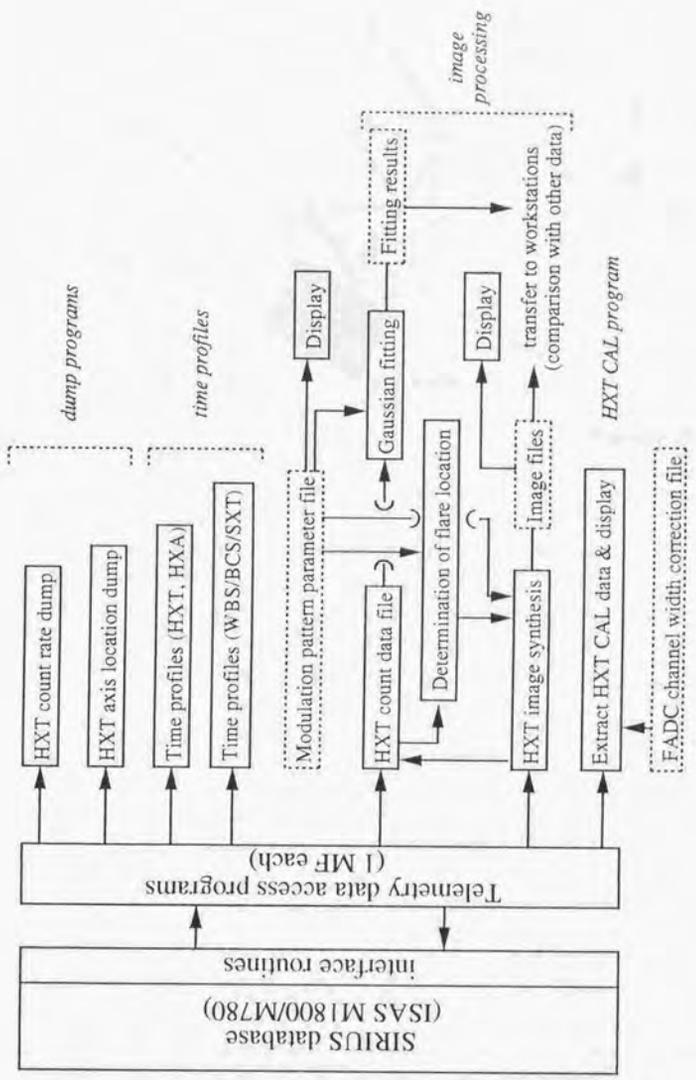
SIRIUS database
(ISAS M1800/M780)
interface routines
Telemetry data access programs
(1 MF each)
HXT count rate dump
HXT axis location dump
Time profiles (HXT, HXA)
Time profiles (WBS/BCS/SXT)
Modulation pattern parameter file
HXT count data file
Determination of flare location
HXT image synthesis
Extract HXT CAL data & display
FADC channel width correction file
Gaussian fitting
Display
Display
Fitting results
Image files
transfer to workstations
(comparison with other data)
dump programs
time profiles
HXT CAL program
image processing

Figure 5.1

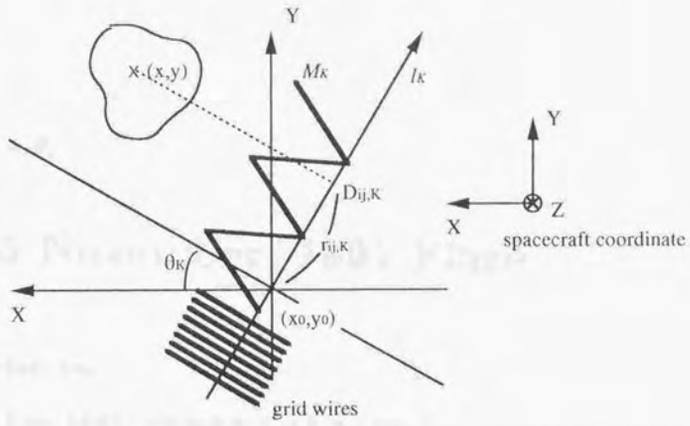
Y
x.(x,y)
Mκ
Iκ
Dij,κ
rij,κ
θκ
X
(xo,yo)
grid wires
Y
Z
X
spacecraft coordinate

Figure 5.2

Chapter 6

The 15 November, 1991 Flare

6.1 Introduction

In this chapter, I describe HXT observations of an intense solar flare which occurred at 22:34 UT on 15 November, 1991. This flare was well observed with HXT as well as other instruments aboard *Yohkoh*. Observations of the solar flare hard X–ray sources with unprecedented temporal and spatial resolution (0.5 s and 5″, respectively), together with ground–based observations, enable us to discuss (a) how (hard X–ray) flare initiates with respect to the global magnetic field structure, (b) spatial relation between flaring loops, in which energy release in the early phase of the flare took place, and the loops in which impulsive energy release is going on, (c) location of flaring loops corresponding to individual spikes seen in hard X–ray time profiles; is a single loop flaring repeatedly, or different loops are flaring for the individual spikes ? (d) Particle acceleration after the impulsive phase and relation between flaring loops in the impulsive and the post–impulsive phases, *i.e.* evolution of flaring loops with time, and (e) production of high temperature plasmas and location of loops filled with such plasmas with respect to the loops in which significant particle acceleration took place (*i.e.* loops mentioned in the above (b) – (d)).

In section 6.2 I describe overall features of hard X–ray sources, to give general view on how this (hard X–ray) flare developed with time. In section 6.3 detailed analyses on the hard X–ray sources, especially on their double–source structure above $\gtrsim$ 30 keV, will be presented. In section 6.4, I discuss the nature of hard X–ray sources, especially of the double sources. In section 6.5, a brief summary of HXT observations of this event will be given.

6.2 General Description of the Event

The hard X–ray ($\gtrsim$ 20 keV) flare commenced at 22:34 UT on 15 November, 1991 in an active region NOAA 6919 (S14W19). The *GOES* X–ray class of this flare is X1.5 and the Hα importance is 2B. *Yohkoh* observed this flare from the beginning until the end of hard X–ray emission above 20 keV (at 22:44 UT). Figure 6.1 shows time profiles of this flare in the four

energy bands of HXT. The flare–mode was triggerd at 22:34:38 UT. Besides hard X–ray images, HXT provides spatially averaged incident spectra of flares as well as spatially resolved ones using the four energy bands. Assuming a spatially–averaged, power–law incident spectrum of $I(\varepsilon) = A_{20}(\varepsilon/20\ \mathrm{keV})^{-\gamma}$ photons/s/cm^2/keV, I estimated photon index γ and flux A_{20} at 20 keV from M2/M1 and H/M2 bands count data pairs (see Inda–Koide 1993 for details of this procedure). Figure 6.2 shows time profiles of parameters γ and A_{20}. When the spacecraft entered night (at around 22:46:30 UT), there was still some excess hard X–ray counts above the background level by ~ 40 cts/s/SC in the L band and ~ 2 cts/s/SC in the M1 band. However X–ray counts in the energy bands above 33 keV (*i.e.* in the M2 and H bands) returned to their background level by 22:43 UT. A preliminary report on the HXT observations of this flare is given by Sakao *et al.* 1992.

The SXT (section 3.2.2) obtained sequence of excellent soft X–ray images of the flare with various filters. The flare was so intense that SXT also observed white–light brightenings with its optical telescope (Hudson *et al.* 1992). BCS (section 3.2.3) obtained Ca XIX resonance line spectra from the beginning of the flare to 22:37 UT and plasma velocities are derived from the spectra (Culhane *et al.* 1993). After 22:37 UT, the BCS saturated due to increased X–ray counts. The WBS instruments (section 3.2.4) obtained energy spectra of the flare (Yoshimori *et al.* 1992, Kawabata *et al.* 1993). Nuclear γ–ray lines as well as continuum γ–ray emission were observed with GRS. The *Yohkoh* data were downlinked at a DSN station in Madrid.

This flare was also observed with the Solar X–Ray/Cosmic Gamma–Ray Burst Experiment (Hurley *et al.* 1992) aboard the *Ulysses* spacecraft in an energy range of 15–150 keV, together with hard X–ray and γ–ray spectrometers aboard Pioneer Venus Orbiter (PVO) and Compton Observatory/GRO (Kane *et al.* 1993*a*, 1993*b*), which enabled multi–spacecraft stereoscopic observations of the flare.

Together with observations from spacecrafts, the flare was well–observed in Hα and in Ca II K–line at the Mees Solar Observatory (MSO) in Hawaii (Canfield *et al.* 1992, 1993, Wülser *et al.* 1993, 1994). Snapshots of photospheric magnetic field during the flare were obtained by the Stokes V–polarimeter (Mickey 1975) at the MSO. The MSO observations cover a time interval between 22:00 and 22:43 UT, *i.e.*, well covering pre–flare time interval as well as flare interval itself.

There were also radiometer observations at the Nobeyama and Toyokawa Solar Radio Observatories in Japan. The radio observations were made at seven frequencies; namely, 1, 2, 3.75, and 9.4 GHz at Toyokawa, and 17, 35, and 80 GHz at Nobeyama, respectively (figure 6.3; courtesy Enome, S.).

As is seen in figure 6.4, hard X–ray sources in this flare showed a clear pattern of evolution. In order to summarize the HXT observations according to the time profile shown in figure 6.1, I divided the flare into three phases : (a) *precursor phase* (22:34–22:37 UT), (b) *impulsive phase* (22:37–22:38 UT), (c) *post–impulsive phase* (22:38–22:41 UT), and (d) *decay phase* (after 22:41 UT). In the following, I describe general description of the development of flare hard X–ray sources according to the above phases.

6.2.1 Precursor Phase

The most prominent feature seen in the precursor phase is that the hard X–ray sources scatter across an area with a spatial extension greater than 1′ (figure 6.4 (a),(b)). For comparison, in figure 6.4 (c) I showed hard X–ray sources in the M1 band observed during the impulsive phase. The impulsive phase sources are located in a rather compact region (within $\sim 30'' \times 30''$), in contrast to the precursor phase images. I can say that in the precursor phase, hard X–ray sources extend over a wider area; *e.g.* some $\gtrsim 20,000$ km away from the main energy release site in the impulsive phase. Just before the onset of the impulsive phase, as is seen in figures 6.4 (a) and (b), the source in the left–hand side shows a continual expansion along the magnetic neutral line.

In the off–band Ca II K–line filtergram images taken at MSO, the flaring site began to brighten at 22:28:08 UT, which is ~ 8 minutes before the onset of the flare in hard and soft X–rays. There was an Hα filament eruption starting at about 22:20 UT (Canfield *et al.* 1993), ~ 14 minutes before the hard and soft X–ray flare onset.

Also at MSO, red–shifted bright and compact patches (flare kernels) were observed at the Hα + 3.0 Å wavelength (Wülser *et al.* 1993, 1994). Figure 6.5 (a) shows an overlay of an HXT image (M1 band; grayscale) to an Hα red–wing image (3 Å shifted from the line center; contours). Figure 6.5 (b) is an overlay of an SXT image to the same Hα image as (a). Magnetic neutral lines are shown in the figures in dashed lines. We notice that hard X–ray sources are visible at the south–east (SE) and the north–west (NW) kernels. However in the north–east (NE) kernel we do not see hard X–ray emission although the NE and SE kernels are bright in soft X–rays.

During the precursor phase, BCS observed a blue shifted component in the Ca XIX resonance line spectra as is shown in figure 6.6 (a) by the solid histogram (Culhane *et al.* 1993). The Ca XIX spectra indicate plasma upflow velocities of about 250 km/s. Figure 6.6 (b) shows time profile of the upflow velocities overlaid with hard X–ray count rates observed with HXS (section 3.2.4) in the 20–60 keV range. The blue–shifted component (respresenting plasma upflow) was observed at least 60 s before the hard X–ray enhancement observed with HXS, and the inferred plasma upflow velocity did not change significantly during 22:33:40 UT and 22:36:00 UT.

6.2.2 Impulsive Phase

The impulsive bursts comprise three separate and distinct spikes (figure 6.1); I call these spikes P1, P2, and P3, and the valleys between them V1 and V2. Figure 6.7 shows temporal evolution of the hard X–ray sources in the M1 and M2 bands. In the lowest energy band (the L band; 14–

23 keV) only single sources are seen throughout the impulsive phase. The single sources, which seem to connect the double sources seen in the higher energy bands (see below), did not show large structural changes during the impulsive phase. In the energy bands above 23 keV we also see a single source at P1 and V1, while at and after the time of P2, double sources, separated from each other by $13'' - 16''$, are seen in the energy bands above M2 (*i.e.*, above 33 keV). These double sources are located on both sides of the magnetic neutral line. The separation between the double sources becomes larger with time ($\sim 13''$ at P2 while $\sim 16''$ at 22:38:00 UT). In the M1 band the double sources are seen at the peaks of the spikes P2 and P3. On the other hand in the valleys V1, V2, and after the 3 rd spike (at 22:38:00 in figure 6.7) the hard X-ray images differ greatly between the 23-33 keV band (M1) and the energy bands above 33 keV. In the M1 band a single-source structure dominates, and it splits into double sources as the X-ray intensity increased toward P2 and P3 peaks. The single source is located at the magnetic neutral line. Accompanying with this structural evolution, the energy spectrum showed the well-known soft-hard-soft evolution (*e.g.* Kane and Anderson 1970, Dennis and Schwartz 1989) during the individual spikes (see figure 6.2 (a)). Thus it can be said that the harder-spectrum component originates mainly from the double-source structure, and the softer-spectrum component from the single source located between the double sources. In the H band, the hard X-ray sources showed the same structure at the same location as in the M2 band, *i.e.* the single source at P1 and V1, the double sources at and after the time of P2.

6.2.3 Post-Impulsive Phase

In the post-impulsive phase which starts at about 22:38:00 UT, we see that there are still a plenty of microwave emissions in the frequency range above 17 GHz (figure 6.3), suggesting that accleration of electrons are continuing and there are still many energetic electrons existent and emitting microwaves.

In figure 6.8 I show post-impulsive phase hard X-ray sources in the M1 (top) and M2 (bottom) bands. In the M2 band (and also in the H band), hard X-ray sources show a double-source structure just as in the impulsive phase but the separation of the two sources are larger than that in the impulsive phase; the separation increases with time. In the impulsive phase, the separation is $\sim 13''$ at the second spike (P2) and it increased to be $\sim 16''$ at the end of the impulsive phase. In the post-impulsvie phase, the separation is $\sim 20''$ at 22:38:50 UT while it further increased to be $\sim 31''$ at around 22:39:22 UT, when 35 GHz (and 17 GHz) microwave time profile showed a valley as is seen in figure 6.3. Together with this increase in separation, the angle sustained by the double sources and the magnetic neutral line became larger with time; the double sources rotated with each other counter-clockwise. Also it is interesting to note that the southern source became brighter than the northern source after 22:39:22 UT.

Using a Gaussian fitting procedure which will be described in section 6.3 and, in detail, in section 7.3.1, I obtained photon index γ for each of the hard X-ray sources in figure 6.8 at around

22:39:31 UT (M1 band : 22:39:31 UT - 22:39:32 UT, M2 band : 22:39:30 UT - 22:39:33 UT). Photon index for each of the double sources seen in the figure is roughly the same as $\gamma_{\rm DS} \sim 3.5$, which is in good agreement with γ derived from the H/M2 count ratio (see figure 6.2). On the other hand, the loop-like structure, which is significant in the M1 band image, originating from the southern source B in figure 6.8 and extending towards the west, has a much softer energy spectrum with $\gamma_{\rm L} > 6$, or with a temperature as high as $T_e \sim 3.5 \times 10^7$ K assuming single-temperature thermal emission. Therefore the observed difference in γ between the M2/M1 and H/M2 band data in figure 6.2 can be explained by the presence of this soft loop-like component in the M1 band, which could be emissions from a thermal plasma whose temperature reaching to or exceeding 30 MK.

During the impulsive and the post-impulsive phases, a white-light flare was observed with the aspect sensor of SXT (Hudson *et al.* 1992). Relation between the hard X-ray double sources and the white-light flare, as well as the spatial evolution of the double sources will be discussed in section 6.3.

6.2.4 Decay Phase

After 22:40:30 UT, hard X-ray time profiles show smooth and gradual decay. The smooth decay of hard X-ray emission may be attributed to the fact that no additional particle acceleration is taking place; the hard X-rays may be emitted by high temperature plasmas produced by the flare. Assuming that the observed HXT counts originate from a single temperature thermal emission of a plasma, electron temperature ($T_e^{\rm HXR}$) and emission measure ($EM^{\rm HXR}$) of the plasma at 22:44:00 UT are estimated to be $T_e^{\rm HXR} = 2.3 \times 10^7$ K and $EM^{\rm HXR} = 4.7 \times 10^{48}$ /cm^3, from the L and M1 bands count data pair.

On the other hand, we can also estimate electron temperature (T_e) and emission measure (EM) of the plasma in the decay phase from radio data taken at the Nobeyama and Toyokawa radio observatories. Figure 6.9 shows the radio spectrum of this flare at 22:44:00 UT. As is seen in the figure, radio flux density at and above 17 GHz has a nearly constant value of ~ 100 sfu (1 sfu $= 10^{-22}$ W/m^2/Hz). This constant radio flux density suggests that radio emission above 17 GHz is optically thin thermal emission while emission at 9.4 GHz (~ 32 sfu) is optically thick (see *e.g.* Shimabukuro 1972, Švestka 1976). There may be additional component seen at the frequencies of 2 and 3.75 GHz. The radio flux density S (erg/s/cm^2/Hz) is given as follows :

$$\begin{aligned} S(\nu, T_b) &= \frac{2k_B\nu^2}{c^2} T_{\rm b}\Omega \\ &= \frac{2k_B\nu^2}{c^2} T_{\rm eff}\Omega(1 - e^{-\kappa_\nu z}) , \end{aligned} \tag{6.1}$$

where Ω is the solid angle subtended by the thermal source, κ_ν is the absorption coefficient, z is the linear thickness of the emitting region, $T_{\rm b}$ and $T_{\rm eff}$ are brightness and effective temperature, respectively (Dulk 1985). In the case of thermal Bremsstrahlung emission, the absorption

coefficient κ_ν is given as :

$$\kappa_\nu \sim \xi n_e^2 T_e^{-\frac{3}{2}} \nu^{-2} \quad (/\mathrm{cm}) \qquad (\xi \sim 0.2)\ . \tag{6.2}$$

Hence in optically thin ($e^{-\kappa_\nu z} \sim 1 - \kappa_\nu z$) and thick ($e^{-\kappa_\nu z} \sim 0$) frequency regions, the flux density is given as :

$$\begin{aligned} S_{thin} &= \frac{2\xi k_B}{c^2} T_e^{-\frac{1}{2}} \Omega n_e^2 z &&= 0.86 \left(\frac{T_e}{10^7\ \mathrm{K}}\right)^{-\frac{1}{2}} \left(\frac{EM}{10^{48}\ \mathrm{cm}^{-3}}\right) \quad (\mathrm{sfu})\ , \\ S_{thick} &= \frac{2k_B\nu^2}{c^2} T_e \Omega &&= 0.14 \left(\frac{T_e}{10^7\ \mathrm{K}}\right) \left(\frac{\nu}{1\ \mathrm{GHz}}\right)^2 \left(\frac{l}{10^9\ \mathrm{cm}}\right)^2 \quad (\mathrm{sfu})\ , \end{aligned} \tag{6.3}$$

where l is the size of the thermal source. The hot thermal source observed with HXT would produce, *e.g.* optically thin radio flux of $S_{thin} = 3$ sfu, which is two orders of magnitude lower than the observed flux of $\sim$ 100 sfu. On the other hand, if I assume the size l of the source (projected on the surface of the sun) to be $\sim 30''$ from SXT images of this flare, then the temperature and emission measure of the plasma are estimated to be $T_e = 5.1 \times 10^6$ K and $EM = 8.3 \times 10^{49}$ /cm^3. Such a plasma would produce no hard X-ray count detectable even in the L band. Hence it can be said that the thermal plasma which HXT observed is different from what is seen in the microwave frequencies, or at least there is a plasma with differencial emission measure whose high-temperature, low-emission measure tail is observed with HXT while its low-temperature, high-emission measure portion with microwaves.

6.3 Behavior of the Double Sources

As is shown in the previous section, one of the prominent features of the hard X-ray sources in this flare is that the double sources, which are seen during the impulsive and post-impulsive phases (especially in the energy bands above 33 keV), change their location systematically with respect to the magnetic neutral line as the flare develops. In this section, I mainly focus on behavior of the double sources, such as (1) temporal variation of hard X-ray flux from each of the double sources, (2) location of the double sources with respect to the photospheric magnetic field, and (3) energy spectral hardness of the double sources.

6.3.1 Hard X-ray Emission from the Double Sources

In order to examine in detail the points (1) and (3), I developed a Gaussian model fitting procedure. Details on this procedure are given in section 7.3.1. As the MEM, which we usually use for the HXT image synthesis, is a non-linear procedure, quantities evaluated from MEM images (such as hard X-ray flux from each of the double sources) need be dealed with careful consideration. On the contrary, the Gaussian fitting procedure is suited for deriving quantitative values necessary for the current study.

Using the Gaussian fitting procedure, time variations of hard X-ray flux (S_i in eq.(7.1)) from each of the double sources are analyzed for the 2nd and 3rd spikes in the M2 and H bands. Figure

6.10 shows a result of the fitting for the 3rd spike in the M2 band (22:37:45 UT - 22:37:55.5 UT). In figure 6.10 (a), thick solid and dashed lines show time profiles of hard X-ray flux from the northern (hereafter source A) and southern sources (hereafter source B), respectively. Temporal resolution of the plot is 0.5 s. Thin solid line in the figure denotes spatially-integrated incident hard X-ray flux while dotted line is the sum of fluxes from sources A and B. Error bars indicate 1σ level. Cross-correlation between these time profiles shows that the two sources emit hard X-rays simultaneously within 0.1 s at 1σ level (figure 6.10 (b)). The Gaussian fitting to the H band data gives essentially the same result as in the M2 band.

Spectral hardness of each of the double sources is obtained by comparing S_i for the same data set in the M2 and H bands as is shown in eq.(7.3). Figure 6.11 shows time profiles of the hardness for the sources A (solid line) and B (dashed line) during the 3rd spike (22:37:46.5 UT to 22:37:55.5 UT) for every 0.5 s integration. Typical error (at 1σ level) is about 10 % of each hardness value. In this figure, we see that the brighter source A shows a systematically harder energy spectrum than the darker source B. If we assume a power-law photon incident spectrum, photon spectral indices γ_A and γ_B would be $\gamma_A \sim 2$ and $\gamma_B \sim 2.5$, respectively.

Since this flare was also well observed at MSO, we can compare location of the double sources with a photospheric magnetic field map (magnetogram) taken at MSO between 21:05:59 UT and 22:35:59 UT. Figure 6.12 shows an overlay of the double sources in the M2 band at the time of P3 (22:37:49 UT) with the magnetogram. Procedure for making overlay is also described in section 7.3.1. The brighter source A is located in a positive polarity region (thin solid contours) whose longitudinal magnetic field strength $B_A \sim +100$ G while the darker source B is in a negative polarity region (dashed contours) with $B_B \sim -400$ G. As the magnetogram was taken closely in time with the flare, rotation of the sun due to the time difference between hard X-ray and magnetic field images need not be taken into account. Accuracy of the overlay is, then, mainly determined by the overlay between HXT and SXT images and the overall accuracy is less than $5''$.

6.3.2 Relation Between Impulsive and Post-Impulsive Phase Double Sources

One interesting behavior of the double sources during the impulsive and post-impulsive phases is that they changed their location in a systematic manner. The angle sustained by the double sources and the magnetic neutral line becomes larger with time, i.e., the double sources rotated with respect to each other. Also the separation between the double sources increased. This is clearly seen in figure 6.13. In figure 6.13 (b), I show an overlay of the double sources in the post-impulsive phase (solid line; 22:39:50 UT) and the impulsive phase (dashed line; 22:37:37 UT) together with the magnetic neutral line.

6.3.3 Relation with White–Light Flare

During the impulsive and the post–impulsive phase, a white–light flare was observed with the aspect telescope of SXT. To enhance contrasts of images, the initial frame taken at 22:34:58 UT was subtracted from a sequence of observed optical images (courtesy Strong, K.T. and Hudson, H.S). In figure 6.14 a white light flare image obtained with the above method is overlaid with the hard X–ray sources in the M2 band at the time of P3 (22:37:49 UT). They show close correspondence with each other. In figure 6.13 (a) hard X–ray sources in the post–impulsive phase (22:38:49 UT) is overlaid with the white–light image. Here again we see close spatial correspondence of hard X–ray sources with the white–light flare.

6.4 Interpretation and Discussion

6.4.1 Precursor Phase Phenomena

Flare trigger

The hard X–ray sources seen in the precursor phase (figures 6.4, 6.5) are located at remote sites ($\sim$ 20,000 km) from the main energy release site of the impulsive phase. The hard X–ray sources elongated along the magnetic neutral line just before the onset of the impulsive phase. These observations suggest that some instability which caused activation or deformation of surrounding loops eventually led to the impulsive energy release (see figure 6.15 (a)).

Furthermore, Hα filament eruption was observed to start about 14 minutes prior to the hard X–ray detection with HXT, and even $\sim$ 8 minutes before the brightening in an off–band Ca II K–line filtergram images. They are consistent with results obtained by Kahler *et al.* (1988) that filament activation may start prior to the flare onset. Also, Harrison (1986) reported that some coronal mass ejections would precede the onset of flares (see also a review by Kahler 1992). These observations suggest that global re–structuring of coronal magnetic field tends to precede the onset of, at least, some flares.

Plasma upflow

In figure 6.5 (a) we see that in the precursor phase at around 22:35:00 UT, hard X–ray sources are visible at the south–east (SE) and the north–west (NW) Hα red–shifted kernels while in the north–east (NE) kernel we do not see hard X–ray emission although the NE and SE kernels are bright in soft X–rays (figure 6.5 (b)). During the precursor phase, BCS observed blue–shifted component suggesting plasma upflows. Using HXT, SXT, BCS, and Hα data, Wülser *et al.* (1994) have studied the difference in the origin of Hα red–wing kernels. After showing that the bulk of the soft X–ray emission observed with BCS and SXT comes from the same plasma, they found that the total momentum of upward flowing material derived from the BCS and

SXT observations is in agreement with the total momentum of downflowing material at the red–shifted kernels. This suggests that chromospheric evaporation (Antonucci *et al.* 1982) is taking place. Combining derived downflow plasma velocity v_d at each kernel ($v_d^{\rm SE} \sim 32$ km/s, $v_u^{\rm NW} \sim 19$ km/s, and $v_u^{\rm NE} \sim 42$ km/s, respectively) with a flare loop model developed by Fisher (1989), they concluded that the NW kernel, which is bright in hard X–rays, is formed by electron precipitation while the NE kernel, which is barely visible in hard X–rays, is formed by thermal conduction.

The above result indicates that electron precipitation, as well as thermal conduction, is taking place well before ($\sim$ 3 minutes) the impulsive energy release, in large–scale magnetic loops other than the rather compact loops in which impulsive hard X–ray bursts took place.

6.4.2 Hard X–ray Double Sources

Flux correlation

The double–source structure seen in the impulsive phase most likely corresponds to the footpoints of a flaring loop (Sakao *et al.* 1992, Canfield *et al.* 1992). During the spikes P2 and P3, each of the double sources in the M2 band as well as in the H band emits hard X–rays simultaneously within 0.1 s at 1 σ level. The observed simultaneity can naturally be explained if hard X–rays from the double sources are emitted by high–energy electrons whose velocity $v_e \gtrsim 0.3c$ corresponding to a kinetic energy greater than 30 keV. Thermal source models (Brown *et al.* 1979, Smith and Lilliequist 1979) assume that anomalous conduction fronts which are produced by impulsive heating near the loop top travel downwards to the footpoints along the flaring loop at the ion sound speed $v_i = \sqrt{k_B T_e / m_p}$, giving $v_i \sim 3 \times 10^{-3} c = 1{,}000$ km/s for $T_e \sim 10^8$ K. It is unlikely that the conduction fronts can account for the observed simultaneity as follows. If the conduction fronts with $v_i \sim 1{,}000$ km/s is responsible for the hard X–ray emission as thermal source models suggest, then the region where impulsive heating took place should be located within $\pm$50 km from the midway between the footpoints to make the double sources brighten simultaneously within 0.1 s. If I assume a semi–circular loop of radius $\sim 8''$ (= 6,000 km), then the loop length will be 1.9×10^4 km which implies that the allowed region has a fraction of only $\sim$ 1 % with respect to the loop length. Thermal source models can explain the observation only if the energy release site is located precisely at the midpoint of the flaring loop, which is not likely.

Evolution of the sources

During the impulsive phase, the separation of the double sources, which were clearly seen in the energy bands above 23 keV, became larger at P3 than at P2. The increasing separation of the double sources suggests a multiple loop system flaring successively with rising energy release sites. Eack spike would correspond to the energy release taking place in a different magnetic

loop. It is interesting to note that only a single source was observed at P1. This is probably because the length of the loop was so short that the corresponding two footpoints were not resolved by HXT, or the ambient plasma density was so high that the hard X-rays were emitted near the loop top.

In the post-impulsive phase, we still see significant microwave emission at 17, 35, and 80 GHz (figure 6.3) as well as hard X-ray emission. As it is generally believed that (impulsive) microwave bursts are produced by gyro-synchrotron emission from accelerated electrons (Takakura 1960), it is most likely that acceleration of particles is continued and high energy electrons still exist in the post-impulsive phase. The hard X-ray double sources, which are most likely footpoints of the flaring loop, are still seen in the energy bands above 33 keV. As is shown in figures 6.8 and 6.13, the separation of the double sources increases with time, reaching about 30″ at the end of the post-impulsive phase. Furthermore, it is noteworthy that the angle between the line connecting the double sources and the magnetic neutral line increases with time. Therefore I can say that (1) particle acceleration (and hence energy release) is still going on during the post-impulsive phase, and (2) particle acceleration originally started in a low lying, more sheared magnetic loop just above the neutral line and the acceleration took place successively in overlying, less sheared loops with rising energy release sites as the flare went on, throughout the impulsive and the post-impulsive phases. A shematic drawing of the proposed loop geometry is shown in figure 6.15 (b).

Asymmetry of the sources

In figure 6.7 we see there is asymmetry in brightness of the double sources in the impulsive phase (as well as in the post-impulsive phase). Comparison with photospheric magnetic field (figure 6.12) shows that the brighter source is located in a weaker magnetic field region than the darker one (longitudinal magnetic field strength $B_A \sim 200$ G and $B_B \sim 400$ G, respectively).

Electrons precipitating downwards along a magnetic field line with initial pitch angle θ_0 will increase their pitch angle due to momentum transfer between the parallel and parpendicular components with respect to the magnetic field line and will be reflected when the following condition is satisfied :

$$\theta_0 = \cos^{-1}\sqrt{1 - \frac{B_0}{B}} \ . \tag{6.4}$$

Here B_0 is the magnetic field strength at which electrons are injected, and B is the field strength at which electrons are reflected (mirror point). The loss cone is defined as the range of pitch angles θ which satisfies $\theta < \theta_0$ or $\theta > \pi - \theta_0$. Electrons with pitch angles $\theta < \theta_0$ (*i.e.* parallel, rather than parpendicular, to the field line) will then precipitate from the region whose field strength is B.

As the double sources are most likely footpoints of flaring magnetic loop(s), the above result suggests that the footpoint with stronger magnetic field (corresponds to source B) has stronger magnetic field convergence and hence have less electron precipitation than the footpoint with weaker field (source A) due to magnetic mirroring. This point will be statistically examined in the next chapter by several impulsive flares observed with HXT (see section 7.4.5).

Energy-dependent behavior in the impulsive phase

In the impulsive phase, hard X-ray sources greatly differed between those below 33 keV (L and M1 bands) and in the energy bands above 33 keV (M2 and H bands). In the valleys between the spikes, the hard X-ray sources showed single-source structures in the M1 band while double-source structures in the energy bands above 33 keV. These observations suggest the followings : At the peaks acceleration of electrons takes place and the electrons are confined in such a way that higher-energy electrons have a higher escape probability towards the footpoints. At the valleys when the acceleration weakens, lower energy electrons near the loop top still survive due to longer lifetimes because of lower plasma density there and emit X-rays (Kiplinger *et al.* 1983). Note that the ambient electron density, n_e, seen along trajectory of energetic electrons with its energy E, may characterize the burst decay time $\tau(E, n_e)$ such that

$$\tau(E, n_e) \sim \left(\frac{1}{E}\frac{dE}{dt}\right)^{-1} = 2 \times 10^8 E^{\frac{3}{2}} n_e^{-1} \quad \text{(s)} \quad (E \text{ in keV; } n_e \text{ in cm}^3) \ , \tag{6.5}$$

implying longer lifetime of electrons in lower density plasma near the loop top in comparison with electrons precipitating towards the footpoints where the plasma density is high. The observed soft-hard-soft spectral evolution through the individual spikes (figure 6.2) can be explained by the difference in lifetimes of lower energy electrons near the loop top and higher energy electrons precipitating to the footpoints.

Melrose and Brown (1976) have studied energy spectra of hard X-rays from the loop top, where electrons are trapped, and the loop footpoints, where precipitating electrons from the trap emit X-rays interacting with dense and cold ambient plasma. The have assumed that the precipitation of electrons from the trap region is caused by Coulomb scattering of the electrons into the loss cone and that the scattering is described in terms of diffusion in pitch angle of the trapped electrons. Pitch angle diffusion occurs at a rate $\nu_D = 2\nu_E$ (Trubnikov 1965), where ν_E is the energy loss rate of electrons due to Coulomb collisions :

$$\frac{dE}{dt} = -\nu_E E \ . \tag{6.6}$$

The quantity ν_E is numerically given as follows (see also eqs. (2.5) and (2.6)) :

$$\nu_E \simeq 5 \times 10^{-9} n_i E^{-\frac{3}{2}} \ , \tag{6.7}$$

where E is in units of keV. They have found that in the case of 'weak diffusion limit' (Kennel 1969), where the scattering of electrons into the loss cone is not dominant, electron precipitation rate ν_p is described as :

$$\nu_p \sim \nu_D \propto E^{-\frac{3}{2}} \ , \tag{6.8}$$

which gives smaller precipitation rate for higher-energy electrons. They also found that the resultant spectra of the emitted hard X-rays from the loop top and the footpoints have similar intensity and spectral shape with each other. This may not be able to explain the observed changes in the structure of the hard X-ray sources in the M1 band.

Relation with white-light brightening

As is shown in figures 6.14 and 6.13 (a), we see clear correspondence between hard X-ray and white-light sources both in the impulsive and the post-impulsive phases. This suggests that both hard X-rays and white-light emissions have a common origin, most likely due to precipitating electrons downwards to the footpoints along the loop (Hudson 1972, Kurokawa *et al.* 1988). Rust and Hegwer (1975) argued that, from the close temporal correspondence of hard X-ray and white-light intensities of the 7 August, 1972 flare, the hard X-ray source must have had a close spatial correspondence with the white light brightening. The result presented here is the first direct observation of such a correspondence.

6.4.3 Production of High Temperature Plasmas

In figure 6.2, power-law photon indices derived from M2/M1 and H/M2 bands count ratio differed by about 1.3 in the post-impulsive phase. This can be explained by appearance of a loop-like source seen in the M1 band (figure 6.8). From the Gaussian fitting procedure, I pointed out in section 6.2.3 that the photon indices for the double sources are similar ($\gamma_{DS} \sim 3.5$) with the value derived from the M2 and H bands pair, in which only double sources are seen. On the other hand, the loop-like source shows a softer spectrum than those from the double sources with the photon index $\gamma_L > 6$. This soft spectrum is also consistent with thermal emission from high temperature plasmas as high as $T_e \sim 3.5 \times 10^7$ K. The loop-like structure seen in the M1 band seems to originate from one of the double sources (source B in figure 6.8), but it elongates in a different direction from the other double source. Therefore it is suggested that high temperature plasma was produced by electron bombardment at the southern footpoint B, which is consistent with the chromospheric evaporation scenario. It seems that the high temperature plasma thus produced filled a different loop from the one in which energy release took place.

6.5 Summary and Conclusion

An intense impulsive flare, which occurred at 22:34 UT on 15 November, 1991, was observed with HXT, as well as other instruments aboard *Yohkoh*, in unprecedented detail. Hard X-ray sources in the precursor phase (22:34–22:37 UT) are located at remote sites ($\sim$ 20,000 km) from the main energy release site in the impulsive phase. On the contrary, hard X-ray sources in the impulsive phase are located in a rather compact region in contrast to the precursor

phase images. This suggests that some instability which caused activation or deformation of surrounding magnetic fields eventually led to the impulsive energy release. With this respect, it is interesting to point out that Hα filament eruption and brightenings in the off-band Ca II K-line were reported more than 8 minutes prior to the hard X-ray detection, giving support to an idea that global re-structuring of coronal magnetic field tend to precede occurrence of some flares. In the meanwhile, combined SXT, BCS, and Hα observations revealed that the chromospheric evaporation is likely to be taking place during the precursor phase and that different mechanisms (electron beams and heat conduction) are responsible for the flare kernels seen in the Hα red-wing images.

In the impulsive phase which lasted about 1 minute (22:37–22:38 UT), we see double sources located on both sides of the magnetic neutral line in the energy bands above 23 keV (M2 and H bands). The double sources emit hard X-rays simultaneously within 0.1 s at 1σ level, strongly suggesting that hard X-rays are emitted by accelerated electrons and the double sources correspond to the footpoints of a flaring loop. Double sources are seen also in the post-impulsive phase (22:38–22:41 UT), suggesting that particle acceleration is still taking place. The double sources show a systematic movement during the impulsive and post-impulsive phases : the separation between the double sources increased (from $\sim 15''$ to $\sim 30''$) with the angle sustained by the sources and the magnetic neutral line increasing. These observations suggest that particle acceleration originally started in a low lying, more sheared magnetic loop just above the neutral line and the acceleration took place successively in overlying less sheared loops with rising energy release sites. The double sources show good spatial correspondence with white-light brightenings observed with the optical telescope of SXT. This suggests that, at least for this flare, white-light brightenings are caused by accelerated electrons precipitating towards the footpoints of the loop.

Comparison of the double sources with longitudinal photospheric magnetic field has shown that the brighter source is located in the weaker magnetic field region than the darker one. This suggests that the footpoint with stronger magnetic field has stronger magnetic field convergence and has less electron precipitation than the other footpoint, hence is darker in hard X-rays.

The behavior of hard X-ray sources in the impulsive phase differed significantly between the M1 and M2 (or H) bands, at least after the time of P2 in figure 6.7 (at 22:37:37 UT) : at the peaks (P2 and P3) both M1 and M2 band images show double-source structure. On the other hand, in the valleys (V2 and at 22:38:00 UT), M1 band images show single sources while M2 band sources remain double. These observations suggest that higher-energy electrons precipitate towards the footpoints while lower-energy electrons remain near the top of the loop. Such energy dependent behavior of accelerated electons is inconsistent with the partial precipitation model, as far as weak scattering process is operating, which suggests that energy spectra of hard X-rays emitted from the loop top and the footpoints are similar in intensity and in spectral shape.

An important suggestion obtained from this study is that the double sources, seen in the non-thermal energy bands of HXT (typically $\gtrsim$ 30 keV), would give us essential information

on the characteristics of hard X–ray emission as well as propagation/confinement of accelerated electrons and acceleration mechanisms themselves. In the next chapter, I present HXT observations of hard X–ray double sources in impulsive flares, analyze characteristics of the double sources, and discuss physical implications derived from the analyses, with respect to the magnetic field geometry of flaring loops.

Figure Captions

Figure 6.1: Time plots of the hard X–ray count rates in the HXT four energy bands of the 1991 November 15 flare. The average counting rates (derived from 0.5 s integration) of the 64 imaging elements of HXT are given (after Sakao *et al.* 1992)

Figure 6.2: Time profiles of (a) power–law photon index γ, and (b) hard X–ray flux A_{20} at 20 keV, for the 15 November, 1991 flare with temporal resolution of 0.5 s. The index γ is derived using M2/M1 (solid line) and H/M2 (dashed line) band count data pairs. Here, incident photon spectrum $I(\varepsilon)$ is assumed to have the form $I(\varepsilon) = A_{20}(\varepsilon/20\ \mathrm{keV})^{-\gamma}$ photons/s/cm^2/keV (ε : in units of keV). We see that the two γ's show good agreement with each other before 22:38 UT while after that time, they differ by about $\Delta\gamma \sim 1.3$.

Figure 6.3: Cm–to–mm wave time profiles of the 1991 November 15 flare at 2, 17, and 35 GHz observed at Toyokawa (2 GHz) and Nobeyama (17 and 35 GHz) Solar Radio Observatories, with data integration time of 1 s. Time profiles of radio flux density and polarization degree are shown in each figure.

Figure 6.4: Hard X–ray sources (in the L band for (a), (b), and (d), and in the M1 band for (c), respectively) at different phases of the 15 November, 1991 flare : (a) precursor phase; (b) precursor phase, but just before the onset of the impulsive phase; (c) impulsive phase where the magnetic neutral line derived from the MSO magnetogram is overlaid; (d) post–impulsive phase. The contour levels are 18, 25, 35, 50, and 71 % of the maximum brightness for each image. The data averaging time for the image (c) is 0.5 s, while for the other images the data averaging intervals are shown in the images (after Sakao *et al.* 1992).

Figure 6.5: (a) HXT image (grayscale; black in white) overlaid with the Hα flare kernels (labelled as NE, SE, and NW) observed at the Mees Solar Observatory. Solid (dashed) contours in the figure indicates the Hα red–wing (+3 Å) (blue–wing (–3 Å)) excess emission. The HXT image is from the M1 band, integrated from 22:34:56–22:35:10 UT. The magnetic neutral line is shown in dashed line. (b) SXT image (grayscale; white in black) overlaid with MSO Hα and magnetograph data. The SXT image was taken at 22:35:04 through SXT's Beryllium filter. Both (a) and (b) have the same field of view of $80'' \times 80''$. Solar north is up and east is to the left (after Wülser *et al.* 1994).

Figure 6.6: (a) Ca XIX resonance line spectrum (solid line) observed with BCS at 22:34:45 UT. Dotted line represents plasma at rest, which is shown for comparison. (b) Plasma upflow velocity from fits to the Ca XIX spectra superimposed on a hard X–ray lightcurve obtained with HXS (after Culhane *et al.* 1993).

Figure 6.7: HXT images at the peaks and valleys of spikes during the impulsive phase (*top* : M1 band, *bottom* : M2 band). The size of each image is $37'' \times 37''$. Magnetic neutral lines are shown in P2 and V2 images in the M1 band. The data averaging times are 1, 1.5, 0.5, 0.5, 0.5, and 1 s for the M1 band images, and 1.5, 3, 0.5, 1.5, 1, and 2 s for the M2 band images, respectively. The countour levels are the same as in figure 6.4 (after Sakao *et al.* 1992).

Figure 6.8: HXT images (*top* : M1 band, *bottom* : M2 band) in the post-impulsive phase. Each image has the same image size of $59'' \times 59''$. The center of each image is the same as in figure 6.7. The contour levels are the same as in figure 6.4 except an additional 13 % contour level. The data averaging time (in UT) is shown at the top of each image. Location of the double sources seen in the M2 band images shifted between 22:39:20 UT - 22:39:24 UT, when 35 GHz (also 17 GHz) microwave time profile showed a valley.

Figure 6.9: Radio spectrum in the decay phase of the 15 November, 1991 flare at 22:44:00 UT. Data points at 2, 3.75, and 9.4 GHz are taken at Toyokawa and 17, 35, and 80 GHz are at Nobeyama Solar Radio Observatories, respectively.

Figure 6.10: (a) Time variation of hard X-ray fluxes from the double sources from 22:37:45 UT to 22:37:55.5 UT obtained from the Gaussian fitting procedure. Time resolution of the plot is 0.5 s. Thick solid line and dashed line denote fluxes from source A and B in figure 6.12, respectively. Thin solid line denotes spatially-integrated incident hard X-ray flux while dotted line is the sum of fluxes from sources A and B. Error bars in the figure indicate 1σ level. (b) Correlation between hard X-ray fluxes from sources A and B. Error bars indicate 1σ level.

Figure 6.11: Temporal variation of spectral hardness (derived from the H/M2 bands count ratio) for each of the double sources in the 3rd spike (aournd P3) from 22:37:46.5 UT to 22:37:55.5 UT. Time resolution of the plot is 0.5 s. Solid line denotes the hardness for source A while dashed line is for source B. Typical 1σ level for each data point is ± 10 % of each value. If we assume a power-law photon incident spectrum, corresponding photon spectral indices for sources A and B would be $\gamma_A \sim 2$ and $\gamma_B \sim 2.5$, respectively.

Figure 6.12: Overlay of M2 band hard X-ray sources at P3 (22:37:49 UT; thick solid contours) with a vector magnetogram taken at MSO between 21:05:59 UT and 22:35:59 UT. Thin solid contours represent positive polarity while dashed contours negative polarity. The contour levels for the longitudinal magnetic field strength are $\pm$ 50, 100, 200, 400, 800, 1600, and 3200 G for positive (+) and negative (−) polarity, respectively. Short straight lines indicate transverse magnetic field strength.

Figure 6.13: Hard X-ray sources in the post-impulsive phase in the M2 band (solid contours). (a) 22:38:47–22:38:50 UT, overlaid with an image of the white-light flare observed with SXT (dashed contours). (b) 22:39:48–22:39:52 UT. Hard X-ray sources in the impulsive phase (at 22:37:37 UT) are overlaid as dashed contours. The magnetic neutral line is shown in the image. Both images (a) and (b) have the same size of $59'' \times 59''$ (after Sakao *et al.* 1993).

Figure 6.14: Overlay of a hard X-ray image (in the M2 band; solid contours) with white-light flare (dashed contours) at P3 (22:37:49 UT). The contour levels are 20, 40, 60, and 80 % for the hard X-ray image and the same levels for the white-light image with the 20 % contour removed. The white-light image was obtained with a 238 ms exposure while the data accumulation time for the hard X-ray image is 1 s (after Sakao *et al.* 1992).

Figure 6.15: Possible geometry of flaring magnetic loops in (a) the precursor phase and (b) the impulsive and the post-impulsive phases of the 15 November, 1991 flare.

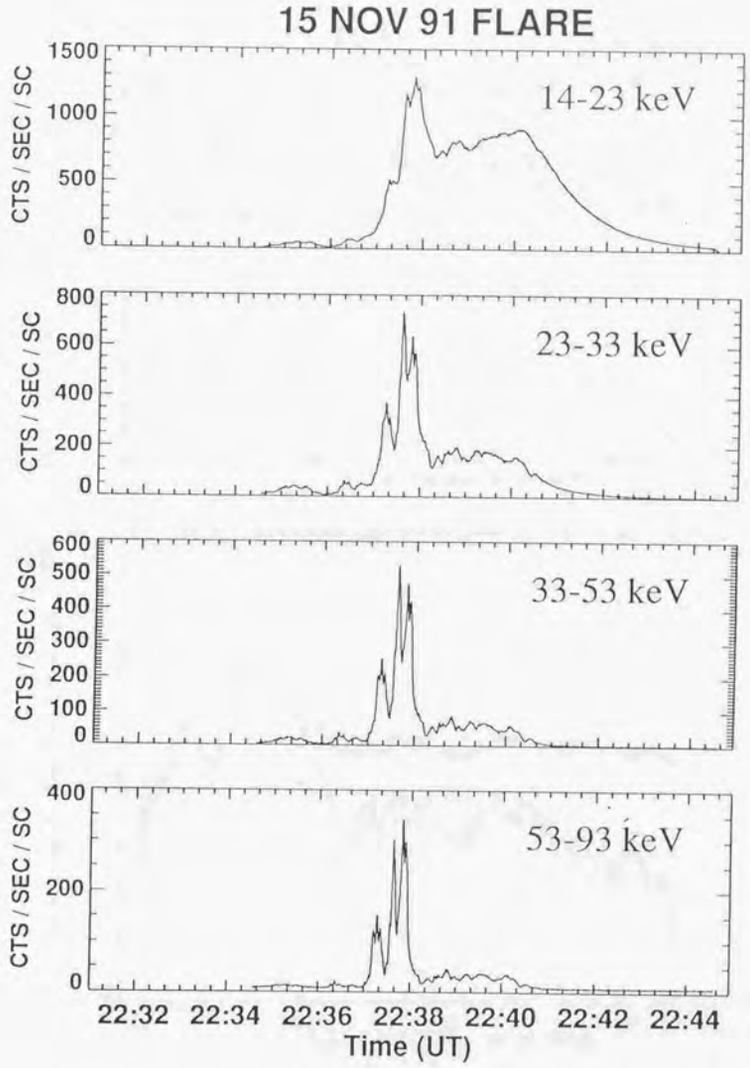
15 NOV 91 FLARE
14-23 keV
23-33 keV
33-53 keV
53-93 keV
CTS / SEC / SC
1500
1000
500
0
800
600
400
200
100
22:32 22:34 22:36 22:38 22:40 22:42 22:44
Time (UT)

Figure 6.1

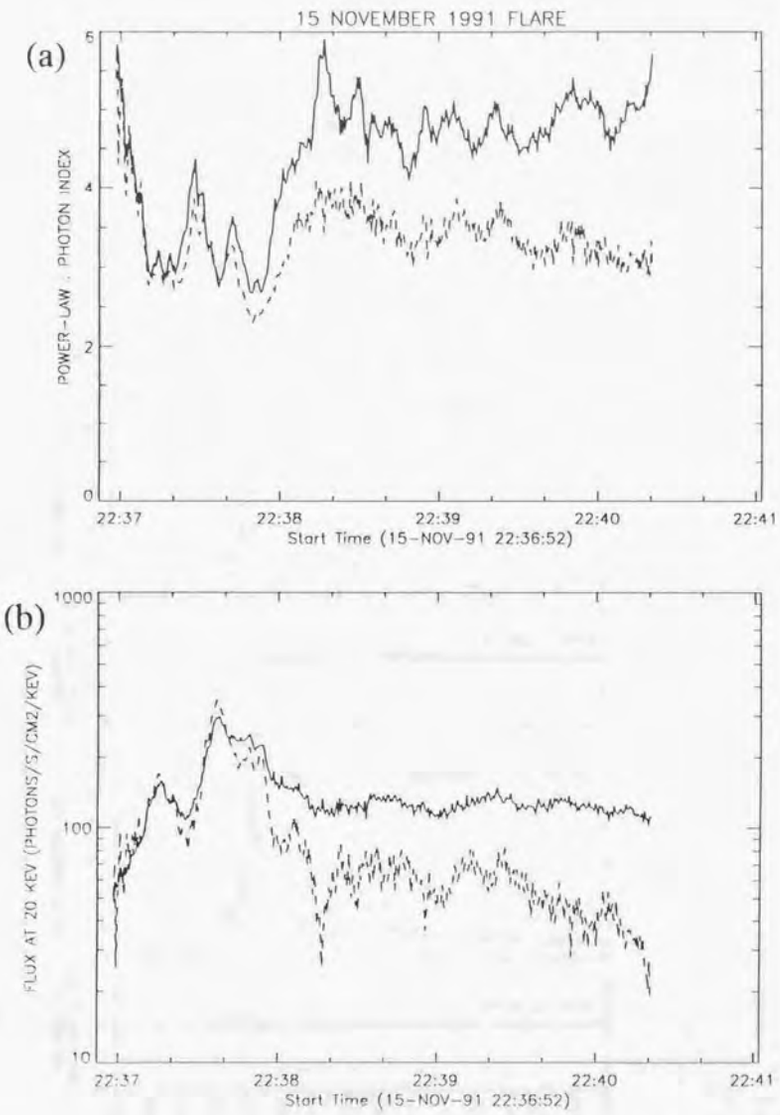
15 NOVEMBER 1991 FLARE
(a)
POWER-LAW : PHOTON INDEX
0
2
4
6
22:37
22:38
22:39
22:40
22:41
Start Time (15-NOV-91 22:36:52)
(b)
FLUX AT 20 KEV (PHOTONS/S/CM2/KEV)
10
100
1000
22:37
22:38
22:39
22:40
22:41
Start Time (15-NOV-91 22:36:52)

Figure 6.2

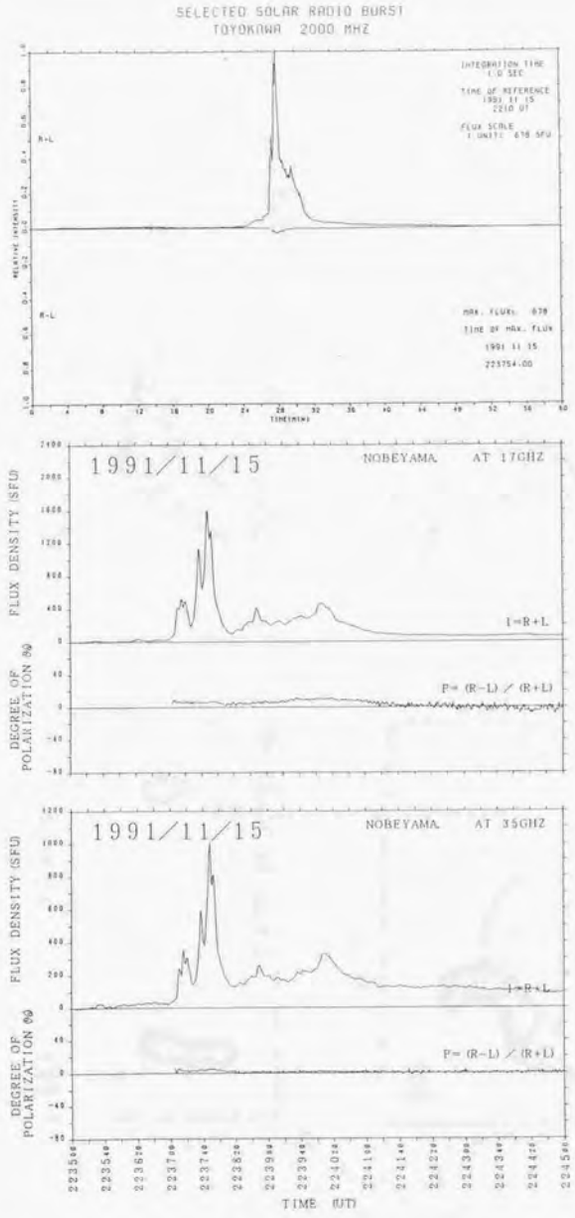
SELECTED SOLAR RADIO BURST
TOYOKAWA 2000 MHZ
INTEGRATION TIME
1.0 SEC
TIME OF REFERENCE
1991 11 15
2210 07
FLUX SCALE
1 UNIT: 676 SFU
R+L
R-L
MAX. FLUX: 678
TIME OF MAX. FLUX
1991 11 15
223754.00
TIME(MIN)
1991/11/15
NOBEYAMA AT 17GHZ
FLUX DENSITY (SFU)
I=R+L
DEGREE OF POLARIZATION %
P= (R-L) / (R+L)
1991/11/15
NOBEYAMA AT 35GHZ
FLUX DENSITY (SFU)
I=R+L
DEGREE OF POLARIZATION %
P= (R-L) / (R+L)
TIME (UT)

Figure 6.3

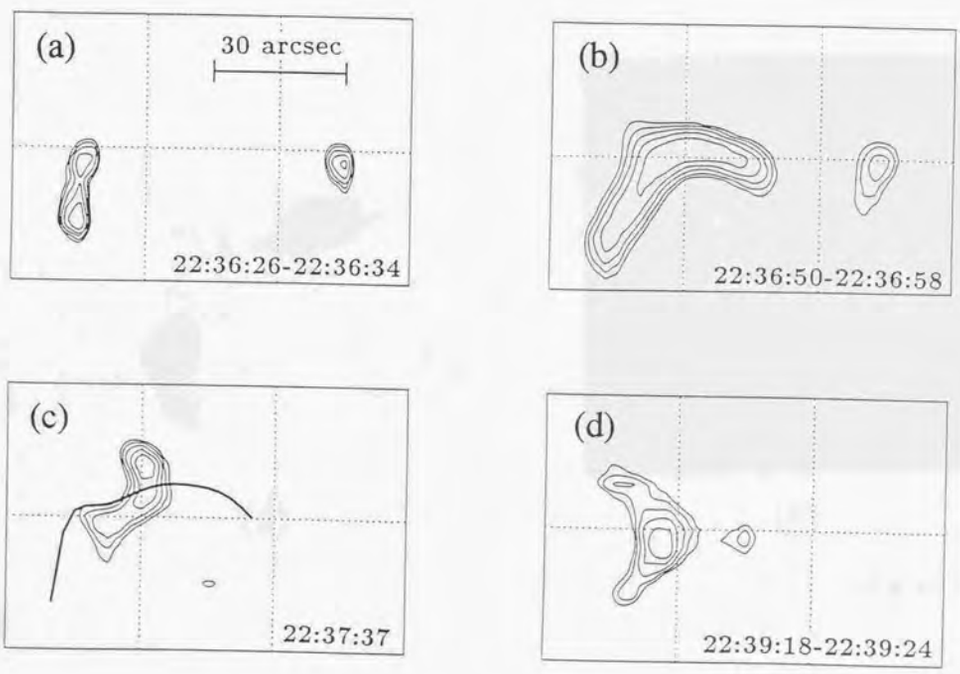
(a)
30 arcsec
22:36:26-22:36:34
(b)
22:36:50-22:36:58
(c)
22:37:37
(d)
22:39:18-22:39:24

Figure 6.4

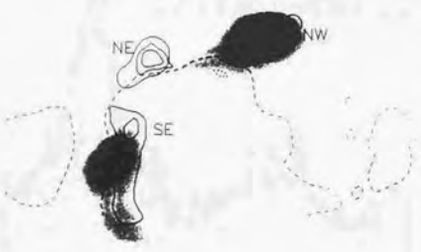

(a)

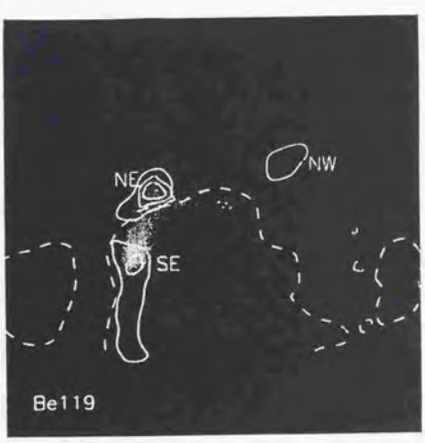

(b)

Figure 6. 5

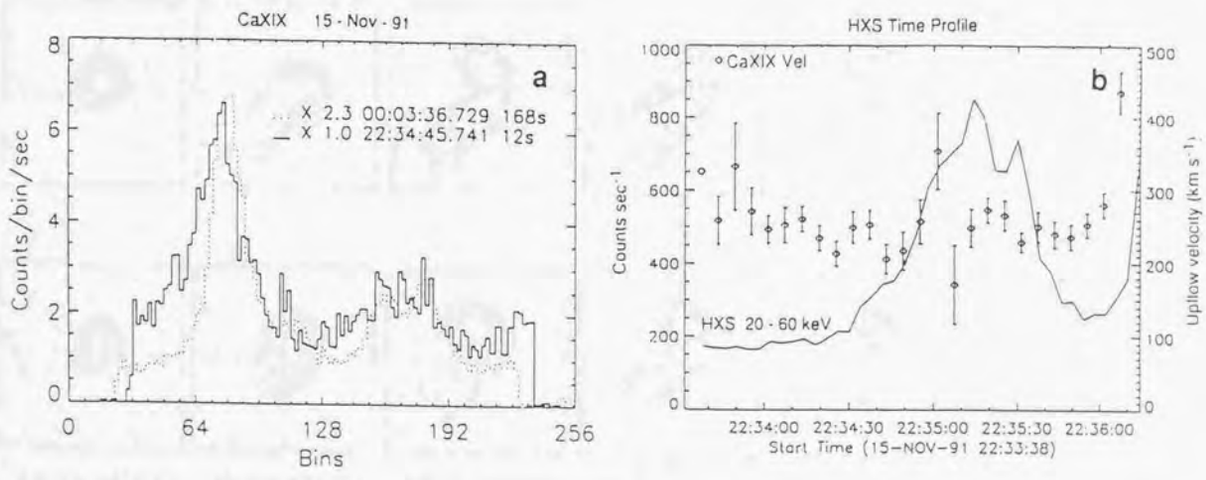
CaXIX 15 - Nov - 91
a
... X 2.3 00:03:36.729 168s
— X 1.0 22:34:45.741 12s
Counts/bin/sec
Bins
HXS Time Profile
CaXIX Vel
b
HXS 20 - 60 keV
Counts sec⁻¹
Upflow velocity (km s⁻¹)
22:34:00 22:34:30 22:35:00 22:35:30 22:36:00
Start Time (15-NOV-91 22:33:38)

Figure 6.6

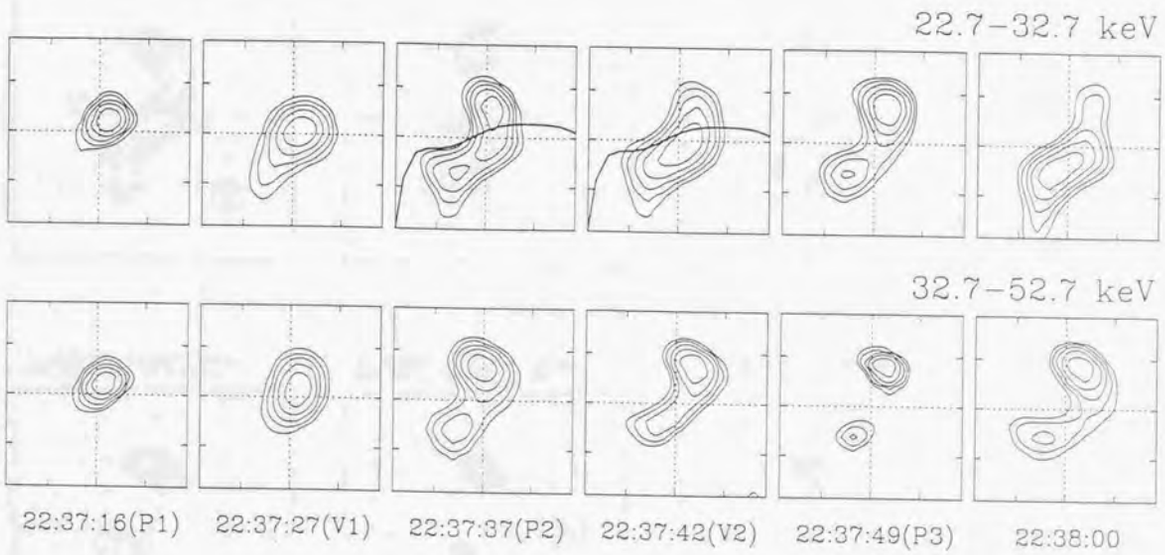
22.7–32.7 keV
32.7–52.7 keV
22:37:16(P1)
22:37:27(V1)
22:37:37(P2)
22:37:42(V2)
22:37:49(P3)
22:38:00

Figure 6.7

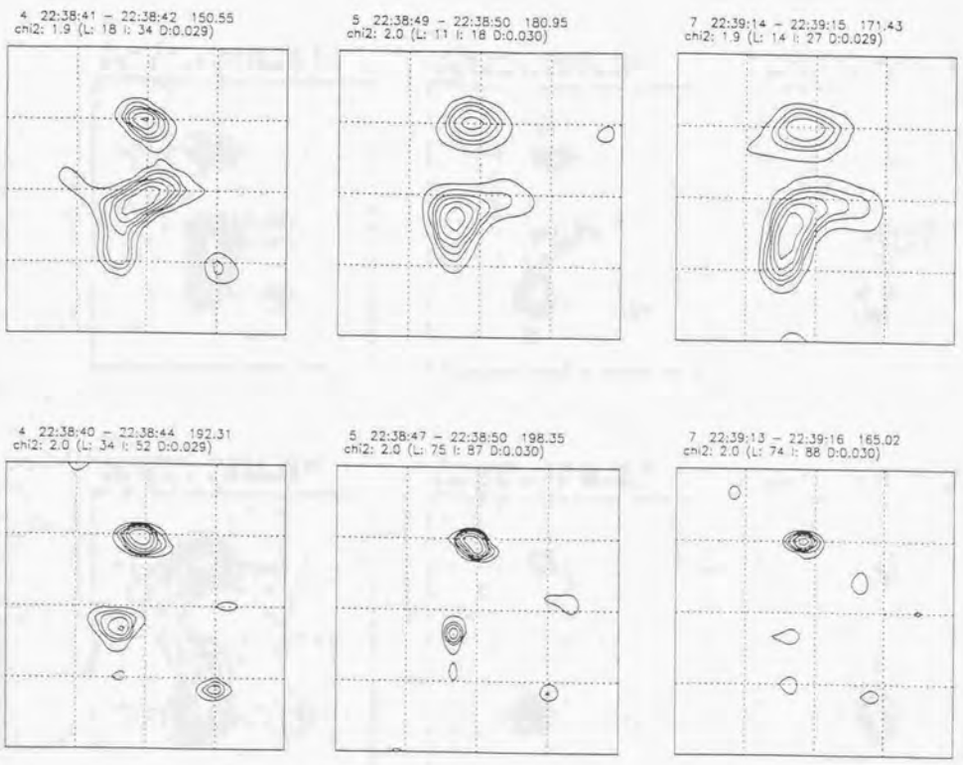
4 22:38:41 – 22:38:42 150.55
chi2: 1.9 (L: 18 I: 34 D:0.029)
5 22:38:49 – 22:38:50 180.95
chi2: 2.0 (L: 11 I: 18 D:0.030)
7 22:39:14 – 22:39:15 171.43
chi2: 1.9 (L: 14 I: 27 D:0.029)
4 22:38:40 – 22:38:44 192.31
chi2: 2.0 (L: 34 I: 52 D:0.029)
5 22:38:47 – 22:38:50 198.35
chi2: 2.0 (L: 75 I: 87 D:0.030)
7 22:39:13 – 22:39:16 165.02
chi2: 2.0 (L: 74 I: 88 D:0.030)

Figure 6.8

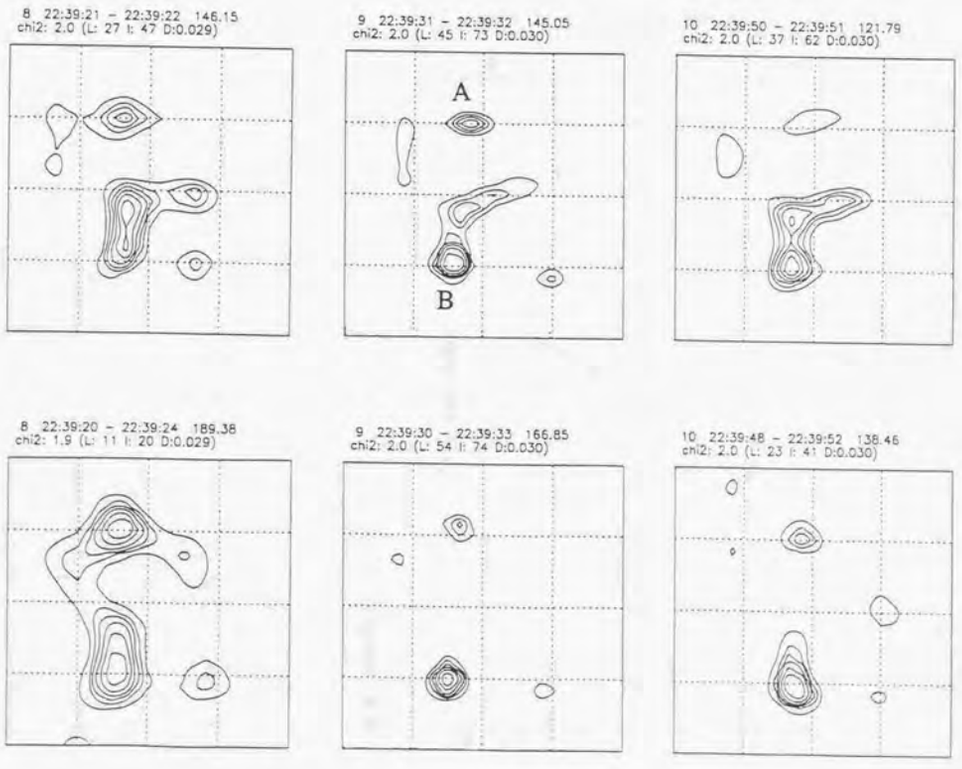

Figure 6.8 (*continued*)

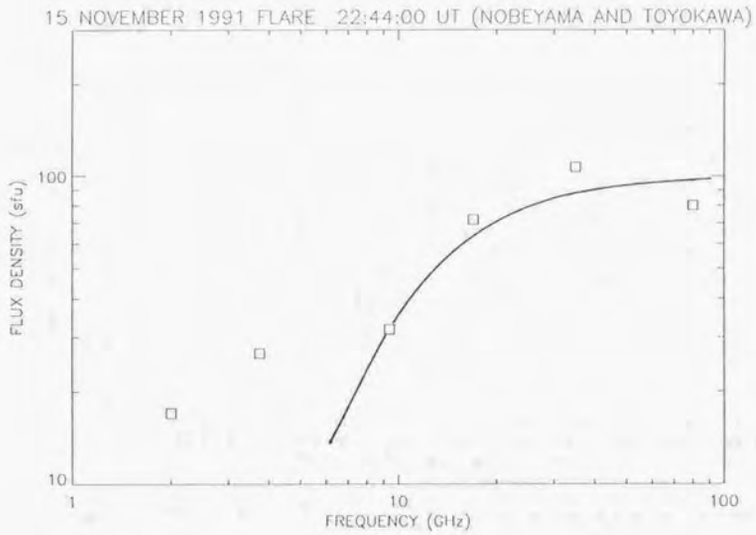
15 NOVEMBER 1991 FLARE 22:44:00 UT (NOBEYAMA AND TOYOKAWA)
FLUX DENSITY (s.f.u.)
100
10
1
10
100
FREQUENCY (GHz)

Figure 6.9

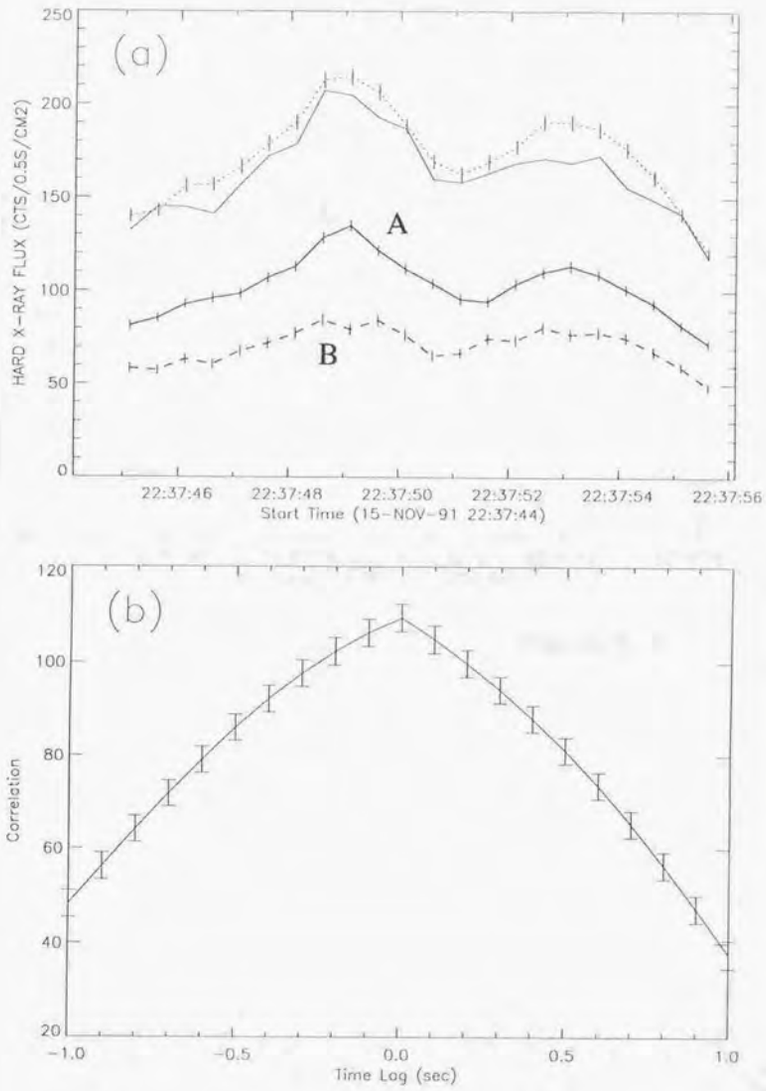
(a)
HARD X-RAY FLUX (CTS/0.5S/CM2)
250
200
150
100
50
0
A
B
22:37:46
22:37:48
22:37:50
22:37:52
22:37:54
22:37:56
Start Time (15-NOV-91 22:37:44)
(b)
Correlation
120
100
80
60
40
20
-1.0
-0.5
0.0
0.5
1.0
Time Lag (sec)

Figure 6.10

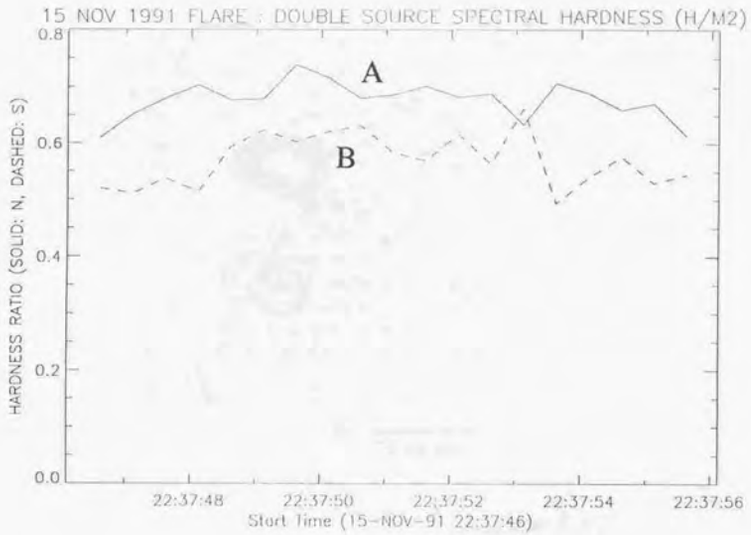
15 NOV 1991 FLARE : DOUBLE SOURCE SPECTRAL HARDNESS (H/M2)
HARDNESS RATIO (SOLID: N, DASHED: S)
0.8
0.6
0.4
0.2
0.0
A
B
22:37:48
22:37:50
22:37:52
22:37:54
22:37:56
Start Time (15-NOV-91 22:37:46)

Figure 6.11

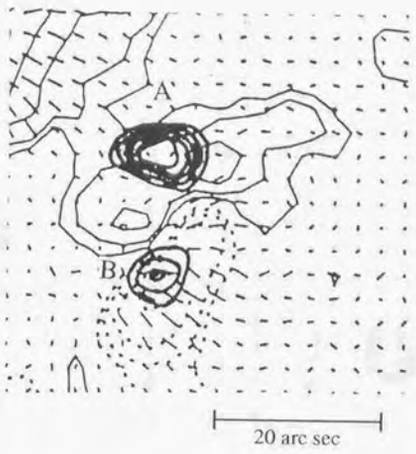

Figure 6.12

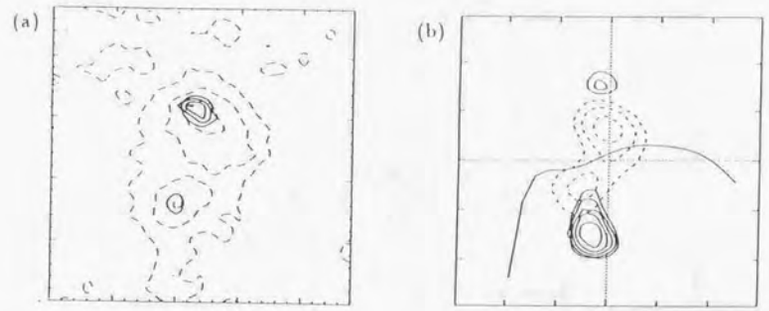

Figure 6.13

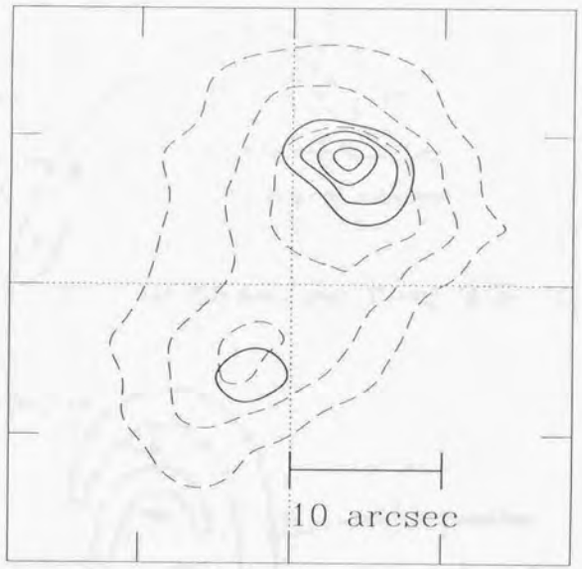

Figure 6.14

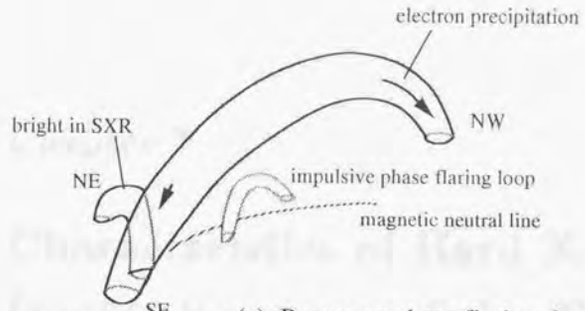

(a) Precursor phase flaring loops (~22:35 UT)

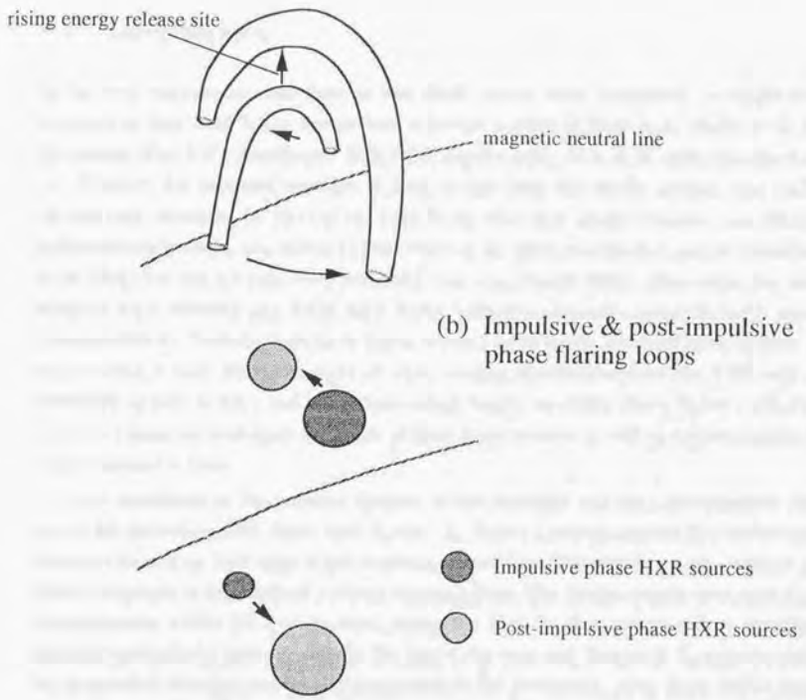

(b) Impulsive & post-impulsive phase flaring loops

Figure 6.15

Chapter 7

Characteristics of Hard X–ray Double Sources in Solar Flares

7.1 Introduction

In the early observations with *Hinotori* and *SMM*, several authors reported the double–source structure in their hard X–ray images from a limited number of flares (*e.g.*, Hoyng *et al.* 1981, Duijveman *et al.* 1982, Tanaka and Zirin 1985, Tanaka 1987, Nitta *et al.* 1990; see also chapter 2). However, for temporal variation of hard X–rays from the double sources, due maily to the low time resolution ($\sim$ 10 s) of the hard X–ray telescopes aboard *Hinotori* and *SMM*, the differentiation between non–thermal (Duijveman *et al.* 1982) and thermal models (MacKinnon *et al.* 1985) has not yet fully been successful (see, *e.g.*, Dennis 1988). Also rather low energy range of both *Hinotori* and *SMM* hard X–ray telescopes (typically below 20 keV), possibly contaminated by thermal emissions of flares, prevents us to derive firm conclusion on solar flare non–thermal events. From this point of view, imaging observations from the HXT with time resolution as high as 0.5 s and in multiple energy bands, especially above 30 keV, will give us a unique chance to investigate the origin of hard X–ray sources as well as electron acceleration sites in magnetic loops.

As is mentioned in the previous chapter, in the impulsive and the post–impulsive phases of the 15 November, 1991 flare, hard X–ray ($\gtrsim$ 30 keV) sources showed the double–source structure located on both sides of the magnetic neutral line. This double–source structure most likely corresonds to footpoints of a flaring magnetic loop. The double sources emit hard X–rays simultaneously within 0.1 s at 1σ level, suggesting that the flare energy release (specifically particle acceleration) takes place near the top of the loop and that hard X–rays are emitted by accelerated electrons precipitatig downwards to the footpoints. Also, these double sources showed a systematic change in location; the separation of the double sources increased with time and the angle sustained by the double sources and the magnetic neutral line became larger with

time. These observational facts suggest that particle acceleration in the flare first took place in a low-lying, strongly sheared magnetic loop, and the acceleration took place successively in overlying, less sheared loops with rising energy release site.

As is suggested by the above example, hard X-ray imaging observations of footpoint sources (manifesting themselves as double sources) are the key clues to understand the origin of hard X-ray emission, particle acceleration, propagation of accelerated particles, and sites of particle acceleration with respect to magnetic loops.

From such a point of view, I analyze solar flare double sources seen in the non-thermal energy bands ($\gtrsim$ 30 keV) of HXT with emphasis on (1) temporal correlation in hard X-ray flux between the double sources, (2) locations of the double sources with respect to the corresponding photospheric magnetic field, and (3) hard X-ray spectra of the double sources.

In the next section (section 7.2), I describe a statistical study of hard X-ray source morphology. In section 7.3 I present detailed case studies of several impulsive flares, and find some tendency in the above (1)-(3). In section 7.4, I discuss physical implications of the observed tendency. Finally in section 7.5, I summarize HXT observations of the double sources.

7.2 A Statistical Study

In this section, I describe statistical study of morphology of hard X-ray sources observed with HXT above 30 keV, specifically in the M2 band. As is mentioned in the previous section, hard X-ray imaging observations with *SMM* and *Hinotori* were made only below $\sim$ 20 keV range, where possible contamination of thermal emission from high temperature plasmas is present. Hard X-ray sources of purely non-thermal origin will only be observed with imagings in the $\gtrsim$ 30 keV range and if there is a systematic tendency in the morphology of hard X-ray sources, it would reflect some fundamental characteristics of hard X-ray emission with respect to the magnetic field structure. Hence a statistical study of hard X-ray ($\gtrsim$ 30 keV) source morphology will be quite important. In the following, I use M2 band images, rather than H band ones, to increase the number of flares available for the statistics.

Figure 7.1 shows examples of hard X-ray sources in the M2 band in six different flares. All the images in the figure have the same image size of $124'' \times 124''$. In figures 7.1 (a)-(c), bulk of hard X-ray emissions originates from double sources. Such a double-source structure is most frequently seen in the M2 band. In figures 7.1 (d) and (e), only single sources are seen. While (d) shows simple single source, lower brightness contours in (e) show a possible loop-like structure. In figure 7.1 (f), hard X-ray emission originates from three discrete sources.

Table 7.1 is a list of HXT flares used for the statistical study. The flares are selected in such a way that they have peak count rates in the M2 band of $\geq$ 30 cts/s/SC and occurred between October 1991 and December 1992. In the table, morphological classification of hard X-ray images in the M2 band at the peak of hard X-ray emission (in the M2 band) is shown : I

classified hard X-ray sources in the M2 band into three morphological classes; i.e., single source (SGL), double sources (DBL), and multiple sources which consist of more than two discrete sources.

A total of 33 flares, though not necessarily were observed from the beginning till the end, matches the criterion. Among these, 5 events were either (a) behind-the-limb events thus missing emissions from footpoints (15 December, 1991, 11 August, 1992, and 2 November, 1992 events), (b) long duration events (LDEs) lasting more than 1 hour in the L band with no impulsive behavior in the observed hard X-ray time profiles (30 October, 1992 and 2 November, 1992 events), or (c) no background data was available (26 December, 1991 event). Thus these 5 events are excluded from the current classification. Together with the morphological classification, I list in the table *GOES* soft X-ray class (in 1-8 Å), the Hα importance, NOAA active region number in which flares occurred, and the location of Hα flare. These information is obtained from the *Solar Geophysical Data*. Also I list count rates (in units of cts/s/SC) in the four energy bands of HXT at the peak time of M2 band count rate to give information on the spectral hardness.

Numbers of flares which belong to either of the above morphological classification (single, double, and multiple sources) out of the 28 events are summarized in table 7.2. I also show in the table results with an increased threshold peak count rate in the M2 band (50 cts/s/SC). The results with the threshold count rates of 30 cts/s/SC and 50 cts/s/SC do not differ significantly. We see that about 40 % of impulsive flares show double sources as long as they are not behind the limb events. The rest of the flares show either multiple- ($\gtrsim$ 30 %) or single-source structure ($\lesssim$ 30 %).

As is seen in tables 7.1 and 7.2, even if we exclude single sources, in more than 70 % of the impulsive flares presented here hard X-ray sources above 30 keV consist of discrete sources. Especially double sources, which are most commonly seen ($\sim$ 40 %) in the M2 band, are quite often located on both sides of the magnetic neutral line. Moreover, they seem to be located on both ends of a long, thin structure which is seen in the L band which possibly traces a flaring magnetic loop (Kosugi 1993). This suggests that the double-source structure, seen in the non-thermal hard X-ray range ($\gtrsim$ 30 keV), is not just a chance encounter of two distinct single sources, but it refrects fundamental characteristics in the hard X-ray emission process : at least in impulsive flares, hard X-rays above 30 keV are emitted mainly from footpoints of flaring magnetic loops.

Multiple sources consisting of three or more discrete sources may be an ensamble of double sources. As is shown in the next section, we often see double sources with asymmetric hard X-ray brightness. Hence it is possible that sometimes the asymmetry is so large that one of a pair of double sources is not imaged with HXT due to a limited dynamic range of HXT (typically $\sim$ 10 %; see also section 7.4.3), producing odd numbers of discrete sources. As for the single sources, the following three cases are likely : (1) asymmetry in hard X-ray brightness of double sources is so large that one of a pair of double sources is not imaged with HXT, (2) the separation

of double sources is so small that the sources are not well resolved by HXT, thus an apparent single source is imaged, or (3) hard X-ray sources actually show single-source structure, *e.g.* hard X-rays originate from the top of a flaring magnetic loop.

7.3 Case Studies

In this section, I analyze HXT observations of the following seven flares : (1) 15 November, 1991 flare (22:37 UT), (2) 3 December, 1991 flare (16:36 UT), (3) 7 February, 1992 flare (11:54 UT), (4) 16 December, 1991 flare (4:56 UT), (5) 10 September, 1992 flare (22:53 UT), (6) 10 November, 1991 flare (6:48 UT), and (7) 2 November, 1991 flare (6:47 UT). All the flares with their M2 band peak count rates exceeding 50 cts/s/SC in table 7.1 are studied here. These flares are selected according to that (a) they are impulsive flares showing impulsive spikes in their hard X-ray time profiles (time scales of spikes ranging from $\sim$ 10 s to $\sim$ 30 s), (b) double-source structure is seen in the HXT energy band above 33 keV (specifically in the M2 band), (c) relatively intense flares whose maximum X-ray count rates in the M2 band typically being more than 50 cts/s/SC. The criterion (c) is set so that temporal variation of hard X-ray intensity from each of the double sources is studied with time resolution typically as high as 1 s. Only the 7 February, 1992 flare does not meet criterion (c); peak count rate of this flare in the M2 band is 34 cts/s/SC. However, as this flare shows clear double sources and photospheric magnetic field data is available, here I included this flare as a case study.

Figure 7.2 show time profiles of the seven flares in the four energy bands of HXT. We see a wide variety of time profiles of impulsive spikes in the figure with time scales ranging from $\sim$ 10 s (*e.g.* 15 November, 1991 flare) to nearly 1 minute (2 November, 1991 flare) in the M2 band. It can be said that the observed double-source structure in these flares is not related to a specific hard X-ray time profile.

7.3.1 Method of Analysis

Gaussian fitting procedure

The Maximum Entropy Method (MEM), which we are using for image synthesis of HXT (*c.f.* section 5.1.3), is an image restoration procedure with a non-linear characteristic. Hence, it is sometimes not so easy to derive quantitative values, such as X-ray flux from each of the double sources seen in MEM images, unless the images are well-converged. Also as the MEM procedure requires (time-integrated) hard X-ray counts of typically $\gtrsim$ 100 cts/SC to make images with enough statistical significance, it is sometimes difficult to study behavior of hard X-ray sources with high time resolution, especially for rather modest flares. In order to study temporal and spectral behavior of hard X-ray emission from each of the double sources with high time resolution, I developed a Gaussian model fitting procedure. This procedure approximates

hard X-ray source distribution by a certain number of two-dimensional circular Gaussian sources (figure 7.3). The procedure has the following advantages over the MEM procedure : (1) As the procedure has a linear characteristic, it can handle quantitative values of hard X-ray sources (such as flux from each of the double sources) properly, and results of the fitting can be properly evaluated with the χ^2 statistics. (2) As the procedure makes model fitting to simple circular Gaussian profiles, it gives satisfactory fitting even if the time integrated counts are less than 100 cts/SC; say, typically around 30–50 cts/SC, hence suited to study more flares than MEM. On the other hand, the Gaussian fitting procedure is not suited for obtaining precise shape of hard X-ray sources. Nevertheless, it does not affect the following analyses significantly as long as the sources imaged with the MEM procedure show (nearly circular) double-source structure.

Let the i-th Gaussian source B_i be expressed as follows :

$$B_i(x,y;\ S_i,w_i,X_i,Y_i) = \frac{S_i}{2\pi w_i^2}\exp\left\{-\frac{(x-X_i)^2+(y-Y_i)^2}{2w_i^2}\right\}\ , \tag{7.1}$$

where (X_i, Y_i) denotes the center position and w_i the size of the source, respectively. Note that the full width at half maximum (FWHM) of the source is $\sim 2.35w_i$. In the fitting procedure, w_i, x, y, X_i, and Y_i are given in units of HXT pixel ($= 2.47''$; *c.f.* section 5.1.3). Hard X-ray brightness distribution $B_{\rm HXR}$ is assumed to be an ensamble of N circular Gaussian sources :

$$B_{\rm HXR}(x,y) = \sum_{i=1}^{N} B_i(x,y;\ S_i,w_i,X_i,Y_i)\ . \tag{7.2}$$

From $B_{\rm HXR}$, hard X-ray counts b_K ($K = 1 \sim 64$) from the 64 collimators are derived using eq.(5.14). These counts are compared with background-subtracted observed counts b_K^0, and the best-fit parameters for each of the Gaussian sources, such as location (X_i, Y_i) and hard X-ray flux S_i, are obtained by the linear least-squares method (Bevington 1969). Goodness of fit is evaluated by the reduced χ^2 values, $\chi^2_{\rm red}$, which are defined in eq.(5.19). If the approximation with circular Gaussian source profiles gives a consistent result with the observations, then $\chi^2_{\rm red} \lesssim 1$. If $\chi^2_{\rm red} > 1$ then it implies that the actual hard X-ray sources (1) do not have Gaussian profiles, (2) are not circular, *e.g.* elongated to a certain direction, and/or (3) there are additional sources present other than the double sources. In the following analysis, I nominally obtain reduced χ^2 values of $\chi^2_{\rm red} \sim 3-5$, which is fairly in consistent with the observations although MEM images give smaller χ^2 values. It is worthwhile to stress that hard X-ray flux S_i, obtained by the Gaussian fitting, is quite insensitive to *e.g.* size of double sources as is described below.

When applying this procedure for analyzing double sources, the Gaussian fitting with setting all S_i, w_i, X_i, and Y_i as free parameters (*i.e.*, total of 8 free parameters in the case of $N = 2$) usually gives satisfactory results. However, to make the fitting more stable even when the counting statistics is not very good and/or the separation of double sources is near the resolution limit of HXT, in the subsequent analysis I fixed values of w_i to be 1.0 (HXT pixel; *i.e.* 2.47″). This sets the FWHM value of a Gaussian source to be $\sim 6''$. I compared S_i and (X_i, Y_i) between

different w_i values. An example of the results is shown in figure 7.8, where I show S_i's in the M2 band for $w_i = 1.0$ and 1.5. Two sets of S_i are nearly the same with each other; thus to fix w_i to a reasonable value (say, 1.0) does not have serious influence on the source flux S_i. As we are mainly interested in hard X-ray flux from the double sources, hereafter we apply Gaussian fitting procedure with fixed w_i's.

By applying the Gaussian fitting in two adjacent energy bands of HXT for the same sets of data, we can derive spectral hardness of $i-$th double source $H_i^{m/n}$ which is defined as

$$H_i^{m/n} = \frac{S_i^m}{S_i^n} . \tag{7.3}$$

Here S_i^m (S_i^n) is hard X-ray flux from the $i-$th Gaussian component in the energy band m (n). I mainly choose m to be the H band and n to be the M2 band as long as counting statistics allows. When counts in the H band are too weak, I set m to M2 and n to M1, instead.

Comparison with photospheric magnetic fields

Observed double sources are overlaid with photospheric magnetic fields (magnetograph data) as follows. First, hard X-ray images are overlaid with SXT images using HXA information, with a typical accuracy of $\sim 3''$. As the optical telescope of SXT, which is well-aligned with the soft X-ray telescope and the offset is measured within $1''$ accuracy, optical images of sunspots can be well overlaid with continuum sunspot images taken with magnetographs. If the sunspot images are taken at different times between SXT and magnetographs, then the magnetograms are overlaid with correction for the rotation of the sun. Following this procedure, hard X-ray double sources are overlaid with photospheric magnetic fields (see also section 4.11.3). Magnetograms used in this analysis are taken at Mees Solar Observatory (hereafter, MSO) in Hawaii or at Okayama Astrophysical Observatory (hereafter, OAO; Sakurai 1991, 1992). Accuracy of the overlay between hard X-ray sources and magnetograms is typically no larger than $5''$.

In the next section (section 7.3.2), I denote strength of longitudinal photospheric magnetic field where source A (B), one of the double sources, is located as B_A (B_B). Sign of the quantity B_A and B_B indicates magnetic polarity (plus : positive, minus : negative, respectively).

7.3.2 Individual Flares

(1) 15 November, 1991 flare (X1.5)

The double sources seen in this flare have been discussed in detail in the previous chapter (*c.f.* figure 7.2 (a)). Here I briefly summarize observed characteristics of the double sources in the impulsive phase (see figure 6.7). Figure 6.12 shows overlay of the double sources in the M2 band at 22:37:49 UT and photospheric magnetic field map taken at MSO between 21:05:59 UT and 22:35:59 UT. The brighter source A is located in a positive polarity region with $B_A \sim +100$ G and the darker source B is in a negative polarity region with $B_B \sim -400$ G. The Gaussian

fitting procedure shows that the flux ratio $R_{A/B} \equiv S_A/S_B$ in the M2 band, where S_i is given in section 7.3.1, is about $R_{A/B} \sim 1.5$ as is seen in figure 6.10 (a). Simultaneity of hard X-ray emission from the double sources is quite good; with relative time lag $\Delta\tau = 0.0 \pm 0.1$ s at 1σ level (figure 6.10 (b)). From figure 6.11, we see that energy spectrum of source A is systematically harder than that of source B. Assuming power-law photon spectrum, I obtained photon indices $\gamma_A \sim 2.0$ and $\gamma_B \sim 2.5$.

(2) 3 December, 1991 flare (X2.2)

This flare commenced on 3 December, 1991 at 16:33 UT in NOAA active region 6952 near the east limb. The Hα flare location and importance were N17E72 and 2B, respectively. The *GOES* soft X-ray class of this flare was X2.2. Figure 7.2 (b) shows hard X-ray time profiles of this flare observed in the four energy bands of HXT. The time profiles show spiky components in the energy bands above 33 keV while the profiles are relatively smooth below 33 keV. Detailed analysis of this flare will be reported by Inda-Koide (1993).

Hard X-ray sources in the M2 and H bands show the double source structure (figure 7.4) with the south-western source (hereafter source A) brighter than the north-eastern one (hereafter source B). The separation between sources A and B is $\sim 14''$.

Figure 7.5 is an overlay of an H band hard X-ray image at the peak of hard X-ray burst (16:36:17 UT) and a vector magnetogram taken at MSO from 21:35:15 UT to 22:28:35 UT. The brighter source A is located in a negative polarity region (dashed contours) whose longitudinal magnetic field strength $B_A \sim -80$ G while the source B is in a positive polarity region (thin solid contours) with $B_B \sim +300$ G.

Figure 7.6 (a) shows time profiles of hard X-ray flux in the M2 band for the double sources (thick solid and dahsed lines for source A and B, respectively) in the time interval 16:36:00 UT to 16:36:44 UT using the Gaussian fitting procedure with time resolution of 1 s. Flux ratio $R_{A/B}$ is $R_{A/B} \sim 1.3$ during this interval. The overall simultaneity of hard X-ray fluxes from the double sources is good; with the cross-correlation analysis giving a time lag of 0.0 ± 0.2 s (figure 7.6 (b)). However, at spike P1 in figure 7.6 (a), we see that rapid increase in hard X-ray intensity at around 16:36:06 UT is mostly due to increased emission from source A. A similar analysis using the H band data with time resolution of 1 s gives essentially the same result. This individual behavior of X-ray emissions from sources A and B will be discussed later.

Figure 7.7 shows temporal variation of spectral hardness $H^{H/M2}$ (*c.f.* eq.(7.3)) of each of the double sources with time resolution of 1 s from 16:36:00 UT to 16:36:44 UT. In the figure solid line denotes the hardness for source A while dashed line is for source B. Source A shows systematically larger spectral hardness than source B throughout the impulsive phase of this flare. If we assume power-law photon spectrum, we obtain $\gamma_A \sim 3.0$ and $\gamma_B \sim 3.5$ at around 16:36:17 UT.

(3) 7 February, 1992 flare (M3.7)

This flare commenced on 7 February, 1992 at about 11:46 UT in NOAA active region 7035. The Hα flare location and importance were S21W53 and 2B, respectively, with the *GOES* soft X-ray class being M3.7. The flare showed several impulsive spikes between 11:51 UT and 11:55 UT, with the one at around 11:54:30 UT (hereafter P2) is most insense and has the hardest energy spectrum among the spikes (figre 7.2 (c)). I call the spike at around 11:53:40 UT as P1 in the following explanation.

During spike P2, hard X-ray sources showed the double source structure (figure 7.9) in the energy bands M1 to H, with the southern source A being brighter than the northern source B. The separation between the sources is $\sim 17''$. On the other hand, during spike P1, many discrete sources (more than four) are seen in addition to the double sources in P2, suggesting flaring of multiple loops. Although the difference in flaring loops between spikes P1 and P2 is itself interesting, here I concentrate on behavior of the double sources seen in spike P2.

Figure 7.10 is an overlay of the M2 band double sources near the peak of P2 (11:54:21 UT – 11:54:27 UT) and a vector magnetogram taken at OAO from 2:38:56 UT to 4:25:20 UT. The brighter source A is located in a negative polarity region (dashed contours) whose longitudinal magnetic field strength $B_A \sim -30$ G while the darker source B is in a positive polarity region (thin solid contours) with $B_B \sim +200$ G.

Figure 7.11 (a) shows time profiles of hard X-ray flux in the M2 band from the double sources (thick solid and dashed lines for source A and B, respectively), which were obtained by the Gaussian fitting procedure, during the time interval between 11:54:03 UT and 11:54:45 UT. Each data point in the figure corresponds to a 2 s data accumulation, due to rather low hard X-ray count rates. The figure shows that the flux ratio $R_{A/B}$ is about $R_{A/B} \sim 1.5$, and that hard X-ray flux from the double sources vary simultaneously, with the time lag of $\Delta\tau = 0.0^{+1.0}_{-0.7}$ s, *i.e.*, consistent with no time lag within statistical uncertainty (figure 7.11 (b)).

Spectral hardness of the double sources are derived from the M1 and M2 band data in the same way as before. Figure 7.12 shows time variation of spectral hardness of the double sources $H^{M2/M1}$ taken from 11:54:03 UT to 11:54:45 UT. Data are accumulated every 2 s to improve counting statistics. In the figure source A (solid line) shows systematically harder energy spectra than source B (dashed line). Assuming a power-law photon incident spectrum, photon indices are derived as $\gamma_A \sim 2.5$ and $\gamma_B \sim 3.0$ around the peak of spike P2.

(4) 16 December, 1991 flare (M2.7)

The flare commenced on 16 December, 1991 at $\sim$ 4:54 UT in NOAA active region 6961. The Hα flare location and importance were N04W45 and SF, respectively (figure 7.2 (d)). The *GOES* soft X-ray class of this flare was M2.7.

Figure 7.13 shows hard X-ray images of this flare in the M2 and H bands at around the peak time of hard X-ray emission. During the impulsive phase hard X-ray sources in the energy bands above 23 keV (*i.e.* in the M1, M2, and H bands) show double sources, separated by $\sim 28''$ and located on both sides of the magnetic neutral line. After the impulsive phase (*i.e.* after 4:56:20 UT) there appears a loop-like structure connecting one of the double sources (southern source; source A) and the midpoint between the double sources. Detailed description on HXT observations of this flare, from a viewpoint of chromospheric evaporation, is given by Culhane *et al.* (1994).

Figure 7.14 is an overlay of M2 band hard X-ray sources and an OAO vector magnetogram taken from 2:50:04 UT to 4:04:59 UT (Culhane *et al.* 1994). The double sources (thick solid contours in the right hand side) are located in an opposite polarity region; source A in positive polarity region (thin solid contours) $B_A \sim +300$ G, and source B in negative polarity region (dashed contours) $B_B \sim -700$ G, respectively.

Figure 7.15 (a) shows hard X-ray flux time profiles in the M2 band for the double sources from 4:56:02 UT to 4:56:17 UT using the Gaussian fitting procedure, with time resolution of 1 s. The ratio of flux from the double sources $R_{A/B}$ is $R_{A/B} \sim 0.8$; *i.e.* source B is brighter than source A in the M2 band. However, in the H band, source A is almost as bright as source B with $R_{A/B} \sim 1.0$. The overall simultaneity of hard X-ray fluxes between the double sources is, again, good; with the cross-correlation analysis giving a time lag of $\Delta\tau = 0.0 \pm 0.2$ s (figure 7.15 (b)). A similar analysis on the H band data gives essentially the same result.

Figure 7.16 shows energy spectral hardness of the double sources derived from the M2 and H band data. Source A shows harder energy spectra than source B : assuming a power-law photon spectrum, we obtain photon indices $\gamma_A \sim 3.4$ and $\gamma_B \sim 3.8$ around the peak of the impulsive phase.

(5) 10 September, 1992 flare (M3.2)

This flare commenced on 10 September, 1992 at 22:51 UT in NOAA active region 7276 (figure 7.2 (e)). The Hα flare location and importance were N12E41 and 2B, respectively. The *GOES* soft X-ray class of this flare was M3.2. Magnetic field data for this flare was not available.

Figure 7.17 shows M2 band hard X-ray sources of the flare during the impulsive phase (22:52:29.6 UT – 22:52:31.6 UT). We see double sources separated by $\sim 25''$ in the M2 band images. This double-source structure is also clearly seen in the other energy bands (*i.e.* L, M1, and H bands). The northern source (hereafter source A) is brighter than the southern one (hereafter source B).

In figure 7.18 (a) I show hard X-ray flux time profiles in the M2 band for the double sources from 22:52:13 UT to 22:52:35 UT, with 1 s time resolution. The flux ratio $R_{A/B}$ is $R_{A/B} \sim 1.3$ and the time profiles show a high simultaneity; hard X-ray fluxes from the double sources vary simultaneously within 0.2 s at 1σ level as is shown in figure 7.18 (b).

Figure 7.19 shows temporal variation of spectral hardness of the double sources. Data are

accumulated every 1 s to improve counting statistics. For this flare, spectral hardness of sources A and B are about the same with corresponding power-law photon indices $\gamma_A \sim \gamma_B \sim 2.3$.

(6) 10 November, 1991 flare (M2.2)

This flare commenced at 6:47 UT on 10 November, 1991 in NOAA AR 6919 (Hα location S14E53). The *GOES* X-ray class of this flare is M2.2 and the Hα importance is 2B (figure 7.2 (f)). *Yohkoh* observed this flare from the beginning, but at 6:48:30 UT the spacecraft entered the South Atlantic Anormaly (SAA), where the high-voltage outputs of HXT are reduced to avoid possible damages of the detector photomultipliers (see section 3.1.2 and 4.5.2), hence we could not obtain *Yohkoh* data except SXT after this time. Magnetic field data for this flare is not available.

Hard X-ray sources of this flare show double sources separated by $\sim 46''$ with additional two sources; each of these additional sources was located near either of the double sources as shown in figure 7.20. The fitting procedure with four Gaussian sources shows that emissions from the additional sources are not significant with respect to the double sources (fluxes from the northern and southern additional sources are less than 7 % and 15 % of the total flux, respectively) and hard X-ray fluxes from sources A and B in figure 7.20 show essentially the same time profiles as those obtained by the fitting with two Gaussian sources. Hence, in this analysis I use the Gaussian fitting procedure with two sources.

Figure 7.21 (a) shows hard X-ray flux temporal variation in the M2 band for the double sources from 6:48:25 UT to 6:48:39 UT (thick solid line is for source A while dashed line for source B). Each of the data was accumulated for 1 s to improve counting statistics. In the M2 band, hard X-ray fluxes from sources A and B are nearly the same; $R_{A/B} \sim 1.0$, while in the H band source A seems to be brighter than source B with $R_{A/B} \sim 1.2$. Simultaneity of hard X-ray fluxes from the double sources is generally good; with the time lag $\Delta\tau = 0.2^{+0.3}_{-0.3}$ s (figure 7.21 (b)). This means that sources A and B emit hard X-rays simultaneously within statistical uncertainty.

Figure 7.22 shows time profiles of spectral hardness of the double sources from 6:48:25 UT to 6:48:39 UT, with time resolution of 1 s (solid line: source A, dashed line: source B), with source A showing a tendency to have a harder energy spectrum than source B. Assuming a power-law photon spectrum, photon indices $\gamma_A \sim 2.5$ and $\gamma_B \sim 3.0$ are obtained.

(7) 2 November, 1991 flare (M9.1)

This flare commenced at 6:43 UT on 2 November, 1991 in NOAA AR 6891 (Hα location S13W61; figure 7.2 (f)). The *GOES* X-ray class of this flare is M9.1 and the Hα importance 1B. SXT observed white-light brightenings with its optical telescope. Observations of this flare with SXT and HXT are reported by McTiernan *et al.* (1993).

Figure 7.23 shows double sources in the M2 band at the peak of hard X-ray emission (6:45:45 UT – 6:45:46 UT). The double sources, which are seen in all of the four energy bands at the peak time of hard X-ray emission, are separated with each other by $\sim 34''$. The double sources seem to well match with the white-light brightenings.

Photospheric magnetic field data for this flare is available from MSO, which is taken from 17:56:59 UT to 19:55:06 UT on 1 November, 1991. Although the difference in time between the magnetogram and the flare is quite large, the brighter source A seems to be located in the stronger longitudinal magnetic field region (positive polarity) with $B_A \sim +400$ G while the darker source B in the weaker region (negative polarity) : $B_B \sim -100$ G.

Figure 7.24 (a) shows hard X-ray (M2 band) time profiles for the individual sources in the M2 band from 6:45:20.5 UT to 6:46:18.5 UT with time resolution of 0.5 s (thick solid line for source A and thin solid line for source B). Solid line corresponds to source A and dashed line to source B in figure 7.23. Ratio of hard X-ray fluxes from the double sources is $R_{A/B} \sim 1.5$. There is an apparent difference in hard X-ray peak times; the hard X-rays from source A precedes source B by ~ 1.5 s. Moreover, small spikes denoted as 'S' in figure 7.24 (a) seem to originate only from the source A; no spiky structure corresponding to 'S' is seen in the time profile of source B. Figure 7.24 (b) shows the the result of cross-correlation analysis of the hard X-ray time profiles between the double sources. As temporal variation of hard X-ray flux from source A differs significantly from that of source B, the overall correlation is not good.

Figure 7.25 shows time variation of the spectral hardness for the same time interval as figure 7.24 (a) with a data accumulation interval of 0.5 s. The spectral hardness of sources A and B are almost the same, with photon indices of the power-law photon spectrum $\gamma_A \sim \gamma_B \sim 3.0$ around the peak of hard X-ray emission (at around 6:45:45 UT).

7.3.3 Summary of Observations

Results of temporal/spectral behavior of the double sources (in the M2 band) mentioned above are summarized in table 7.3. In the table, the following quantities are given : (a) Difference in flux from the double sources in the M2 band; in the form of flux ratio $R_{A/B} = S_A/S_B$. S_A and S_B are obtained by the Gaussian fitting procedure (S_i in eq.(7.1) corresponds to S_A and S_B). (b) Relative time lag $\Delta\tau$ of hard X-ray fluxes between the double sources derived by the cross-correlation analysis (together with 1σ level). Here $\Delta\tau > 0$ means that source A lags source B. (c) As an indicator of spectral hardness, photon indices γ_A and γ_B assuming power-law photon spectra. Note that in the 7 February, 1992 flare, photon indices are derived from the M1 and M2 bands count data pair while the M2 and H bands were used for the other flares. (d) Strength of longitudinal photospheric magnetic field B_A and B_B in which the double sources (sources A and B) are located.

From this table, the followings are pointed out :

- In most of the flares (6 out of 7), simultaneity of hard X-ray fluxes from the double sources are quite high; showing no time lag (*i.e.*, $\Delta\tau = 0.0$) within statistical uncertainty.

- Three out of 5 events show that brighter footpoints tend to have harder energy spectra than darker ones ($S_A > S_B \rightarrow \gamma_A < \gamma_B$ and vice versa). There are two cases (the 10 September, 1992 and the 2 November, 1991 flares) that the spectral hardness is roughly the same ($\gamma_A \sim \gamma_B$) despite there is a difference in S_A and S_B. But none of the darker source shows harder spectra than the brighter ones; in the 16 December, 1991 flare, source A in figure 7.15 (a) is darker than source B with $R_{A/B} \sim 0.8$ in the M2 band. However, in the H band source A is almost as bright as source B with $R_{A/B} \sim 1.0$, yeilding a harder energy spectrum than source B, which is also consistent with the tendency discussed here. Also in the 10 November, 1991 flare, $R_{A/B} \sim 1.0$ in the M2 band while $R_{A/B} \sim 1.2$ in the H band, hence yielding a harder spectrum for source A than source B. If we add these two flares, we can say that five out of 7 events show the above tendency.

- For the 5 events for which magnetograms are available, all of the double sources are located on both sides of the magnetic neutral line. Also, three out of the 5 flares show that the brighter footpoint tends to be located in a weaker photospheric magnetic field region ($S_A > S_B \rightarrow |B_A| < |B_B|$ and vice versa), regardless of the magnetic polarity. Also we see that the 16 December, 1991 flare is consistent with this tendency by the same reason as is described in the previous item. Thus we can say that four out of the 5 events show this tendency. There is one exception which shows the opposite tendency, *i.e.* the brighter footpoint is located in the stronger magnetic field (2 November, 1991).

Implications from these observations will be discussed in the next section.

7.4 Interpretation and Discussion

7.4.1 Fundamental Structure of Hard X-ray Sources

Among 28 intense impulsive flares observed with HXT during the 15 months from 1 October, 1991 to 31 December, 1992, hard X-ray sources of the flares most frequently ($\sim$ 40 %) showed double-source structure in the M2 band (tables 7.1 and 7.2). When the double sources are seen, they are located on both sides of the magnetic neutral line. These observations suggest that the hard X-ray double sources, seen in the purely non-thermal energy range ($\gtrsim$ 30 keV), are mangetically conjugate and are not formed as a result of simple chance encounter of two individual single sources, *i.e.* non-thermal hard X-rays are emitted mainly from the footpoints of a single flaring magnetic loop, at least in impulsive flares, which is one of the fundamental characteristics in the hard X-ray emission process. It is interesting to point out that, in several flares it is shown that the double sources correspond to the footpoints of flaring loops from

combined imaging observations with soft X-rays and Hα, as well as the L band images of HXT (Kosugi *et al.* 1992, Sakao *et al.* 1992, Kosugi 1993). Hence, it is suggested that the double-source structure is the fundamental structure of impulsive flare hard X-ray sources in the non-thermal energy range.

Apart from the double sources, the rest of the flares show either single- or multiple-source structure. As for multiple sources, they may be an ensamble of double sources. This is supported by several combined hard and soft X-ray imaging observations from *Yohkoh*; for example, Hudson *et al.* (1994) have shown that in an impulsive flare commenced on 26 January, 1992, hard X-ray multiple sources in the M2 band correspond to footpoints of individual flaring loops seen with SXT. Sometimes we see odd numbers of sources in hard X-ray images. Such images are produced if asymmetry of fluxes from double sources is so large, due to asymmetry in magnetic field strength around the double sources (section 7.4.5), that the flux from one of a pair of double sources is below the dynamic range of HXT (typically $\sim$ 10 %). The same idea is applied to the observed single sources, *i.e.* if one of the double sources is so weak in hard X-rays to be imaged with HXT, then the other source would be observed as a single source. Also some other possibilities need be considered; such as (1) the separation of double sources is so small for HXT to be imaged as double sources, hence an apparent single source is imaged, and (2) hard X-rays are emitted near the top of a flaring loop. These possibilities can be examined by detailed comparison of hard X-ray images with soft X-ray images and photospheric magnetic fields in the future study.

7.4.2 Simultaneous Brightening of Hard X-ray Double Sources

Among seven intense impulsive flares which show the double-source structure in the M2 band, six showed good simultaneity in hard X-ray fluxes from the double sources, *i.e.*, the relative time lag $\Delta\tau$ is consistent with 0.0 s within 1σ level (table 7.3). There is only one exception (2 November, 1991) in which the peak times of hard X-ray emission from the double sources differ by $\sim$ 1.5 s. In this case, as is seen in figure 7.24 (a), emission from one of the double sources (source A) shows spikes 'S' which is not seen for source B. If this spiky temporal variation of source A took place near the peak of the hard X-ray emission, then a superposition of this spiky component in source A time profile would cause the apparent time lag of $\sim$ 1.5 s even though non-spiky X-ray emissions from sources A and B might show good simultaneity.

The fact that the double sources emits hard X-rays simultaneously strongly suggests that, at least in impulsive flares, hard X-rays are emitted by accelerated electrons which stream down toward footpoints of a single flaring magnetic loop. Hard X-ray emission caused by beams of accelerated ions (mainly protons; Simnett 1986, 1991, Heristchi 1986) may not be the case as is shown below.

Simnett (1986) has reviewed difficulties in the electron beam hypothesis and has argued instead that the bulk of released flare energy resides in beams of protons whose energy is typically

a few hundred keV. The accelerated protons stream down towards the footpoints along magnetic loops, producing very high temperature plasmas ($T_e \sim 10^7 - 10^9$ K) and hard X-rays are emitted by thermal Bremsstrahlung of electrons in the high temperature plasmas near the footpoints. Simnett (1991) has argued that, instead of thermal Bremsstrahlung emission, the accelerated ions cause runaway acceleration of electrons near the footpoints and non-thermal hard X-rays are emitted by the accelerated electrons in the chromospheric portion of the footpoints. Heristchi (1986) has proposed that hard X-rays are emitted by inverse Bremsstrahlung of high energy protons interacting with ambient electrons.

In any case, since proton velocity v_p for an kinetic energy of several hundreds keV (*e.a.*, $\sim$ 400 keV) is $v_p \sim 0.03c$ (c : light velocity) and, if conbined with our result, this would imply that the acceleration site need be located exactly at the midpoint of the flaring loop. In order to explan the observed simultaneity of footpoint emissions (say, within 0.1 s), only a region of $\Delta l \sim 900$ km is allowed on both sides of the midpoint along the loop. This Δl is only 4 % of the loop length for a typical footpoint separation of 20″ (assuming a semi-circular loop), and it is quite unlikely that proton acceleration always takes place in such a narrow and specified region of the flaring loop for six independent flares.

It is worth while mentioning that, even apart from this observed simultaneity, inverse Bremsstrahlung process of high energy protons as the origin of hard X-rays has been rejected due to the large number of protons required to produce the observed hard X-ray flux (Emslie and Brown 1985); $10^3 - 10^4$ times larger number of protons are required than those required to explain the observed γ-rays for the same flare.

Thermal Bremsstrahlung emission from a very high temperature plasma ($T \geq 10^8$ K) as the origin of hard X-rays (Smith and Lilliequist 1979, Batchelor *et al.* 1985) may also be unable to explain the simultaneity of emissions from the double sources. According to this type of thermal models, plasmas around the energy release site are impulsively heated up to $T \sim 10^8$ K and are temporalily confined behind a pair of ion-acoustic conduction fronts which are formed in the flaring loop. These conduction fronts move towards the footpoints at the ion sound speed $v_i \sim 1000$ km/s. While the bulk of the released energy is contained in this very high temperature plasma, high-energy electrons in the tail of the thermal distribution whose velocity exceeding $v_{esc} > v_e(m_i/m_e)^{1/6} \sim 3v_e$ (v_e : electron thermal velocity) can escape from the thermal conduction front ('dissipative thermal model'; Machado 1991).

Such a conduction front is difficult to explain the observed simultaneity of footpoint brightening. As is similar to the above result, length Δl of the allowed energy release region along the loop would be $\Delta l \sim 100$ km even for a time lag of $\Delta\tau = 0.2$ s, thus again quite hard to expect that the energy release site is located just at the midpoint of the flaring loop in six flares. Even if the high-energy electrons escaping from the conduction fronts are responsible for the emission from the double sources, it implies that hard X-ray emission in the energy range $\gtrsim 30$ keV is nearly of non-thermal (thick-target) origin.

7.4.3 Individual Hard X-ray Emission from Double Sources

Although the overall simultaneity of temporal variation of the double sources is quite good, there are some cases that one of the double sources emits hard X-rays which lack the corresponding spikes in the other source, such as the one in the 2 November, 1991 flare. Also in the 3 December, 1991 flare, we see that emission from source A (southern source) increases impulsively around spike P1 (figure 7.6 (a)) while the emission from source B does not show such rapid increase. Such individual behaviors of footpoint emission may be explained qualitatively if energy release takes place in several magnetic loops such as in loop-loop interaction models (*e.g.*, Sakai and Ohsawa 1987). In these models, energy release and subsequent particle acceleration take place at site where two loops interact with each other. If the magnetic loop geometry is the one shown in figure 7.26 and the two footpoints labeled F_2 and F_3 are located close enough with each other, then these two footpoints may not be resolved by HXT. Also due to a limited dynamic range of HXT (typically $\sim$ 10 %), there is a possibility that one of the footpoint pair (in the case of figure 7.26, the one labeled as F_4) is not observed with HXT, if the asymmetry in hard X-ray fluxes from the two footpoints is so large. If accelerated electrons propagate along loop L_1, then we may observe the two footpoints F_1 and F_2 (also F_3) brighten simultaneously. On the other hand, if the electrons propagate along loop L_2, only emission from F_3 (*i.e.*, F_2) is expected to increase. It is interesting to note that both in the 2 November, 1991 and 3 December, 1991 flares, brighter (and larger) footpoints show increase in hard X-ray emission independent of the other footpoint.

7.4.4 Footpoint Energy Spectra

In table 7.3, we see a tendency that the brighter footpoint has a harder energy spectrum than the darker one. Although there are some cases that spectral hardness is roughly the same despite significant difference in flux between the double sources (10 September, 1992 and 2 November, 1991 flares), none of the darker footpoint has a harder spectrum than the brighter one. Simple field-aligned acceleration may be difficult to explain this tendency according to the following reason : if more energetic electrons have smaller pitch angles than lower energy ones, as is expected from field-aligned acceleration process, then one would expect that the darker footpoint shows a harder energy spectrum. Since the darker footpoint is expected to have stronger magnetic field convergence than the brighter one (section 7.4.5), lower energy electrons with large pitch angles cannot precipitate into the darker footpoints due to magnetic mirroring, hence hard X-rays from the darker footpoint would have a relatively harder spectrum than the brighter footpoint spectrum.

Two scenarios are plausible, though they do not conflict with each other, to explain the observations. One is to attribute the observed tendency to particle (electron) acceleration process itself and the other is to propagation and hard X-ray emission process of the accelerated

electrons. The former is that energetic electrons are accelerated parpendicular to magnetic field lines, such as in betatron acceleration (*e.g.*, Brown and Hoyng 1975). Brown and Hoyng have studied a large flare on 4 August, 1972. They argued that electrons are accelerated by betatron process due to expanding coronal magnetic loop and have shown that the observed flux – spectral index evolution (Hoyng *et al.* 1976) can well be explained by this process.

It is also interesting to note that from observations of flares with *SMM* GRS in the 0.3–1 MeV range, Vestrand *et al.* (1987) found that events near the limb had, on the average, harder γ-ray energy spectra than those of the disc event with average difference in power-law photon index $\Delta\gamma = 0.37 \pm 0.11$. Calculations have shown that the observed spectral difference can be explained if γ–rays have peak intensities in directions tangential to the photosphere (*i.e.*, nearly parpendicular to magnetic field lines), or if γ–rays have a downwardly beamed Gaussian distribution (Petrosian 1985, Dermer and Ramaty 1986). Also, it was reported that out of a sample of 150 γ-ray events, nearly 40 % have occurred at heliocentric angles θ exceeding $\sin\theta > 0.9$ (Vestrand *et al.* 1987). As continuum γ–rays in this energy range are believed to be produced by Bremsstrahlung of accelerated electrons with ambient ions, these results suggest that accelerated electrons have a certain directivity, which might give support to the above scenario.

The latter scenario for explaining the spectral difference between the two footpoints is as follows. If electrons precipitating downwards to the darker footpoint do not reach deep in the corona, due to strong magnetic field convergence, it is possible that hard X–rays are emitted higher in the corona than those from the brighter footpoint. In such a case, hard X–ray emissions from the darker footpoint region may be a blend of both thick and thin target emissions due to lower plasma density. On the other hand, emission from the brighter footpoint is consisted of nearly pure thick target emission due to dense ambient plasma deep in the corona (figure 7.27). For a power–law energy spectrum of injected electrons, thin target interaction produces a power–law hard X–ray spectrum with softer spectral slope than that produced by thick target interaction (Hudson *et al.* 1978; see also section 2.2.1). Therefore, a blend of both thick and thin target emissions from the darker footpoint will have a softer energy spectrum than the brighter footpoint emission, which is qualitatively consistent with the tendency presented above.

7.4.5 Relation of Footpoint Brightness and Photospheric Magnetic Field

Among seven flares studied here, 6 showed difference in hard X–ray flux S_A and S_B from the double sources in the M2 band during the impulsive phase (table 7.3). Comparison with photospheric magnetic field measurements show that the double sources are located on both sides of the magnetic neutral line, and that one of the pair of double sources located in the weaker magnetic field region tends to be the brighter one in hard X–rays than the one in the stronger magnetic field (4 out of 5 flares show such a tendency), regardless of magnetic polarity. This suggests that magnetic field lines near the footpoint with the weaker photospheric field is less

converged than the lines near the other footpoint just as is suggested in section 7.4.4 (figure 7.27), thus having more electron precipitation due to smaller magnetic mirroring effect and hence more hard X–rays are emitted than the other.

7.5 Summary and Conclusion

I have examined M2 band hard X–ray images of a total of 28 impulsive flares (from October 1991 to December 1992) whose M2 band count rate ≥ 30 cts/s/SC , at the peak time of the M2 band count rates. Hard X–ray sources most frequently (~ 40 %) show double sources which are located on both sides of a magnetic neutral line. This suggests that the double sources are the fundamental structure (*i.e.* footpoints of a flaring loop) of solar flare hard X–ray sources in the non–thermal energy range ($\gtrsim 30$ keV), at least for impulsive flares.

Using seven flares out of the above 28, I studied in detail the following characteristics of the double sources : (1) temporal variation of hard X–ray fluxes from the double sources, (2) energy spectra of the double sources, and (3) location of the double sources with respect to the photospheric magnetic field. The analysis show the followings :

(1) In most cases (6 out of the seven flares), the double sources emit hard X–rays simultaneously, within a fraction of a second. This strongly suggests that hard X–rays are emitted near the footpoints of a single flaring magnetic loop by accelerated electrons, and that accelerated ions (mainly protons) and thermal conduction fronts are not possible candidates for the origin of observed hard X–ray emissions.

(2) The brighter footpoint tends to have a harder energy spectrum than the darker footpoint (5 out of 7). In two cases (10 September, 1992 and 2 November, 1991), spectral hardness of the double sources are about the same although there is a difference in hard X–ray fluxes from the double sources. However, none of the darker source shows a harder spectrum. This result is not expected from simple field–aligned electron acceleration models while it can be explained by the following (a) or (b). (a) If hard X–rays from the darker footpoint are emitted in the corona higher than the brighter footpoint due to a stronger magnetic field convergence (magnetic mirroring), the hard X–rays are expected to be a mixture of both thick and thin target emissions due to lower ambient plasma density. On the other hand, hard X–rays from the brighter footpoint is mostly emitted by the thick target interaction; due to the weaker field convergence, precipitating electrons can reach deep in the corona where the ambient plasma density is high. As the thin target emission produces a softer hard X–ray spectrum than the thick target emission for the same parent electron energy spectrum, X–rays from the brighter footpoint will have a harder spectrum than the darker footpoint. (b) Electrons are accelerated parpendicular to magnetic field lines as in the case of betatron acceleration. If the higher energy electrons have larger pitch angles than the lower energy ones, then the brighter footpoint, which has less field convergence, will have more precipitation of higher energy electrons than the darker

footpoint, hence producing a harder X-ray spectrum.

(3) The brighter footpoint tends to be located in the weaker longitudinal magnetic field region than the darker one (4 out of 5). This suggests that the brighter footpoint has less magnetic field convergence thus having more electron precipitation, hence brighter in hard X-rays than the other footpoint. From these observatoins, we see that magnetic field configuration of the flaring loop in fact plays an essential role in the propagation of accelerated electrons as is suggested in the item (2).

The above summary clearly indicates that detailed studies on non-thermal hard X-ray sources, especially double sources, are the key clues to solve the fundamental characteristics of solar flare hard X-ray emissions, propagation of accelerated electrons, and particle acceleration mechanisms themselves. Subsequent analyses, together with soft X-ray, radio, and optical observations, are expected to give us more fruitful information on such characteristics.

Table 7.1: Hard X-ray images in the M2 band.

No.	Date	Peak time[1] (UT)	GOES/Hα	NOAA	Hα Loc.	HXT counts[2] (cts/s/SC) L	M1	M2	H	Morphology	Remarks
1	91/10/24	22:37:50	M9.8/1N	6981	S12E47	1145	322	73	22	3~4	
2	91/10/27	05:40:27	X6.1/2B	6891	S13E17	2296	2696	2248	1363	3~4	
3	91/11/02	06:45:45	M9.1/1B	6891	S14W62	539	388	251	125	DBL	
4	91/11/09	20:52:13	M1.4/1B	6906	S16W67	93	105	80	54	4	
5	91/11/10	06:48:34	M2.2/2B	6919	S14E56	194	217	151	80	DBL	
6	91/11/10	20:09:25	M7.9/1N	6919	S13E45	386	181	135	98	SGL	
7	91/11/13	21:16:18	M1.3/—	—	—	39	52	38	26	3~4	
8	91/11/15	22:37:50	X1.5/3B	6919	S14W19	1292	731	528	341	DBL	
9	91/11/17	01:57:49U[3]	M1.5/1N	6919	S14W34	134	120	73	37	SGL	
10	91/12/03	16:36:17	X2.2/2B	6952	N17E72	2916	1113	502	233	DBL	
11	91/12/04	17:43:24	M4.1/SN	6952	N17E58	89	70	36	20	DBL	
12	91/12/15	18:32:50	M1.4/—	—	—	162	157	152	137	—	(a)
13	91/12/16	03:13:10	C7.8/1B	6972	S10E69	45	43	36	30	SGL	
14	91/12/16	04:56:07	M2.7/SF	6961	N04W45	300	292	154	57	DBL	
15	91/12/26	10:48:53	M4.6/—	—	—	359	89	59	35	—	(c)
16	91/12/26	21:36:57	M4.2/1B	6985	S15W25	149	140	84	40	SGL	
17	91/12/30	23:06:37	M4.6/2B	6985	S14W34	108	84	48	30	SGL	
18	92/01/26	15:28:39	X1.0/3B	7012	S16W66	765	643	362	141	4~5	
19	92/02/02	11:33:26	C5.5/SN	7042	S11E41	60	74	49	27	DBL	
20	92/02/07	11:54:29	M3.7/2B	7035	S21W53	68	47	35	28	DBL	
21	92/02/14	23:07:38	M7.0/2B	7056	S12E02	1085	918	514	202	3~4	
22	92/02/15	21:29:40	M5.5/1B	7056	S16W13	44	45	33	28	DBL	
23	92/06/25	17:54:03	M1.4/1B	7205	N09W69	199	100	30	15	3~4	
24	92/07/08	09:46:32	X1.2/1B	7220	S12E46	731	455	228	102	4~5	
25	92/07/16	16:55:34	M6.8/2B	7222	S10W63	103	119	91	61	3~4	
26	92/08/11	13:47:47	C7.2/SN	7248	S14W43	66	65	33	20	DBL	
27	92/08/11	22:25:27	M1.4/—	—	—	99	77	34	18	—	(a)
28	92/08/20	09:04:06	M2.9/1B	7260	N17W27	148	94	34	15	SGL	
29	92/09/10	22:52:26	M3.2/2B	7276	N12E41	107	142	138	99	DBL	
30	92/09/11	06:04:51	M1.4/1B	7276	N14E34	69	93	72	51	SGL	
31	92/10/28	10:10:41	C2.6/1F	7321	S24W38	42	55	40	28	SGL	
32	92/10/30	17:30:10B[4]	X1.7/2N	7321	S26W63	223	76	40	28	—	(b), (d)
33	92/11/02	02:59:30B[4]	X9.0/2B	7321	S23W90	5278	624	56	15	—	(a), (d)

(1) Peak time in M2 band count rate.
(2) HXT count rates in the four energy bands at the time of peak count rate in the M2 band.
(3) Peak time is uncertain due to noise in telemetry data.
(4) M2 count rate peaked before the beginning of HXT observation.

(a) Behind-the-limb events (missing emissions from footpoints).
(b) Long duration events (LDEs) with no impulsive behavior in hard X-ray time profiles.
(c) No background data was available.
(d) The impulsive phase (if any) was not observed with HXT.

Table 7.2: Morphological classification of M2 band hard X–ray sources (1991 October – 1992 December)

Threshold	30 cts/s/SC		50 cts/s/SC	
Number of total events :	33		20	
On disk / Not LDE / Images available :	28		17	
M2 images at the peak :				
Double	12	(43 %)	6	(35 %)
Single	8	(28.5 %)	4	(24 %)
Multiple (≥3)	8	(28.5 %)	7	(41 %)

Table 7.3: Summary result of temporal/spectral behavior of the double sources.

Flare	*GOES* X-ray class	Flux ratio $R_{A/B} = S_A/S_B$	Flux simultaneity[c] $\Delta\tau$ (s)	Spectral hardness γ_A	γ_B	B (longitudinal)[f] B_A (G)	B_B (G)
91/11/15	X1.5	~ 1.5	0.0 ± 0.1	2	2.5	$\sim +100$	~ -400
91/12/03	X2.2	~ 1.3	0.0 ± 0.2	3	3.5	~ -80	$\sim +300$
92/02/07	M3.7	~ 1.5	$0.0^{+1.0}_{-0.7}$	2.5[e]	3[e]	~ -30	$\sim +200$
91/12/16	M2.7	~ 0.8[a]	0.0 ± 0.2	3.4	3.8	$\sim +300$	~ -700
92/09/10	M3.2	~ 1.3	0.0 ± 0.3	2.3	2.3	—	—
91/11/10	M2.2	~ 1.0[b]	$0.2^{+0.3}_{-0.5}$	2.5	3	—	—
91/11/02	M9.1	~ 1.5	~ -1.5[d]	3–4	3–4	$\sim +400$	~ -100

(a) $R_{A/B} \sim 1.0$ in the H band.
(b) $R_{A/B} \sim 1.2$ in the H band.
(c) $\Delta\tau > 0$ indicates that emission from source A lags that from source B.
(d) Derived from the difference in peak times between the emissions from the double sources.
(e) Derived from M2/M1 bands cout data pair while H/M2 bands are used for the other flares.
(f) (+) indicates that the corresponding source is located in a positive magnetic polarity region while (−) indicates a negative polarity region.

Figure Captions

Figure 7.1: Examples of hard X-ray double ((a), (b), and (c)), single ((d) and (e)), and multiple (f) sources seen in the M2 band of HXT. All the images have the same image size of $124'' \times 124''$. The contour levels are 9, 18, 25, 35, 50, and 71 % of the maximum brightness for each image. The data averaging time interval is shown at the top of each image.

Figure 7.2: Hard X-ray time profiles (in the four energy bands of HXT) of the (a) 15 November, 1991, (b) 3 December, 1991, (c) 7 February, 1992, (d) 16 December, 1991, (e) 10 September, 1992, (f) 10 November, 1991, and (g) 2 November, 1991 flares. The average counting rates (derived from 0.5 s integration) of the 64 subcollimators of HXT are given.

Figure 7.3: Schematic drawing of the concept of the Gaussian fitting procedure. A set of counts from the 64 detectors are obtained for model brightness distribution (ensamble of two-dimensional circular Gaussian sources). This set of count data is compared with the observed count set and the model map is modified using the liner least-square method. See text for details.

Figure 7.4: Hard X-ray images of the 3 December, 1991 flare in the four energy bands of HXT at the peak of hard X-ray emission at 16:36:17 UT. The contour levels are 13, 18, 25, 35, 50, and 71 % of the maximum brightness for each image. North is up, east is to the left in each image.

Figure 7.5: Overlay of H band hard X-ray sources at 16:36:17 UT (thick solid contours) with a vector magnetogram taken at MSO from 21:35:15 UT to 22:28:35 UT. Thin solid contours represent positive polarity while dashed contours negative polarity. The contour levels for the longitudinal magnetic field strength are $\pm$ 50, 100, 200, 400, 800, 1600, and 3200 G for positive (+) and negative (−) polarity, respectively. Short straight lines indicate transverse magnetic field strength.

Figure 7.6: (a) Time variation of hard X-ray flux from the double sources from 16:36:00 UT to 16:36:44 UT in the M2 band obtained by the Gaussian fitting procedure. Time resolution of the plot is 1 s. Thin solid line denotes spatially-integrated incident hard X-ray flux. Thick solid line and dashed line denote fluxes from source A and B in figure 7.4, respectively. Dotted line is the sum of source A and B fluxes. Error bars in the figure indicate 1σ level. (b) Correlation between hard X-ray fluxes from sources A and B. Error bars indicate 1σ level.

Figure 7.7: Temporal variation of spectral hardness (H/M2 band) of each of the double sources with time resolution of 1 s from 16:36:00 UT to 16:36:44 UT. Solid line denotes the hardness for source A while dashed line is for source B.

Figure 7.8: Temporal variation of hard X-ray flux from the double sources in the 3 December, 1991 flare in the M2 band with different w_i in eq.(7.1). Solid lines denote flux obtained by the Gaussian fitting with $w_i = 1.0$ while dashed lines $w_i = 1.5$. The solid and dashed lines match well with each other (see text for details).

Figure 7.9: Hard X-ray image of the 7 February, 1992 flare in the M2 band at the peak of spike P2 (see text). The data averaging time interval is 11:54:21 UT - 11:54:27 UT. The contour levels are 13, 18, 25, 35, 50, and 71 % of the maximum brightness. Size of the image is $124'' \times 124''$

Figure 7.10: Overlay of M2 band hard X-ray sources at the peak of spike P2 (thick solid contours) and a vector magnetogram taken at OAO from 2:38:56 UT - 4:25:20 UT. Thin solid contours represent positive polarity while dashed contours negative polarity. The contour levels for the longitudinal magnetic field strength are $\pm$ 18, 36, 91, 182, 370, and 1030 G for positive (+) and negative (−) polarity, respectively. Transverse magnetic field strength is not shown in the figure.

Figure 7.11: (a) Time variation of hard X-ray flux from the double sources between 11:54:03 UT and 11:54:45 UT in the M2 band. Each data point corresponds to a 2 s data accumulation. Thick solid line is for source A in figure 7.9 while dashed line is for source B. Thin solid line and dotted line have the same meaning as in figure 7.6. Error bars in the figure indicate 1σ level. (b) Correlation between hard X-ray fluxes from sources A and B. Again error bars indicate 1σ level.

Figure 7.12: Temporal variation of spectral hardness (M2/M1 band) of each of the double sources with temporal resolution of 2 s from 11:54:03 UT to 11:54:45 UT. Solid line denotes source A while dashed line source B.

Figure 7.13: Hard X-ray images of the 16 December, 1991 flare in the M2 and H bands (left and right, respectively) around the peak of the impulsive burst. The contour levels are the same as in figure 7.9 with an additional 9 % level. Data integration time intervals are 4:56:08 UT - 4:56:12 UT and 4:56:10 UT - 4:56:14 UT for M2 and H band images, respectively. Both images have the same image size of $124'' \times 124''$.

Figure 7.14: Overlay of hard X-ray double sources in the M2 band (thick solid contours in the right hand side of the figure) and a vector magnetogram taken at OAO from 2:50:04 UT to 4:04:59 UT (after Culhane *et al.* 1994). The contour levels for the magnetogram is the same as in figure 7.10.

Figure 7.15: (a) Time variation of hard X-ray flux from the double sources of the 16 December, 1991 flare from 4:56:02 UT to 4:56:17 UT in the M2 band, with temporal resolution of 1 s. Thick solid line is for source A in figure 7.13 while dashed line is for source B. Thin solid line and dotted lines have the same meaning as in figure 7.6. Error bars in the figure indicate 1σ level. (b) Correlation between hard X-ray fluxes from sources A and B. Error bars indicate 1σ level.

Figure 7.16: Energy spectral hardness of the double sources derived by taking count ratio between the M2 and H band. Solid line corresponds to source A while dashed line to source B in figure 7.13.

Figure 7.17: A hard X-ray image (in the M2 band) of the 10 September, 1992 flare near the peak time of hard X-ray emission. The data averaging time interval is 22:52:29 UT – 22:52:31 UT. The contour levels are the same as in figure 7.13. Size of the image is $124'' \times 124''$.

Figure 7.18: (a) Time variation of hard X-ray flux from the double sources seen in the 10 September, 1992 flare from 22:52:13 UT to 22:52:35 UT in the M2 band with temporal resolution of 1 s. Thick solid line is for source A in figure 7.17 while dashed line is for source B. Thin solid line and dotted line have the same meaning as in figure 7.6. Error bars in the figure indicate 1σ level. (b) Correlation between hard X-ray fluxes from sources A and B. Error bars indicate 1σ level.

Figure 7.19: Temporal variation of spectral hardness (H/M2 band) of each of the double sources with temporal resolution of 1 s from 22:52:13 UT to 22:52:35 UT. Solid line denotes the hardness for source A while dashed line is for source B.

Figure 7.20: Hard X-ray images of the 10 November, 1991 flare in the M2 band. *Left* : 6:48:31 UT – 6:48:32 UT. We see additional two sources each of which located near either of bright double sources denoted as A and B. *Right* : 6:48:34 UT – 6:48:35 UT (at the peak of hard X-ray emission), when we see that bulk of the hard X-ray emission originates from the double sources. The contour levels are the same as in figure 7.13. Size of the image is $124'' \times 124''$.

Figure 7.21: (a) Temporal variation of hard X-ray flux from the double sources in the M2 band from 6:48:25 UT to 6:48:39 UT. Each data point corresponds to a 1 s data accumulation. Thick solid line is for source A in figure 7.20 while dashed line is for source B. Thin solid line and dotted line have the same meaning as in figure 7.6. Error bars in the figure indicate 1σ level. (b) Correlation between hard X-ray fluxes from sources A and B. Again error bars indicate 1σ level.

Figure 7.22: Temporal variation of spectral hardness (H/M2 band) of each of the double sources with temporal resolution of 1 s from 6:48:25 UT to 6:48:39 UT. Solid line denotes source A while dashed line source B.

Figure 7.23: Hard X-ray double sources (in the M2 band) seen in the impulsive phase of the 2 November, 1991 flare. These double sources are seen in all of the four energy bands of HXT. The contour levels are the same as in figure 7.13. Size of the image is $124'' \times 124''$.

Figure 7.24: (a) Hard X-ray flux time profile for the double sources from 6:45:20.5 UT to 6:46:18.5 UT in the M2 band. Thick solid line corresponds to source A while dashed line to source B. Thin solid line and dotted line have the same meaning as in figure 7.6. Error bars indicate 1σ level. (b) Cross-correlation of hard X-ray time profiles of the double sources. Each error bar indicate 1σ level. The figure shows that the correlation of hard X-ray emission from the double sources is not very good. This is due to significant individual behavior in emission from source A as is shown in (a).

Figure 7.25: Temporal variation of spectral hardness (H/M2 band) of each of the double sources with temporal resolution of 0.5 s from 6:45:20.5 UT to 6:46:18.5 UT. Solid line corresponds to source A while dashed line to source B.

Figure 7.26: Possible configuration of magnetic loops for explaining individual behavior in hard X-ray emission from double sources.

Figure 7.27: Schematic drawing of a flaring magnetic loop which has asymmetric geometry at the footpoints due to difference in photospheric magnetic field strength.

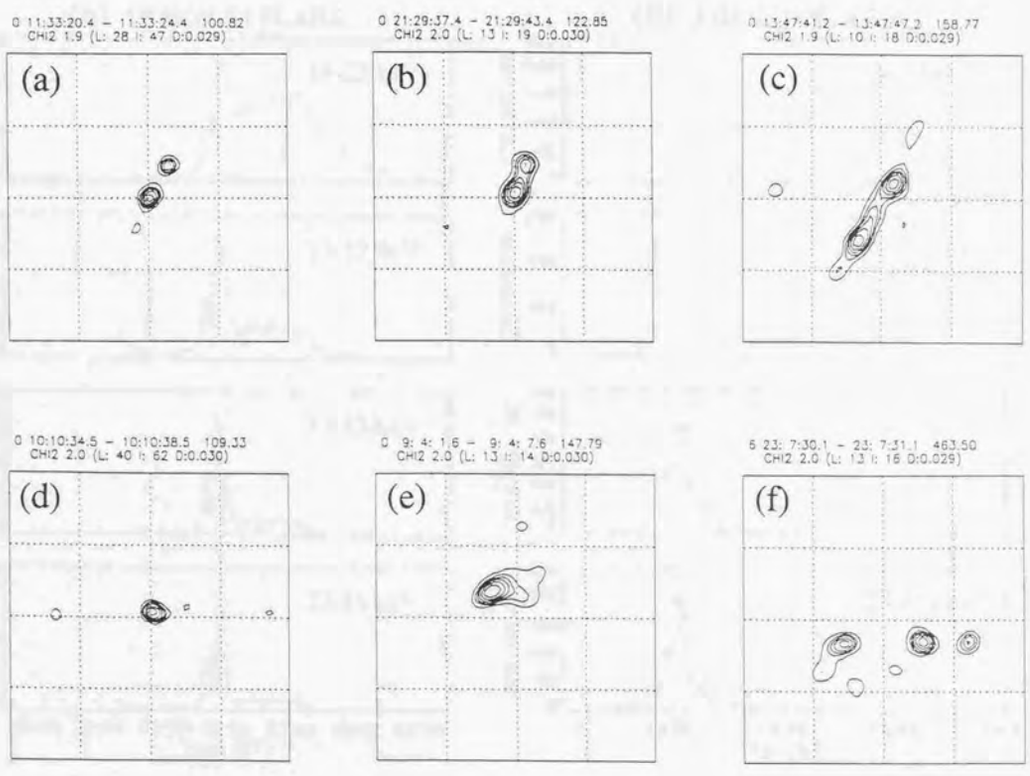
0 11:33:20.4 – 11:33:24.4 100.82
CHI2 1.9 (L: 28 I: 47 D:0.029)
(a)
0 21:29:37.4 – 21:29:43.4 122.85
CHI2 2.0 (L: 13 I: 19 D:0.030)
(b)
0 13:47:41.2 – 13:47:47.2 158.77
CHI2 1.9 (L: 10 I: 18 D:0.029)
(c)
0 10:10:34.5 – 10:10:38.5 109.33
CHI2 2.0 (L: 40 I: 62 D:0.030)
(d)
0 9: 4: 1.6 – 9: 4: 7.6 147.79
CHI2 2.0 (L: 13 I: 14 D:0.030)
(e)
6 23: 7:30.1 – 23: 7:31.1 463.50
CHI2 2.0 (L: 13 I: 16 D:0.029)
(f)

Figure 7.1

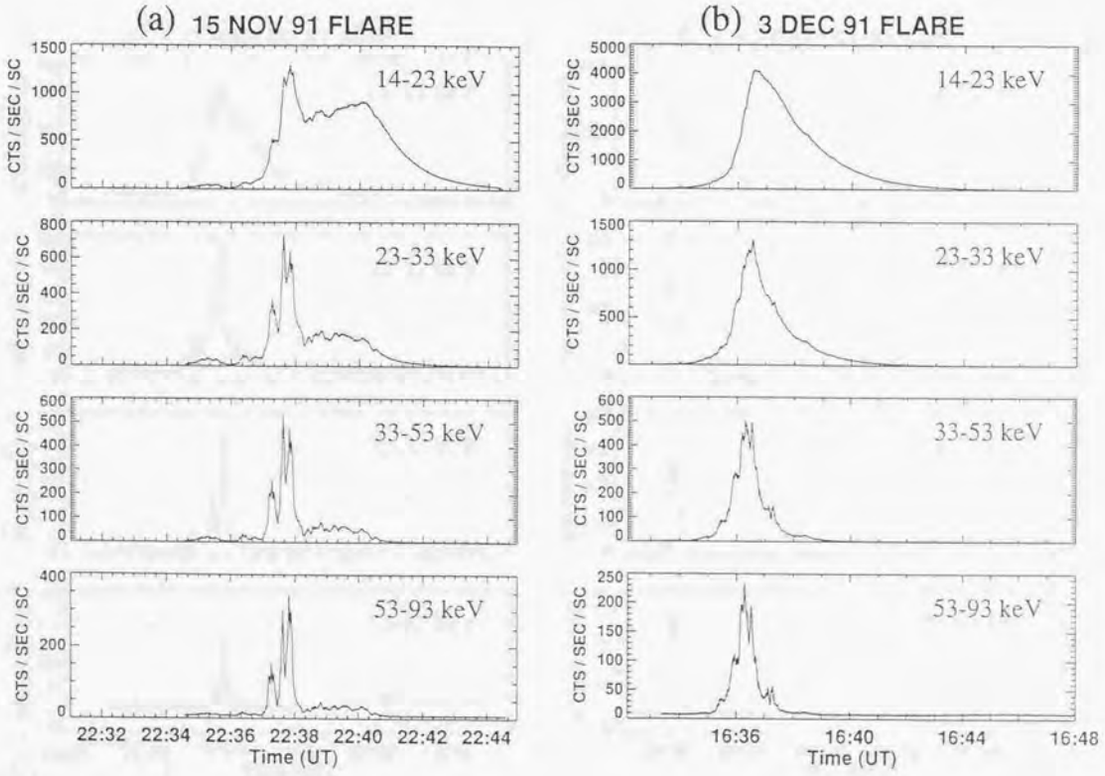
(a) 15 NOV 91 FLARE
(b) 3 DEC 91 FLARE
CTS / SEC / SC
14-23 keV
23-33 keV
33-53 keV
53-93 keV
22:32 22:34 22:36 22:38 22:40 22:42 22:44
16:36 16:40 16:44 16:48
Time (UT)

Figure 7.2

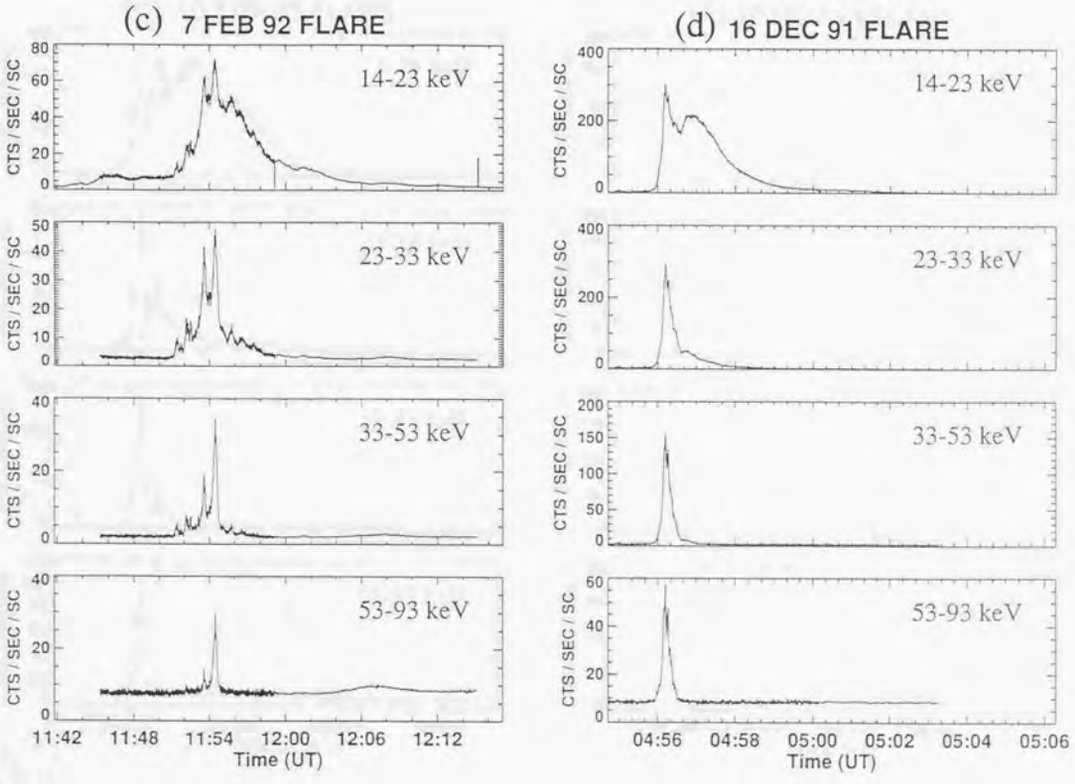

Figure 7.2 (*continued*)

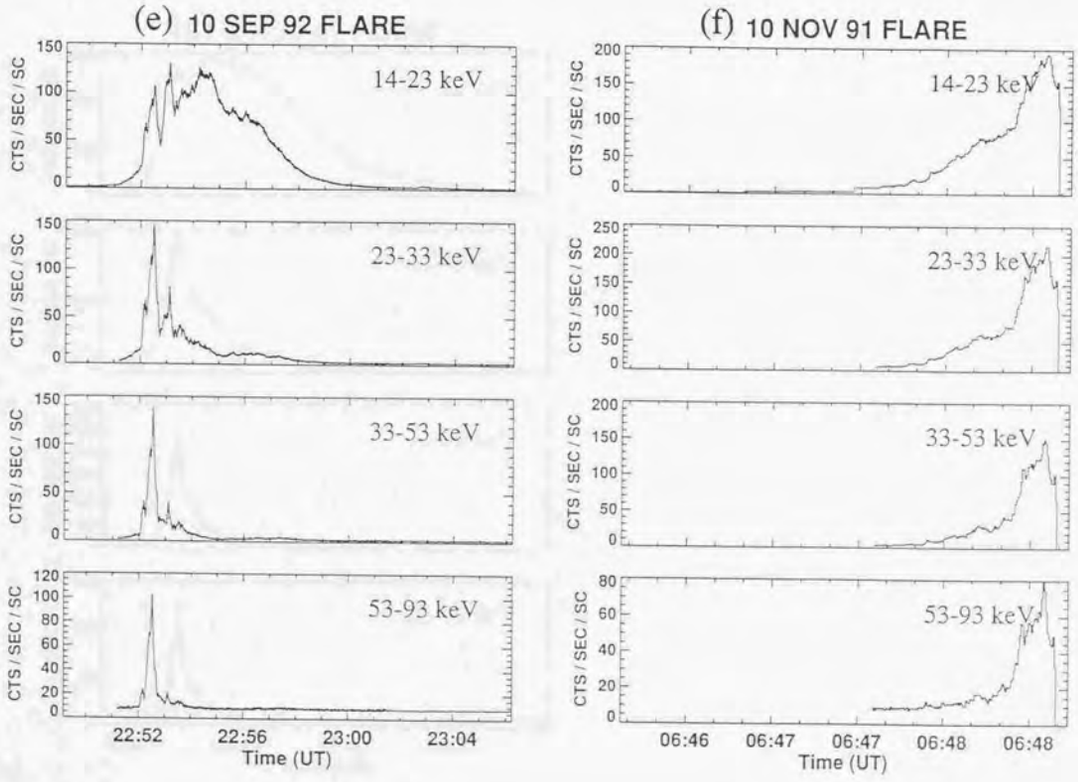

Figure 7.2 (*continued*)

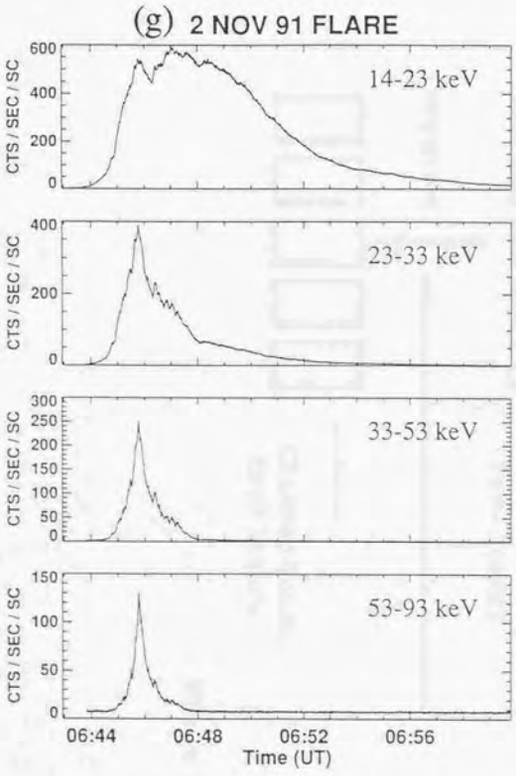

Figure 7.2 (*continued*)

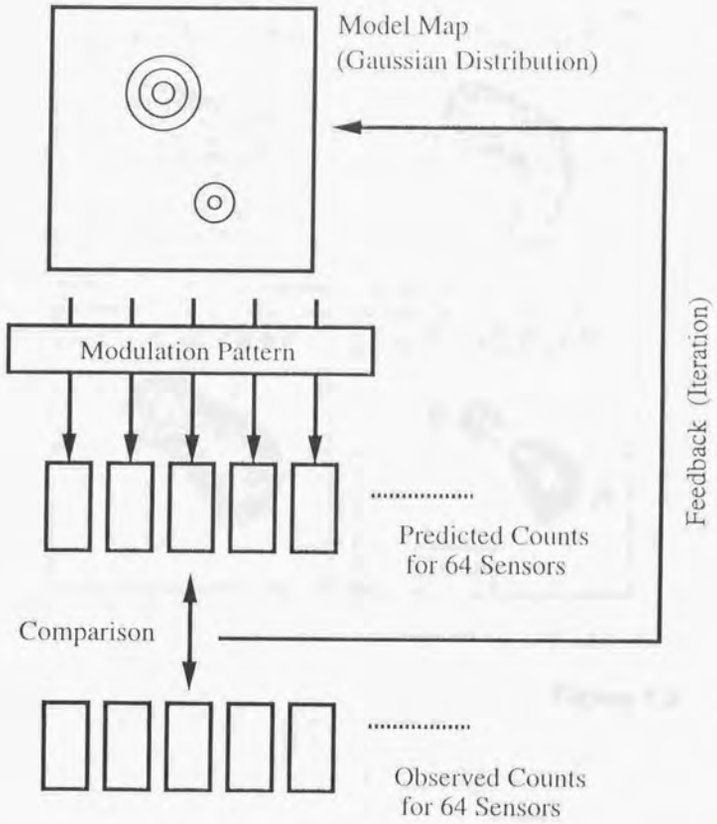
Model Map
(Gaussian Distribution)
Modulation Pattern
Predicted Counts
for 64 Sensors
Feedback (Iteration)
Comparison
Observed Counts
for 64 Sensors

Figure 7.3

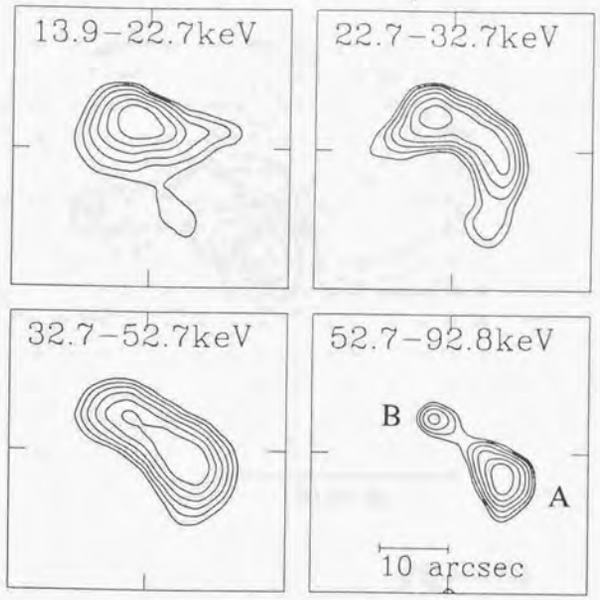
HXT Images of 3-Dec-1991 X2.2 Flare
(16:36:17 UT)
13.9-22.7keV
22.7-32.7keV
32.7-52.7keV
52.7-92.8keV
B
A
10 arcsec

Figure 7.4

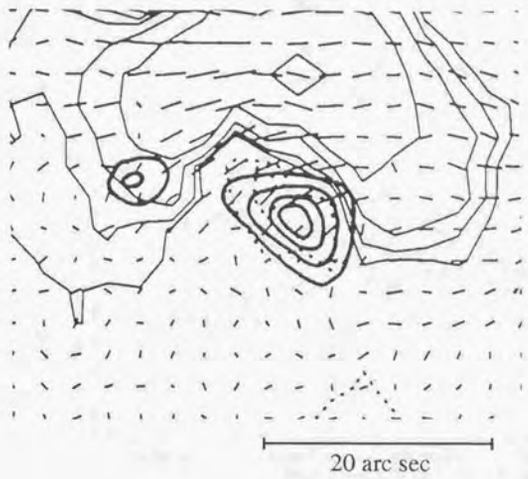

Figure 7.5

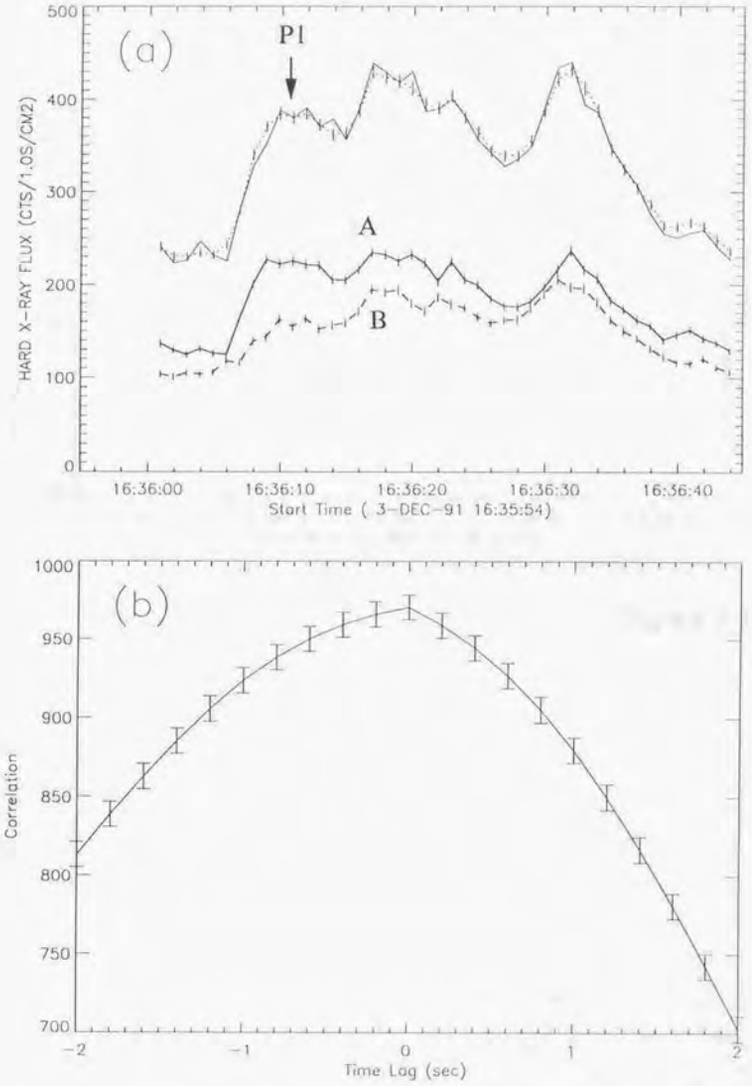
(a)
PI
A
B
HARD X-RAY FLUX (CTS/1.0S/CM2)
500
400
300
200
100
0
16:36:00
16:36:10
16:36:20
16:36:30
16:36:40
Start Time (3-DEC-91 16:35:54)
(b)
Correlation
1000
950
900
850
800
750
700
−2
−1
0
1
2
Time Lag (sec)

Figure 7.6

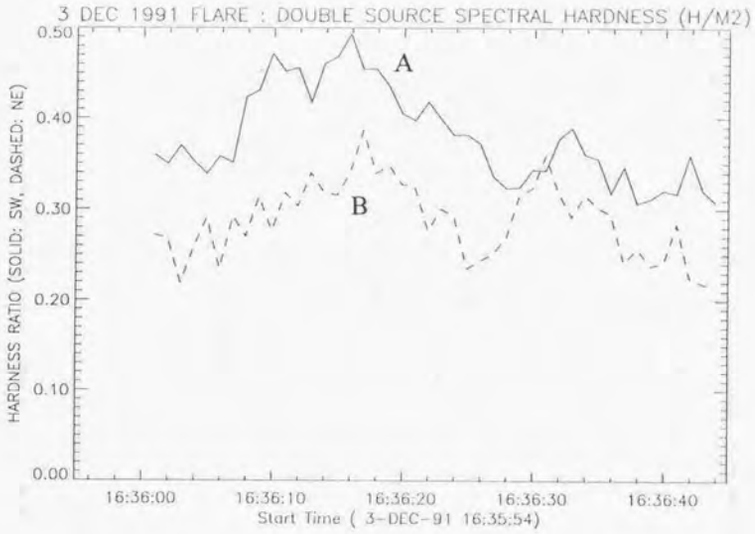
3 DEC 1991 FLARE : DOUBLE SOURCE SPECTRAL HARDNESS (H/M2)
HARDNESS RATIO (SOLID: SW, DASHED: NE)
0.50
0.40
0.30
0.20
0.10
0.00
A
B
16:36:00
16:36:10
16:36:20
16:36:30
16:36:40
Start Time (3-DEC-91 16:35:54)

Figure 7.7

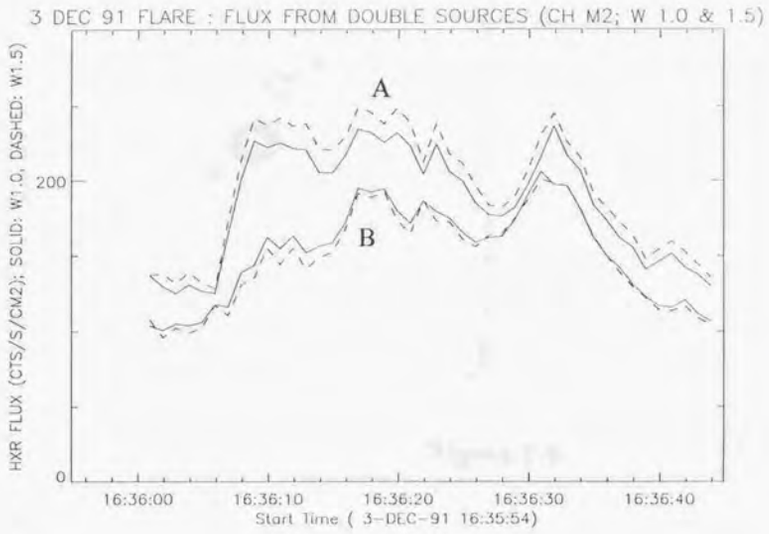
3 DEC 91 FLARE : FLUX FROM DOUBLE SOURCES (CH M2; W 1.0 & 1.5)
HXR FLUX (CTS/S/CM2); SOLID: W1.0, DASHED: W1.5)
200
0
A
B
16:36:00
16:36:10
16:36:20
16:36:30
16:36:40
Start Time (3-DEC-91 16:35:54)

Figure 7.8

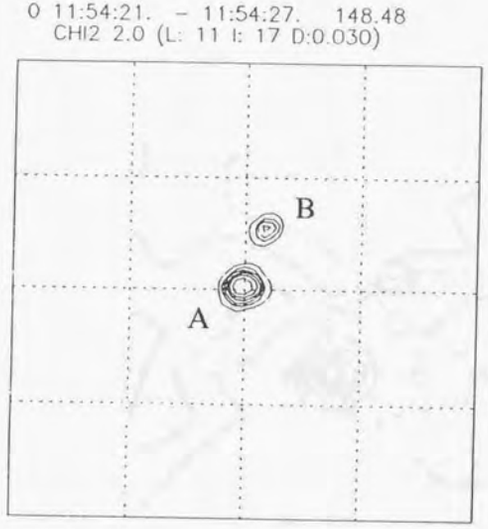

Figure 7.9

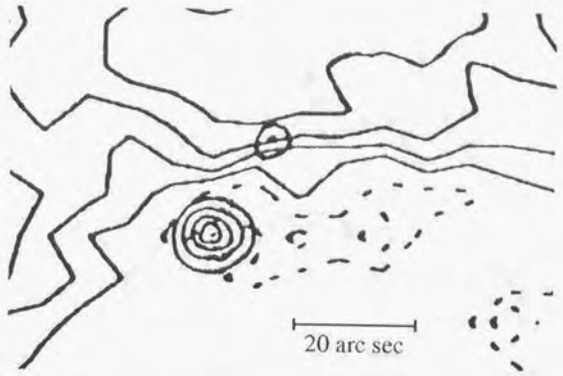

Figure 7.10

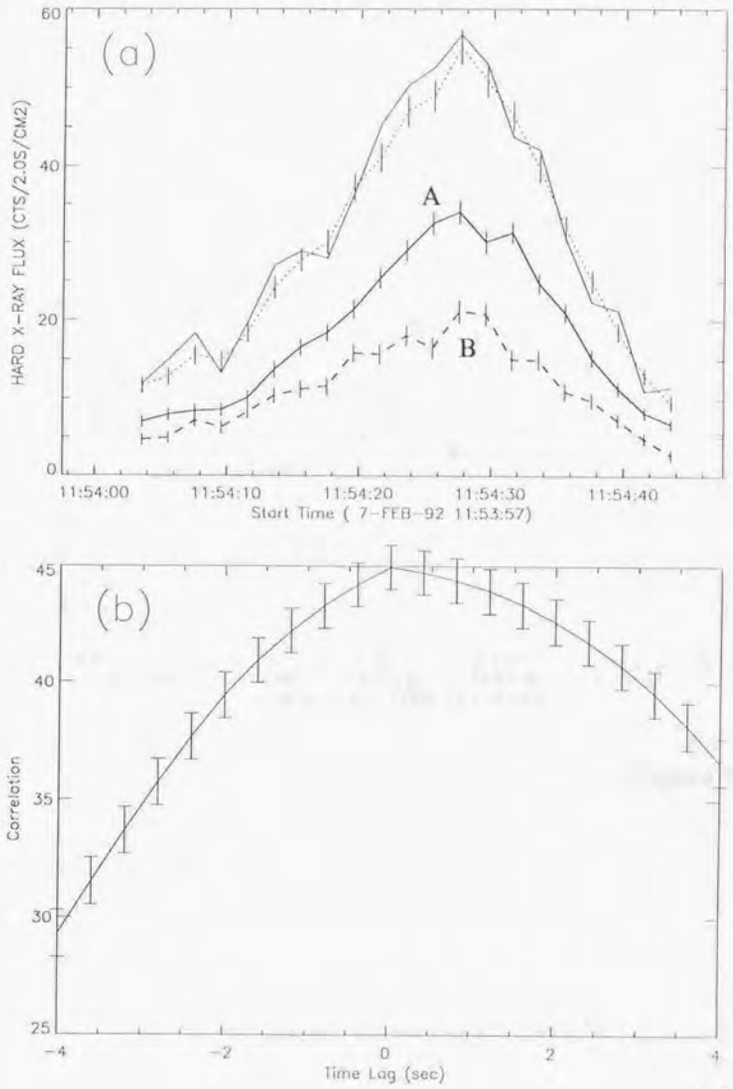
(a)
HARD X-RAY FLUX (CTS/2.0S/CM2)
60
40
20
0
A
B
11:54:00
11:54:10
11:54:20
11:54:30
11:54:40
Start Time (7-FEB-92 11:53:57)
(b)
Correlation
45
40
35
30
25
-4
-2
0
2
4
Time Lag (sec)

Figure 7.11

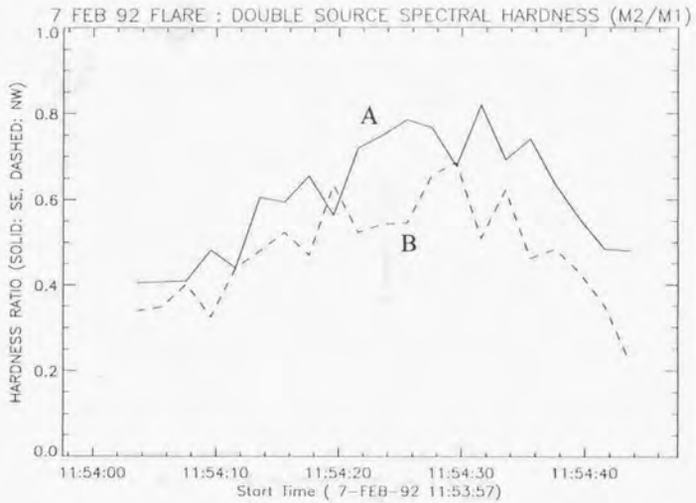
7 FEB 92 FLARE : DOUBLE SOURCE SPECTRAL HARDNESS (M2/M1)
HARDNESS RATIO (SOLID: SE, DASHED: NW)
1.0
0.8
0.6
0.4
0.2
0.0
A
B
11:54:00
11:54:10
11:54:20
11:54:30
11:54:40
Start Time (7-FEB-92 11:53:57)

Figure 7.12

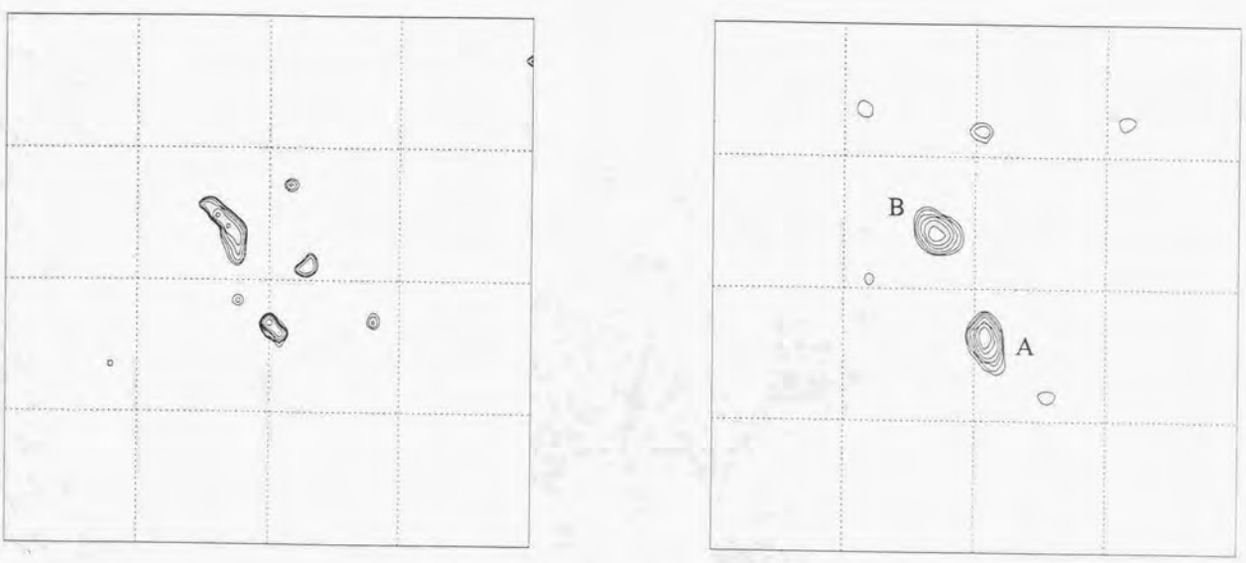

Figure 7.13

Figure 7.14

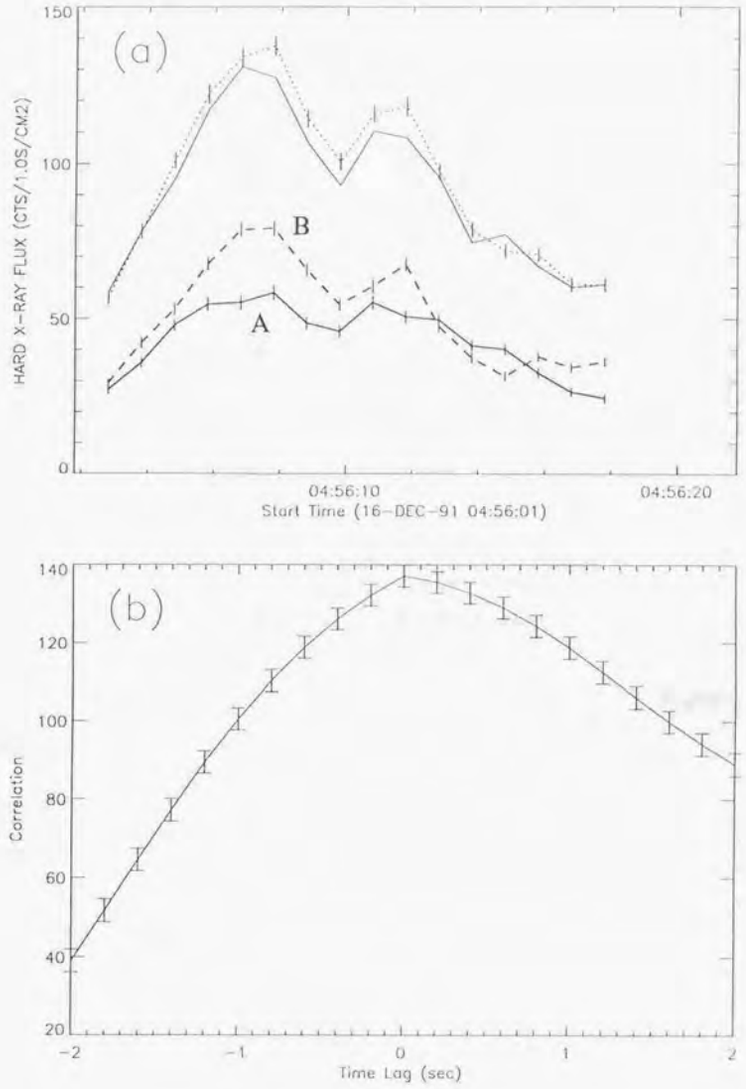
(a)
HARD X-RAY FLUX (CTS/1.0S/CM2)
150
100
50
0
B
A
04:56:10
04:56:20
Start Time (16-DEC-91 04:56:01)
(b)
Correlation
140
120
100
80
60
40
20
-2
-1
0
1
2
Time Lag (sec)

Figure 7.15

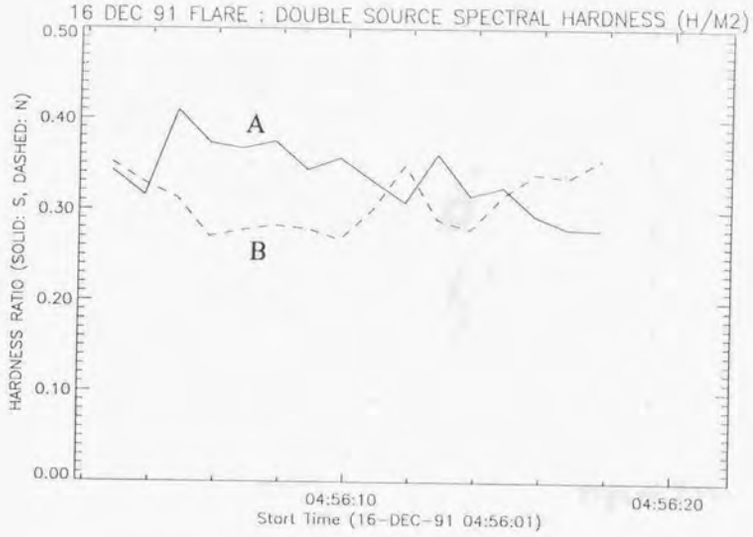
16 DEC 91 FLARE : DOUBLE SOURCE SPECTRAL HARDNESS (H/M2)
HARDNESS RATIO (SOLID: S, DASHED: N)
0.50
0.40
0.30
0.20
0.10
0.00
A
B
04:56:10
04:56:20
Start Time (16-DEC-91 04:56:01)

Figure 7.16

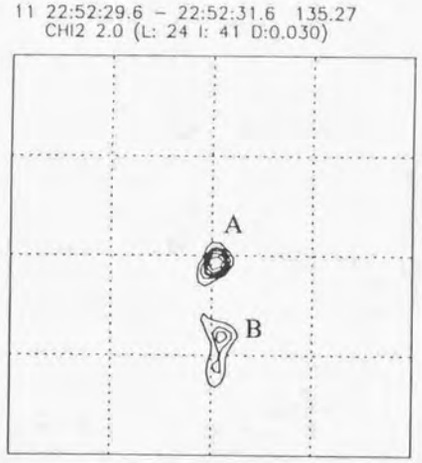

Figure 7.17

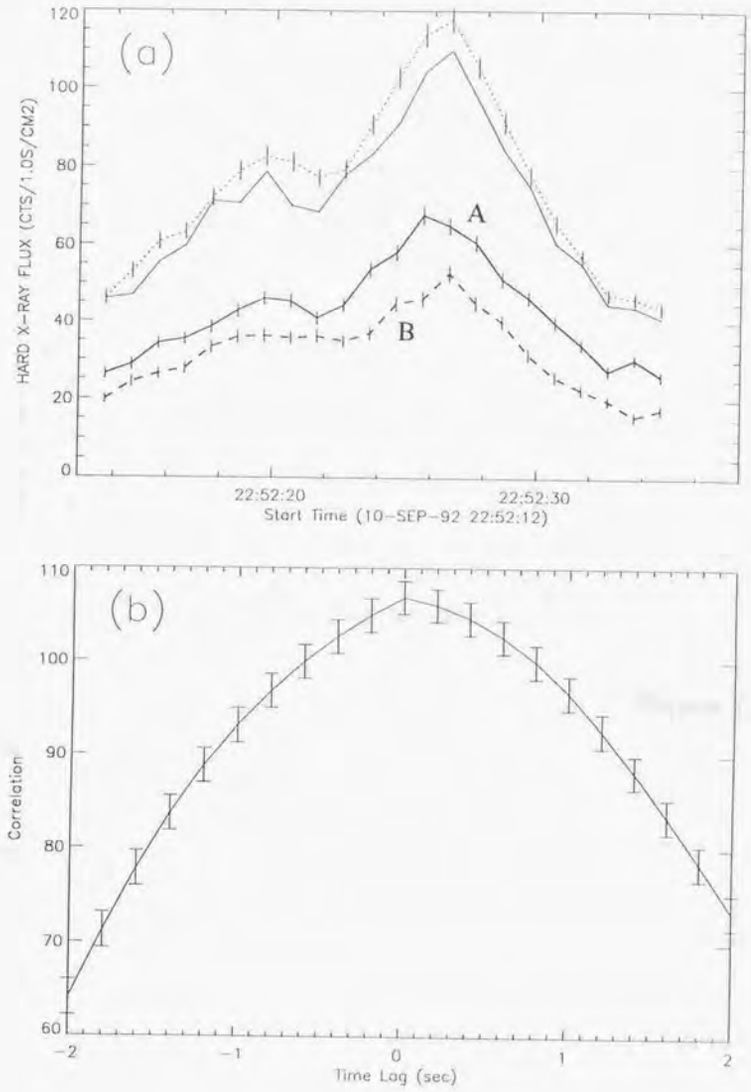
(a)
HARD X-RAY FLUX (CTS/1.0S/CM2)
120
100
80
60
40
20
0
A
B
22:52:20
22:52:30
Start Time (10-SEP-92 22:52:12)
(b)
Correlation
110
100
90
80
70
60
-2
-1
0
1
2
Time Lag (sec)

Figure 7.18

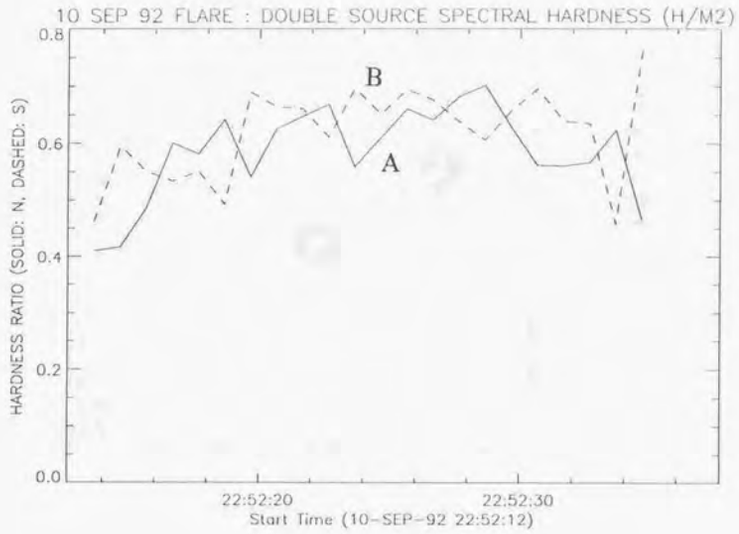
10 SEP 92 FLARE : DOUBLE SOURCE SPECTRAL HARDNESS (H/M2)
HARDNESS RATIO (SOLID: N, DASHED: S)
0.8
0.6
0.4
0.2
0.0
B
A
22:52:20
22:52:30
Start Time (10-SEP-92 22:52:12)

Figure 7.19

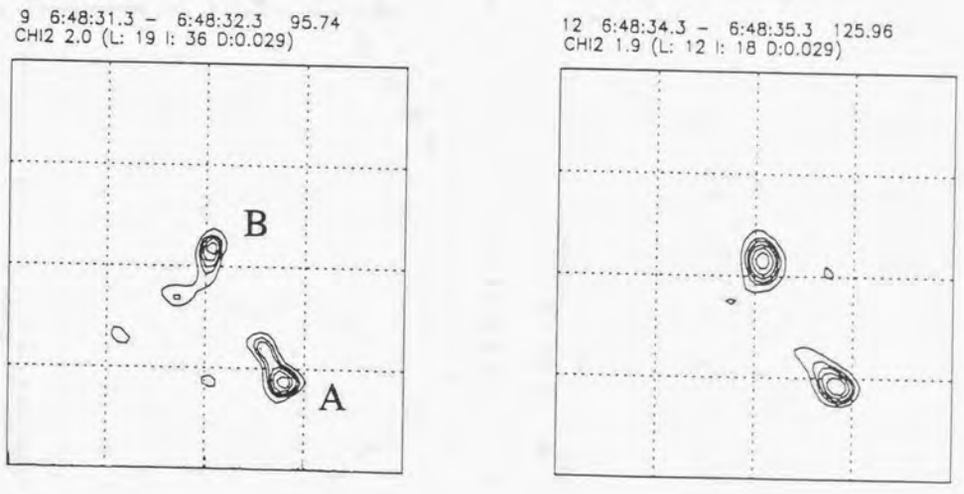
9 6:48:31.3 – 6:48:32.3 95.74
CHI2 2.0 (L: 19 I: 36 D:0.029)
B
A
12 6:48:34.3 – 6:48:35.3 125.96
CHI2 1.9 (L: 12 I: 18 D:0.029)

Figure 7.20

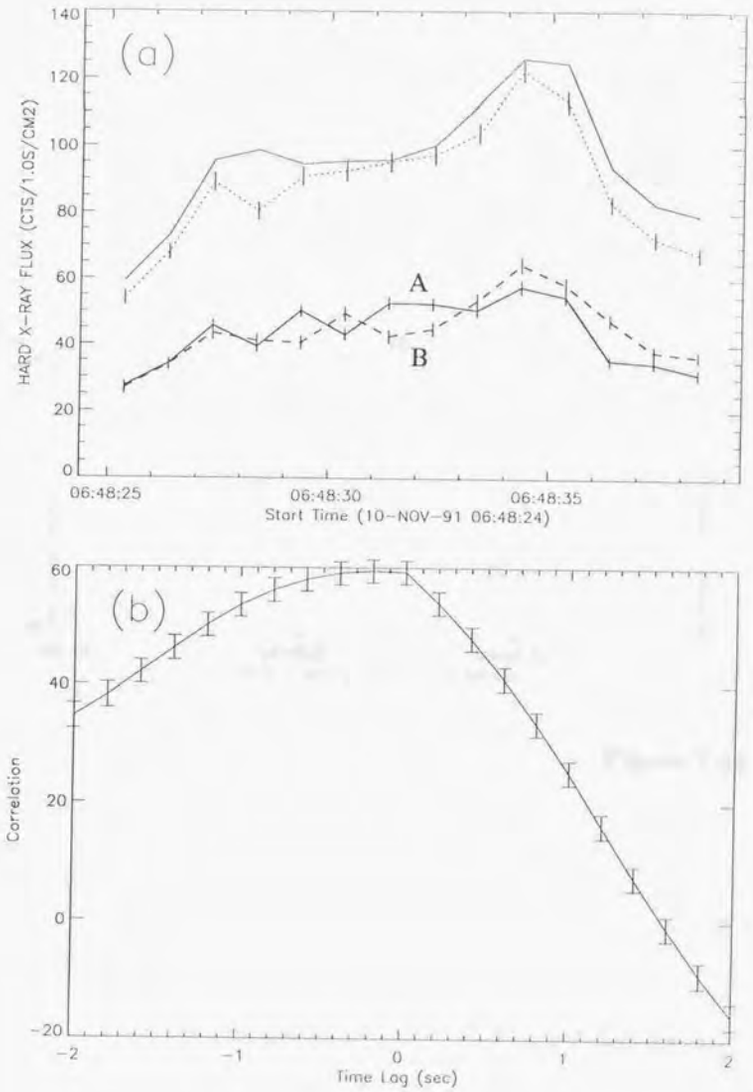
(a)
HARD X-RAY FLUX (CTS/1.0S/CM2)
140
120
100
80
60
40
20
0
A
B
06:48:25
06:48:30
06:48:35
Start Time (10-NOV-91 06:48:24)
(b)
Correlation
60
40
20
0
-20
-2
-1
0
1
2
Time Lag (sec)

Figure 7.21

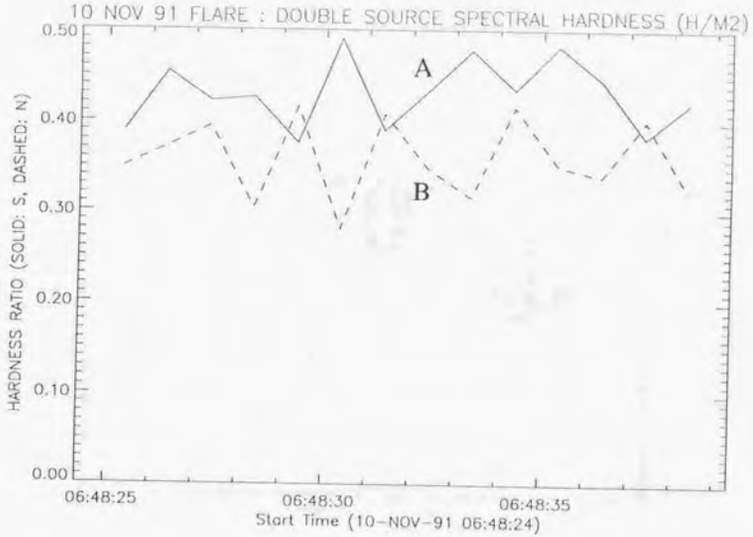
10 NOV 91 FLARE : DOUBLE SOURCE SPECTRAL HARDNESS (H/M2)
HARDNESS RATIO (SOLID: S, DASHED: N)
0.50
0.40
0.30
0.20
0.10
0.00
A
B
06:48:25
06:48:30
06:48:35
Start Time (10-NOV-91 06:48:24)

Figure 7.22

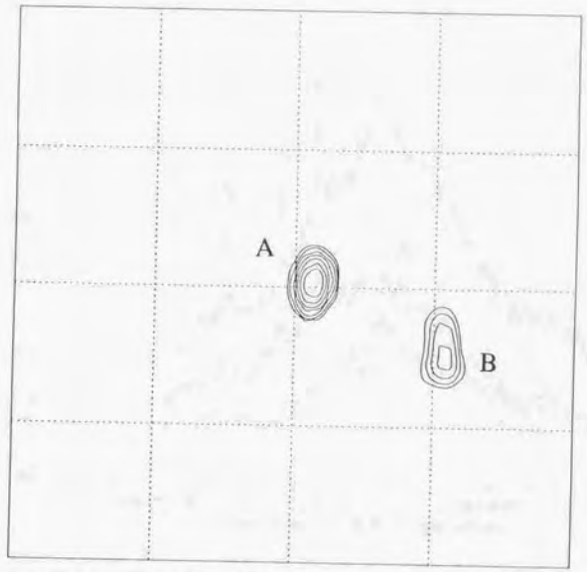

Figure 7.23

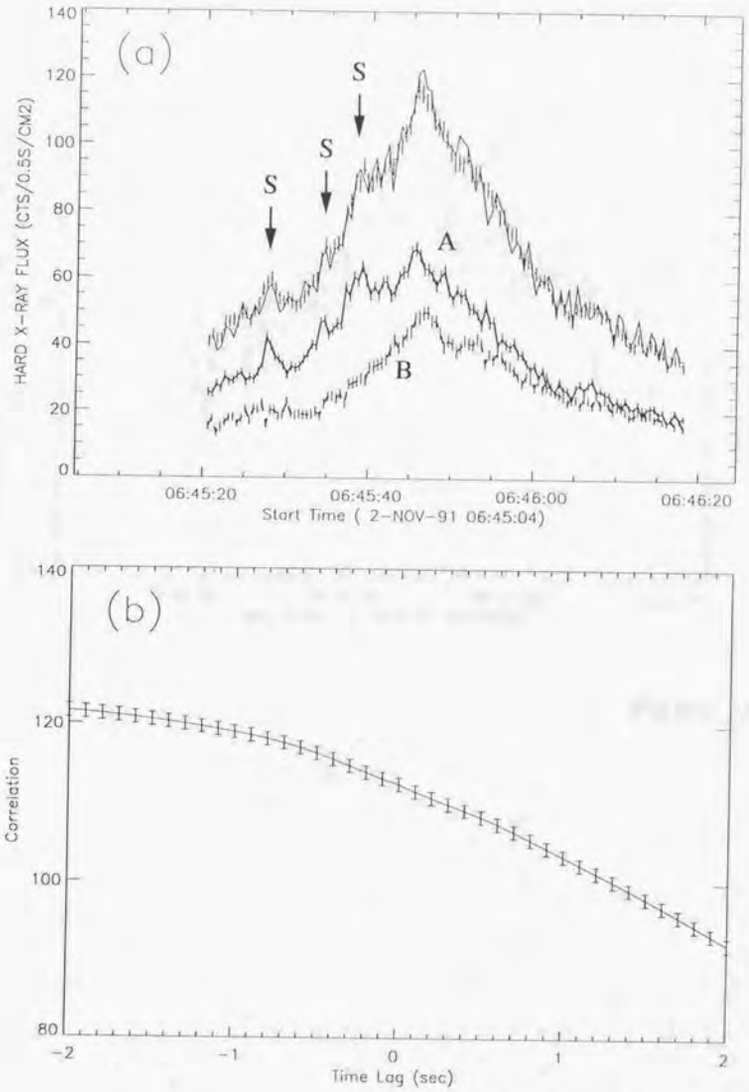
(a)
S
S
S
A
B
HARD X-RAY FLUX (CTS/0.5S/CM2)
140
120
100
80
60
40
20
0
06:45:20
06:45:40
06:46:00
06:46:20
Start Time (2-NOV-91 06:45:04)
(b)
Correlation
140
120
100
80
-2
-1
0
1
2
Time Lag (sec)

Figure 7.24

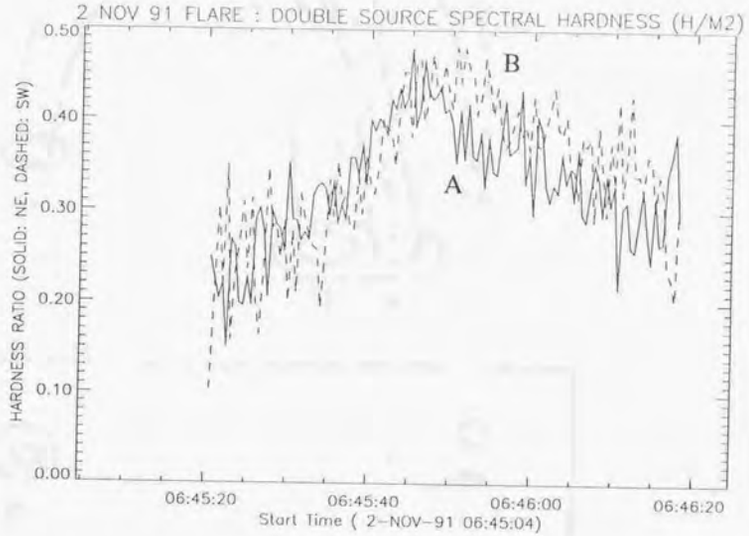
2 NOV 91 FLARE : DOUBLE SOURCE SPECTRAL HARDNESS (H/M2)
HARDNESS RATIO (SOLID: NE, DASHED: SW)
0.50
0.40
0.30
0.20
0.10
0.00
A
B
06:45:20
06:45:40
06:46:00
06:46:20
Start Time (2-NOV-91 06:45:04)

Figure 7.25

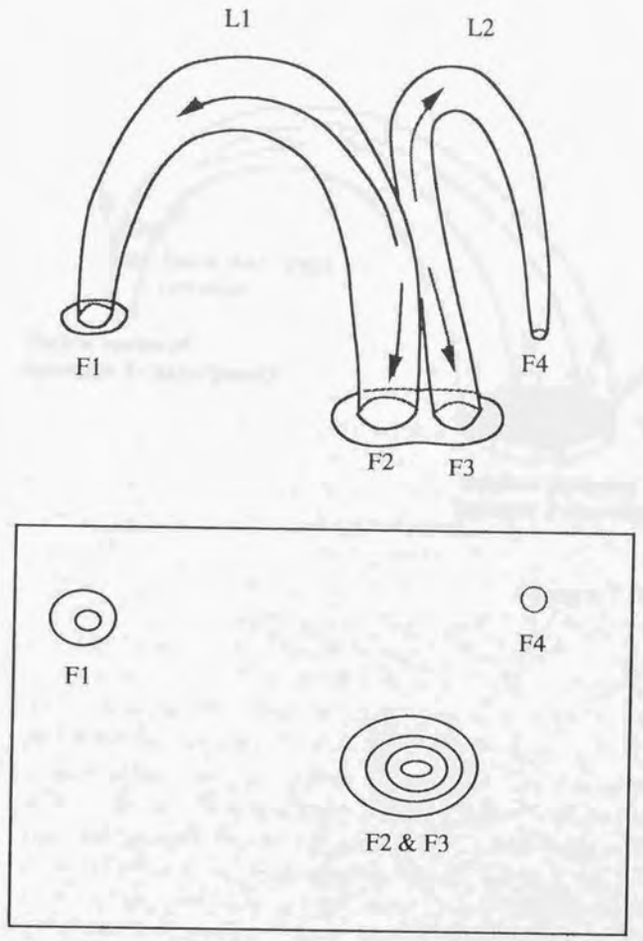

Figure 7.26

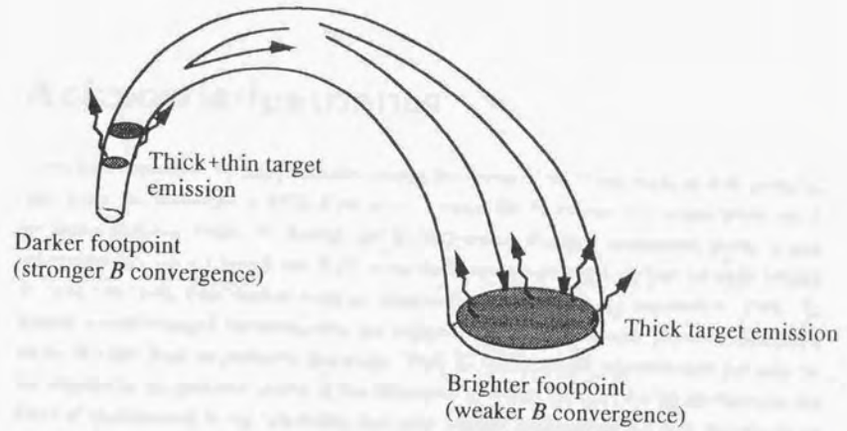
Thick+thin target
emission
Darker footpoint
(stronger B convergence)
Thick target emission
Brighter footpoint
(weaker B convergence)

Figure 7.27

Acknowledgements

I have been supported by many scientists during the course of my thesis work, as well as during fabrication and operation of HXT. First of all, I would like to express my largest gratitude to my thesis advisors, Profs. T. Kosugi and K. Makishima, for their continuous guidance and encouragement since I joined the HXT experiment seven years ago. Their attitude toward deriving the truth from various complex observational facts was very impressive. Prof. T. Kosugi is acknowledged for stimulating and enjoyable discussions on solar physics. I learned a lot on this field from his profound knowledge. Prof. K. Makishima is acknowledged not only for his support in my graduate course at the University of Tokyo but also for his guidance to the fields of experimental X–ray astronomy and solar physics; he provided me with the chance to join the HXT experiment. Also I learned a lot from his way of overcoming difficulties which we had met in the HXT experiments before the launch.

I also would like to express my hearty thanks to Dr. T. Murakami, with whom I carried out various pre–launch experiments at the Institute of Space and Astronautical Science (ISAS). His knowledge and skillness in experimental work was indispensable for the successful operation of HXT. Prof. Y. Ogawara is sincerely acknowledged for his continuous support not only in the HXT experiment, but also in the whole *Yohkoh* mission.

Essential contribution to the HXT experiment and data analyses by Messrs M. Sawa, S. Masuda, Ms. M. Inda–Koide, Mr. K. Yaji, and Prof. T. Takakura, as well as continuous support and encouragement from Profs. H. Nakajima, K. Shibasaki and the late Prof. K. Kai are greatly acknowledged. Thanks are due to Drs. T. Dotani, T. Kii, T. Ohashi, T. Tsuru, M. Ishida, and T. Takeshima for useful discussions as well as valuable supports at the University of Tokyo and at ISAS. Prof. T. Sakurai is acknowledged for kindly providing me magnetogram data taken at Okayama Astrophysical Observatory.

An international collabolation with several foreign institutes played an essential role in the analyses of HXT data. I would like to express my sincere thanks to Profs. L.W. Acton, R.C. Canfield, and Drs. H.S. Hudson, J.–P. Wülser, and T.R. Metcalf for their valuable suggestions and contributions to my data analyses; especially Dr. J.–P. Wülser is greatly acknowledged for his excellent contribution in co–aligning HXT images with SXT images.

The HXT experiment is a joint product of both scientists and engineers. Messrs K. Taguchi, K. Tanimoto, S. Kobayashi, and T. Ishizuka of Meisei Electric Co., Ltd. are acknowledged for their design and fabrication of the HXT electronics and detector assembly; Messrs T. Noguchi

and Y. Kakitsubo of Nihon Hikoki Co., Ltd. for fabrication of the HXT collimator body. Engineers of Dai-Nihon Insatsu Co., Ltd. and Toray Precision Co., Ltd. are also greatly acknowledged for their fabricating HXT grids, and Hamamatsu Photonics Co., Ltd. for preparing the photomultiplier tubes.

The operation of *Yohkoh* satellite is supported by many scientists and engineers including foreign facilities. It is my pleasure to express my thanks to Messrs T. Kato and K. Shuto of ISAS, and the staff of NASA's Deep Space Network stations (Madrid, Canberra, and Goldstone) for managing downlink, transfer, and archival of *Yohkoh* data.

Last of all, I would like to express my sincere appreciation to all those who have supported, and are supporting the *Yohkoh* mission. I hope that HXT will output much more fruitful scientific results in understanding high-energy aspects of solar flares in the near future.

References

Acton, L.W. 1968 : *Astrophys. J.*, **152**, 305.

Acton, L.W., Culhane, J.L., Gabriel, A.H., Bentley, R.D., Bowles, J.A., Firth, J.G., Finch, M.L., Gilbreth, C.W., Guttridge, P., Hayes, R.W., Joki, E.G., Jones, B.B., Kent, B.J., Leibacher, J.W., Nobles, R.A., Patrick, T.J., Phillips, K.J.H., Rapley, C.G., Sheather, P.H., Sherman, J.C., Stark, J.P., Springer, L.A., Turner, R.F., and Wolfson, C.J. 1980 : *Solar Phys.*, **65**, 53.

Antonucci, E., Gabriel, A.H., Acton, L.W., Culhane, J.L., Doyle, J.G., Leibacher, J.W., Machado, M.E., Orwig, L.E., and Rapley, C.G. 1982 : *Solar Phys.*, **78**, 107.

Antonucci, E., Gabriel, A.H., and Dennis, B.R. 1984 : *Astrophys. J.*, **287**, 917.

Arnoldy, R.L., Kane, S.R., and Winckler, J.R. 1968 : *Astrophys. J.*, **151**, 711.

Bai, T., and Ramaty, R. 1979 : *Astrophys. J.*, **227**, 1072.

Bai, T., and Dennis, B.R. 1985 : *Astrophys. J.*, **292**, 699.

Bai, T. 1986 : *Astrophys. J.*, **308**, 912.

Bai, T., and Sturrock, P.A. 1989 : *Ann. Rev. Astron. Astrophys.*, **27**, 421.

Batchelor, D.A., Crannell, C.J., Wiehl, H.J., and Magun, A. 1985 : *Astrophys. J.*, **295**, 258.

Benz, A.O. 1987 : *Solar Phys.*, **1987**, 1.

Bevington, P.R. 1969 : *Data Reduction and Error Analysis for the Physical Sciences*, (McGraw-Hill, New York).

Bradt, H., Garmire, G., Oda, M., Spada, G., Sreekantan, B.V., Gorenstein, P., and Grusky, H. 1968 : *Space Sci. Rev.*, **8**, 471.

Brown, J.C. 1971 : *Solar Phys.*, **18**, 489.

Brown, J.C. 1974 : in *Solar γ-, X-, and EUV Radiation*, ed. Kane, S.R., Joint AIS-COSPAR Symp., No.68, (Reidel, Dordrecht), pp.245.

Brown, J.C., and Hoyng, P. 1975 : *Astrophys. J.*, **200**, 734.

Brown, J.C., Melrose, D., and Spicer, D.S. 1979 : *Astrophys. J.*, **228**, 592.

Burnight, T.R. 1949 : *Phys. Rev.*, **76**, 165.

Byram, E.T., Chubb, T.A., and Friedman, H. 1956 : *J. Geophys. Res.*, **61**, 251.

Canfield, R.C., Metcalf, T.R., Strong, K.T., and Zarro, D.M. 1987 : *Nature*, **326**, 165.

Canfield, R.C., Zarro, D.M., Metcalf, T.R., and Lemen, J.R. 1990 : *Astrophys. J.*, **348**, 333.

Canfield, R.C., Hudson, H.S., Leka,K.D., Mickey, D.L., Metcalf, T.R., Wuelser, J.-P., Acton, L.W., Strong, K.T., Kosugi, T., Sakao, T., Tsuneta, S., Culhane, J.L., Phillips, A., and Fludra, A. 1992 : *Publ. Astron. Soc. Japan*, **44**, L111.

Canfield, R.C., Blais, K.A., McClymont, A.N., Metcalf, T.R., Reardon, K.P., Wülser, J.-P., Acton, L.W., Kurokawa, H., and Hirayama, T. 1993 : in *Proc. International Yohkoh Science Meeting* (Tokyo, Japan), in press.

Chubb, T.A., Kreplin, R.W., and Friedman, H. 1966 : *J. Geophys. Res.*, **71**, 3611.

Cliver, E.W., Dennis, B.R., Kiplinger, A.L., Kane, S.R., Neidig, D.F., Sheeley, N.R., Jr., and Koomen, M.J. 1986 : *Astrophys. J.*, **305**, 920.

Craig, I.J.D., and Brown, J.C. 1976 : *Astron. Astrophys.*, **49**, 239.

Crannell, C.J., Frost, K.J., Matzler, C., Ohki, K., and Saba, J.L. 1978 : *Astrophys. J.*, **223**, 620.

Culhane, J.L., Hiei, E., Doschek, G.A., Cruise, A.,M., Ogawara, Y., Uchida, Y., Bentley, R.,D., Brown, C.,M., Lang, J., Watanabe, T., Bowles, J.A., Deslattes, R.D., Feldman, U., Fludra, A., Guttridge, P., Henins, A., Lapington, J., Magraw, J., Mariska, J.T., Payne, J., Phillips, K.J.H., Sheather, P., Slater, K., Tanaka, K., Towndrow, E., Trow, M.W., and Yamaguchi, A. 1991 : *Solar Phys.*, **136**, 89.

Culhane, J.L., Phillips, A.T., Pike,C.D., Fludra, A., Bentley, R.D., Bromage, B., Doschek, G.A., Hiei, E., Inda, M., Mariska, J.T., Phillips, K.J.H., Sterling, A.C., and Watanabe, T. 1993 : *Adv. Space Res.*, **13**, No.9, 303.

Culhane, J.L., Phillips, A.T., Inda-Koide, M., Kosugi, T., Fludra, A., Kurokawa, H., Makishima, K., Pike, C.D., Sakao, T., Sakurai, T., Doschek, G., and Bentley, R.D. 1994 : in preparation.

Dennis, B.R., Frost, K.J., and Orwig, L.E. 1981 : *Astrophys. J. Lett.*, **244**, L167.

Dennis, B.R. 1982 : *OSO-8 Internal Technical Memorandum*, NASA Goddard Space Flight Center, (Greenbelt, Maryland).

Dennis, B.R. 1985 : *Solar Phys.*, **100**, 465.

Dennis, B.R. 1988 : *Solar Phys.*, **118**, 49.

Dennis, B.R. and Schwartz, R.A. 1989 : *Solar Phys.*, **121**, 75.

Dermer, C.D., and Ramaty, R. 1986 : *Astrophys. J.*, **301**, 962.

Doscheck, G. 1983 : *Solar Phys.*, **86**, 9.

Dreicer, J. 1959 : *Phys. Rev.*, **115**, 238.

Duijveman, A., Hoyng, P., and Machado, M.E. 1982 : *Solar Phys.*, **81**, 137.

Dulk, G.A. 1985 : *Ann. Rev. Astron. Astrophys.*, **23**, 169.

Elcan, M.J. 1978 : *Astrophys. J. Lett.*, **226**, L99.

Emslie, A.G., and Brown, J.C. 1985 : *Astrophys. J.*, **295**, 648.

Feldman, U., Doschek, G.A., and Kreplin, R.W. 1982 : *Astrophys. J.*, **260**, 885.

Fisher, G.H. 1989 : *Astrophys. J.*, **346**, 1019.

Frieden, B.R. 1972 : *J. Opt. Soc. Am.*, **62**, 511.

Frost, K.J. 1969 : *Astrophys. J. Lett.*, **158**, L159.

Frost, K.J., and Dennis, B.R. 1971 : *Astrophys. J.*, **165**, 655.

Gull, S.F. and Daniell, G.J. 1978 : *Nature*, **272**, 686.

Harrison, R.A. 1986 : *Astron. Astrophys.*, **162**, 283.

Heristchi, D. 1986 : *Astrophys. J.*, **311**, 474.

Högbom, J.A. 1974 : *Astron. Astrophys. Suppl.*, **15**, 417.

Holman, G.D. 1985 : *Astrophys. J.*, **293**, 584.

Hoyng, P., Brown, J.C., and van Beek, H.F. 1976 : *Solar Phys.*, **48**, 197.

Hoyng, P., Machado, M.E., Duijveman, A., Boelee, A., de Jager, C., Fryer, R., Galama, M., Hoekstra, R., Imhof, J., Lafleur, H., Maseland, H.V.A.M., Mels, W.A., Schadee, A., Schrijver, J., Simnett, G.M., Svestka, Z., van Beek, H.F., van Tend, W., van der Laan, J.J.M., van Rens, P., Werkhoven, F., Willmore, A.P., Wilson, J.W.G., and Zandee, W. 1981 : *Astrophys. J. Lett.*, **244**, L153.

Hudson, H.S. 1972 : *Solar Phys.*, **24**, 414.

Hudson, H.S., Canfield, R.C., and Kane, S.R. 1978 : *Solar Phys.*, **60**, 137.

Hudson, H.S. 1991 : *Bull. Am. Astron. Soc.*, **23**, 1064.

Hudson, H.S., Acton, L.W., Hirayama, T., and Uchida, Y. 1992 : *Publ. Astron. Soc. Japan*, 44, L77.

Hudson, H.S., Strong, K.T., Dennis, B.R., Zarro, D., Inda, M., Kosugi, T., and Sakao, T. 1994 : *Astrophys. J. Lett.*, in press.

Hurley, K., Sommer, M., Atteia, J.-L., Boer, M., Cline, T. Cotin, F., Henoux, J.-C., Kane, S., Lowes, P., Niel, M., Van Rooijen, J., and Vedrenne, G. 1992 : *Astron. Astrophys. Suppl.*, **92**, 401.

Ichimoto, K. and Kurokawa, H. 1984 : *Solar Phys.*, **93**, 105.

Inda, M. 1991 : Master Thesis, University of Tokyo (written in Japanese).

Inda-Koide, M. 1993 : PhD Thesis., University of Tokyo.

Jackson, J.D. 1962 : *Classical Electrodynamics*, (J.Wiley and Sons, New York).

Johns, C.M., and Lin, R.P. 1992 : *Solar Phys.*, **137**, 121.

Kahler, S.W. 1971*a* : *Astrophys. J.*, **164**, 365.

Kahler, S.W. 1971*b* : *Astrophys. J.*, **168**, 319.

Kahler, S.W., Moore, R.L., Kane, S.R., and Zirin, H. 1988 : *Astrophys. J.*, **328**, 824.

Kahler, S.W. 1992 : *Ann. Rev. Astron. Astrophys.*, **30**, 113.

Kai, K., Kosugi, T., and Nitta, N. 1985 : *Publ. Astron. Soc. Japan*, **37**, 155.

Kane, S.R. 1969 : *Astrophys. J.*, **157**, L139.

Kane, S.R., and Anderson, K.A. 1970 : *Astrophys. J.*, **162**, 1003.

Kane, S.R. 1974 : in *Coronal Disturbances*, ed. Newkirk, G., Proc. IAU Symp. No. 57, (Reidel, Dordrecht), pp.105.

Kane, S.R., Frost, K.J., and Donnelly, R.F. 1979 : *Astrophys. J.*, **234**, 669.

Kane, S.R., McTiernan, J.M., Loran, J., Lemen, L., Yoshimori, M., Ohki, K., and Kosugi, T. 1993*a* : *Adv. Space Res.*, **13**, No.9, 237.

Kane, S.R., Hurley, K., McTiernan, J.M., and Sommer, M. 1993*b* : *Adv. Space Res.*, **13**, No.9, 241.

Kawabata, K., Ogawa, H., and Suzuki, I 1983 : *Solar Phys.*, **86**, 247.

Kawabata, K., Yoshimori, M., Suga, K., Morimoto, K., Hiraoka, T., Sato, J., and Ohki, K. 1993 : *Astrophys. J. Suppl.*, in press.

Kennel, C.F., 1969 : *Rev. Geophys.*, **7**, 379.

Kiplinger, A.L., Dennis, B.R., Frost, K.J., and Orwig, L.E. 1983 : *Astrophys. J.*, **273**, 783.

Knoepfel, H., and Spong, D.A. 1979 : *Nucl. Fusion*, **19**, 785.

Kondo, I. 1982 : in *Proc. Hinotori Symp. on Solar Flares*, eds. Tanaka, Y. Tanaka, K., Matsuoka, M., Ohki, K., Kondo, I., Hirayama, T., and Nishi, K. (Institute of Space and Astronautical Science, Tokyo), pp.3.

Kosugi, T., Dennis, B.R., and Kai, K. 1988 : *Astrophys. J.*, **324**, 1118.

Kosugi, T., Makishima, K., Murakami, T., Sakao, T., Dotani, T., Inda, M., Kai, K., Masuda, S., Nakajima, H., Ogawara, Y., Sawa, M., and Shibasaki, K. 1991 : *Solar Phys.*, **136**, 17.

Kosugi, T., Sakao, T., Masuda, S., Makishima, K., Inda, M., Murakami, T., Ogawara, Y., Yaji, K., and Matsushita, K. 1992 : *Publ. Astron. Soc. Japan*, **44**, L45.

Kosugi, T. 1993 : in *Physics of Solar and Stellar Coronae*, eds. Linsky, J.F., and Serio, S. (Kluwer, Netherlands), pp.131.

Kreplin, R.W. 1961 : *Ann. Geophys.*, **152**, 17.

Kurokawa, H., Takakura, T., and Ohki, K. 1988 : *Publ. Astron. Soc. Japan*, **40**, 357.

Lin, R.P., and Hudson, H.S. 1976 : *Solar Phys.*, **50**, 153.

Lin, R.P., Schwartz, R.A., Pelling, R.M., and Hurley, K.C. 1981 : *Astrophys. J. Lett.*, **251**, L109.

Lin, R.P., Schwartz, R.A., Kane, S.R., Pelling, R.M., and Hurley, K.C. 1984 : *Astrophys. J.*, **283**, 421.

Lin, R.P., and Schwartz, R.A. 1987 : *Astrophys. J.*, **312**, 462.

Machado, M.E., 1991 : *Phil. Trans. R. Soc. Lond.* A., **336**, 425.

MacKinnon, A.L., Brown, J.C., and Hayward, J. 1985 : *Solar Phys.*, **99**, 231.

Makishima, K., Ogawara, Y., Miyamoto, S., Muranaka, N., and Oda, M. 1977 : *ISAS Research Note*, **29**, (Institute of Space and Astronautical Science, Tokyo).

Makishima, K. 1982 : in *Proc. Hinotori Symp. on Solar Flares*, eds. Tanaka, Y., Tanaka, K., Matsuoka, M., Ohki, K., Kondo, I., Hirayama, T., and Nishi, K. (Institute of Space and Astronautical Science, Tokyo), pp.120.

Makishima, K., Miyamoto, S., Murakami, T., Nishimura, J., Oda, M., Ogawara, Y., and Tawara, Y. 1978 : in *New Instrumentation for Space Astronomy*, eds. Van Hucht, K. and Vaiana, G.S. (Pergamon, New York), pp.277.

Masuda, S. 1993 : PhD Thesis., University of Tokyo.

Matsushita, K., Masuda, S., Kosugi, T., Inda, M., and Yaji, K. 1992 : *Publ. Astron. Soc. Japan*, **44**, L89.

Mätzler, C., Bai, T., Crannell, C.J., and Frost, K.J. 1978 : *Astrophys. J.*, **223**, 1058.

McTiernan, J.M., Kane, S.R., Loran, J.M., Lemen, J.R., Acton, L.W., Hara, H., Tsuneta, S., and Kosugi, T. 1993 : *Astrophys. J. Lett.*, **416**, L91.

Melrose, D.B. and Brown, J.C 1976 : *Monthly Notices Roy. Astron. Soc.*, **176**, 15.

Mickey, D.L. 1975 : *Solar Phys.*, **97**, 223.

Morrison, M.D., Lemen, J.R., Acton,L.W., Bentley, R.D., Kosugi,T., Tsuneta, S., Ogawara, Y., and Watanabe, T. 1991 : *Solar Phys.*, **136**, 105.

Mozer, F.S., Cattell, C.A., Hudson, M.K., Lysak, R.L., Temerin, M., and Torbert, R.B. 1980 : *Space Sci. Rev.*, **27**, 155.

Nariai, K. : 1987, *Appl. Optics*, **26**, 4428.

Nariai, K. : 1987, *Appl. Optics*, **27**, 345.

Neupert, W.M. 1968 : *Astrophys. J. Lett.*, **153**, L59.

Nitta, N., Dennis, B.R., and Kiplinger, A.L. 1990 : *Astrophys. J.*, **353**, 313.

Oda, M. 1983 : *Adv. Space Res.*, **2**, No.4, 207.

Ogawara, Y., Takano, T., Kato, T., Kosugi, T., Tsuneta, S., Watanabe, T., Kondo, I., and Uchida, Y. 1991 : *Solar Phys.*, **136**, 1.

Orwig, L.E., Frost, K.J., and Dennis, B.R. 1980 : *Solar Phys.*, **65**, 25.

Peterson, L.E., and Winckler, J.R. 1959 : *J. Geophys. Res.*, **64**, 697.

Petrosian, V. 1985 : *Astrophys. J.*, **209**, 987.

Rust, D.M. and Hegwer, F. 1975 : *Solar Phys.*, **40**, 141.

Sakai, J.-I., and Ohsawa, Y. 1987 : *Space Sci. Rev.*, **46**, 113.

Sakao, T., Kosugi, T., Masuda, S., Inda, M., Makishima, K., Canfield, R.C., Hudson, H.S., Metcalf, T.R., Wuelser, J.-P., Acton, L.W., and Ogawara, Y. 1992 : *Publ. Astron. Soc. Japan*, 44, L83.

Sakao, T. Kosugi, T., Masuda, S., Yaji, K., Inda-Koide, M., and Makishima, K. 1993 : in *Proc. International Yohkoh Science Meeting* (Tokyo, Japan), in press.

Sakurai, T. 1983 : *Solar Phys.*, **86**, 339.

Sakurai, T. 1985 : *Solar Phys.*, **95**, 311.

Sakurai, T. 1991 : Okayama Observatory Solar Vector Magnetograms.

Sakurai, T. 1991 : *Phil. Trans. R. Soc. Lond.* A., **336**, 339.

Sakurai, T. 1992 : Okayama Observatory Solar Vector Magnetograms.

Sawa, M. *et al.* 1993 : in preparation.

Shimabukuro, F.I. 1972 : *Solar Phys.*, **23**, 169.

Simnett, G.M. 1986 : *Solar Phys.*, **106**, 165.

Simnett, G.M. 1991 : *Phil. Trans. R. Soc. Lond.* A **336**, 439.

Simnett, G.M. and Haines, M.G. 1991 : *Solar Phys.*, **130**, 253.

Smith, D.F., and Lilliequist, C.G. 1979 : *Astrophys. J.*, **232**, 582.

Spitzer, L., Jr. 1962 : *Physics of Fully Ionized Gases*, 2nd ed. (Interscience, New York).

Švestka, Z. 1976 : *Solar Flares*, (Reidel, Dordrecht), pp.140.

Syrovatskii, S.I. 1966 : *Soviet Astron. AJ.* **10**, 270.

Takakura, T. 1960 : *Publ. Astron. Soc. Japan*, **12**, 55.

Takakura, T., and Kai, K. 1966 : *Publ. Astron. Soc. Japan*, **18**, 57.

Takakura, T. 1969 : *Solar Phys.*, **6**, 122.

Takakura, T., Ohki, K., Shibuya, N., Fujii, M., Matsuoka, M., Miyamoto, S., Nishimura, J., Oda, M., Ogawara, Y., and Ota, S. 1971 : *Solar Phys.*, **16**, 454.

Takakura, T., 1983 : *Astrophys. J. Lett.*, **270**, L83.

Takakura, T., Tanaka, K., and Hiei, E. 1984*a* : *Adv. Space Res.*, **4**, 143.

Takakura, T., Ohki, K., Sakurai, T., Wang, J.L., Xuan, J.Y., Li, S.C., and Zhao, R.Y. 1984*b* : *Solar Phys.*, **94**, 359.

Tanaka, K., Watanabe, T., Nishi, K., and Akita, K. 1982 : *Astrophys. J. Lett.*, **254**, L59.

Tanaka, K. 1983 : in *Activity in Red-Dwarf Stars*, eds. Byrne, P.B., and Rodonò, M., IAU Coll. 71, (Reidel, Dordrecht), pp.307.

Tanaka, K., Nitta, N., Akita, K., and Watanabe, T. 1983 : *Solar Phys.*, **86**, 91.

Tanaka, K., and Zirin, H. 1985 : *Astrophys. J.*, **299**, 1036.

Tanaka, K. 1986 : *Publ. Astron. Soc. Japan*, **38**, 225.

Tanaka, K. 1987 : *Publ. Astron. Soc. Japan*, **39**, 1.

Tanaka, K. and Zirin, H. 1985 : *Astrophys. J.*, **299**, 1036.

Tanaka, Y. 1983 : *Solar Phys.*, **86**, 3.

Trubnikov, B.A., 1965 : in *Reviews of Plasma Physics*, Vol.1, (Consultants Bureau, New York), pp.205.

Tsuneta, S. 1983 : in *Proc. of Japan-France Seminar on Active Phenomena in the Outer Atmosphere of the Sun and Stars*, eds. Pecker, J.C., and Uchida, Y., CNRS and L'Observatoire de Paris, (Paris, France), pp.243.

Tsuneta, S., Takakura, T., Nitta, N., Ohki, K., Tanaka, K., Makishima, K., Murakami, T., Oda, M., and Ogawara, Y. 1984*a* : *Astrophys. J.*, **280**, 887.

Tsuneta, S., Nitta, N., Ohki, K., Takakura, T., Tanaka, K., Makishima, K., Murakami, T., Oda, M., and Ogawara, Y. 1984*b* : *Astrophys. J.*, **284**, 827.

Tsuneta, S. 1985 : *Astrophys. J.*, **290**, 353.

Tsuneta, S. 1987 : *Solar Phys.*, **113**, 35.

Tsuneta, S., Acton, L., Bruner, M., Lemen, J., Brown, W., Caravalho, R., Catura, R., Freeland, S., Jurcevich, B., Morrison, M., Ogawara, Y., Hirayama, T., and Owens, J. 1991 : *Solar Phys.*, **136**, 37.

Van Beek, H., Hoyng, P., Lafleur, B., and Simnett, G.M. 1980 : *Solar Phys.*, **65**, 39.

Vaiana, G.S., Reidy, W.P., Zehnpfennig, T., Van Speybroeck, L, and Giacconi, R. : 1968, *Science*, **161**, 564.

Vestrand, W.T., Forrest, D.J., Chupp, E.L., Rieger, E., and Share, G.H. 1987 : *Astrophys. J.*, **322**, 1010.

Vilmer, N., Kane, S.R., and Trottet, G. 1982 : *Astron. Astrophys.*, **108**, 306.

Vlahos, L, and Papadopoulos, K. 1979 : *Astrophys. J.*, **233**, 717.

Vlahos, L., Machado, M.E., Ramaty, R., Murphy, R.J., Allisandrakis, C., Bai, T., Batchelor, D., Benz, A.O., Chupp, E., Ellison, D., Evenson, P., Forrest, D.J., Holman, G., Kane, S.R., Kaufmann, P., Kundu, M.R., Lin, R.P., Mackinnon, A., Nakajima, H., Pesses, M., Pick, M., Ryan, J., Schwartz, R.A., Smith, D.F., Trottet, G., Tsuneta, S., and Van Hoven, G. 1984 : in *Energetic Phenomena in Solar Flares*, Proc. of SMM Workshop, eds. Kundu, M.R., and Woodgate, B., Chapter 2.

Willingale, R. 1981 : *Monthly Notices Roy. Astron. Soc.*, **194**, 359.

Winglee, R.M., Kiplinger, A.L., Zarro, D.M., Dulk, G.A., and Lemen, J.R. 1992 : *Astrophys. J.*, **375**, 366.

Wu, S.T., de Jager, C., Dennis, B.R., Hudson, H.S., Simnett, G.M., Strong, K.T., Bentley, R.D., and Bornmann, P.L. 1986 : in *Energetic Phenomena on the Sun, SMM Flare Workshop Proceedings*, NASA CP–2376, eds. Kundu, M.R., and Woodgate, B.E., (Greenbelt, Maryland), Chapter 5.

Wülser, J.–P., Canfield, R.C., Acton, L.W., Culhane, J.L., Phillips, A., Fludra, A., Sakao, T., Masuda, S., and Kosugi, T. 1993 : in *Proc. International Yohkoh Science Meeting* (Tokyo, Japan), in press.

Wülser, J.–P., Canfield, R.C., Acton, L.W., Culhane, J.L., Phillips, A., Fludra, A., Sakao, T., Masuda, S., Kosugi, T., and Tsuneta, S. 1994 : *Astrophys. J.*, in press.

Yoshimori, M., Okudaira, K., Hirasima, Y., Igarashi, T., Akasaka, M., Takai, Y., Morimoto, K., Watanabe, T., Ohki, K., Nishimura, J., Yamagami, T., Ogawara, Y., and Kondo, I. 1991 : *Solar Phys.*, **136**, 69.

Yoshimori, M., Takai, Y., Morimoto, K., Suga, K., Ohki, K., Watanabe, T., Yamagami, T., Kondo, I., and Nishimura, J. 1992 : *Publ. Astron. Soc. Japan*, **44**, L51.

Zarro, D.M., Canfield, R.C., Strong, K.T., and Metcalf, T.R. 1988 : *Astrophys. J.*, **324**, 582.